Jacquin, Tom (2025) *Laser-induced graphene-based elastomer nanocomposites for soft sensing applications*. PhD thesis.

https://theses.gla.ac.uk/85655/

Laser-Induced Graphene-Based Elastomer Nanocomposites for Soft Sensing Applications

Tom Jacquin, MRes, MA

SUBMITTED IN FULFILMENT OF THE REQUIREMENTS FOR THE DEGREE OF
DOCTOR OF PHILOSOPHY

JAMES WATT SCHOOL OF ENGINEERING
COLLEGE OF SCIENCE & ENGINEERING

University of Glasgow

06 2025

Abstract

Laser-induced graphene (LIG) has gained significant attention as a multifunctional material for flexible and wearable sensor technologies due to its exceptional electrical conductivity, mechanical flexibility, and tunable properties. This thesis presents a comprehensive study of the fabrication, characterization, and application of LIG-polymer nanocomposites, emphasizing the optimization of their electromechanical and thermomechanical performance for soft strain sensing applications.

The fabrication process emphasizes the precise tailoring of LIG properties through controlled laser processing and strategic composite design. In addition to doping LIG with conductive nanoparticles to enhance electrical sensitivity and structural robustness, the integration of LIG with polymer matrices such as PDMS was systematically optimized to modulate the composite's mechanical flexibility and thermal responsiveness. The effects of laser parameters, substrate interactions, and doping strategies on the microstructure, porosity, and conductivity of the LIG network were thoroughly investigated. This approach enabled the tuning of both electromechanical and thermomechanical behaviour to suit soft sensing applications. Environmental factors, including humidity and temperature, were also considered, as they significantly influence the stability and performance of the composite in real-world conditions.

In addition to experimental advancements, the development of a LabVIEW/Python platform for electromechanical testing is highlighted. This platform provided an efficient and precise system for characterizing the strain-resistance behaviour of LIG-polymer composites, enabling the acquisition of high-resolution data critical to this work.

A theoretical model was developed to elucidate the relationship between strain distribution and resistance in LIG-polymer composites. The model incorporates Gaussian strain distributions and integrates experimental resistance-strain data with finite element simulations to quantify the effective resistance under thermal and mechanical loads. Simulations of strain distribution under thermal expansion revealed that temperature-induced narrowing of strain distributions significantly impacts the composite's resistance response.

Applications of the LIG-polymer composites were explored across diverse fields, including healthcare and robotics, demonstrating the potential of these sensors for wearable health monitoring, soft robotics, and adaptive environmental sensing. Experimental results validated the proposed models and highlighted the influence of laser processing and doping on sensor performance, enabling a deeper understanding of the interplay between material properties and device functionality.

By bridging experimental characterization, theoretical modelling, and practical application, this thesis advances the development of LIG-based strain sensors, providing a foundation for future innovations in soft and wearable electronics.

Contents

Abstract iii

Acknowledgements xiv

Declaration xv

Abbreviations xvi

Papers and conferences xviii

Funding xix

1 Introduction 1
- 1.1 Overview 1
- 1.2 Motivation 1
- 1.3 Objectives 2
- 1.4 Thesis organisation 3

2 Literature Review 6
- 2.1 Graphene 6
- 2.2 Laser induced graphene 9
  - 2.2.1 LIG production techniques 9
  - 2.2.2 Properties of LIG for Sensor Applications 13
  - 2.2.3 Applications of LIG sensors 15
- 2.3 Conventional Soft Strain Sensors 18
  - 2.3.1 Working Principle of Resistive Strain Sensors 19
  - 2.3.2 Improvement Strategies for Resistive Strain Sensors 20
  - 2.3.3 Challenges in Conventional Strain Sensors 24
- 2.4 LIG-Polymer Composites for Soft Strain Sensors 30
  - 2.4.1 Advantages of LIG-Based Soft Strain Sensors 31
- 2.5 Common Applications of LIG-nanocomposites Sensors 31
  - 2.5.1 Healthcare and Wearable Sensors 32
- 2.6 Summary 36

3 Methodology 38
- 3.1 Introduction 38
- 3.2 LIG and LIG-Nanocomposites Manufacturing 39
- 3.3 Material characterisation 40
- 3.4 Mechanical characterization 44
  - 3.4.1 Performance Metrics for Strain Sensors 44
  - 3.4.2 Strain Measurements 44

3.5 Centralized system 46
3.6 Thermal Characterization 48
3.7 Wi-Fi and Bluetooth Communication 49
3.8 Conclusion 51

4 LIG nanocomposites 52
4.1 Introduction 52
4.2 LIG Formation 53
    4.2.1 Laser Characteristics 53
4.3 Parameters Affecting LIG Formation 54
    4.3.1 Influence of Laser Power on LIG Resistance 54
    4.3.2 Effect of Scanning Speed on LIG Resistance 56
    4.3.3 Impact of Focal Distance on LIG Resistance 57
    4.3.4 Effect of PPI on LIG Resistance 57
    4.3.5 Structural Characterization 58
4.4 LIG nanocomposites 62
    4.4.1 Fabrication 62
    4.4.2 Electromechanical properties 65
    4.4.3 Influence and Optimization of Laser Parameters 65
    4.4.4 Impact of Multiple Laser Passes and Lasing Orientation 66
    4.4.5 Summary of Findings 70
    4.4.6 Selection of Optimal Parameters for Subsequent Work 71
    4.4.7 Influence of Strain Frequency 72
    4.4.8 Fatigue Testing 74
    4.4.9 Influence of design 76
    4.4.10 Theoretical Model 78
4.5 Conclusion 80

5 Heat Insensitive LIG Strain Sensors 81
5.1 Introduction 81
5.2 Heat Sensitivity of LIG 82
5.3 Static Heat Sensitivity of LIG-PDMS Composites 82
5.4 Dynamic Heat sensitivity of LIG-PDMS composites 85
    5.4.1 Theoretical model 87
    5.4.2 Model Limitations 90
5.5 Conclusion 92

6 Wettability control of LIG 93
6.1 Introduction 93
6.2 Theoretical framework 94
6.3 Contact angle measurements 95
6.4 Results 96
6.5 Hygroscopy 98
6.6 Conclusion 101

7 LIG nanocomposites doping 102
7.1 Introduction 102
7.2 Overview of LIG Doping Strategies 103
    7.2.1 One-Step In Situ Modification 103
    7.2.2 Multi-Step Approaches: Duplicated Laser Pyrolysis Method 103

7.2.3 Advancements in LIG Performance through Doping 106
7.3 Silver doping of LIG 106
7.3.1 Photoreduction of Silver Nitrate to Elemental Silver 107
7.3.2 Preparation of the Samples 107
7.3.3 Material characterisation 109
7.4 Silver Nanowire Doping of LIG 120
7.4.1 Fabrication 120
7.4.2 Characterization 121
7.5 Conclusion 122

8 Applications 124
8.1 Introduction 124
8.2 Body Movement Monitoring 125
8.2.1 Variability Across Individuals 126
8.2.2 Influence of Sensor Placement 127
8.2.3 Future Directions and Challenges 129
8.3 Respiration monitoring LIG strain sensors 129
8.3.1 Breathing Detection 130
8.4 Actuators 137
8.5 Conclusion 143

9 Conclusion and Future perspectives 144
9.1 Conclusion 144
9.2 Challenges and Future Perspectives 145

List of Tables

2.1 Performance Comparison of Stretchable Strain Sensors 28

4.1 Oxygen content for samples manufactured at high fluence (7% speed) and low fluence (13% speed) 61

List of Figures

1.1 Thesis chapters organisation 5

2.1 Annual Growth in Graphene Research: Number of Publications Per Year 7
2.2 a)The two graphene sub-lattices (red and blue) and unit cell; b)Sigma and pi bonds in graphene; c)Electronic band structure of metals, insulators and graphene. 8
2.3 Annual Growth in LIG Research: Number of Publications Per Year 9
2.4 Proposed thermal decomposition of PI according to [17]. 10
2.5 a) Schematic showing the influence of focal plane distance on LIG formation; b) Schematic illustrating the influence of DPI and PPI settings on LIG formation. 11
2.6 Various carbon sources used for LIG production: a) Food sources such as bread, coconut, and potato [18]; b) Leaves [24]; c) Wood [25]; d) Paper [26]; e) Fabrics [27]; f) PI [16]. Adapted from [28] 12
2.7 Various modifications and fabrication approaches for LIG: a) Morphology control through laser parameter optimization [29]; b) Property tuning using controlled atmospheres [35]; c) LIG doping and composites; d) Transfer of LIG to polymers; e) LIG functionalization for biosensors; f) Creation of three-dimensional LIG structures [36]. Adapted from [28]. 13
2.8 Examples of LIG-based gas sensors: a) LIG-Pd composite sensor for hydrogen (H_2) detection, leveraging palladium's affinity for hydrogen molecules [49]; b) Stretchable LIG sensor for nitrogen oxides (NO_x) monitoring, demonstrating resilience under mechanical deformation [50]; c) Cement-embedded LIG sensor for multi-gas detection in industrial applications [39]; d) LIG-MoS_2 composite sensor for NO_2 detection, utilizing the synergistic effects of molybdenum disulfide and LIG to enhance sensitivity and selectivity [51]. 16
2.9 Examples of LIG-based energy storage devices: a) Overview of LIG-based energy storage technologies, highlighting their potential for integration with flexible and wearable electronics [55]; b) LIG-MnO -based flexible, symmetric, and asymmetric MSCs demonstrating high capacitance and stable cycling performance [53]; c) Electrochemical performance comparison of LIG-MSCs with varying H_3BO_3 loadings, showcasing the impact of boron doping on capacitance enhancement [54]; d) Nitrogen-doped LIG electrodes with conductive poly(3,4-ethylenedioxythiophene) (PEDOT) coating, demonstrating improved charge storage capability and energy efficiency [52]. 18
2.10 Simulation of inter-particle distance distribution in a conductive dispersion: a) Schematic representation of conductive particle displacement under uniaxial strain, assuming a Poisson's ratio of zero; b) Statistical distribution of inter-particle distances, where the average separation is indicated by the dotted line. 19

2.11 (a)-(c) Schematic illustration of flexible EGaIn strain sensor fabrication (adapted from [68, 69]). (b)-(d) Example of a soft strain sensor utilizing EGaIn (adapted from [69, 70]). 21
2.12 a) CNT-PDMS composite fabrication schematic (adapted from [73]); b) Alternative CNT-PDMS fabrication approach (adapted from [74]); c) CB-PDMS composite fabrication schematic (adapted from [75]). 22
2.13 Performance summary of soft strain sensors 30
2.14 LIG-based strain sensors for motion monitoring applications: a) LIG-PDMS nanocomposite sensor demonstrating high flexibility and responsiveness for diverse motion detection [158]; b) LIG-PDMS-based wearable sensor for real-time sports motion monitoring, enabling performance optimization and injury prevention [160]; c) LIG-PI nanocomposite sensor applied for joint movement analysis and sleep monitoring, highlighting its potential in clinical and biomedical applications [159]. 33
2.15 LIG-based smart textiles for wearable sensing applications: a) Direct laser-patterned LIG on woven, non-woven, and knit textiles, highlighting its adaptability to different fabric structures [163]; b) LIG-based e-textile on Kevlar, demonstrating high mechanical robustness for demanding applications [162]; c) Multifunctional textile sensors integrated with textile-based metamaterials, enabling cross-body communication and advanced wearable functionalities [161]. 34
2.16 LIG-based sensors for advanced human-machine interfaces and robotics: a) Lip-reading recognition system using LIG-based sensors for silent speech detection [164]; b) LIG-based TENGS enabling simultaneous wireless control and tactile pattern recognition [165]; c) Enhanced LIG sensors incorporating gold nanoparticles and titanium oxide for robotic arm control [166]; d) LIG-based PI-PDMS bi-structure for real-time EMG monitoring and human–soft actuator interaction [167]. 36

3.1 Chapter 3 Objectives Flowchart 39
3.2 a) Schematic overview of the LIG-nanocomposites fabrication process; b) LIG formed on a thin PI substrate; c) LIG-PDMS nanocomposite being peeled from a thick PI substrate; d) Complete LIG-PDMS sensor with integrated electrodes. 40
3.3 Example results from the characterization of LIG: a) Raman spectrum of LIG synthesized from commercial PI, highlighting key vibrational modes; b) X-Ray Diffraction (XRD) pattern of powdered LIG extracted from the PI film, indicating its crystallinity [16]; c)SEM image showcasing the surface morphology of LIG; d)EDX data for a sample of LIG, providing elemental composition analysis. 42
3.4 Schematic of the horizontal stage setup, showing the integration of the Zaber motorized linear stage and the custom 3D-printed/laser-cut sample holder. . . 45
3.5 User interface for the LabVIEW-based control program, enabling precise control of the motorized stage and data acquisition system. 46
3.6 User interface for the Python-based control program, offering flexibility in strain application and data visualization. 47
3.7 Schematics of the centralized system for tool control and data collection . . . 48
3.8 a) Heated 3D Printer Bed setup; b) Humidity chamber 49
3.9 a) Wiring diagram of the wireless module; b) Chip housing and sensors attached 51

4.1 Chapter 4 Objectives Flowchart 53
4.2 a) Graphene quality from thick PI film; b) Graphene quality from thin PI film. 55
4.3 Influence of laser power on the electrical resistance of LIG. 56
4.4 Influence of laser speed on the electrical resistance of LIG. 56
4.5 Influence of laser focal offset on the electrical resistance of LIG. 57
4.6 Influence of PPI settings on the electrical resistance of LIG. 58
4.7 a) Raman spectra of LIG samples fabricated at different laser speeds with a fixed power of 20%; b) Raman spectra of LIG samples fabricated at different laser powers with a fixed speed of 8%. 59
4.8 a) Distribution of I_D and I_G values; b) I_D/I_G ratio for LIG samples fabricated at different laser speeds with a fixed power of 20%; c) I_D/I_G ratio for LIG samples fabricated at different laser powers with a fixed speed of 8%. 60
4.9 a) SEM images of a 20_7 LIG sample at different magnifications; b) SEM images of a 20_13 LIG sample at different magnifications. 61
4.10 a) Schematic of the LIG-composite fabrication process; b) Photograph of the LIG-composite at rest and under torsion, illustrating its flexibility; c) Nanocomposite sensor image illustrating the electrode attachment. 64
4.11 SEM image of a LIG-PDMS nanocomposite at different magnifications. a) At 1000x; b) At 10,000x. 64
4.12 Maximum relative change in resistance for different LIG-PDMS composites manufactured with varying laser settings. a) Effect of laser power at 20% strain; b) Effect of laser speed at 20% strain. 65
4.13 a Cyclic testing at 20% strain for a 14_7 sample; b) Filtered data using a Savitzky-Golay filter applied to the 14_7 sample data; c) Cyclic testing at 20% strain for a 20_7 sample. 66
4.14 Examples of linearity evaluation: a) A highly linear sample with a high R^2 value; b) A non-linear sample with a lower R^2 value. 68
4.15 Illustration of drift measurement across 20 loading cycles, showing resistance peak evolution. 68
4.16 Schematic representation of hysteresis evaluation by integrating the absolute difference between loading and unloading curves. 69
4.17 Performance assessment of the fabricated sensors: a) R^2 values for loading (blue) and unloading (red) phases across various samples, indicating the linearity of sensor response; b) Hysteresis values as defined in Equation 4.4, reflecting energy loss during strain cycles; c) Drift values calculated using Equation 4.3, demonstrating sensor stability over multiple cycles. 70
4.18 Absolute resistance change for a single LIG-based strain sensor subjected to cyclic strain at four different periods, maintaining constant strain amplitude. . 72
4.19 Absolute resistance change for a single LIG-based strain sensor subjected to cyclic strain at four different periods, plotted against the number of cycles. . . 73
4.20 Ratio of the initial maximum relative resistance change to the relative resistance change after 200 cycles for sensors tested at different periods. 73
4.21 Decay constants (τ) obtained from exponential fits for sensors tested at various strain periods. Lower τ values indicate faster stabilization. 74
4.22 Relative change in resistance between consecutive cycles for 1000 cycles of mechanical loading, with a 10-cycle rolling average applied to reduce noise. . . 75
4.23 a) Strain/Resistance curve for three different samples at 30% strain; b) Simulation result for the same samples shown in A; c) Strain distribution across all three samples according to the simulation. 77

4.24 Comparison between experimental resistance values and theoretical predictions derived from simulation results at 15% applied strain. The experimental data (solid line) and simulated results (dashed line) are overlaid to illustrate deviations and alignment. 79

5.1 Chapter 5 Objectives Flowchart 81
5.2 Temperature-dependent resistance profiles of raw graphene samples manufactured under varying speed and power conditions. Solid lines represent average responses, and shaded areas depict the range of measurements. a) Resistance change for samples 20_13, 20_10, and 20_7 (constant power, varying speed); b) Resistance change for samples 20_7, 17_7, and 14_7 (constant speed, varying power). 83
5.3 Temperature-dependent resistance profiles of LIG-PDMS composites. Solid lines represent average responses, and shaded areas depict the range of measurements. a) Resistance change for composites 20_13, 20_10, and 20_7 (constant power, varying speed); b) Resistance change for composites 20_7, 17_7, and 14_7 (constant speed, varying power). 84
5.4 Illustration of PDMS expansion under heating. 85
5.6 Experimental setup for dynamic heating tests, where a heat gun was secured above the samples on the moving stage to record the electrical response during temperature variations. 85
5.5 Evaluation of heat sensitivity and strain sensitivity for LIG-PDMS composites. a) Heat sensitivity, assessed through the slope of resistance change curves in Figure 5.3; b) Gauge factor of the same sensors, representing strain sensitivity; c) Ratio of heat sensitivity to gauge factor, illustrating the balance between thermal and strain responses. 86
5.7 a) Effect of heating on samples during cyclic stretching (10% strain applied) at high cycle speed; b) Effect of heating on strain testing at slower cycle speed (10% strain applied); c) Effect of heating on samples during static loading (10% strain applied); d) Effect of strain on thermal sensitivity of the sensors for an optimised sample 86
5.8 a) Resistance versus strain for the 20_7 and 20_13 samples; b) Effective resistance as a function of σ for both samples. 89
5.9 a) Standard deviation of the strain distribution at various temperatures; b) Relative change in effective resistance as a function of temperature for the 20_7 and 20_13 samples. 90

6.1 Chapter 6 Objectives Flowchart 94
6.2 a) Interface of the custom Python application for contact angle measurement; b) Comparison of contact angle values obtained using the DSA30 software and the custom-built software, highlighting the accuracy and reliability of the custom tool. 95
6.3 Contact angle measurements for LIG samples prepared with different laser parameters, demonstrating tunable wettability ranging from super-hydrophobic to complete wettability. 96
6.4 a) LIG sample engineered for super-hydrophobicity, demonstrating minimal liquid spreading; b) LIG sample engineered for complete wettability, showing rapid liquid infiltration into the graphene network. 97

6.5 a) Chequerboard pattern on PI film demonstrating combined hydrophilic and hydrophobic regions; b) Tonic water illuminated under UV light, highlighting the controlled liquid containment within the patterned areas. 98
6.6 Relative change in resistance for LIG samples with different contact angles under varying humidity conditions. Higher contact angles, indicative of more hydrophobic surfaces, exhibit lower sensitivity to humidity due to reduced water penetration into the graphene network. 99
6.7 Relative change in resistance for two different LIG samples under varying humidity conditions. One set of samples exhibits a decrease in resistance with increasing humidity, likely due to enhanced capillary-driven reorganization in a more porous network. 100
6.8 Relative change in resistance for different LIG-PDMS nanocomposites exposed to varying humidity levels. A consistent 6% decrease is observed at 60% humidity, with low variance across laser conditions. 101

7.1 Chapter 7 Objectives Flowchart 102
7.2 Different strategies for LIG modification: a) Illustration of the duplicated laser pyrolysis method (adapted from [188]); b) Illustration of incorporating dopants by mixing them directly into the substrate (adapted from [186]); c) Illustration of adding a dopant layer on top of the substrate before laser processing (adapted from [189]). 105
7.3 Schematic illustration of the silver nitrate doping process onto LIG, followed by laser-assisted reduction. 108
7.4 Photographs of LIG samples doped with varying volumes of silver nitrate solution. A noticeable build-up of solid deposits is seen at the edges, increasing with the number of deposited drops. 109
7.5 Raman spectra of LIG samples produced with one or two laser passes, showing characteristic D and G bands. 110
7.6 Raman spectra of LIG samples doped with one drop of $AgNO_3$ and reduced at various laser powers. 110
7.7 Raman spectra of LIG samples doped with three drops of $AgNO_3$ and reduced at various laser powers. 111
7.8 Raman spectra of LIG samples doped with five drops of $AgNO_3$ and reduced at various laser powers. 111
7.9 Raman spectra of LIG samples doped with one drop of $AgNO_3$ but not reduced using the laser. The additional peak at lower wavenumbers is still observed. . . 112
7.10 SEM images of doped LIG samples. a-b) Doped with one drop of $AgNO_3$; c-d) Doped with five drops of $AgNO_3$; e-f) Doped with one drop of $AgNO_3$ but not reduced using a laser. 113
7.11 EDX analysis showing the elemental composition of Carbon, Oxygen, and Silver in the doped LIG samples. 114
7.12 XPS spectra of a pristine LIG sample, highlighting the Carbon 1s (~284 eV) and Oxygen 1s (~533 eV) peaks. 115
7.13 XPS spectra of LIG samples doped with one drop of $AgNO_3$ and reduced at different laser powers. 116
7.14 XPS spectra focusing on specific binding energy regions: a) Carbon 1s area; b) Oxygen 1s area; c) Ag 3d area. 117
7.15 XPS spectra highlighting the Nitrogen 1s (~400 eV) peak for samples doped with varying amounts of $AgNO_3$. 118

7.16 Electrical resistance of LIG prepared on thin PI films as a function of temperature, showing a negative TCR. 119
7.17 Electrical resistance of doped LIG samples as a function of temperature, showing an increase in TCR compared to the bare LIG. 120
7.18 FESEM images of silver nanowires on an ITO substrate at different magnifications: a) 2.5k, b) 4.5k, and c) 22k. 121
7.19 Electrothermal characterization of Ag-NWs doped LIG samples, showing a positive TCR, consistent with the metallic nature of silver nanowires. 122

8.1 Chapter 8 Objectives Flowchart 125
8.2 a) Sensors attached to a medical bandage and applied to a knee; b) Resistance data transmitted over Bluetooth for various movements. 126
8.3 Resistance data for different individuals during normal walking. 127
8.4 Influence of sensor placement on resistance data for gait monitoring. 128
8.5 a) Design modifications applied to the bandage, including the use of dental polymer; b) Size comparison between the original and reduced sensors. 131
8.6 a) Sensor placement at three different locations on the torso (image adapted from [200]); b) Comparative breathing patterns recorded at each location. . . 132
8.7 Comparison of breathing signal quality across the four different bandage designs. 132
8.8 a) Two rectangular sensors attached to the base-layer T-shirt; b) Breathing analysis with two sensors, during arm movement (one at a time). 133
8.9 a) ESP-32 for data collection and wireless communication; b) T-shirt affixed with two circular sensors connected to the ESP-32; c) Custom Python program for data visualization and processing. 134
8.10 Demonstration of the respiratory monitoring system using circular sensors during different activities: sitting, typing, standing, and walking. 135
8.11 Breathing data acquired for different individuals performing the same activity using the same device. 136
8.12 Impact of body morphology on data acquisition using the same T-shirt-based sensor system. 137
8.13 a) Actuator manufacturing process; b) Soft actuator deformation at different voltages; c) Relative resistance change of the soft actuator under an activation voltage of 20V. 139
8.14 a) Schematic of the topology sensing experiment; b) Relative resistance change during topology sensing; c) Schematic of the gripping experiment; d) Relative resistance change during the gripping experiment. 140
8.15 a) Sensor on a hill: minimal deformation and low electrical resistance; b) Sensor in a valley: maximum deformation and high electrical resistance. 140
8.16 Experimental images of the gripping process: a) initial stage with no contact; b) intermediate stage with gradual resistance increase due to deformation; c) final stage with complete contact and stabilized resistance. 142

Acknowledgements

First and foremost, I would like to express my deepest gratitude to my supervisor, Dr. Morteza Amjadi, for his invaluable guidance, support, and encouragement throughout my PhD journey. His expertise and dedication have been instrumental in shaping this work and my growth as a researcher.

To my wife, your unwavering love, patience, and belief in me have been my anchor during this journey. Thank you for standing by me through every challenge and triumph.

I am incredibly thankful to Simon Wanstall for his collaboration and insightful discussions, which have significantly enriched my work. I also extend my appreciation to Shubham Grover for his indispensable help on the Assessor project.

To my fellow PhD colleagues in the lab, Xenofon, Kat, Xin, Zhicheng, Zincong and Venkat, your camaraderie, advice, and shared experiences have made this journey all the more memorable. Thank you for your friendship and support.

To my family and friends, your encouragement and faith in me have been a source of strength throughout this process. I am deeply grateful for your constant support and understanding.

Finally, to my volleyball team, thank you for providing a much-needed outlet and a sense of balance amidst the demands of academia. Your companionship has been a vital part of keeping me grounded and sane.

This thesis is a reflection of not just my efforts but the collective support, guidance, and encouragement of all of you. Thank you.

Declaration

I declare that, except where explicit reference is made to the contribution of others, that this dissertation is the result of my own work and has not been submitted for any other degree at the University of Glasgow or any other institution

Tom Jacquin

Abbreviations

- `ADC` - Analog-to-Digital Converter
- `AFM` - Atomic Force Microscopy
- `Ag-NW` - Silver Nanowire(s)
- `AgNP` - Silver Nanoparticles
- `AR` - Augmented Reality
- `BPM` - Beats Per Minute
- `BLE` - Bluetooth Low Energy
- `CB` - Carbon Black
- `CNT` - Carbon Nanotube(s)
- `CNC` - Computer Numerical Control
- `CTE` - Coefficient of Thermal Expansion
- `CVD` - Chemical Vapour Deposition
- `DAQ` - Data Acquisition
- `DPI` - Dots Per Inch
- `ECG` - Electrocardiogram
- `EDX` - Energy-Dispersive X-ray Spectroscopy
- `EGaIn` - Eutectic Gallium–Indium
- `EMG` - Electromyography
- `FESEM` - Field-Emission Scanning Electron Microscopy
- `FWHM` - Full Width at Half Maximum
- `GF` - Gauge Factor
- `GO` - Graphene Oxide
- `HMI` - Human–Machine Interface
- `IoT` - Internet of Things
- `ITO` - Indium Tin Oxide
- `LIG` - Laser-Induced Graphene
- `LSPR` - Localized Surface Plasmon Resonance
- `MSC` - Micro-Supercapacitor
- `NI` - National Instruments
- `PDMS` - Poly(dimethylsiloxane)
- `PECVD` - Plasma-Enhanced Chemical Vapor Deposition
- `PEDOT` - Poly(3,4-ethylenedioxythiophene)
- `PI` - Polyimide
- `PPI` - Pixels Per Inch
- `SEM` - Scanning Electron Microscopy
- `SNR` - Signal-to-Noise Ratio
- `TCR` - Temperature Coefficient of Resistance
- `TEM` - Transmission Electron Microscopy
- `TENG` - Triboelectric Nanogenerator
- `TPU` - Thermoplastic Polyurethane

- `UV` - Ultraviolet
- `VOC` - Volatile Organic Compound
- `VR` - Virtual Reality
- `XPS` - X-ray Photoelectron Spectroscopy
- `XRD` - X-ray Diffraction

Papers and conferences

- IEEENano 2024: Invited speaker ”Thermoelectromechanical Characterization of Laser-Induced Graphene Nanocomposites”
- Censis 2024: Highly commended prize for the poster ”Cost-effective soft strain sensors using laser-induced graphene for breathing monitoring in healthcare applications”
- Publication under review: ”Wearable, Near Temperature Insensitive Laser-Induced Graphene Nanocomposite Strain Sensors”

Funding

This work was supported by the Engineering and Physical Sciences Research Council [Application Ref. xxxxxxx]. The author acknowledges financial support from the ASSESSOR project funded by the Office for Life Sciences (OLS) and The Scottish Government through the SBRI: Overdose detection, response and intervention.

Chapter 1

Introduction

1.1 Overview

In recent years, laser-induced graphene (LIG) has gained significant attention as a versatile material due to its unique properties, such as high electrical conductivity, flexibility, and ease of fabrication. Unlike traditional graphene synthesis methods such as chemical vapour deposition (CVD) and mechanical exfoliation, LIG is fabricated in a single step by irradiating a carbon-rich polymer surface with a laser, directly converting it into a porous graphene structure. This simple, scalable, and cost-effective process positions LIG as a promising candidate for a wide range of applications. Among these applications, soft strain sensors have particularly benefited from the distinctive combination of mechanical flexibility and electrical responsiveness that LIG offers.

Soft strain sensors are key components in wearable electronics, soft robotics, and human-machine interfaces, as they can detect subtle deformations and convert them into measurable electrical signals. The piezoresistive nature of LIG makes it especially well-suited for such sensors, where its electrical resistance changes in response to mechanical deformation. Moreover, the performance of these sensors can be tailored by adjusting the laser fabrication parameters, enabling the design of sensors with customized strain sensitivity and mechanical durability.

1.2 Motivation

The aim of this thesis is to explore and enhance the performance of LIG-based soft strain sensors by addressing key limitations that currently hinder their widespread application. LIG, with its inherent conductivity, mechanical flexibility, and scalable fabrication through laser scribing, has emerged as a highly attractive material for the development of next-generation flexible and wearable electronics. These sensors offer tremendous potential for applications in health monitoring, soft robotics, and human–machine interfaces, where conventional rigid electronics fall short.

Despite this promise, several challenges remain. The performance of LIG-based sensors is often affected by environmental factors such as temperature fluctuations, leading to undesired changes in electrical resistance that can interfere with accurate strain measurements. In addition, issues such as hysteresis, long-term drift, and mechanical fatigue under cyclic loading can compromise reliability. While prior research has primarily focused on optimizing LIG's electrical and mechanical properties, there is a pressing need for a more holistic understanding of how LIG nanocomposites behave under complex, real-world conditions.

This thesis addresses these gaps by developing strategies to improve the environmental stability, mechanical durability, and electromechanical response of LIG-based sensors. Particular emphasis is placed on understanding the coupled effects of strain and temperature on sensor performance, and on designing materials and structures that mitigate these effects without adding complexity or cost. Through systematic experimentation and characterization, this work seeks to expand the practical utility of LIG-based strain sensors and contribute to the broader advancement of scalable, high-performance flexible electronics.

1.3 Objectives

This thesis aims to investigate and enhance the performance, reliability, and environmental robustness of LIG-based nanocomposites for use in soft strain sensing applications. Although LIG offers significant potential due to its multifunctional properties, its practical adoption is limited by several key challenges. This work specifically focuses on addressing these limitations, including the material's sensitivity to temperature fluctuations, which can introduce undesirable variations in electrical resistance and compromise strain measurement accuracy. Furthermore, the thesis tackles the issues of reproducibility in LIG formation and the mechanical durability of LIG-based composites under repeated strain and deformation, both of which are critical for achieving consistent and long-term sensor performance.

To address these limitations, this work focuses on optimizing the laser fabrication process to better control the morphology, porosity, and conductivity of the LIG layer. By systematically studying the influence of laser processing parameters on both the formation of LIG and the electromechanical behaviour of resulting nanocomposites, the research aims to improve consistency and tailor material properties for specific sensing applications. Furthermore, the thesis investigates how environmental factors, particularly temperature, affect sensor behaviour, and explores strategies to mitigate these effects through material design and structural optimization. Beyond the development of robust sensors, the work also seeks to identify and demonstrate application-relevant use cases where LIG-based nanocomposites offer distinct advantages, thus contributing to the growing body of research focused on next-generation flexible and multifunctional sensing platforms.

The specific objectives of this research are:

- **Explore the influence of laser processing parameters** on the formation, morphology, and electrical properties of LIG, with the goal of improving reproducibility and optimizing performance.
- **Characterize the dynamic electromechanical response** of LIG nanocomposites under cyclic strain, focusing on key performance metrics such as sensitivity, hysteresis, linearity, and long-term stability.
- **Study the impact of temperature** on the electromechanical behaviour of LIG nanocomposites, and investigate strategies to mitigate thermal effects on sensor response.
- **Investigate additional performance enhancement strategies**, such as structural design optimizations, or multi-material integration, to improve stability, and sensitivity.
- **Explore application-specific implementations** of LIG nanocomposites in soft sensing systems, assessing their feasibility and performance under conditions relevant to wearable electronics, or robotics.

1.4 Thesis organisation

This thesis is organized into six main chapters, each addressing different aspects of the research:

- **Chapter 2: Literature Review** – Provides a comprehensive overview of graphene, including its fundamental properties, synthesis methods, and functionalization strategies. It explores conventional graphene synthesis techniques, contrasting these with the advantages of LIG fabrication. The chapter further reviews existing applications of LIG in flexible electronics, strain sensing, and energy storage, identifying key limitations and research gaps that this thesis aims to address.
- **Chapter 3: Methodology** – Details the fabrication process for LIG-based nanocomposites, including laser parameters, precursor materials, and post-processing steps. It describes the experimental setup used for electrical, mechanical, and thermal characterization, specifying techniques such as scanning electron microscopy (SEM), Raman spectroscopy, tensile testing, and cyclic strain evaluation.
- **Chapter 4: Controlled Wettability** – Investigates the impact of laser processing parameters on the wettability of LIG, analyzing surface morphology and chemical composition changes. It presents systematic measurements of contact angle variations and their correlation with laser fluence and scan speed during fabrication. The chapter further explores how LIG wettability influences humidity sensing performance, evaluating sensor response to different humidity levels and proposing strategies to enhance environmental stability.

- **Chapter 5: LIG Nanocomposites** – Focuses on the development of LIG nanocomposites by integrating polymer matrices such as polydimethylsiloxane (PDMS) or Ecoflex. It examines the structural, mechanical, and electrical properties of the composites. The chapter also presents the influence of the Kirigami design on nanocomposite performance.
- **Chapter 6: Heat-Insensitive LIG Strain Sensors** – Investigates the temperature sensitivity of LIG-based strain sensors and explores strategies to tune their thermal response. The chapter presents experimental studies on the effects of temperature fluctuations on sensor response. A theoretical model is also proposed to explain the results observed.
- **Chapter 7: LIG Nanocomposites Doping** – Explores the effects of doping LIG nanocomposites with silver nitrate. It assesses how doping influences electrical conductivity and thermal sensitivity.
- **Chapter 8: Applications** – Demonstrates the practical applications of LIG-based sensors across various fields, including wearable electronics, human-machine interfaces, and structural health monitoring. The chapter presents case studies showcasing the integration of LIG sensors in soft robotics and prosthetics.
- **Chapter 9: Conclusion and Future Perspectives** – Summarizes the key findings of the research, emphasizing the advancements made in LIG nanocomposite development and heat-insensitive strain sensing. The chapter discusses how the proposed approaches address the challenges identified in the literature, particularly in terms of environmental stability and electromechanical performance. It also outlines future research directions, including the exploration of alternative fabrication techniques, hybrid material systems, and broader applications in areas such as environmental monitoring, biomedical devices, and smart textiles.

By addressing these key aspects, this thesis aims to contribute to the development of reliable, high-performance LIG-based strain sensors that can operate under varying environmental conditions, expanding their use in diverse real-world applications.

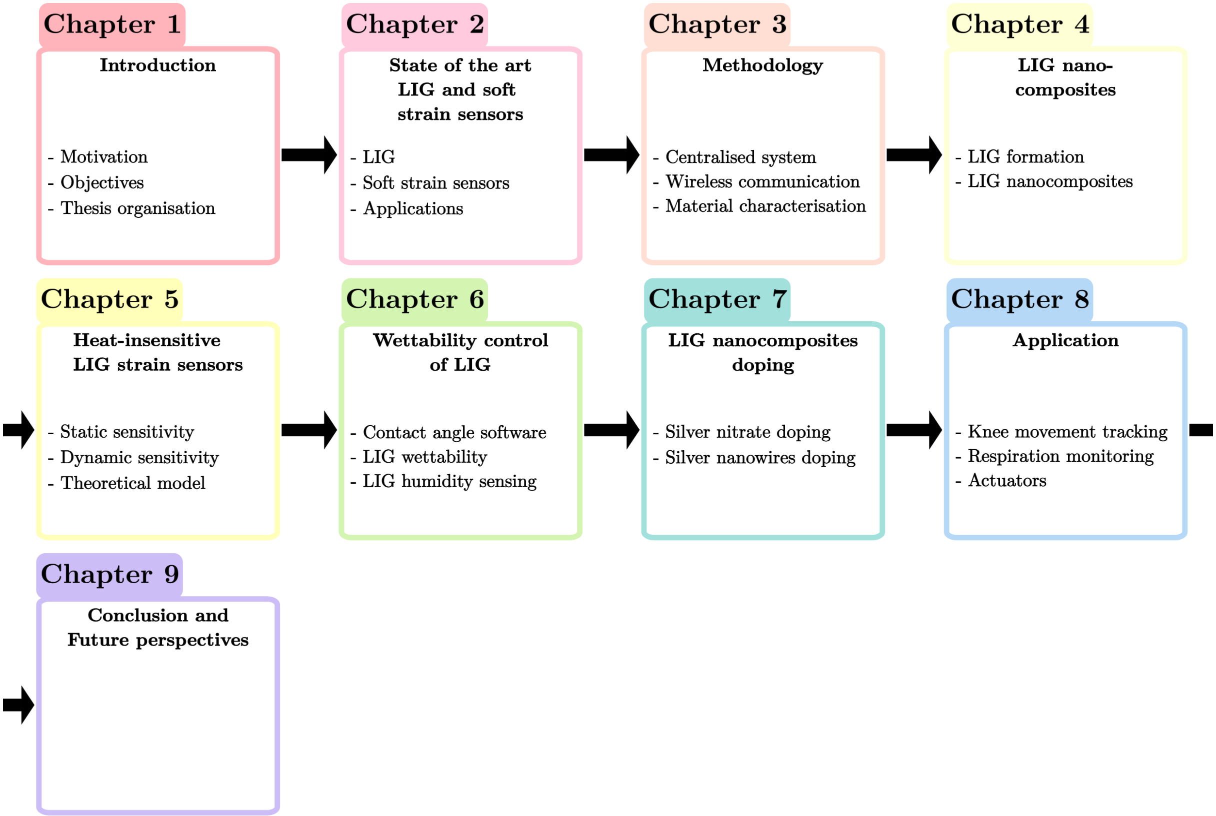

Figure 1.1: Thesis chapters organisation

Chapter 2

Literature Review

In this chapter, we embark on a comprehensive exploration aimed at establishing an understanding of LIG and its intrinsic properties, while elucidating its significance as a prime candidate for low-cost sensor fabrication. At the core of our investigation lies the intricate interplay of laser irradiation with polymeric precursors, leading to the transformation of ordinary substrates into highly conductive graphene structures. We delve into the fundamental principles underlying LIG formation, dissecting the complex chemical and physical processes triggered by the intense photon energy of the laser beam, shedding light on critical factors such as laser power, irradiation time, and precursor composition.

Moreover, we study the operational intricacies of the laser system itself, delineating the multifaceted functionality of various laser parameters and their role in tailoring LIG properties. From pulse duration and repetition rate to wavelength and beam focusing techniques, each aspect of laser operation exerts a distinct influence on the morphology, conductivity, and structural integrity of the resulting graphene network.

2.1 Graphene

Graphene, a two-dimensional allotrope of carbon, consists of a single layer of carbon atoms arranged in a honeycomb lattice structure. Each carbon atom forms strong covalent bonds with three neighbouring atoms, creating an exceptionally stable and robust lattice. This unique atomic configuration imparts a range of remarkable properties to graphene, making it a material of intense scientific and technological interest. Since the seminal review by Castro Neto et al. [1], these properties have been extensively explored, sparking widespread research across multiple disciplines [2–5]. The growing academic interest in graphene is evident in the sharp increase in the number of related publications since 2005, as illustrated in Figure 2.1.

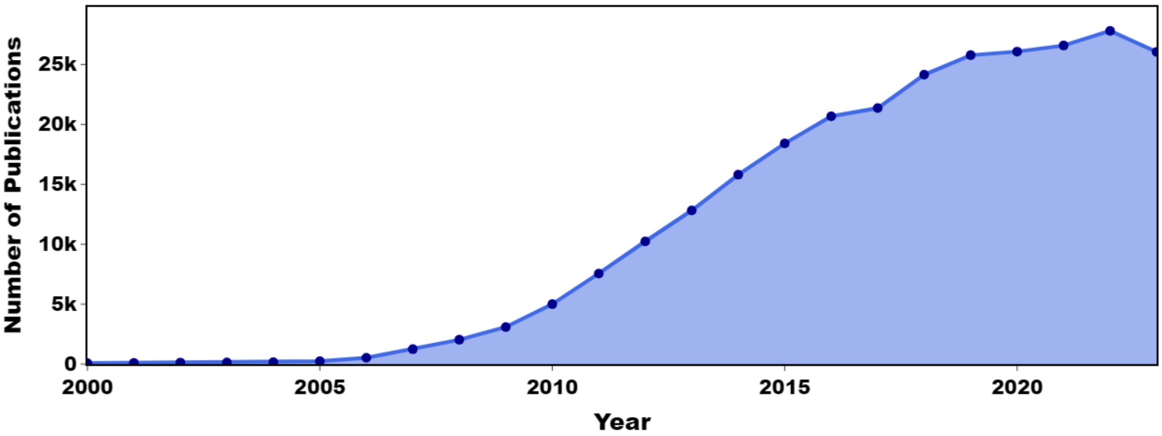

Figure 2.1: Annual Growth in Graphene Research: Number of Publications Per Year

One of the most extraordinary features of graphene is its exceptional electrical conductivity. This property arises from graphene's unique electronic band structure, which allows electrons to move through the material with minimal resistance. The carbon atoms in graphene are arranged in a hexagonal lattice, forming a conjugated pi-bonding network. This structure results in the formation of delocalized pi-electrons that can traverse the graphene lattice with remarkable speed and efficiency, thereby contributing to its high conductivity.

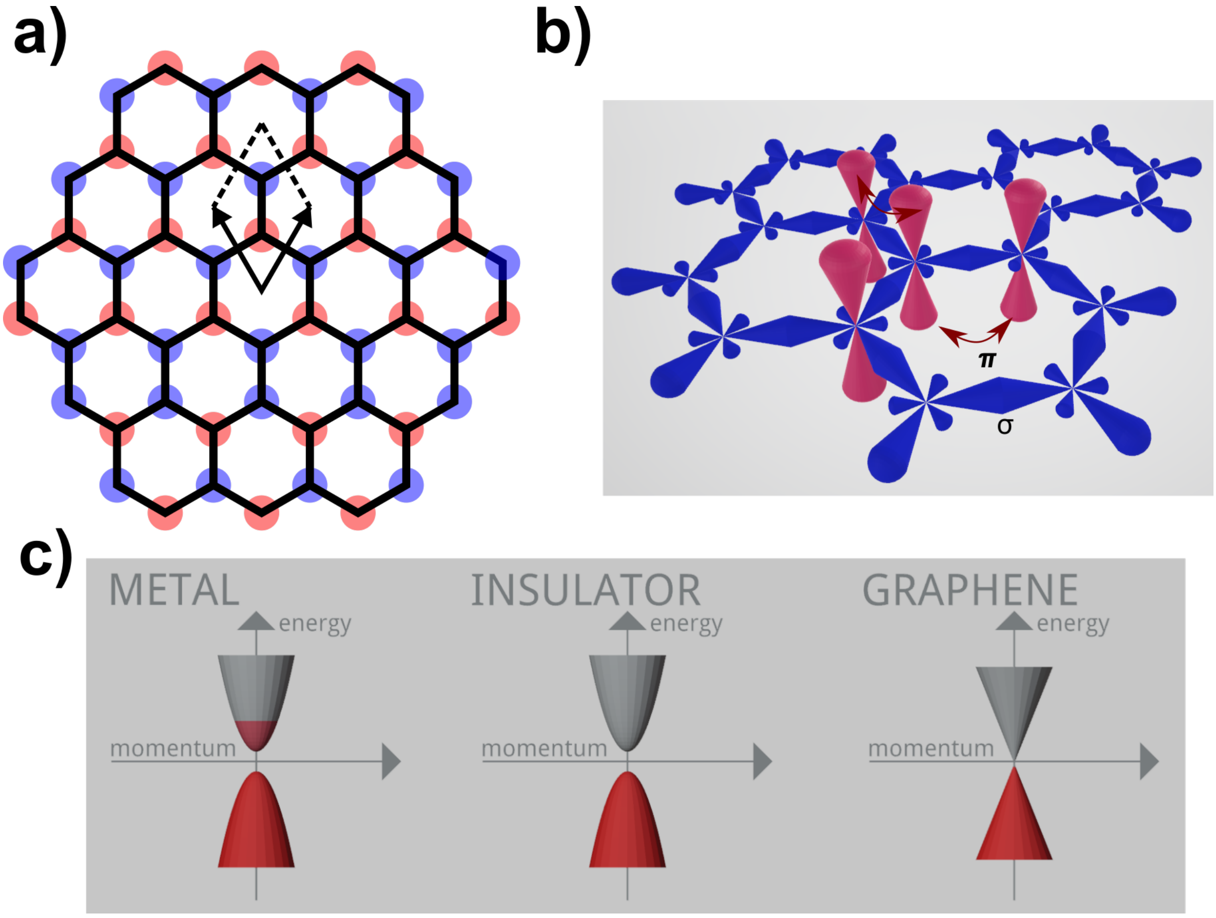

Figure 2.2: a)The two graphene sub-lattices (red and blue) and unit cell; b)Sigma and pi bonds in graphene; c)Electronic band structure of metals, insulators and graphene.

The planar structure of graphene, along with the sp^2 hybridization of carbon orbitals, further enhances its electrical conductivity by facilitating efficient charge transport across the surface. Unlike many other materials, graphene lacks a bandgap in its electronic structure, which means that electrons can move freely across the material without encountering energy barriers. This absence of a bandgap is crucial in maintaining graphene's high conductivity, as it prevents the electron scattering that typically reduces mobility in other materials.

Moreover, the pristine nature of graphene sheets, characterized by the absence of grain boundaries or defects, plays a pivotal role in its exceptional electrical properties. In contrast to traditional semiconductors or metals, where impurities and structural imperfections can impede electron mobility, defect-free graphene allows electrons to travel long distances with minimal scattering. This characteristic leads to an exceptionally low electrical resistance, further underscoring graphene's potential in electronic applications.

Beyond its intrinsic electrical conductivity, graphene exhibits a suite of other remarkable properties, including outstanding mechanical strength [6], superior thermal conductivity [7, 8], and high optical transparency [9]. These combined attributes position graphene as an ideal material for a broad range of advanced applications, including high-performance electronics, supercapacitors [10–12], sensors [13], and transparent conductive coatings [14].

2.2 Laser induced graphene

The principal conventional methods for graphene synthesis include mechanical exfoliation, chemical vapor deposition (CVD), chemical reduction of graphene oxide (GO), and liquid-phase exfoliation. Although these techniques enable the controlled and high-quality production of graphene, they are often costly, time-consuming, and reliant on specialized equipment and complex processing conditions.[15]

2.2.1 LIG production techniques

LIG is a porous form of graphene created by converting carbon-rich precursor materials, typically polyimide (PI), using a high-power laser. The process involves directly writing or patterning graphene onto the PI surface by harnessing the laser's thermal energy, which initiates a pyrolytic reaction. This method offers a scalable and cost-effective approach for producing graphene with applications in electronics, sensing, and energy storage. First introduced by Lin et al. [16], the field has experienced significant growth, as illustrated in Figure 2.3.

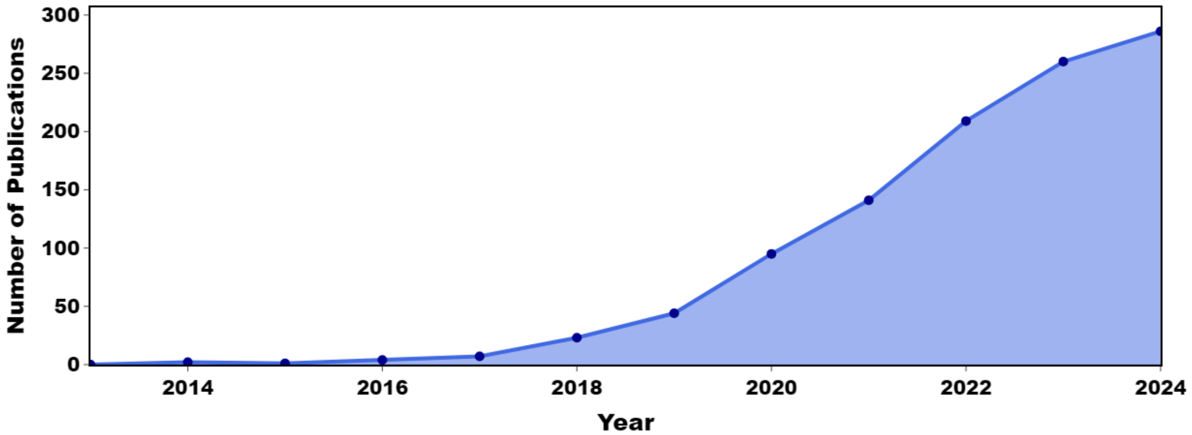

Figure 2.3: Annual Growth in LIG Research: Number of Publications Per Year

The conversion process begins by irradiating the PI surface with a high-power laser, typically a CO_2 laser with a wavelength of approximately 10.6 µm. The laser can operate in either continuous-wave or pulsed modes, depending on the desired characteristics of the final graphene structure. Key parameters, such as laser power density, scanning speed,

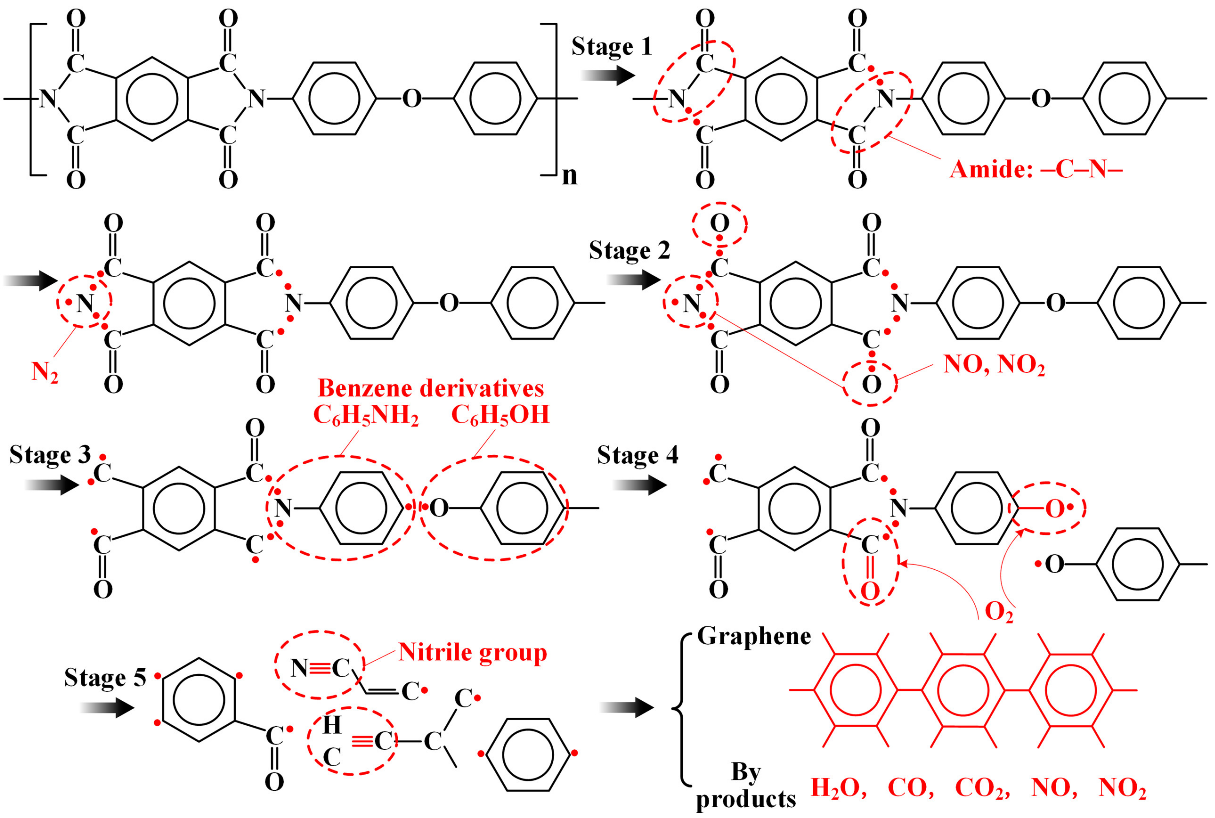

Figure 2.4: Proposed thermal decomposition of PI according to [17].

and focal spot size, must be meticulously controlled to optimize the conversion process. During irradiation, the laser heats the PI surface to temperatures exceeding 2500°C, inducing pyrolysis. The combination of photo-thermal and photochemical effects initiates the decomposition of oxygen-containing groups within the imide system and biphenyl structures of the PI matrix. This process involves the cleavage and recombination of several chemical bonds (C-O, C-N, C-H, and C=O), resulting in the release of various gaseous by-products such as CO, H_2, N_2, CO_2, C_2H_2, and CH_4. Ultimately, these reactions lead to the formation of a conductive, porous, three-dimensional graphene structure [17].

The LIG structure is created through the carbonization of the residual carbon bonds. While carbonization begins at around 400°C, graphitization, which is essential for the formation of high-quality graphene, requires temperatures exceeding 500°C. According to Bai et al., the thermal decomposition process proceeds through five distinct stages, as outlined in the following figure:

The final morphology of the LIG is heavily influenced by both the laser parameters and the intrinsic properties of the PI. Typically, LIG exhibits a highly porous, interconnected structure composed of graphene flakes. The porosity and surface area can be fine-tuned by adjusting the laser power and scanning speed. Higher laser power or slower scanning speeds generally lead to more extensive carbonization, resulting in increased porosity. Conversely, lower power or faster scanning speeds produce less porous structures. While these parameters influence molecular changes in the PI, they can be challenging to quantify. However, other parameters, such as laser defocusing, Pixel Per Inches (PPI) and The Dots per Inches (DPI), exert more easily explainable effects.

By defocusing the laser, the laser spot size increases, leading to partial overlap between successive laser spots as shown in Figure 2.5 a). This overlap creates a more uniform surface, and higher-quality graphene with lower sheet resistance has been reported under these conditions [18].

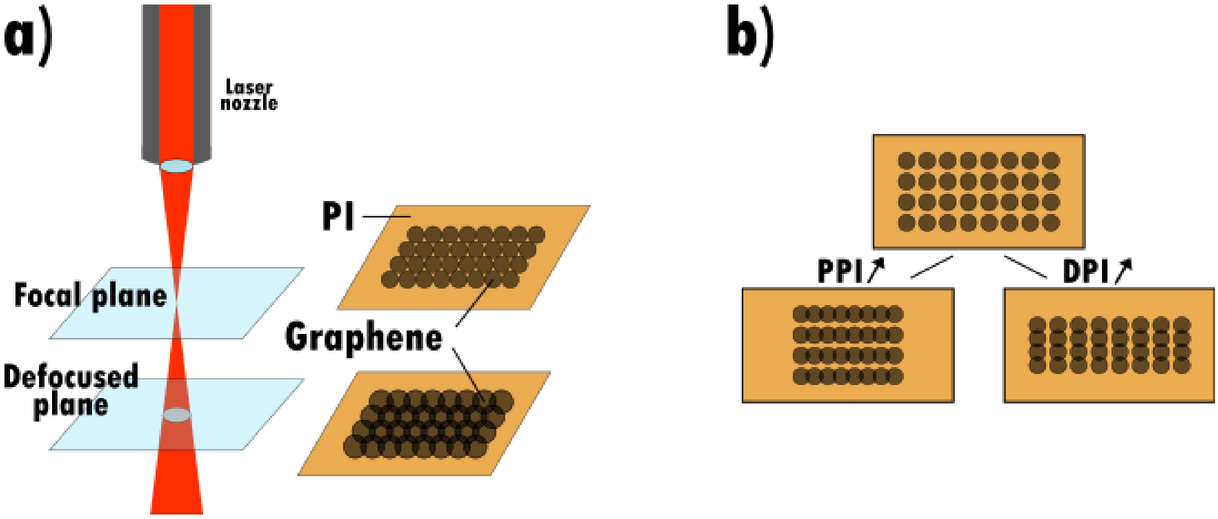

Figure 2.5: a) Schematic showing the influence of focal plane distance on LIG formation; b) Schematic illustrating the influence of DPI and PPI settings on LIG formation.

The DPI setting in the laser cutter software directly influences the vertical resolution of the rastered pattern by controlling the density of laser spots along the vertical axis. Higher DPI values result in a greater number of laser spots per unit area, increasing the resolution and potentially causing more overlap between adjacent spots. This increased overlap can enhance the uniformity of the LIG structure and may also affect the porosity and electrical properties of the resulting material.

Similarly, the PPI setting determines the horizontal resolution by controlling the number of laser pulses fired per inch along the horizontal scanning path. Higher PPI values lead to closer spacing between pulses, resulting in increased overlap along the horizontal axis. This horizontal overlap can significantly influence the morphology of the LIG, impacting both the uniformity of the graphene network and its overall conductivity.

The porous structure of LIG imparts unique properties, including high electrical conductivity, a large surface area, and excellent mechanical flexibility. These attributes make LIG highly suitable for a range of advanced applications, including flexible electronics, supercapacitors, sensors, and wearable devices, where traditional materials often fall short in terms of durability or performance under strain.[19–23]

Recent research has broadened the scope of LIG production by investigating various carbon-rich precursors beyond PI. Materials such as Kevlar, polysulfones, poly(ether imide), polyphenylene sulfide, and lignin have all been successfully converted into LIG. Additionally, polysaccharides like cellulose and starch can be activated for LIG conversion through the incorporation of boric acid or phosphate-based fire retardants. A diverse range of carbon sources used for LIG production is illustrated in Figure 2.6.

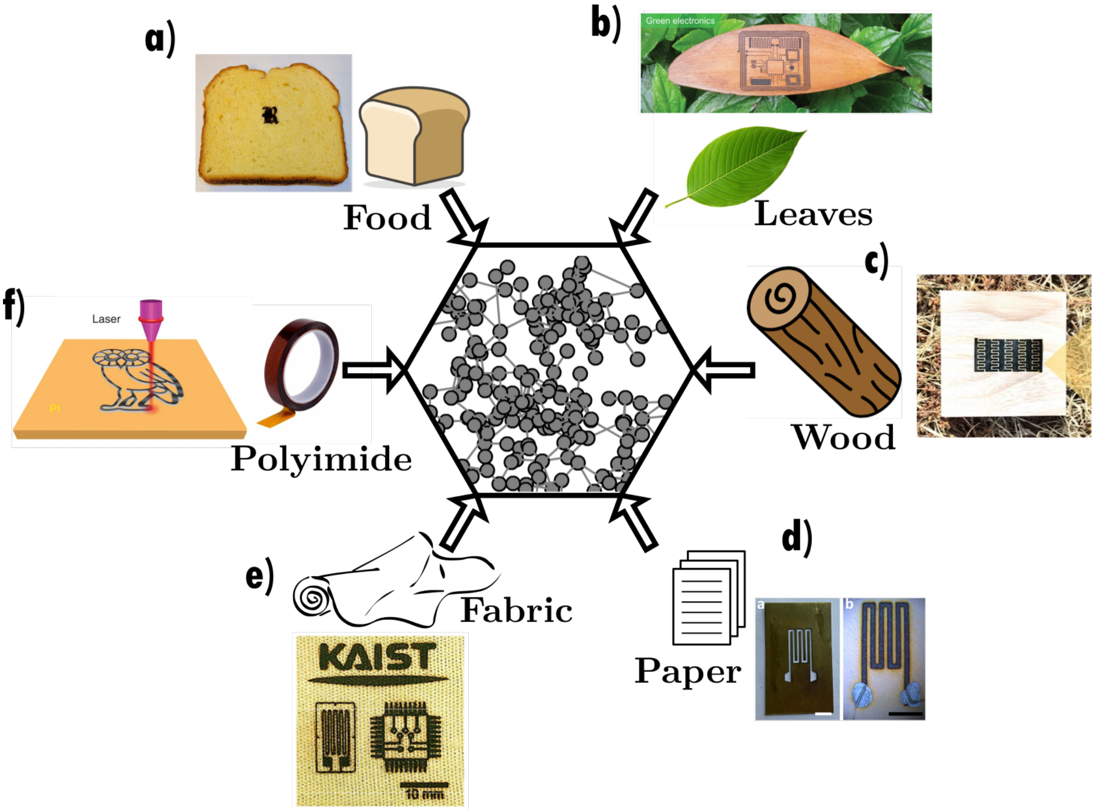

Figure 2.6: Various carbon sources used for LIG production: a) Food sources such as bread, coconut, and potato [18]; b) Leaves [24]; c) Wood [25]; d) Paper [26]; e) Fabrics [27]; f) PI [16]. Adapted from [28]

Figure 2.7 showcases several approaches for modifying LIG, which have been the focus of recent studies. As previously discussed, the laser parameters, such as power, speed, and wavelength, play a crucial role in shaping the morphology and properties of the resulting LIG [29]. Additionally, the use of controlled gas atmospheres during the laser conversion process has emerged as a significant strategy to further refine the material properties of LIG, enabling fine-tuning of its structural and electrical characteristics [30–35].

2.2.2 Properties of LIG for Sensor Applications

LIG has garnered significant attention as a versatile material for various sensing applications. The unique porous structure of LIG offers a high surface area, which enhances its sensitivity in direct sensing applications.

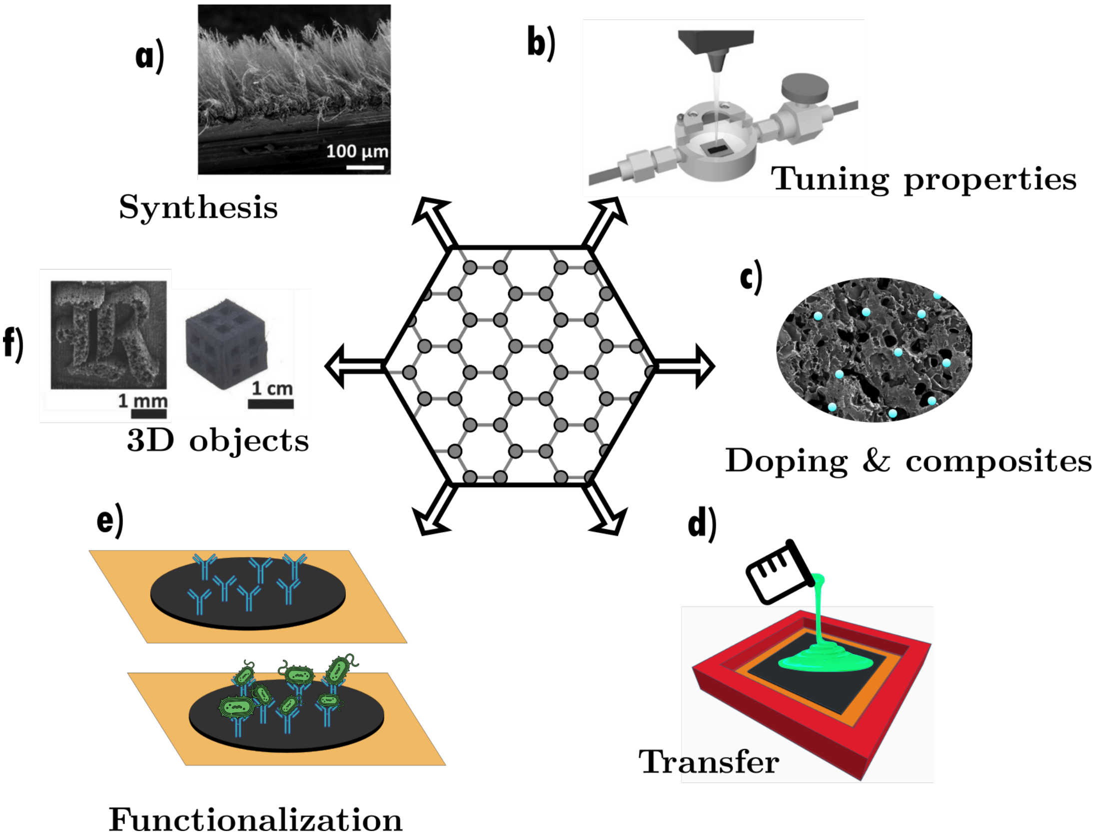

Figure 2.7: Various modifications and fabrication approaches for LIG: a) Morphology control through laser parameter optimization [29]; b) Property tuning using controlled atmospheres [35]; c) LIG doping and composites; d) Transfer of LIG to polymers; e) LIG functionalization for biosensors; f) Creation of three-dimensional LIG structures [36]. Adapted from [28].

One of the key advantages of LIG is its intrinsic ability to interact with different molecules and external stimuli, making it highly suitable for chemical sensing. This characteristic arises from the porous network formed during the laser scribing process, which allows for efficient adsorption of target analytes onto the sensor surface [37, 38]. LIG-based chemical sensors are thus highly effective in detecting a range of volatile organic compounds (VOCs) and gases, which makes them promising candidates for environmental monitoring and industrial safety applications [39–41].

In addition to its use as a stand-alone sensing material, doping LIG with various chemicals has emerged as a powerful strategy to enhance its sensitivity and selectivity towards specific external factors. various doping techniques to tailor LIG for specific applications. These techniques involve introducing different chemical elements either before or after the conversion process to enhance critical properties such as conductivity and sensitivity, which are essential for sensors and electronic devices. For instance, doping LIG with silver nanoparticles has been shown to increase its sensitivity to ammonia and hydrogen sulfide gases, while other dopants like platinum or palladium can improve sensitivity towards hydrogen gas [42–44]. These modifications further expand the range of applications for LIG-based sensors, particularly in gas detection and biochemical analysis.

LIG has also been explored for biochemical sensing, particularly in the detection of biomolecules such as glucose, proteins, and DNA. The large surface area and high conductivity of LIG enable it to serve as an efficient transducer in electrochemical biosensors [45, 46]. When functionalized with enzymes or antibodies, LIG can facilitate the selective detection of biological targets, making it suitable for healthcare applications such as glucose monitoring, cancer biomarker detection, and pathogen identification. Furthermore, the ability to modify LIG with biocompatible coatings allows for its integration into wearable devices, thereby enhancing its potential in continuous health monitoring systems.

Another area where LIG has shown promise is in gas sensing. The porous structure, along with its inherent electrical conductivity, makes LIG highly sensitive to changes in the surrounding environment. LIG gas sensors have demonstrated the ability to detect low concentrations of gases such as nitrogen dioxide, methane, and carbon dioxide [47, 48]. This is particularly valuable in environmental sensing applications where real-time detection of pollutants is critical for ensuring air quality and safety.

Moreover, advanced fabrication methods, such as repeated laser irradiation, have been employed to stack multiple layers of LIG, resulting in three-dimensional structures that resemble LIG foams. These 3D LIG architectures exhibit increased surface area and improved mechanical properties, making them well-suited for applications in energy storage devices, flexible electronics, and a variety of advanced sensor technologies [36].

LIG's versatility as both a stand-alone sensing material and a doped composite material offers significant potential across various domains. Its high surface area, coupled with the ability to fine-tune its properties through doping, makes it highly adaptable for chemical, biochemical, and gas sensing applications. Ongoing research continues to explore new doping strategies and functionalization techniques to enhance the performance of LIG sensors, further broadening their scope of use in industrial, environmental, and healthcare sectors.

2.2.3 Applications of LIG sensors

2.2.3.1 Chemical and Gas Sensing

LIG-based sensors have demonstrated significant potential for chemical and gas sensing applications due to their high specific surface area, tunable surface chemistry, and inherent conductivity. These properties allow LIG sensors to achieve high sensitivity and selectivity in detecting various analytes, including VOCs, hazardous gases, and biomolecules, even at low concentrations. The versatility of LIG enables the development of gas sensors tailored for diverse applications such as environmental monitoring, industrial safety, and medical diagnostics.

One of the key advantages of LIG-based gas sensors is their ability to operate at room temperature, unlike conventional metal oxide-based sensors that often require high operating temperatures to achieve sufficient sensitivity. Furthermore, the porous graphene network formed during laser induction enhances gas adsorption, leading to improved response times and lower detection limits. By modifying the surface chemistry of LIG through doping or composite formation, the selectivity of these sensors can be tailored toward specific target gases, further expanding their applicability.

LIG sensors have been successfully integrated with various functional materials to enhance their gas sensing performance. For instance, LIG-Pd composites have been utilized for hydrogen (H_2) detection due to the high affinity of palladium toward hydrogen molecules, resulting in a rapid and reversible sensing response [49]. Additionally, stretchable LIG sensors have been developed for the detection of nitrogen oxides (NO_x), demonstrating excellent mechanical durability and consistent performance under strain [50]. Cement-embedded LIG sensors offer a robust and scalable solution for real-time monitoring of multiple gas species in construction and industrial environments [39]. Moreover, LIG-MoS_2 composites have shown promising results for NO_2 sensing, leveraging the synergistic effects of molybdenum disulfide and LIG to achieve enhanced sensitivity and selectivity [51].

The adaptability of LIG-based sensors allows for their integration into flexible and stretchable platforms, making them highly suitable for wearable and portable gas monitoring systems. Future advancements in material engineering and surface functionalization are expected to further improve the sensitivity, response time, and stability of LIG-based gas sensors, paving the way for their widespread adoption in next-generation sensing technologies.

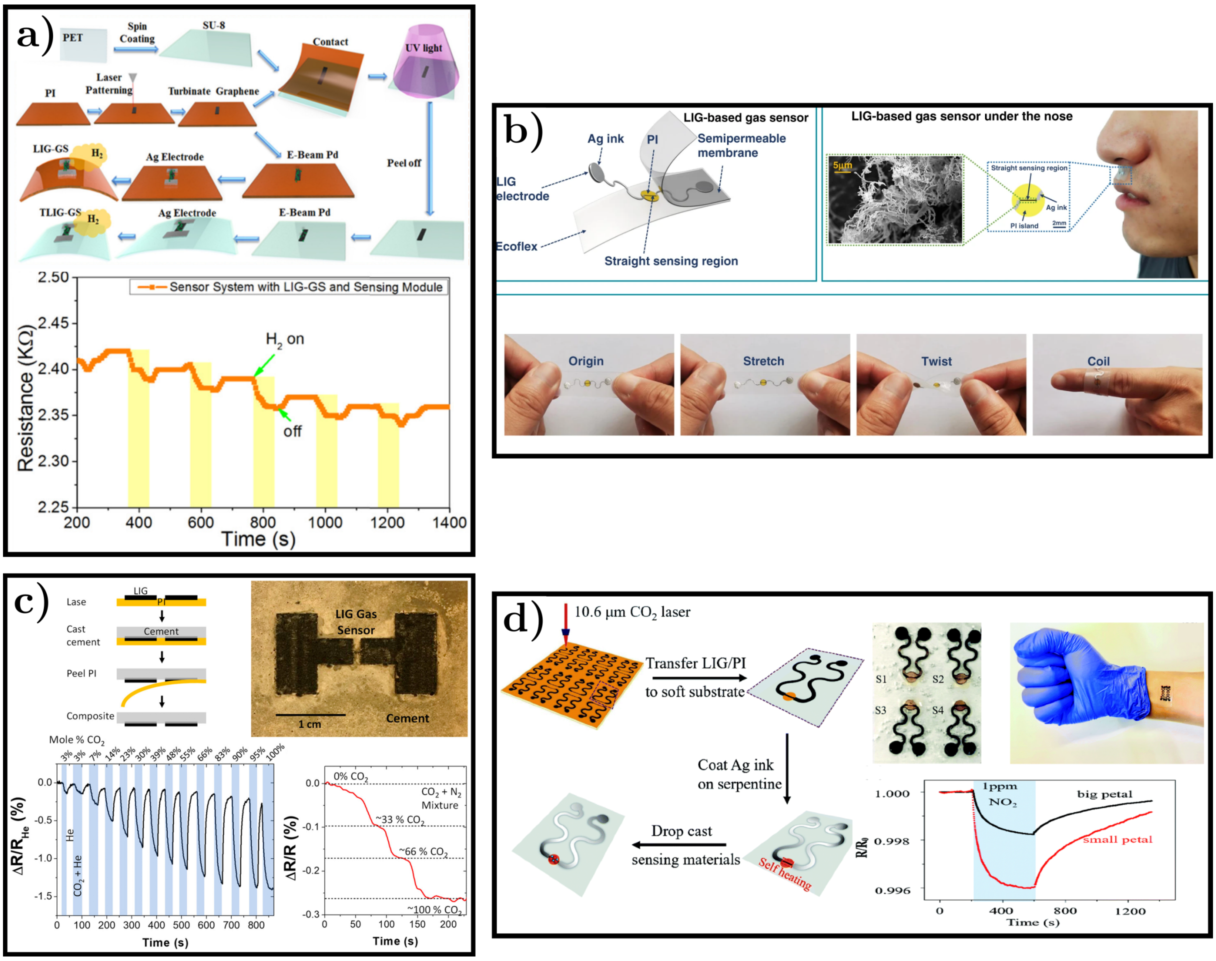

Figure 2.8: Examples of LIG-based gas sensors: a) LIG-Pd composite sensor for hydrogen (H_2) detection, leveraging palladium's affinity for hydrogen molecules [49]; b) Stretchable LIG sensor for nitrogen oxides (NO_x) monitoring, demonstrating resilience under mechanical deformation [50]; c) Cement-embedded LIG sensor for multi-gas detection in industrial applications [39]; d) LIG-MoS_2 composite sensor for NO_2 detection, utilizing the synergistic effects of molybdenum disulfide and LIG to enhance sensitivity and selectivity [51].

2.2.3.2 Energy Storage and Harvesting

Beyond its widespread use in sensing applications, LIG has garnered significant attention for its potential in energy storage and harvesting technologies. Due to its high electrical conductivity, large surface area, and tunable porosity, LIG serves as an excellent electrode material for energy storage devices such as supercapacitors and microsupercapacitors (MSCs). Additionally, LIG's compatibility with flexible substrates and facile patterning through laser processing make it an ideal candidate for next-generation, wearable energy storage systems.

LIG-based supercapacitors exhibit remarkable electrochemical properties, including high capacitance, excellent rate capability, and long cycling stability. These attributes stem from the hierarchical porous structure of LIG, which enhances ion transport and charge storage efficiency. Functionalization strategies such as heteroatom doping (e.g., nitrogen, boron) and the incorporation of pseudocapacitive materials (e.g., MnO_2, conductive polymers) have been explored to further enhance the energy storage capacity of LIG electrodes [52, 53]. Moreover, the development of flexible and stretchable MSCs enables their integration into wearable electronics, allowing for energy storage solutions that can withstand mechanical deformations while maintaining stable performance [54].

In addition to energy storage, LIG has been investigated for energy harvesting applications, including triboelectric nanogenerators and hybrid energy systems. The combination of LIG-based strain sensors with energy storage modules facilitates the development of self-powered wearable electronics, eliminating the need for external power sources. Such multifunctional devices hold significant promise for applications in health monitoring, human–machine interfaces, and Internet of Things (IoT)-enabled systems [55].

Future advancements in LIG-based energy storage and harvesting technologies will likely focus on improving energy density, scalability, and integration with diverse electronic platforms. By optimizing material properties and device architectures, LIG holds the potential to revolutionize self-sustaining, flexible electronics for next-generation wearable and implantable systems.

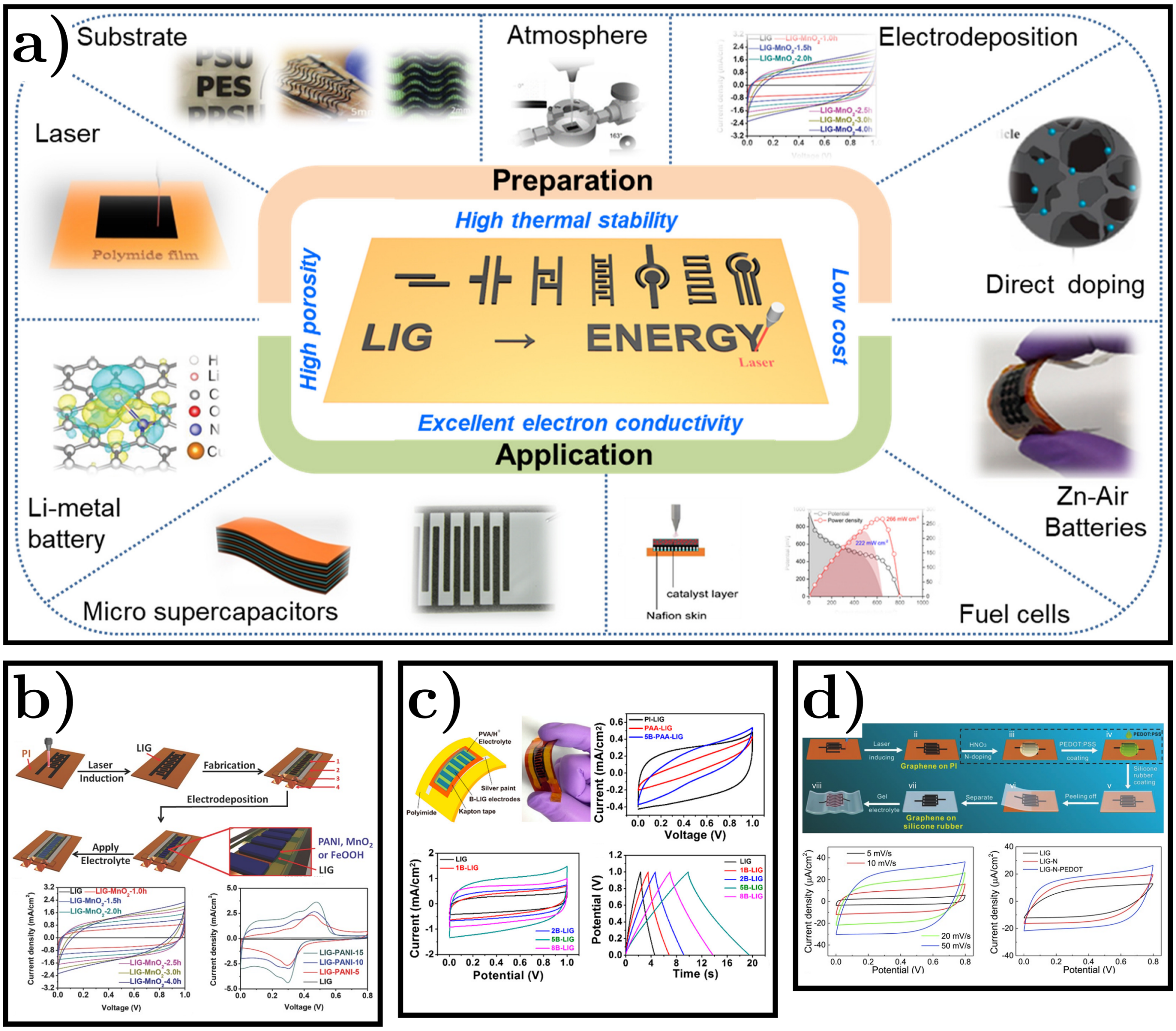

Figure 2.9: Examples of LIG-based energy storage devices: a) Overview of LIG-based energy storage technologies, highlighting their potential for integration with flexible and wearable electronics [55]; b) LIG-MnO -based flexible, symmetric, and asymmetric MSCs demonstrating high capacitance and stable cycling performance [53]; c) Electrochemical performance comparison of LIG-MSCs with varying H_3BO_3 loadings, showcasing the impact of boron doping on capacitance enhancement [54]; d) Nitrogen-doped LIG electrodes with conductive poly(3,4-ethylenedioxythiophene) (PEDOT) coating, demonstrating improved charge storage capability and energy efficiency [52].

2.3 Conventional Soft Strain Sensors

Soft strain sensors play a critical role in various applications due to their ability to detect and quantify deformation through changes in electrical properties. Among the different types of soft strain sensors, the most extensively studied include piezoelectric, resistive, capacitive, triboelectric, and optical sensors [56]. This report focuses specifically on resistive strain sensors, which are widely utilized due to their structural simplicity, ease of fabrication, and high sensitivity to mechanical deformation.

2.3.1 Working Principle of Resistive Strain Sensors

Resistive strain sensors generally comprise two primary components: a conductive sensing element embedded within a flexible matrix [57, 58]. When subjected to mechanical deformation, either stretching or compression, the electrical resistance of the sensor undergoes measurable changes due to variations in the sensing element's length, cross-sectional area, and percolation pathways.

In sensors where conductive materials, such as carbon nanotubes (CNTs), graphene nanoplatelets, or conductive polymers, are dispersed within a polymer matrix, the resistance change is primarily governed by two mechanisms: (1) *Geometric Effects:* Strain-induced elongation increases resistance by reducing the cross-sectional area while increasing length. (2) *Percolation and Tunnelling Effects:* Deformation alters the spatial distribution of conductive elements, increasing inter-particle distances, which in turn raises resistance due to disrupted electron tunnelling or physical disconnection between conductive pathways, as illustrated in Figure 2.10.

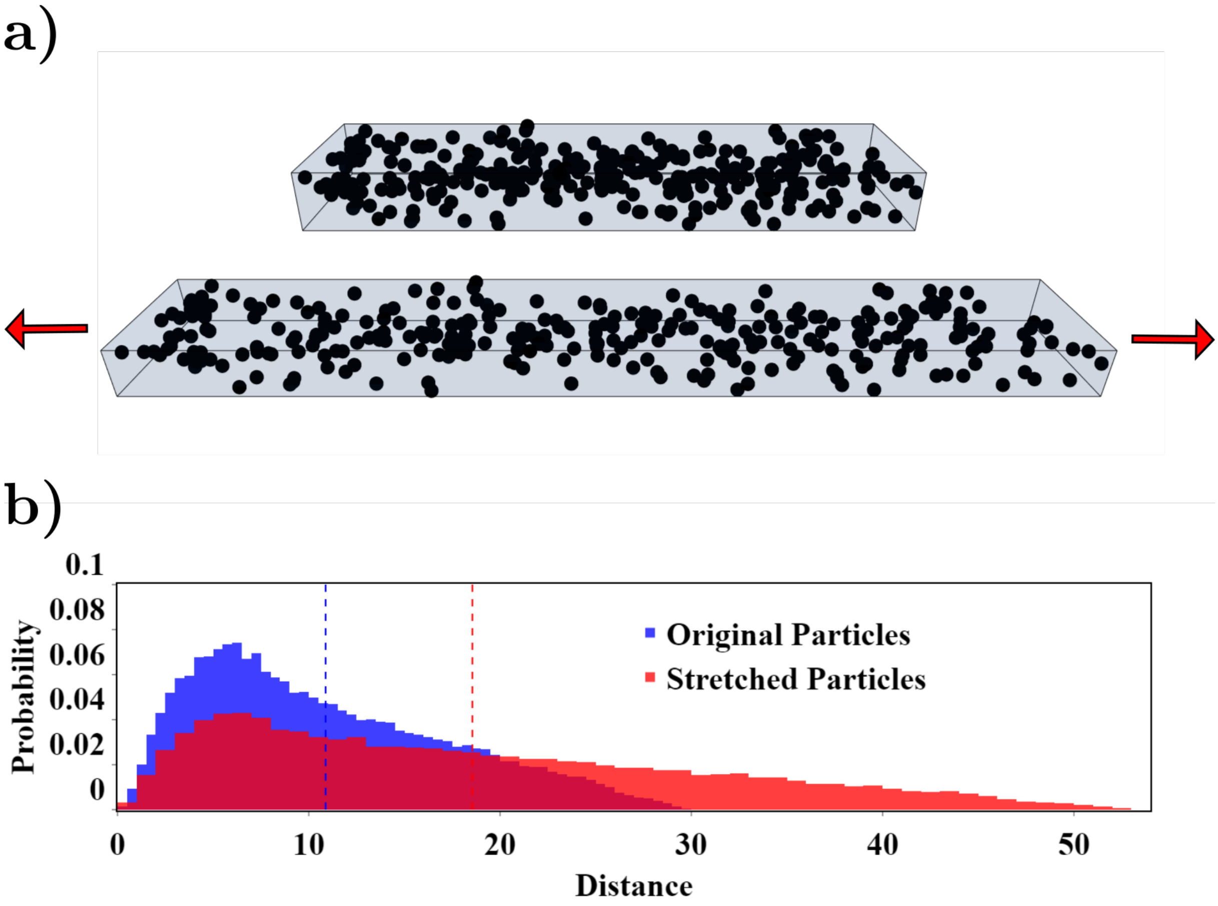

Figure 2.10: Simulation of inter-particle distance distribution in a conductive dispersion: a) Schematic representation of conductive particle displacement under uniaxial strain, assuming a Poisson's ratio of zero; b) Statistical distribution of inter-particle distances, where the average separation is indicated by the dotted line.

Traditional resistive strain sensors were historically limited to detecting strains of up to 5% [58]. However, advancements in materials and fabrication techniques have enabled the development of sensors capable of detecting strains exceeding 100%, significantly broadening their potential applications [59]. Additionally, modern resistive sensors demonstrate reversible resistance changes, allowing the strain state to be inferred through real-time resistance measurements.

2.3.2 Improvement Strategies for Resistive Strain Sensors

The performance of stretchable resistive strain sensors can be improved through innovations in materials or geometry, both of which contribute to enhanced sensitivity, durability, and range. This section discusses some of the most promising advancements in each of these areas.

2.3.2.1 Material Innovations

The selection of materials plays a pivotal role in defining the electromechanical performance, durability, and application scope of strain sensors. Recent advancements in material engineering have led to the development of highly conductive, flexible, and stretchable sensing elements. This section discusses three key material innovations: liquid metals, carbon-based conductive additives, and MXenes.

Liquid Metals

Liquid metals, particularly gallium-based alloys such as Eutectic Gallium-Indium (EGaIn), have gained significant attention in soft sensing applications due to their unique combination of high conductivity and mechanical flexibility [60]. With a low resistivity of approximately $29.4 \times 10^{-6}\ \Omega \cdot \mathrm{cm}^{-1}$ and a liquid state at room temperature, EGaIn facilitates the fabrication of intrinsically stretchable electronic circuits [61–64].

To enhance mechanical robustness and prevent leakage, eutectic gallium–indium (EGaIn) is typically encapsulated within stretchable elastomers such as Ecoflex [62], DragonSkin [65], or PDMS [66]. This encapsulation improves the material's durability while preserving its intrinsic stretchability and electrical properties. Zu et al. demonstrated the potential of EGaIn-based composites in wearable electronics by integrating EGaIn with silver flakes to develop a high-performance electrocardiogram (ECG) monitoring system [67]. Their findings revealed significant improvements in conductivity, strain limit, and electromechanical coupling compared to alternative silver flake composites, with a 176% increase in conductivity, a >600% enhancement in strain limit, and a 277% improvement in electromechanical coupling. These results highlight the advantages of composite formulations in optimizing the electrical and mechanical performance of liquid metal-based sensors.

Despite its advantages, EGaIn has certain limitations, including a low melting point (∼ 15°C), which restricts its use in high-temperature environments. Additionally, its biocompatibility remains under investigation, posing challenges for direct biomedical applications. Further research on alloying strategies and surface stabilization techniques may enable the broader adoption of liquid metals in next-generation flexible electronics.

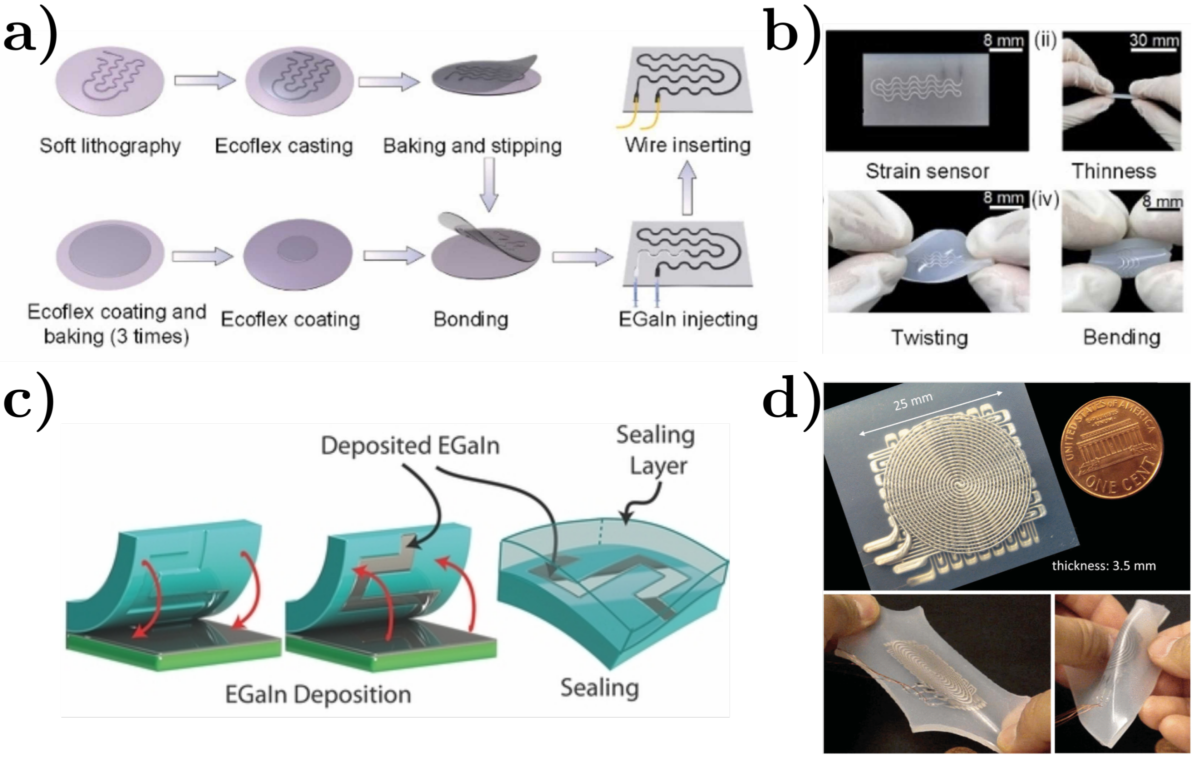

Figure 2.11: (a)-(c) Schematic illustration of flexible EGaIn strain sensor fabrication (adapted from [68, 69]). (b)-(d) Example of a soft strain sensor utilizing EGaIn (adapted from [69, 70]).

Conductive Carbon Additives

Carbon-based nanomaterials such as carbon black (CB), CNTs, and graphene have been extensively explored for their exceptional conductivity, mechanical flexibility, and compatibility with polymer matrices [8]. These materials enable the fabrication of lightweight and stretchable strain sensors with tunable electromechanical properties.

Liu et al. developed a graphene/thermoplastic polyurethane (TPU) nanocomposite, demonstrating a high degree of strain sensitivity and mechanical robustness [71]. Similarly, Zhang et al. enhanced the strain response of TPU-based sensors by incorporating a hybrid composite of carbon black and silver nanoparticles (AgNPs), highlighting the synergistic effects of combining carbon nanostructures with metallic additives [72]. Their study revealed that, compared to strain sensors based solely on carbon black, those incorporating a CB/AgNP composite exhibited an approximately 18-fold improvement in sensitivity at 100% strain. The integration of conductive carbon additives with elastomers such as PDMS or TPU has thus enabled the development of highly stretchable strain sensors with stable long-term performance.

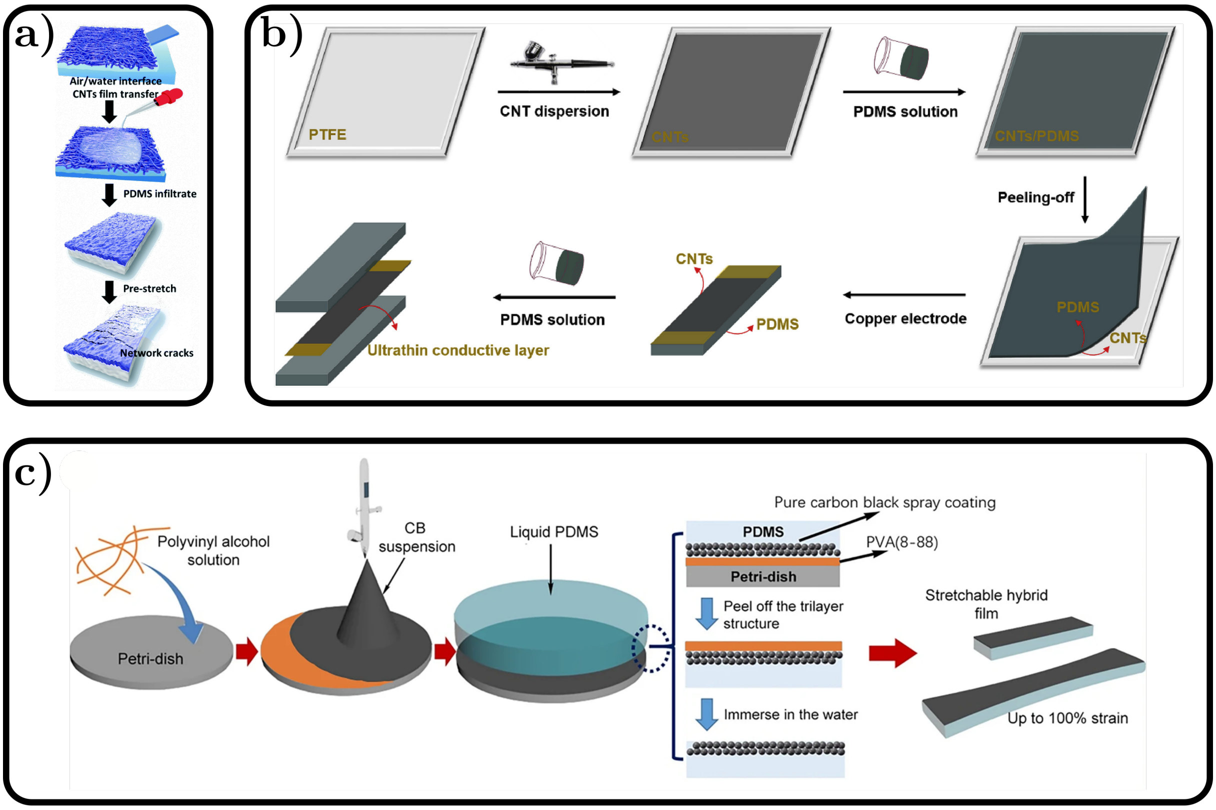

Figure 2.12: a) CNT-PDMS composite fabrication schematic (adapted from [73]); b) Alternative CNT-PDMS fabrication approach (adapted from [74]); c) CB-PDMS composite fabrication schematic (adapted from [75]).

MXenes

MXenes, a novel class of two-dimensional transition metal carbides and nitrides, have emerged as promising candidates for flexible electronics due to their high electrical conductivity and solution processability [76]. The most widely studied MXene, $Ti_3C_2T_x$, exhibits outstanding conductivity ($\sim 100\ \mathrm{S \cdot cm^{-1}}$) and hydrophilicity, making it an excellent candidate for conductive inks in printed electronics [77, 78].

Recent studies have demonstrated the versatility of MXenes in strain sensing applications. Kong et al. developed an MXene-based hydrogel composite with a high gauge factor and an extended working strain range, showcasing MXenes' potential for wearable strain sensors [79]. Furthermore, the combination of MXenes with other nanomaterials has been shown to enhance mechanical resilience and sensing performance. Xu et al. fabricated a CNT/MXene/PDMS composite that exhibited improved stretchability and conductivity, demonstrating its applicability in next-generation soft electronics [80].

The continuous exploration of MXene-based composites and hybrid structures is expected to further expand their capabilities in high-performance strain sensors.

Overall, these material innovations, liquid metals, conductive carbon additives, and MXenes, provide distinct advantages in the development of highly flexible, stretchable, and durable strain sensors. Future research will focus on optimizing their mechanical stability, biocompatibility, and integration into scalable fabrication processes to enable widespread adoption in wearable electronics and human-machine interface applications.

2.3.2.2 Geometrical Enhancements

Beyond material innovations, sensor geometry plays a crucial role in enhancing the performance of strain sensors. Various structural designs have been explored to improve key parameters such as sensitivity, durability, and stretchability, enabling strain sensors to operate more effectively under extreme mechanical deformations. These geometric enhancements primarily focus on engineered surface morphologies, crack propagation mechanisms, and cutting-based structural modifications.

Wrinkled Structures

Wrinkled surface structures have been widely investigated for their ability to improve the mechanical compliance and electromechanical performance of strain sensors. Wrinkles can be induced through pre-stretching the substrate before depositing the sensing layer or by thermally shrinking the substrate post-deposition [81, 82]. This approach allows the sensor to accommodate large deformations while maintaining stable electrical properties.

The localized strain redistribution facilitated by wrinkling enhances both the detection range and GF. Chu et al. demonstrated a GO/PDMS-based wrinkled strain sensor with a stretchability of up to 300% and a strain sensitivity of 0.1%, significantly outperforming conventional planar designs [83]. The tunability of the wrinkle geometry enables tailored strain-sensing characteristics, making this strategy particularly advantageous for applications requiring flexible and stretchable sensors.

Crack-Based Designs

Crack-based strain sensors exploit the formation and propagation of microcracks in the conductive layer to achieve exceptionally high sensitivity. While cracks are typically considered structural defects, controlled microcrack formation enables precise resistance modulation in response to mechanical strain. This bio-inspired approach is similar to the slit-based mechanoreceptors found in spiders, which allow for ultra-sensitive detection of minute deformations [84].

Pre-stretching or cyclic loading of the sensing layer is commonly employed to induce and control crack propagation, significantly enhancing the strain response [85, 86]. Zhou et al. fabricated a crack-based strain sensor by spray-coating CNT ink onto an electrospun TPU fibrous mat, achieving an exceptionally high GF of 428.5 within the 0–100% strain range and an ultra-high GF of 83,982.8 for strains between 220–300%, along with a rapid response time of 70 ms [87]. These crack-based designs are particularly useful for applications demanding high sensitivity at low strain levels while maintaining mechanical durability.

Kirigami-Inspired Structures

Kirigami-based designs, inspired by the traditional Japanese paper-cutting technique, provide an effective strategy for improving the stretchability and mechanical robustness of strain sensors. By incorporating engineered cuts and patterns into the sensing layer, kirigami structures enable controlled out-of-plane deformations, thereby reducing localized strain concentration and preventing premature material failure [88].

This approach not only increases stretchability but also minimizes resistance fluctuations under cyclic loading. Wang et al. demonstrated a kirigami-structured CNT/PDMS composite strain sensor that exhibited significantly enhanced durability and minimal hysteresis, even under repeated high-strain cycles [89]. The scalability and adaptability of kirigami-based designs make them highly suitable for wearable and soft electronic applications, where flexibility and durability are critical.

Overall, these geometric strategies provide innovative pathways for optimizing strain sensor performance, enabling their integration into next-generation soft electronics, wearable systems, and bio-interfacing applications.

2.3.3 Challenges in Conventional Strain Sensors

While strain sensors have made significant advancements in terms of sensitivity, stretchability, and integration into flexible devices, several persistent challenges continue to limit their performance. These challenges are common across various manufacturing techniques and material choices and can significantly impact the accuracy and reliability of sensor readings.

Sensitivity to Environmental Factors: One of the primary challenges in conventional strain sensors is their susceptibility to environmental fluctuations, particularly variations in humidity and temperature. Souri et al. highlighted these limitations in their review, emphasizing the impact of environmental factors on sensor performance [58]. Many polymer-based and composite strain sensors exhibit high sensitivity to ambient humidity levels, as moisture absorption can significantly alter their electrical properties. This can result in resistance or capacitance shifts, leading to erroneous strain readings or enabling unintended humidity sensing [30, 90–92]. The issue is particularly pronounced in hygroscopic materials, such as hydrogels and certain elastomers, which swell upon moisture absorption, further exacerbating signal drift.

Temperature fluctuations also play a crucial role in determining sensor performance. Most strain sensor materials, especially polymers, exhibit temperature-dependent electrical and mechanical properties [93]. For instance, the conductivity of many nanocomposite materials decreases with rising temperatures, while elastomers undergo changes in mechanical stiffness, leading to variations in strain response. These combined effects contribute to sensor output drift, compromising measurement reliability in dynamic thermal environments.

Nankali et al. further demonstrated the significant impact of temperature and humidity on the strain sensing behaviour of CNT–PDMS nanocomposite strain sensors, underscoring the need for improved environmental stability in future sensor designs [94]. Their study reported a 43% decrease in resistance with a 40°C temperature increase, highlighting the strong temperature dependence of the material. Additionally, they observed that variations in relative humidity induced irreversible and permanent changes in sensor performance, further emphasizing the critical challenge of environmental susceptibility in polymer-based strain sensors.

To address these challenges, researchers have investigated temperature compensation algorithms and the development of materials with reduced sensitivity to environmental fluctuations. However, achieving a fully stable strain sensor capable of maintaining consistent performance across diverse environmental conditions remains an active area of research [95–98]. More advanced solutions involve the design of hybrid materials with inherent resistance to humidity and temperature variations, as well as multi-functional sensors that can simultaneously detect and compensate for these environmental influences.

To further mitigate these effects, novel material formulations, advanced packaging strategies, and tailored micro-/nanostructure designs have been proposed [99–101]. For instance, a temperature self-compensated hybrid film composed of graphite and CNTs has been developed to decouple the influence of temperature fluctuations on strain sensor response [99]. Additionally, super-hydrophobic coatings have been employed to prevent moisture penetration into sensing films, thereby enhancing long-term stability in humid environments [100, 102]. Zhang et al. demonstrated that encapsulating CNT–Ecoflex nanocomposite strain sensors between two Ecoflex layers significantly improved their resistance to humidity-induced variations [103].

Despite these advancements, the development of strain sensors with intrinsic immunity to environmental fluctuations remains an ongoing challenge. Future research efforts may focus on refining material compositions, optimizing encapsulation techniques, and integrating multi-modal sensing capabilities to enhance performance and durability in real-world applications.

Hysteresis and Drift in Elastomers: Hysteresis and drift are two significant issues that arise when elastomers are used as the base material for strain sensors. Hysteresis refers to the lag in response between the applied strain and the corresponding electrical output. In other words, the sensor output does not immediately return to its original state when the strain is removed, leading to inaccurate strain measurements in dynamic or repetitive loading scenarios. This is particularly problematic in wearable or robotic applications where the sensor is subjected to continuous deformation.

Elastomers, due to their viscoelastic nature, exhibit both elastic and viscous behaviours, which means that they experience internal friction and energy loss during deformation cycles. This internal friction causes hysteresis and can also lead to mechanical fatigue over time, further degrading sensor performance. Additionally, polymer-based sensors often suffer from long-term drift, where the sensor's baseline signal gradually shifts over time, even in the absence of applied strain. This phenomenon is commonly attributed to the slow relaxation of polymer chains, which causes a continuous change in the material's mechanical properties.

Several strategies have been proposed to reduce hysteresis and drift in elastomer-based strain sensors. One approach is to modify the chemical structure of the elastomer or use additives that reduce viscoelastic effects, thereby improving the material's stability under cyclic loading conditions. Alternatively, integrating rigid or semi-rigid fillers into the elastomer matrix can provide structural reinforcement, reducing both hysteresis and drift [59, 104, 105]. Another approach involves the use of advanced signal processing algorithms to correct for drift and hysteresis during real-time operation [106]. These techniques, while promising, have yet to fully resolve the issue, and continued research is focused on achieving strain sensors with negligible hysteresis and drift.

Limited Stretchability and Mechanical Fatigue: In addition to environmental sensitivity and hysteresis, many conventional strain sensors suffer from limited stretchability and are prone to mechanical fatigue. While significant progress has been made in the development of highly stretchable materials for strain sensors, maintaining consistent performance under large deformations remains a challenge. As summarized in Table 2.1, most sensors exhibit multiple linear regions across extensive strain ranges rather than maintaining a single linear response throughout. This nonlinearity complicates precise strain quantification and necessitates advanced calibration strategies to ensure accurate measurements.

Mechanical fatigue, which is the gradual degradation of material properties due to repetitive loading cycles, further reduces the lifespan of strain sensors. Materials commonly used in strain sensors, such as PDMS and TPU, are susceptible to mechanical degradation, including cracking, delamination, or permanent deformation after extensive cyclic loading. Similarly, despite extensive ongoing research, hydrogels continue to face challenges in maintaining mechanical integrity over repeated use [107, 108]. These issues are particularly concerning for applications that require continuous or long-term operation, such as wearable health monitoring or soft robotics.

To address mechanical fatigue, researchers have investigated various methods for enhancing the durability of stretchable strain sensors. These methods include the use of self-healing materials that can autonomously repair cracks or damage, as well as the incorporation of advanced geometrical structures such as wrinkled or kirigami-inspired designs that can distribute strain more evenly [88, 89, 109, 110]. Nonetheless, achieving long-term mechanical stability in highly stretchable strain sensors remains an active area of investigation.

Future Directions: Although substantial progress has been made in addressing the challenges of conventional strain sensors, many of the solutions are still in their early stages and require further refinement. A critical aspect that remains to be fully addressed is the influence of environmental factors on sensor performance, including temperature variations and humidity effects. While onboard computing and real-time compensation strategies can mitigate these issues, they introduce additional power consumption, which is not ideal for long-term monitoring applications. Alternatively, advanced manufacturing techniques have been explored to enhance sensor stability, but they often involve complex, costly, and time-intensive processes. Future research should therefore focus on developing materials with inherent environmental stability, minimizing hysteresis and drift through both material innovations and efficient signal processing.

Using soft strain sensors reviews, we show here a comprehensive collection of soft strain sensors and there performances in a single table.[56, 58, 111]

Table 2.1: Performance Comparison of Stretchable Strain Sensors

Reference	Sensor Type	Materials	Stretchability (%)	Gauge Factor	Linearity
Ag-based Sensors					
[112]	Resistive	AgNWs-PDMS	70	2-14	Linear up to 40%
[113]	Capacitive	AgNWs-Ecoflex	50	0.7	Linear
[114]	Resistive	AgNWs/PU fiber/PDMS	60	Up to 9557	Nonlinear
[115]	Resistive	Film strip (Ag NPs, PDMS)	70	10.08	1 linear region
[116]	Resistive	Fiber (Ag NWs, Ag NPs, SBS)	220	-	-
[117]	Resistive	Wrinkled film (Ag NWs, PDMS)	30	7.1	2 linear regions
[118]	Resistive	Filled macro porous foam (Ag NWs, TGF, FPU)	60	11.8	-
CNT-based Sensors					
[119]	Resistive	Aligned CNTs-PDMS	280	0.82	Two linear regions
[120]	Capacitive	CNTs-Ecoflex	150	1	Linear
[121]	Capacitive	CNTs-silicone elastomer	100	0.99	Linear
[122]	Resistive	CNTs/Ecoflex fibers	600	Up to 1378	Two linear regions
[123]	Resistive	CNTs nanopaper/PDMS	100	Up to 2.21	Three linear regions
[73]	Resistive	CNTs/prestretched PDMS	100	6-87	Two linear regions
[124]	Resistive	CNTs/PDMS	20	1140	Linear
[125]	Resistive	CNTs/TPU fiber	320	22.1-97.5	Two linear regions
[87]	Resistive	CNTs/prestretched TPU	300	428.5-83982.8	Three linear regions
Graphene-based Sensors					
[126]	Resistive	Graphene foam-PDMS	70	15-29	Linear
[127]	Resistive	Graphene-rubber	800	10-35	Nonlinear
[128]	Resistive	Vertical graphene nanosheets/PDMS	110	32	Linear
[129]	Resistive	PAVG/PDMS	10	5.87-10.28	Linear
[130]	Resistive	NiNPs/rGO/PU sponge/PDMS	65	Up to 3360.1	Two linear regions
[131]	Resistive	Aligned rGO/TPU fibers/PDMS	150	593	Linear
[132]	Resistive	rGO/PDMS	350	18.5-88443	Three linear regions
Polymer-based Sensors					

Continued on next page

Reference	**Sensor Type**	**Materials**	**Stretchability (%)**	**Gauge Factor**	**Linearity**
[133]	Resistive	CBs-PDMS	30	29.1	Linear
[134]	Resistive	CBs-TPE	80	20	Nonlinear
[135]	Resistive	CBs-Ecoflex	400	3.8	Nonlinear
[136]	Resistive	AgNWs-PEDOT:PSS/PU	100	1.07-12.4	Nonlinear
[137]	Resistive	CNTs-PEDOT:PSS/PU	100	8.7-62.3	Nonlinear
[138]	Resistive	CNTs/CBs/silicone rubber/PDMS	120	1.25	Linear
[139]	Resistive	CBs/CNTs/silicone rubber	50	2.18	Linear
Fabric-based Sensors					
[140]	Resistive	Carbonized silk fabric/Ecoflex	500	9.6-37.5	Two linear regions
[141]	Resistive	rGO/cotton bandage	57	416-3667	Two linear regions
[142]	Resistive	GNPs/CBs/fragmented cotton fabric/Ecoflex	400	95.64-102351	Three linear regions
[143]	Resistive	Carbonized cotton/Ecoflex	140	25-64	Two linear regions
Optical Sensors					
[144]	Optical	Au NPs/PDMS	100	9.54 dB/	Linear
[145]	Optical	PDMS fibers	100	3.62 dB/	Linear
[146]	Optical	Polystyrene-based elastomer	300	10 dB/	Nonlinear
[147]	Optical	Graphene/PDMS fibers	100	13.5 dB/	Linear

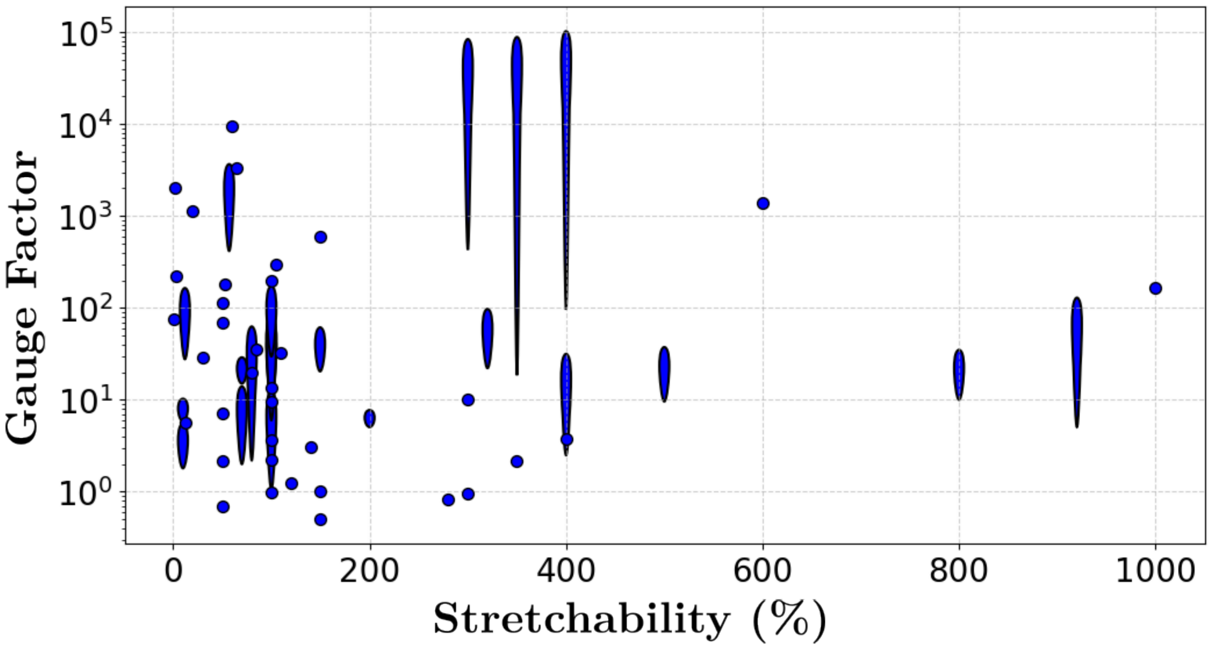

Figure 2.13: Performance summary of soft strain sensors

2.4 LIG-Polymer Composites for Soft Strain Sensors

LIG-polymer composites have garnered significant attention as materials for soft strain sensors due to the exceptional electrical conductivity of graphene combined with the flexibility and resilience of polymer matrices. These composites offer a unique synergy between graphene's conductive properties and the mechanical durability of polymers, resulting in high sensitivity, robustness, and adaptability for applications in wearable electronics, soft robotics, and health monitoring.

The fabrication of LIG-polymer composites involves laser irradiation of a polymer precursor, creating a porous, interconnected graphene network. Critical parameters such as laser wavelength, power, and scanning speed directly influence the structure and quality of the LIG network as described previously. Once formed, the LIG network is embedded within a polymer matrix, which provides mechanical support and flexibility, resulting in a cohesive composite material. Post-fabrication treatments, such as chemical doping or mechanical conditioning, can further enhance the sensor's sensitivity and stability. [16]

The core sensing mechanism in LIG-polymer composites is based on the piezo-resistive effect. Mechanical strain applied to the composite alters the electrical resistance of the LIG network due to changes in the interatomic distances within the graphene structure, affecting electron mobility and scattering. The polymer matrix ensures efficient transfer of mechanical deformation to the LIG network, enabling precise resistance changes that reflect the applied strain. LIG's high carrier mobility and low defect density further enhance this piezo-resistive response, leading to high sensitivity and reliability in strain measurements [148–152].

During mechanical deformation, the LIG network undergoes structural changes that affect its electrical properties. When stretched, microcracks or disrupted conductive pathways may form in the LIG, increasing the sensor's resistance. Conversely, compressing the composite can improve connectivity between graphene flakes, reducing resistance. The polymer matrix's elasticity accommodates these deformations, ensuring the integrity of the graphene network is maintained.

2.4.1 Advantages of LIG-Based Soft Strain Sensors

LIG-based soft strain sensors offer several compelling advantages over conventional strain sensors, making them highly suitable for a range of applications, including wearable electronics, soft robotics, and health monitoring. One of the primary benefits is the simplicity and scalability of the LIG fabrication process. Unlike traditional graphene synthesis methods, which often require complex procedures like CVD or mechanical exfoliation, LIG is created through a straightforward laser irradiation process. This technique allows for rapid, localized production of graphene directly on various polymer substrates without the need for complex transfer steps.

The choice of polymer substrate in LIG-based sensors is highly flexible, enabling customization based on the intended application. Polymers such as PDMS, TPU and Ecoflex are commonly used due to their excellent mechanical properties and compatibility with the LIG process [153–155]. This flexibility allows researchers and manufacturers to optimize sensor properties such as stretchability, durability, and biocompatibility.

In addition to cost efficiency, LIG-based sensors offer tunable electromechanical properties, which can be adjusted by modifying the laser parameters during fabrication. Parameters such as laser power, wavelength, and scanning speed directly influence the quality of the LIG network, allowing for control over the sensor's sensitivity, gauge factor, and operating range [156, 157]. This tunability provides significant versatility, enabling the development of sensors with specific responses to mechanical strain, tailored for particular applications.

2.5 Common Applications of LIG-nanocomposites Sensors

LIG sensors have emerged as highly versatile tools in various fields, offering unique advantages due to their flexibility, conductivity, and ease of fabrication. This section focuses on the primary application areas of LIG-based sensors, highlighting their significance and potential in diverse applications.

2.5.1 Healthcare and Wearable Sensors

In the healthcare sector, LIG-based sensors play a critical role in continuous health monitoring, diagnostics, and rehabilitation. Their high flexibility, biocompatibility, and ability to conform to the human body make them ideal for unobtrusive, wearable health monitoring systems.

2.5.1.1 Motion Monitoring

LIG-based strain sensors have emerged as a promising technology for human motion monitoring due to their exceptional sensitivity, mechanical flexibility, and biocompatibility. Their ability to undergo large deformations while maintaining stable electrical properties enables seamless integration with the skin and underlying tissues, facilitating high-precision detection of a wide range of physiological movements. These sensors provide real-time tracking of joint articulation, muscle contractions, and postural adjustments, making them highly suitable for applications in physical therapy, rehabilitation, and sports performance assessment. Their conformability and lightweight nature allow for long-term, unobtrusive monitoring without compromising wearer comfort or mobility.

One of the key advantages of LIG-based motion sensors is their ability to detect subtle strain variations with high gauge factors, ensuring accurate motion capture even at low strain levels. The integration of LIG with elastomeric substrates such as PDMS and PI has enabled the development of highly stretchable and durable sensor platforms that can accommodate complex deformations encountered during dynamic physical activities. For instance, LIG-PDMS nanocomposite sensors have been employed to monitor joint movements in real time, assisting in rehabilitation strategies by providing quantitative biomechanical data [158]. Similarly, LIG-PI sensors have been utilized for sleep monitoring and detecting involuntary limb movements, contributing to the assessment of neurological conditions and sleep disorders [159].

Furthermore, LIG-based motion sensors have been explored for athletic training and performance optimization, where precise movement tracking is crucial for injury prevention and technique refinement. Their low power consumption and compatibility with wireless data transmission systems make them well-suited for integration into smart textiles and wearable devices, paving the way for next-generation human-machine interfaces and personalized health monitoring solutions [160].

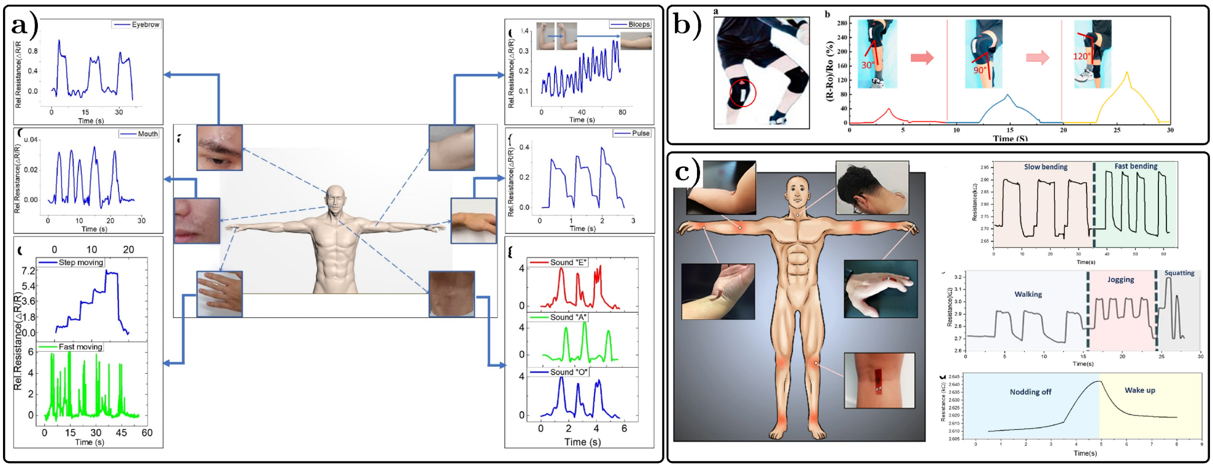

Figure 2.14: LIG-based strain sensors for motion monitoring applications: a) LIG-PDMS nanocomposite sensor demonstrating high flexibility and responsiveness for diverse motion detection [158]; b) LIG-PDMS-based wearable sensor for real-time sports motion monitoring, enabling performance optimization and injury prevention [160]; c) LIG-PI nanocomposite sensor applied for joint movement analysis and sleep monitoring, highlighting its potential in clinical and biomedical applications [159].

2.5.1.2 Smart Clothing

The integration of LIG-based sensors into textiles has revolutionized wearable technology, enabling the development of smart clothing capable of real-time, non-invasive monitoring of physiological parameters such as heart rate, respiration, body movement, and temperature. The inherent properties of LIG, including high electrical conductivity, mechanical flexibility, lightweight structure, and facile laser-based fabrication, make it particularly suitable for seamless integration into various textile substrates, including woven, non-woven, and knitted fabrics. Unlike conventional electronic textiles, which often require rigid components or additional conductive coatings, LIG-based e-textiles offer an all-carbon, highly flexible alternative with superior mechanical durability and environmental stability.

LIG-enabled smart clothing holds significant potential across multiple fields. In sports science, wearable garments with embedded LIG sensors provide detailed biomechanical feedback, allowing athletes to monitor their physiological performance, detect fatigue, and optimize training regimens while reducing the risk of injury. In healthcare, these textiles facilitate continuous health surveillance for individuals with chronic conditions such as cardiovascular diseases and respiratory disorders, enabling early detection of anomalies and real-time health assessment. Additionally, by capturing subtle physiological variations, LIG-based smart textiles contribute to preventive medicine by identifying preclinical symptoms of disease onset, thereby enabling timely intervention [161–163].

The fabrication of LIG-based textile sensors typically involves direct laser patterning of carbonized structures onto fabric surfaces or incorporating LIG-coated fibres into flexible substrates, ensuring excellent adhesion and durability under repeated mechanical stress. Moreover, advancements in textile-integrated metamaterials and hybrid nanocomposites have further enhanced the multifunctionality of LIG-based e-textiles, allowing for simultaneous sensing, energy harvesting, and wireless signal transmission, paving the way for the next generation of smart wearable systems.

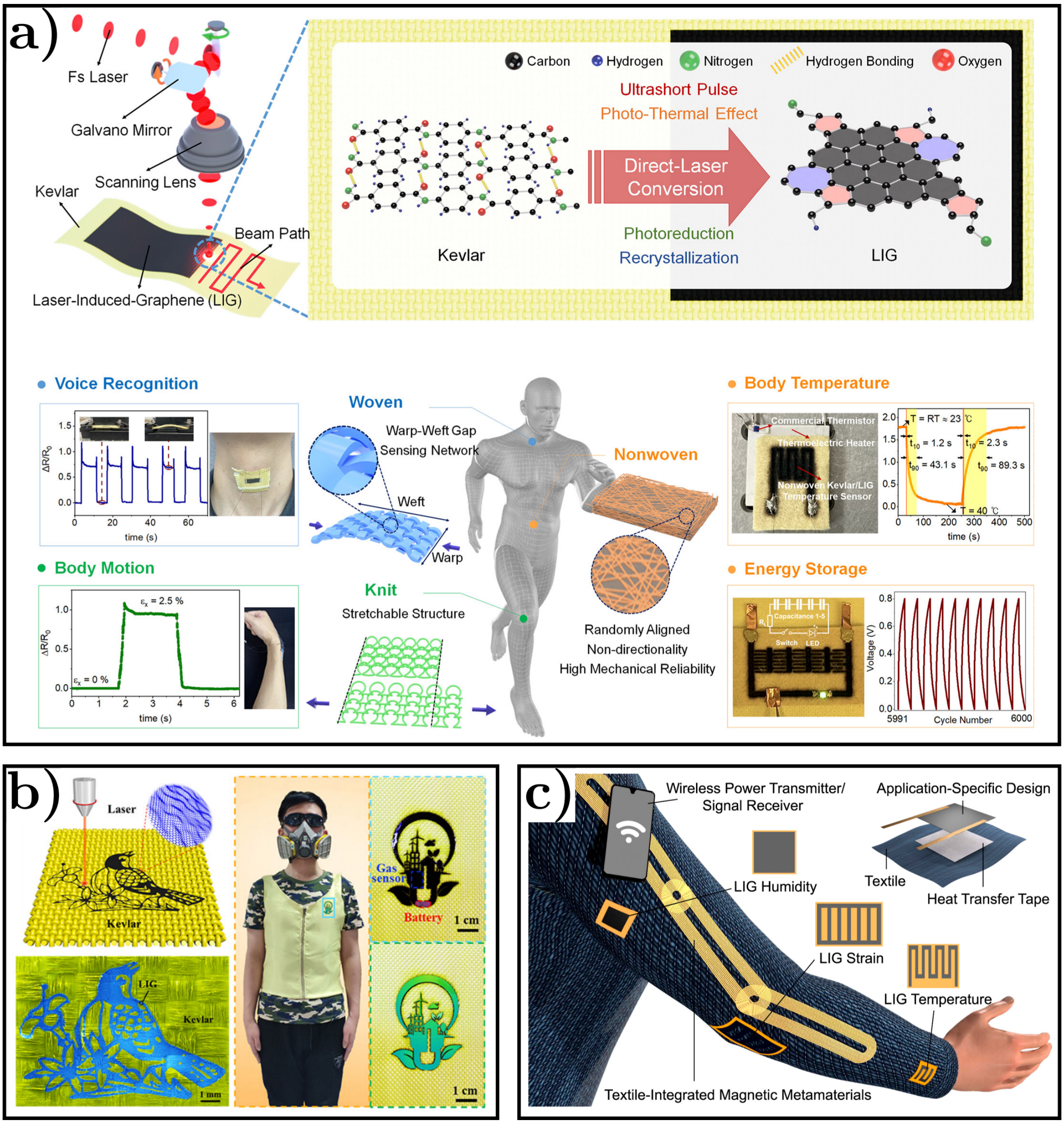

Figure 2.15: LIG-based smart textiles for wearable sensing applications: a) Direct laser-patterned LIG on woven, non-woven, and knit textiles, highlighting its adaptability to different fabric structures [163]; b) LIG-based e-textile on Kevlar, demonstrating high mechanical robustness for demanding applications [162]; c) Multifunctional textile sensors integrated with textile-based metamaterials, enabling cross-body communication and advanced wearable functionalities [161].

2.5.1.3 Robotics and Human-Machine Interfaces (HMI)

LIG-based sensors have gained significant attention in robotics and HMI due to their superior flexibility, high piezoresistive sensitivity, and rapid response times. These characteristics make them highly suitable for real-time motion and force sensing, facilitating improved control, dexterity, and adaptability in robotic systems, prosthetic limbs, and exoskeletons. By providing dynamic feedback on force application and movement precision, LIG sensors contribute to the development of more natural and intuitive robotic interactions, particularly in assistive and rehabilitation technologies [164].

In HMI applications, wearable LIG-based sensors enable seamless and responsive gesture recognition, allowing for enhanced user interaction with electronic systems, virtual reality (VR), and augmented reality (AR) platforms. Their integration into smart gloves, flexible touch interfaces, and brain-machine communication systems has opened new possibilities for immersive digital experiences and assistive communication tools [165]. Recent advances in LIG-based triboelectric nanogenerators (TENGs) have demonstrated their potential in self-powered, wireless gesture recognition systems, enhancing user convenience and system autonomy [166].

Furthermore, hybrid LIG architectures incorporating gold nanoparticles, titanium oxide nanostructures, or multilayer polymer composites have been explored to enhance sensor performance for complex robotic applications, such as adaptive grip force control and real-time electromyography (EMG) monitoring. These advancements enable soft actuators and robotic limbs to interact with humans more effectively, improving rehabilitation strategies and neuroprosthetic integration [167].

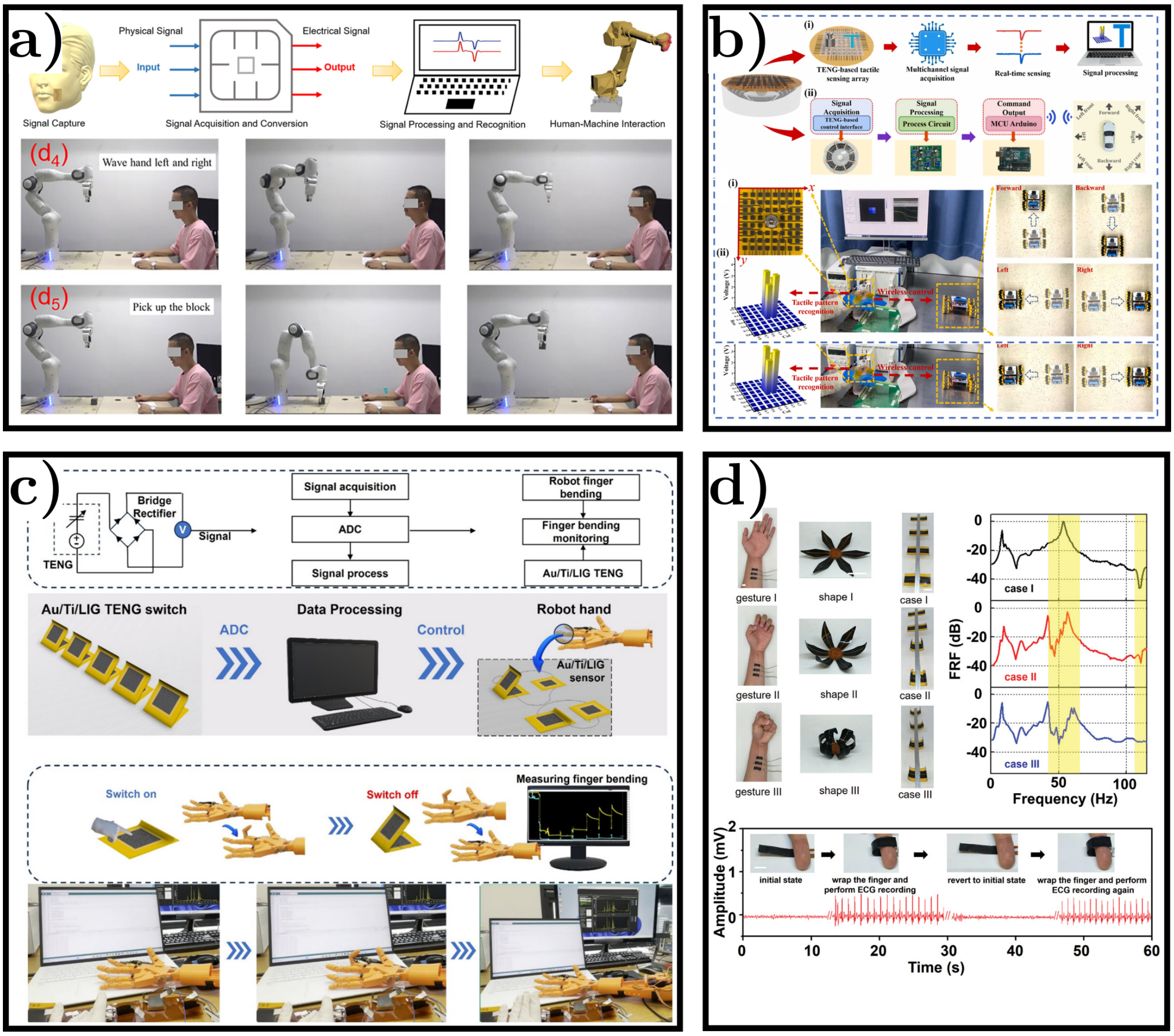

Figure 2.16: LIG-based sensors for advanced human-machine interfaces and robotics: a) Lip-reading recognition system using LIG-based sensors for silent speech detection [164]; b) LIG-based TENGS enabling simultaneous wireless control and tactile pattern recognition [165]; c) Enhanced LIG sensors incorporating gold nanoparticles and titanium oxide for robotic arm control [166]; d) LIG-based PI-PDMS bi-structure for real-time EMG monitoring and human–soft actuator interaction [167].

2.6 Summary

In this chapter, we provided a comprehensive overview of the key concepts, processes, and advancements surrounding the development of LIG for soft strain sensors. We began by exploring graphene, its exceptional properties, and the conventional synthesis methods such as mechanical exfoliation, CVD, and the chemical reduction of GO. While these techniques produce high-quality graphene, they suffer from limitations in scalability, cost, and process complexity, motivating the search for alternative, more accessible fabrication methods.

LIG has emerged as a promising solution, offering a rapid, cost-effective, and scalable approach for producing graphene directly on polymeric substrates. We examined the fundamental mechanisms behind LIG formation, emphasizing the critical role of laser parameters, such as power, pulse duration, wavelength, and scan speed, in dictating the morphology and electrical properties of the resulting graphene structures. Furthermore, we reviewed the characterization techniques used to assess the microstructure and electrical performance of LIG, demonstrating its potential as a functional material for strain sensing applications.

Despite these advantages, significant challenges remain. The intrinsic porosity of LIG, while beneficial for sensing applications, also makes it highly sensitive to environmental factors such as humidity, temperature fluctuations, and mechanical degradation over time. These external influences can lead to signal instability and hinder the reproducibility of sensor performance, which remains a major obstacle to widespread adoption. Additionally, while the integration of LIG with polymeric matrices aims to enhance mechanical robustness and flexibility, the resulting nanocomposites often exhibit inconsistencies in conductivity, adhesion, and durability, particularly under repeated strain cycles. Current strategies to mitigate these effects, such as material doping and surface modifications, have shown promise but do not fully resolve these limitations.

Moreover, while LIG-based soft strain sensors have demonstrated significant potential across diverse fields, including healthcare, robotics, human-machine interfaces, and environmental monitoring, their long-term stability, sensitivity control, and batch-to-batch reproducibility remain unresolved challenges. Addressing these issues is critical for advancing LIG from a laboratory-scale material to a reliable component in commercial sensor technologies.

This summary provides a strong foundation for the experimental and analytical framework described in the next chapter. In the following section, we detail the methodology used for the fabrication, characterization, and optimization of LIG-based nanocomposites, with a particular focus on laser processing techniques, polymer integration, and electromechanical testing, aiming to explore strategies that could mitigate these existing limitations.

Chapter 3

Methodology

3.1 Introduction

This chapter outlines the comprehensive methodology developed for the fabrication, characterization, and testing of LIG-based strain sensors and nanocomposites. Our approach is organized in a logical sequence, beginning with the manufacturing of LIG and its integration into flexible polymeric nanocomposites. Advanced material characterization techniques, including Raman spectroscopy, SEM, EDX, and XPS, are then employed to evaluate the microstructural, chemical, and compositional properties of the sensors.

Following material characterization, we describe custom-designed setups for mechanical testing, including strain measurements, which provide precise insights into the sensor's electromechanical performance. In parallel, thermal characterization protocols using a heated 3D printer bed and a humidity chamber are presented to assess sensor behaviour under varying temperature and humidity conditions.

Central to our methodology is the development of a centralized system for data acquisition and control. Implemented using both LabVIEW and Python-based interfaces, this system integrates all measurement tools to enable automated, synchronized data collection and real-time monitoring. Moreover, the incorporation of wireless communication via Wi-Fi and Bluetooth facilitates remote data transmission, thereby extending the applicability of the sensor system to real-time and long-term monitoring scenarios.

By integrating these diverse techniques and systems, from sensor fabrication to multi-modal testing and centralized control, this methodology provides a robust framework for optimizing LIG-based strain sensors for a wide range of applications.

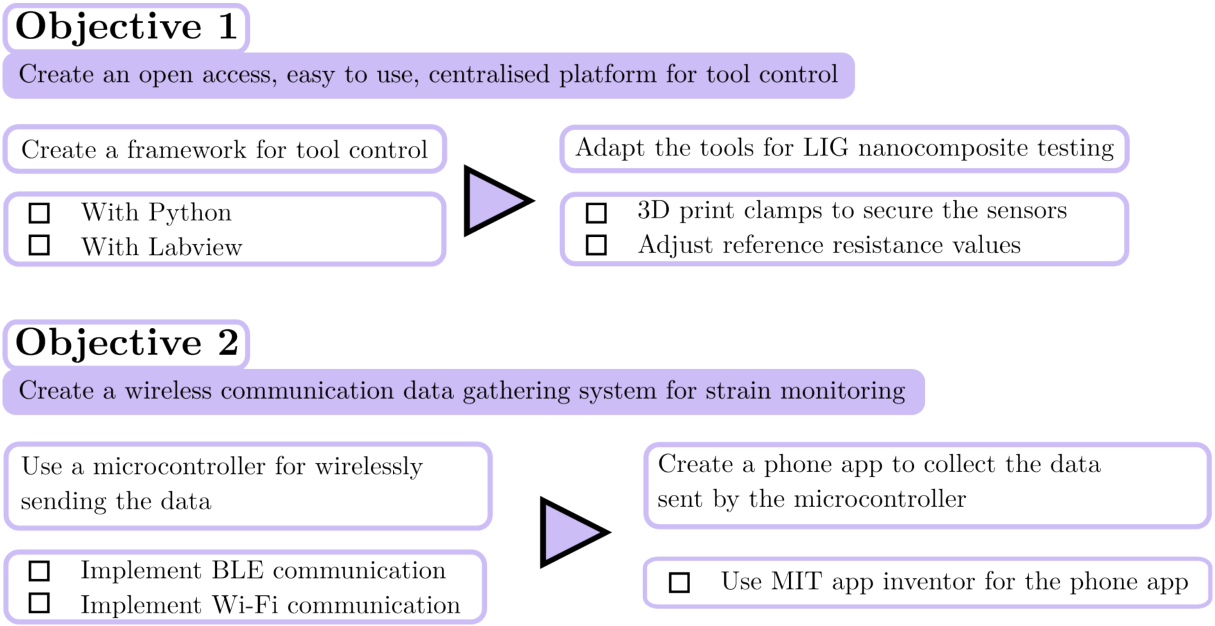

Figure 3.1: Chapter 3 Objectives Flowchart

3.2 LIG and LIG-Nanocomposites Manufacturing

This section details the fabrication protocols used to produce LIG and LIG-based nanocomposites as developed in this thesis. As discussed in Section 2.2, a high-powered laser is employed to convert PI into graphene. In this work, a commercial Trotec Speedy 300 laser system was used for LIG formation. Two types of PI substrates were utilized: a thin film (45 µm) and a thick film (150 µm) (sourced from Craftbot and 3M). In both cases, the PI is initially laminated onto a glass substrate to ensure uniformity during laser processing.

Following laser irradiation, the resulting LIG structures were interfaced with electrodes using silver paste for electrical measurements. To fabricate LIG-nanocomposites, the LIG layer was subsequently integrated with elastomeric matrices. For PDMS-based composites (Sylgard 184, Dow Corning), a 10:1 mixture (base to curing agent) was either poured or spin-coated onto the LIG surface. The samples were then degassed to ensure thorough infiltration of the polymer into the porous LIG network and cured at 90° C for one hour. An analogous procedure was followed for Ecoflex composites. After curing, the nanocomposite films were carefully peeled from the remaining PI substrate, and electrodes were attached using silver paste. This manufacturing protocol can be seen in figure 3.2.

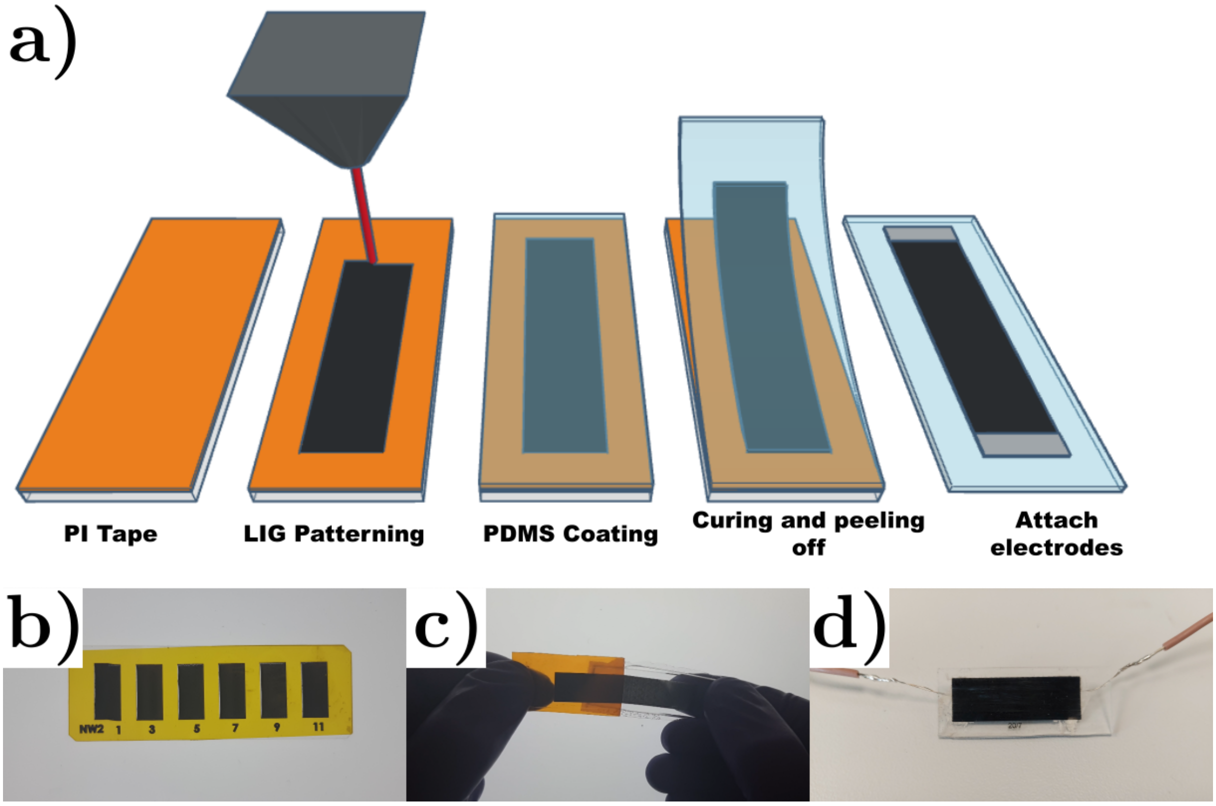

Figure 3.2: a) Schematic overview of the LIG-nanocomposites fabrication process; b) LIG formed on a thin PI substrate; c) LIG-PDMS nanocomposite being peeled from a thick PI substrate; d) Complete LIG-PDMS sensor with integrated electrodes.

3.3 Material characterisation

The characterization of LIG is critical to understanding its structural, chemical, and electrical properties, which directly influence its performance in various applications, particularly in sensing technologies. One of the primary techniques employed in the analysis of LIG is Raman spectroscopy, which provides valuable information regarding the quality, defects, and crystallinity of the graphene structure.

Raman Spectroscopy

Raman spectroscopy is widely regarded as the gold standard for characterizing graphene-based materials, including LIG, as it provides critical insights into structural quality, defect density, and the degree of graphitization. A typical Raman spectrum of graphene features three primary peaks: the **D-band**, **G-band**, and **2D-band**, each of which provides specific information about the material's structural properties [16, 168–170]. An example Raman spectrum is shown in Figure 3.3a.

The **D-band** (Defect Peak), appearing around **1350 cm^{-1}**, is associated with disorder-induced scattering and is indicative of defects such as vacancies, grain boundaries, and functionalized carbon sites. A higher intensity D-band generally corresponds to an increased number of defects or functional groups attached to the graphene surface. In LIG, the intensity of this peak varies based on laser processing conditions, which directly influence the degree of graphitization and the extent of structural disorder. The **G-band** (Graphite Peak), located around **1580 cm^{-1}**, corresponds to the in-plane vibrational mode of sp^2-bonded carbon atoms and is a key marker of graphitic structures. Its intensity relative to the D-band (I_D/I_G ratio) is commonly used to assess material quality, where a higher G/D ratio indicates a more ordered and graphitic structure. The **2D-band** (Second-order D Peak), centred around **2700 cm^{-1}**, serves as a key indicator of the number of graphene layers. In monolayer graphene, this peak is sharp and symmetric, whereas in multilayer graphene, it broadens and becomes asymmetric. In LIG, a low I_{2D}/I_G ratio (typically **<0.5**) suggests a multilayered, turbostratic graphene structure.

Quantitative analysis of these peaks provides deeper insights into LIG's structural characteristics. The **I_D/I_G ratio**, typically ranging from **0.8 to 1.5**, reflects the defect density and disorder level, with higher values (1–1.5) indicating a more defective structure, while lower values (0.1–0.5) suggest better graphitization. Similarly, the **full width at half maximum (FWHM)** of the peaks reveals additional structural details. The **G-band FWHM**, usually within **30–80 cm^{-1}**, tends to be broader than in pristine graphene due to defects, strain, and chemical functionalization induced during laser processing. The **2D-band FWHM**, typically **50–100 cm^{-1}**, further confirms the presence of structural defects and turbostratic disorder. These broadened peaks highlight the non-ideal nature of LIG, distinguishing it from pristine graphene and emphasizing its unique structural characteristics influenced by processing conditions and precursor composition.

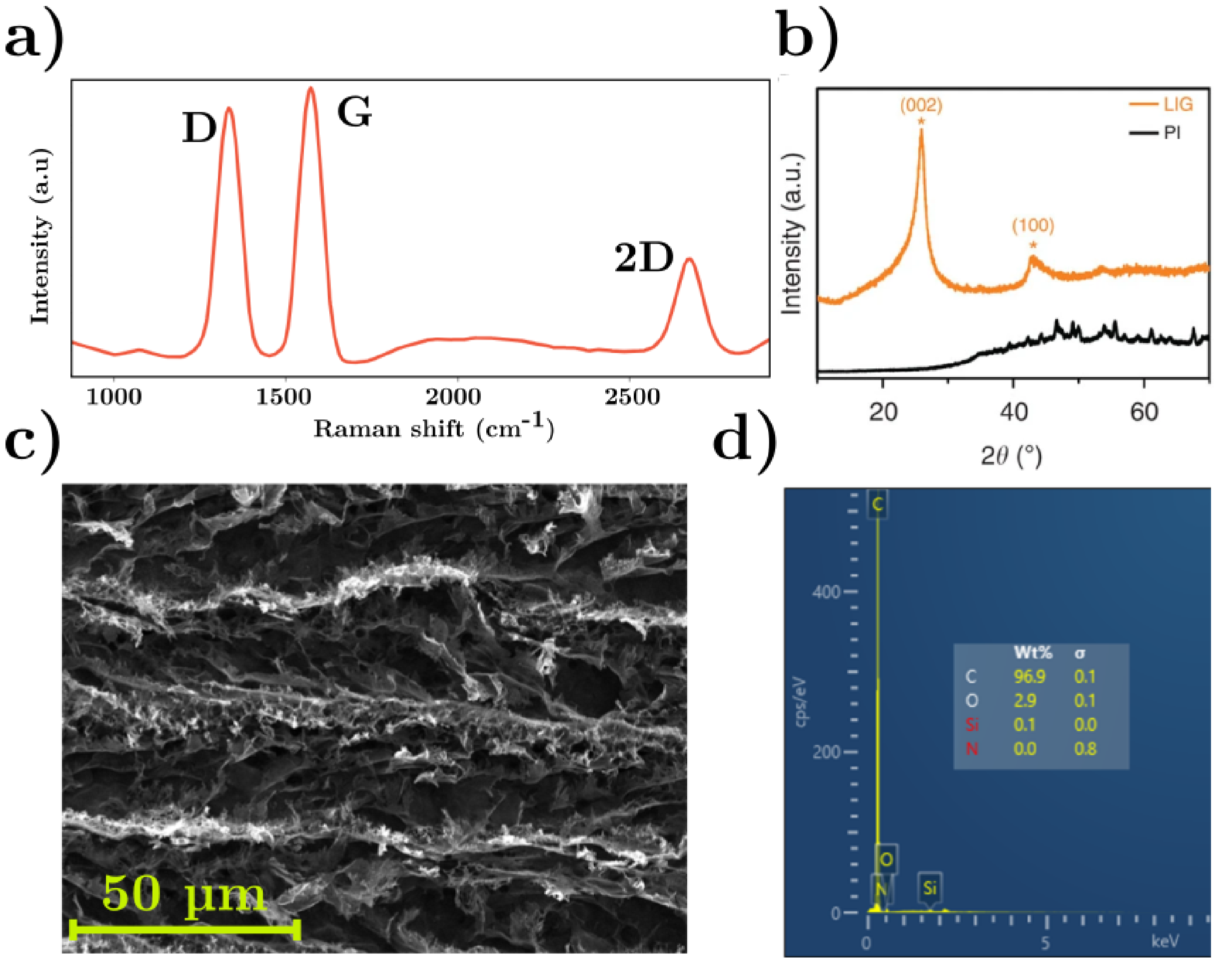

	Wt%	σ
C	96.9	0.1
O	2.9	0.1
Si	0.1	0.0
N	0.0	0.8

Figure 3.3: Example results from the characterization of LIG: a) Raman spectrum of LIG synthesized from commercial PI, highlighting key vibrational modes; b) X-Ray Diffraction (XRD) pattern of powdered LIG extracted from the PI film, indicating its crystallinity [16]; c)SEM image showcasing the surface morphology of LIG; d)EDX data for a sample of LIG, providing elemental composition analysis.

In addition to the position and intensity of these peaks, the full width at half maximum (FWHM) of the peaks can further help quantify the crystalline quality of the material.

Raman spectroscopy was performed using a confocal Raman microscope (LabRAM HR, Horiba Jobin Yvon) with a 532 nm laser source (Ventus 532 laser system, 100 mW power output).

Surface Morphology and Microstructure: The structural characteristics of LIG are typically examined using SEM and atomic force microscopy (AFM), which provide complementary insights into its morphology at different scales.

SEM provides high-resolution images of the LIG surface, revealing its porous structure, as shown in Figure 3.3c). The porosity of LIG significantly enhances its surface area, making it suitable for applications such as sensing and energy storage. Additionally, the microstructure of LIG is influenced by key laser processing parameters, such as power, speed, and wavelength, which affect graphitization and porosity. By analysing SEM images, correlations between fabrication conditions and material properties can be established, allowing for optimization of LIG synthesis [29].

SEM was conducted using a Tescan Clara microscope to examine the microstructure and surface morphology of pristine LIG and nanocomposite films. Additionally, EDX was utilized alongside SEM for elemental analysis, providing a detailed compositional profile of the LIG sensor materials.

Chemical Composition Analysis: Beyond Raman spectroscopy, chemical composition analysis is crucial for determining the degree of carbonization and the residual oxygen content in the LIG. Techniques such as X-ray photoelectron spectroscopy (XPS) and energy-dispersive X-ray spectroscopy (EDX) are commonly employed for this purpose.

- **X-ray Photoelectron Spectroscopy (XPS):** XPS provides information on the elemental composition and the chemical state of the elements present in LIG. The C1s peak in XPS can be deconvoluted into various bonding states (e.g., sp^2 carbon, sp^3 carbon, and C-O bonds) to assess the extent of carbon-oxygen functional groups present in the material. A high ratio of sp^2 carbon relative to oxygen-containing groups indicates a successful reduction of oxygen during the laser conversion process.[34, 156] An Axis Supra+ Kratos anaytical was used for this thesis.
- **Energy-Dispersive X-ray Spectroscopy (EDX):** EDX is often used in conjunction with SEM to map the distribution of elements across the LIG surface. This method is particularly useful for evaluating the homogeneity of doping or additives which are incorporated into the graphene network. The carbon-to-oxygen ratio obtained from EDX analysis can be used to assess the degree of conversion of PI to graphene. A lower oxygen content typically signifies higher-quality LIG with fewer oxygenated defects.[171]

In summary, the characterization of LIG involves a combination of spectroscopic, microscopic, and electrical analyses to provide a comprehensive understanding of its structure and properties. Raman spectroscopy remains a cornerstone technique, offering detailed insights into the crystallinity and defect density, while chemical composition and surface morphology analyses further complement the evaluation of LIG quality. These characterization techniques are essential for optimizing LIG fabrication and tailoring its properties for specific applications, particularly in the field of flexible electronics and soft sensors.

3.4 Mechanical characterization

3.4.1 Performance Metrics for Strain Sensors

The performance of a strain sensor is assessed using several key parameters, each critical to determining its suitability for practical applications:

- **Durability:** Evaluated through cyclic loading tests to assess the sensor's longevity and mechanical robustness under repeated deformation.
- **Signal-to-Noise Ratio (SNR):** Represents the sensor's ability to distinguish strain-induced resistance changes from background noise, directly affecting measurement reliability.
- **Gauge Factor (GF):** A fundamental parameter quantifying the sensor's sensitivity, defined as:

  $$GF = \frac{\Delta R}{R_0 \varepsilon} \tag{3.1}$$

  where ΔR is the change in electrical resistance, R_0 is the initial resistance at 0% strain, and ε is the applied strain, given by:

  $$\varepsilon = \frac{\Delta L}{L_0} \tag{3.2}$$

  where ΔL denotes the change in length, and L_0 is the original length of the sensor.

Advancements in resistive strain sensor design continue to focus on optimizing these performance metrics to enhance sensitivity, mechanical stability, and durability, enabling their integration into emerging applications such as wearable electronics, human-motion tracking, and soft robotics.

3.4.2 Strain Measurements

To enable accurate strain measurements, the experimental setup integrates a Zaber X-LRQ450HP-DE51 motorized linear stage with a custom-designed stand, which combines 3D-printed and laser-cut components to securely hold the samples (Figure 3.4). The Zaber stage provides highly accurate and repeatable linear motion, ensuring controlled strain application to the sensor samples.

Electrical measurements are facilitated by a National Instruments (NI) USB-6363 data acquisition (DAQ) board, which records the voltage across the sensors with high resolution. This integrated system allows for simultaneous measurement of strain and electrical resistance, offering a comprehensive dataset to evaluate sensor performance during mechanical deformation.

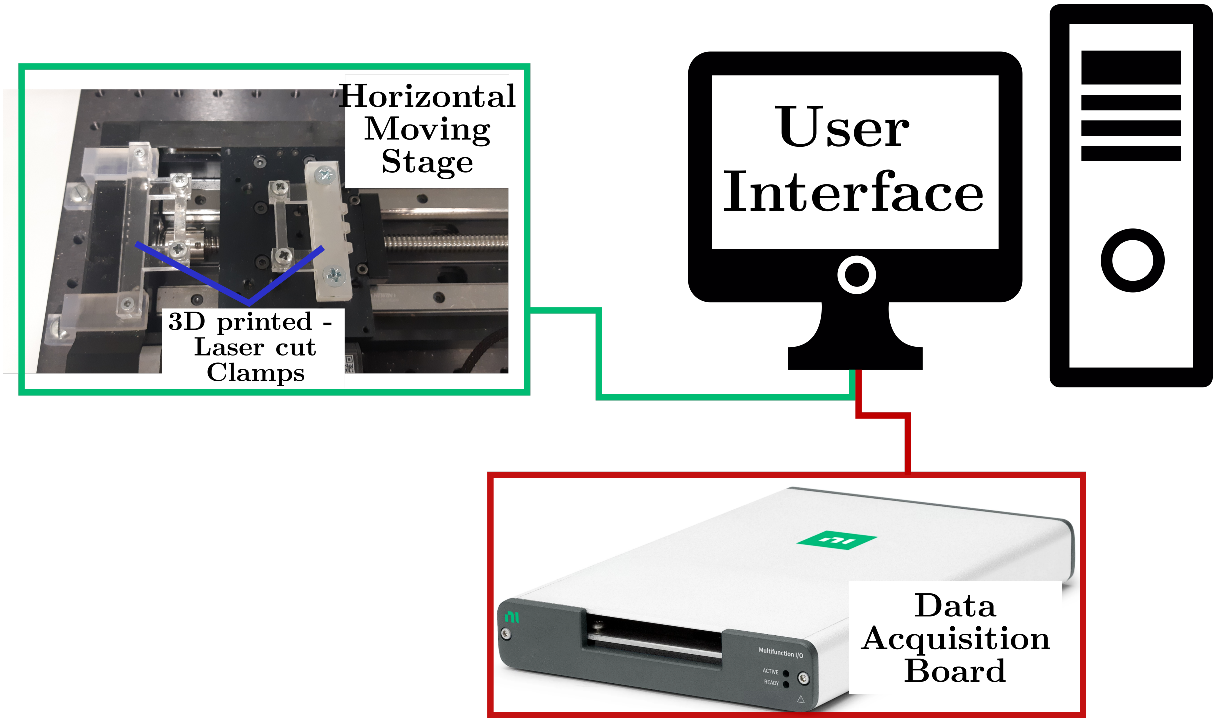

Figure 3.4: Schematic of the horizontal stage setup, showing the integration of the Zaber motorized linear stage and the custom 3D-printed/laser-cut sample holder.

Strain application is managed through a central control interface, which can be implemented using either LabVIEW or Python, depending on the user's preference. The LabVIEW-based control interface (Figure 3.5) and the Python-based alternative (Figure 3.6) both provide a user-friendly platform for real-time control and monitoring. These interfaces ensure seamless communication with the Zaber stage and the DAQ board, allowing users to define detailed strain profiles and customize testing parameters.

The system supports various movement profiles, including cyclic and stepwise motions, with adjustable parameters such as amplitude, period, and the number of cycles. This flexibility allows for the application of a wide range of strain profiles, facilitating detailed studies of sensor response under different mechanical conditions. Real-time data acquisition, recording, and visualization further enhance usability, with both the applied strain and corresponding electrical resistance displayed dynamically.

This experimental setup ensures high precision in mechanical and electrical characterization, offering a platform for analysing and optimizing strain sensors. By combining accurate motion control with high-resolution data capture, the system provides a powerful and flexible tool for evaluating advanced strain sensors and refining their designs to achieve enhanced performance and functionality.

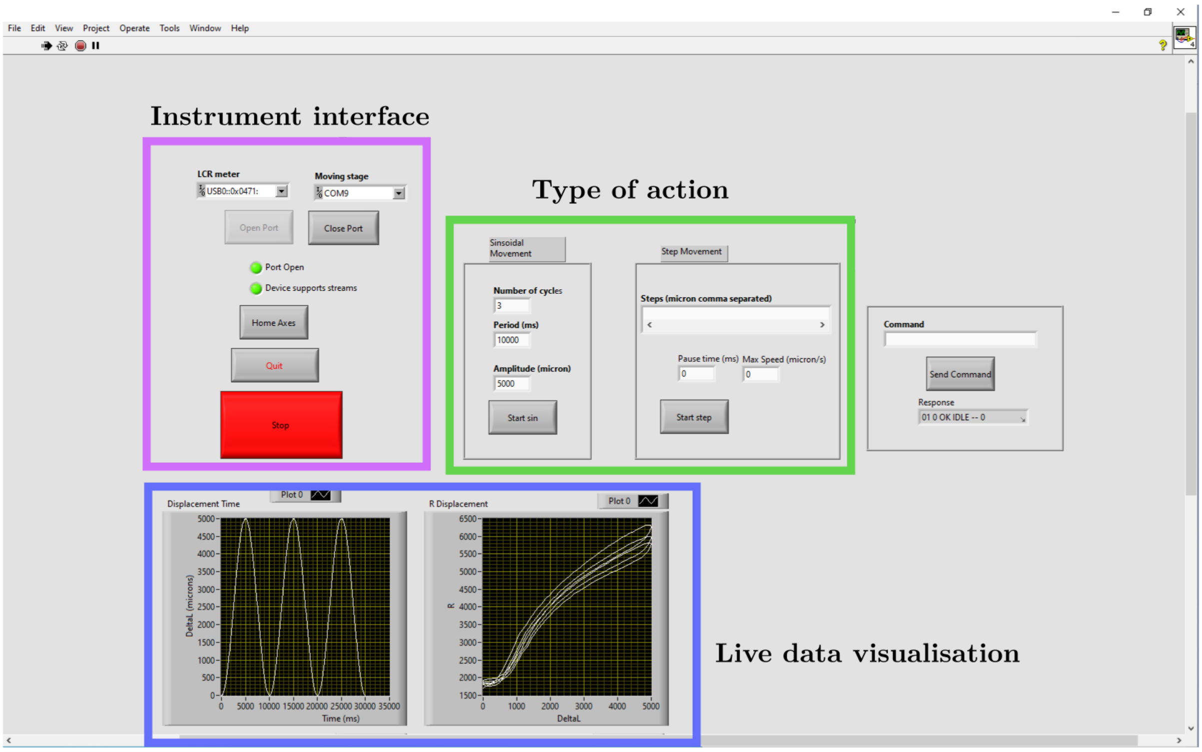

LCR meter: USB0::0x0471:

Moving stage: COM9

Number of cycles: 3

Period (ms): 10000

Amplitude (micron): 5000

Pause time (ms): 0

Max Speed (micron/s): 0

Response: 01 0 OK IDLE -- 0

Figure 3.5: User interface for the LabVIEW-based control program, enabling precise control of the motorized stage and data acquisition system.

3.5 Centralized system

The primary objective of the system is to establish a centralized unit that manages interactions with all measurement tools while facilitating seamless communication across devices. This central unit, implemented via either a LabVIEW or Python-based script, serves as the control hub, coordinating the entire setup for an integrated, automated, and efficient characterization process.

At the heart of this system is a central controller, a computer running LabVIEW or Python, configured to interface with all connected devices and serve as the primary orchestrator for data exchange and synchronization in real time. Both LabVIEW and Python approaches offer distinct advantages: LabVIEW's graphical programming environment supports rapid setup and quick testing, particularly with instruments that it natively supports, while the Python-based approach is well-suited to larger, more complex projects and is easily shareable across multiple PCs due to its license-free, open-source nature.

The Python setup, in particular, combines a PyQt5 interface with Python's native libraries for instrument communication and data acquisition. This setup enables seamless interaction with both NI hardware and serial devices, offering a flexible and scalable solution for comprehensive sensor evaluation. The custom-built PyQt5 interface in the Python system provides a user-friendly platform for managing the

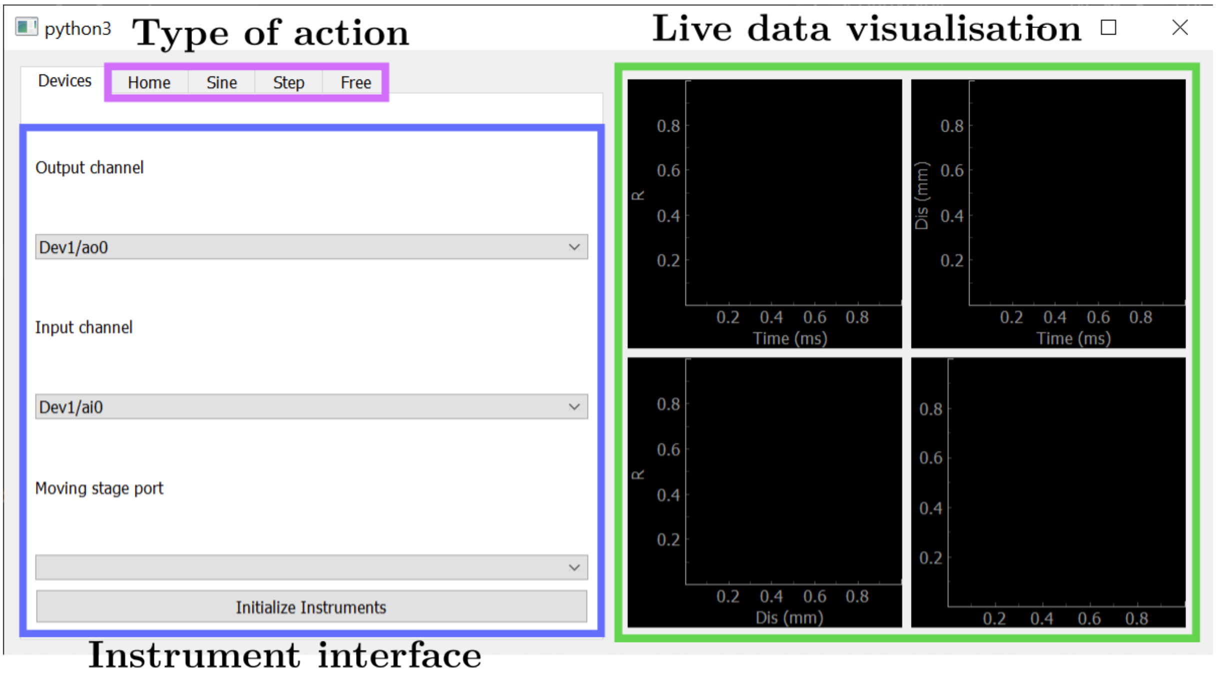

Output channel

Dev1/ao0

Input channel

Dev1/ai0

Moving stage port

Figure 3.6: User interface for the Python-based control program, offering flexibility in strain application and data visualization.

characterization process, while Python's ‘pyserial‘ and ‘pydaqmx‘ libraries facilitate smooth communication with connected instruments. Although the Python setup is initially more complex to configure than LabVIEW, it delivers a license-free and highly customizable solution that adapts well to evolving research needs.

To maximize the efficiency and responsiveness of the Python-based characterization tools, multithreading is employed to handle real-time data acquisition, processing, and visualization in parallel. This multithreading capability allows for dynamic sensor testing without delays or bottlenecks, complementing the LabVIEW system's quick prototyping capabilities. Both systems enable precise measurement of key parameters, such as strain and electrical resistance, while automating data collection and processing to minimize human error and improve consistency.

A standout feature of this centralized system is its modularity: additional tools and sensors can be integrated as required, making the system adaptable to new sensor technologies and research demands. Both the LabVIEW and Python setups effectively manage data flow between sensors and the central controller, while the Python system offers added customization without license restrictions. The PyQt5 interface in the Python setup further enhances synchronization, allowing for easy expansion and integration of new tools or sensors as research evolves.

In summary, while the LabVIEW-based system excels in ease of setup for rapid testing, the Python-based approach provides a cost-effective, and scalable alternative for material characterization, incorporating the benefits of open-source software and parallel processing capabilities. Together, these configurations form a comprehensive, flexible solution for detailed strain sensor analysis across a wide range of experimental applications.

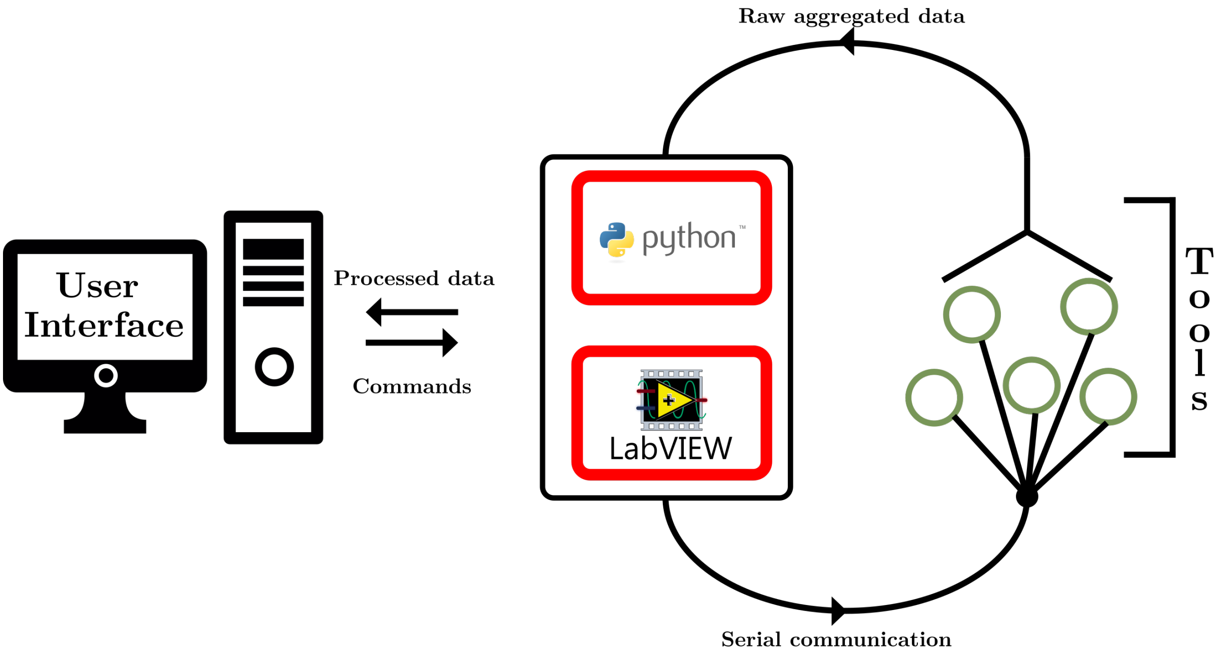

Figure 3.7: Schematics of the centralized system for tool control and data collection

Dynamic electrothermal characterisation
For dynamic thermal testing, a 858D SMD Hot Air Rework Soldering Station is placed at a distance of 2 cm from the samples to test and set at a temperature of our choosing to heat the samples up.

3.6 Thermal Characterization

For the thermal characterization of the strain sensors, two distinct protocols have been established in collaboration with Simon Wanstall from Heriot-Watt University:

Heated Bed of 3D Printer
The first protocol utilizes the heated bed of a Creality Ender 3 Pro 3D printer, which has been adapted to serve as a controlled thermal source. The heated bed is connected to a NI USB-6363 DAQ board, allowing monitoring and control of temperature. A custom Python script was developed to manage the heating process, providing fine control over the temperature profile.

To measure the sensor resistance during thermal exposure, the previously described LabVIEW data gathering system was used. Additionally, an auxiliary loop incorporates a DC95F103WN negative temperature coefficient of resistance (TCR) thermistor (Amphenol Advanced Sensors) placed near the sensors, along with a second reference resistor. This thermistor provides real-time monitoring of the temperature experienced by the sensors, ensuring reliable thermal characterization data.

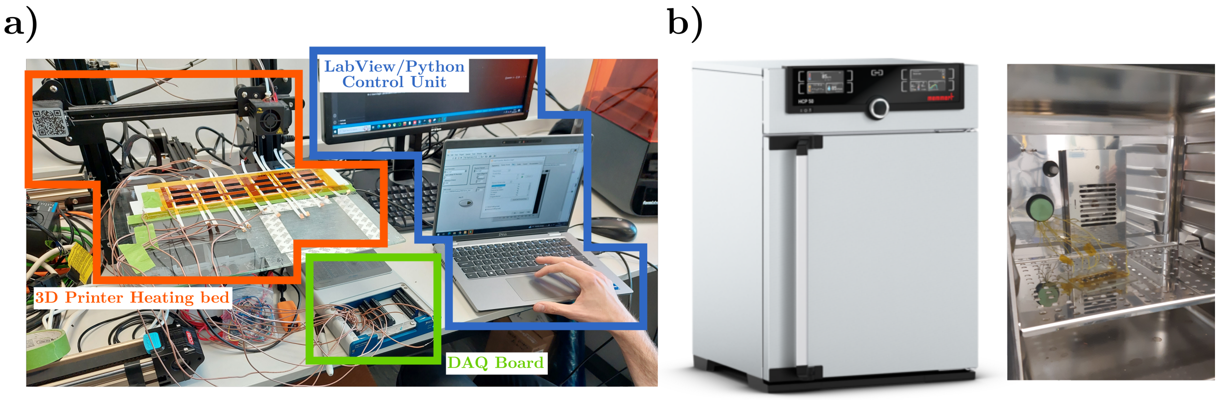

Figure 3.8: a) Heated 3D Printer Bed setup; b) Humidity chamber

Humidity Chamber

The second approach employs a Memmert HCP50 humidity chamber, which provides control over both temperature and humidity. This protocol enables detailed studies of sensor behaviour under specific environmental conditions. Samples are connected to external wires that are routed out of the chamber, allowing resistance measurements to be taken without disrupting the controlled environment. A Keysight U1242C multimeter is used to accurately measure the resistance of the samples, ensuring high-resolution data on the thermal response of the sensors.

Both approaches offer flexible platforms for the comprehensive thermal characterization of strain sensors, allowing for the evaluation of sensor performance across a wide range of thermal conditions.

3.7 Wi-Fi and Bluetooth Communication

In applications such as health monitoring, where patients may not remain stationary for extended periods, wired systems can be impractical due to their restrictive and cumbersome nature. Wireless data acquisition and communication are therefore essential in modern soft sensor systems, enabling real-time monitoring, seamless data transmission, and remote access across diverse use cases. As part of our development of advanced soft sensor technology, we designed and implemented a wireless data acquisition system leveraging both Wi-Fi and Bluetooth communication protocols.

At the core of this system is an ESP32 microcontroller, chosen for its versatility and low-power consumption, which makes it well-suited for wearable and portable applications. The ESP32 was integrated with a voltage divider circuit (see Figure 3.9a) to ensure accurate sensor data capture by scaling down the sensor output voltage to levels compatible with the ESP32's analog-to-digital converter (ADC). This allowed accurate measurement of the sensor's resistance changes during mechanical deformation, with the added benefit of minimal signal noise and interference.

The wireless communication system was designed to transmit data through two distinct channels:

Bluetooth low energy (BLE) was implemented to enable short-range communication with mobile devices, providing real-time data access and feedback. A custom mobile application was developed using MIT App Inventor, offering a user-friendly interface for displaying the sensor data in graphical format. The BLE system was optimized to prioritize low latency and stable data transmission, allowing users to visualize dynamic changes in sensor signals without delays.

Wi-Fi communication was integrated to enable long-range wireless data transfer. This feature allows the sensor to connect to local networks, transmitting data to remote servers or cloud platforms for real-time monitoring and analysis. The Wi-Fi capability significantly extends the potential applications of the soft sensor system, making it feasible for industrial monitoring, environmental sensing, and continuous health monitoring in smart home or hospital settings. The data can be streamed to any connected device, such as a smartphone, tablet, or computer, allowing for remote access and control of the sensor.

The combination of Bluetooth and Wi-Fi communication ensures that the soft sensor system is highly versatile, capable of functioning in both local and remote monitoring environments. The ESP32's dual communication capabilities make it particularly suited for medical and wearable applications, where users may want to access data locally via Bluetooth during short-term monitoring sessions or stream data via Wi-Fi for long-term, continuous tracking.

As shown in Figure 3.9b, the compact size of the ESP32 and associated circuitry allows for seamless integration into wearable systems. The sensors can be affixed to medical bandages making the setup non-intrusive and comfortable for patients. This wireless setup was successfully employed to monitor strain and motion on joints such as the knee, where the sensor data provided valuable insights into movement patterns and rehabilitation progress.

The implementation of Wi-Fi and Bluetooth communication in our soft sensor system significantly enhances the usability and versatility of the sensors, allowing for real-time, wireless data transmission in a range of applications. Whether for local, short-range monitoring via Bluetooth or long-range remote access via Wi-Fi, this system presents a practical solution for integrating soft sensors into modern smart systems. This adaptability is crucial in fields such as medical diagnostics, wearable technology, industrial automation, and remote sensing, where wireless communication is a key enabler for widespread deployment and scalability.

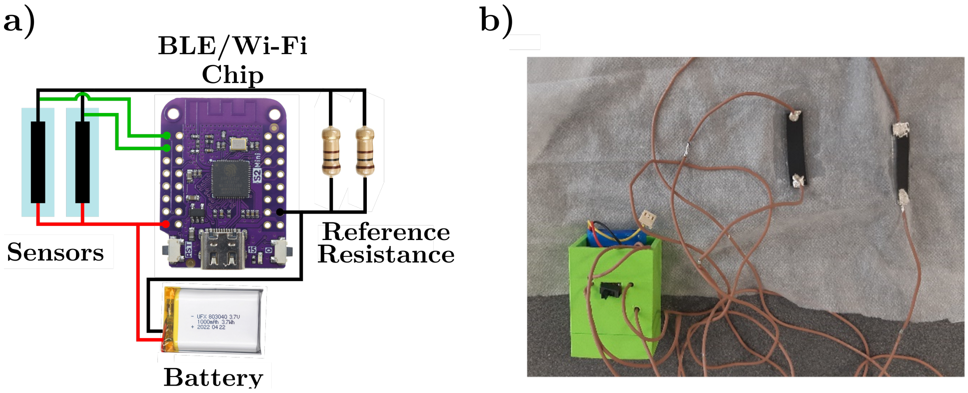

Figure 3.9: a) Wiring diagram of the wireless module; b) Chip housing and sensors attached

3.8 Conclusion

This chapter has presented the development and implementation of a comprehensive system for the synchronized characterization of strain sensors. By integrating a range of measurement devices, both custom-built and commercially available, and controlling them through LabVIEW or Python interfaces, we have ensured precise evaluations of strain and electrical resistance. The modular, automated, and real-time data acquisition capabilities of the system offer significant flexibility, making it adaptable to various experimental conditions.

Advanced material characterization techniques, such as SEM, XPS, EDX, and Raman spectroscopy, have been utilized to provide crucial insights into the structural and chemical properties of the sensors, ultimately contributing to the optimization of sensor performance. The incorporation of dynamic electrothermal characterization, including thermal testing and humidity control, allows for the evaluation of sensor performance under a range of thermal and environmental conditions. Additionally, the integration of wireless communication extends the applicability of the system, facilitating remote data collection and real-time monitoring.

With this methodology established, the next chapter will focus on the fabrication and analysis of LIG nanocomposites. It will explore the synthesis, properties, and performance of these materials, underscoring their potential to enhance the functionality of strain sensors. This progression from the system setup to material enhancement lays a solid foundation for advancing the understanding of LIG-based sensor technologies.

Chapter 4

LIG nanocomposites

4.1 Introduction

LIG nanocomposites have gained significant attention due to their exceptional properties, such as high conductivity, mechanical flexibility, and ease of fabrication. This chapter focuses on the formation of LIG structures, the factors influencing their electrical and mechanical properties, and the integration of LIG into nanocomposites for a range of applications. Key parameters, including laser power, scanning speed, focal distance, and PPI, are explored to understand their effects on the resistance and performance of LIG structures. Additionally, the influence of LIG on the formation of composites with elastomers like PDMS and Ecoflex is discussed, along with the electromechanical characterization of these composites. The chapter also delves into post-fabrication modifications, such as kirigami patterns, to optimize the mechanical and electrical properties of the LIG nanocomposites for specific applications.

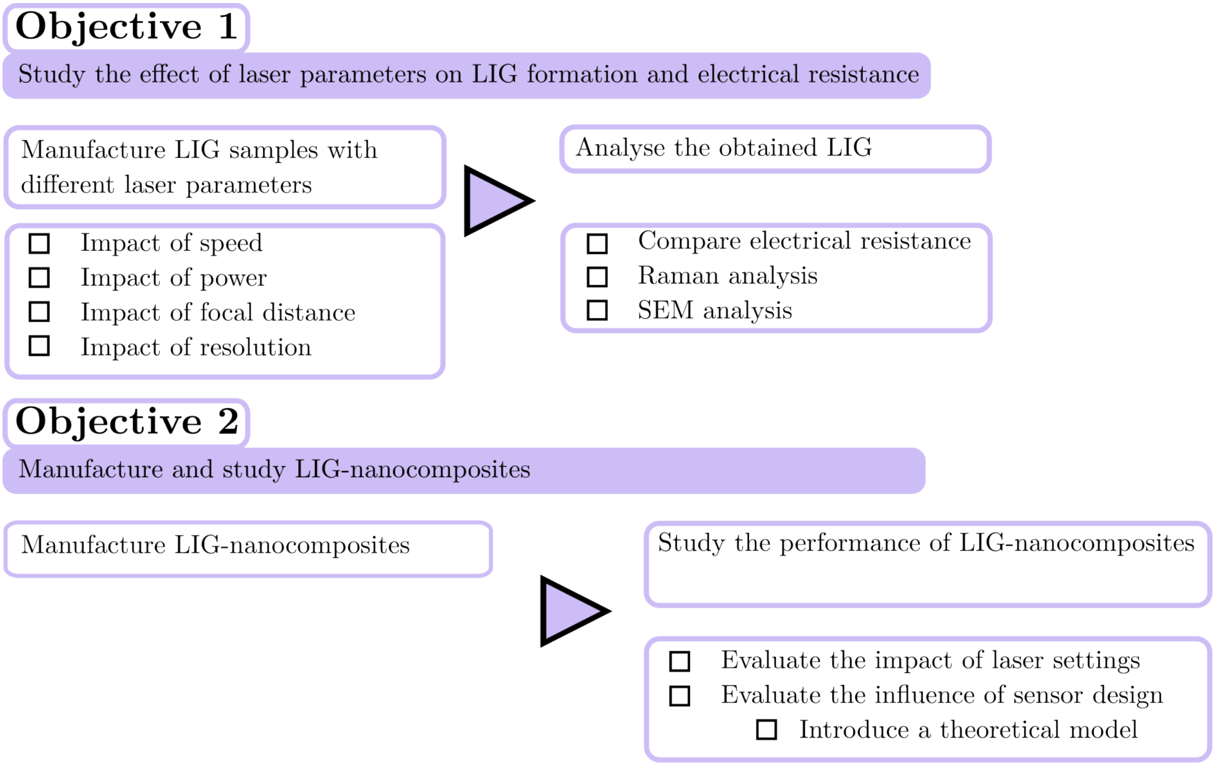

Figure 4.1: Chapter 4 Objectives Flowchart

4.2 LIG Formation

4.2.1 Laser Characteristics

Commercial laser cutters, widely employed for LIG synthesis, utilize high-intensity laser beams to induce localized heating, breaking chemical bonds in the precursor material and facilitating graphitization. At the core of a laser cutter is a laser resonator, typically containing either a CO_2 gas mixture or a solid-state medium such as a crystal or fibre. When an electrical current is passed through this medium, it stimulates the emission of photons, which are then amplified as they bounce between two mirrors within the resonator [172, 173].

Once the photons reach a critical energy level, they escape through a partially reflective mirror, forming a coherent, high-intensity beam. This laser beam is then directed toward the target material through a series of mirrors and lenses, which precisely control its position and focus. To ensure accurate patterning, laser systems are equipped with computer numerical control (CNC) systems that interpret digital design files, allowing for precise control over the laser's path and energy distribution.

Several adjustable laser parameters influence the energy delivered to the material, impacting the efficiency of LIG formation. These include power settings, scanning speed, focal distance, and resolution metrics such as DPI for raster engraving and PPI for cutting mode. Each of these factors governs the thermal energy transfer, affecting the extent of carbonization and the structural characteristics of the resulting graphene. For example, higher power settings or lower scanning speeds increase the energy absorption, promoting deeper graphitization, whereas adjustments to the focal plane influence the energy density received by the material.

4.3 Parameters Affecting LIG Formation

The electrical properties of LIG, particularly its electrical resistance, are strongly influenced by the laser processing parameters. Key factors such as laser power, scanning speed, focal distance, and PPI resolution play a significant role in determining the quality and conductivity of the resulting graphene. Understanding these parameters is essential for optimizing LIG properties to meet specific application requirements. This section examines their effects on LIG resistance, supported by experimental data.

4.3.1 Influence of Laser Power on LIG Resistance

Laser power plays a fundamental role in determining LIG quality. It controls the energy delivered to the polymer precursor, driving the photo-thermal conversion process that forms graphene.

Higher laser power generally increases the photo-thermal effect, promoting a more complete conversion of the polymer into graphene. However, excessive power can lead to over-carbonization or material ablation, which disrupts the graphene structure and introduces defects, thereby raising resistance due to incomplete graphitization.

Conversely, if the laser power is too low, the energy may be insufficient for full carbonization, resulting in a higher amount of amorphous carbon and a less conductive network. This establishes an optimal range of laser power where resistance is minimized by balancing effective graphene formation with controlled energy input.[16, 34]

The energy transferred from the laser to the substrate, quantified as fluence $\boldsymbol{H}$, depends on laser power $\boldsymbol{P}$, DPI, and scanning speed $\boldsymbol{V}$ as follows:

$$H = \frac{P \cdot \mathrm{DPI}}{V} \tag{4.1}$$

When incorporating pulse frequency $\boldsymbol{F}$ and PPI, the fluence can also be expressed as:

$$H = \frac{P \cdot \mathrm{PPI} \cdot \mathrm{DPI}}{F} \tag{4.2}$$

The substrate also influences graphene quality, as thermal properties vary across materials. For consistency, all experiments used a 1 mm glass substrate, balancing thermal conductivity and substrate uniformity. Additionally, the relationship between fluence and scanning speed is non-linear due to kinetic effects in the graphitization process, further underscoring the complex interaction between parameters.[174]

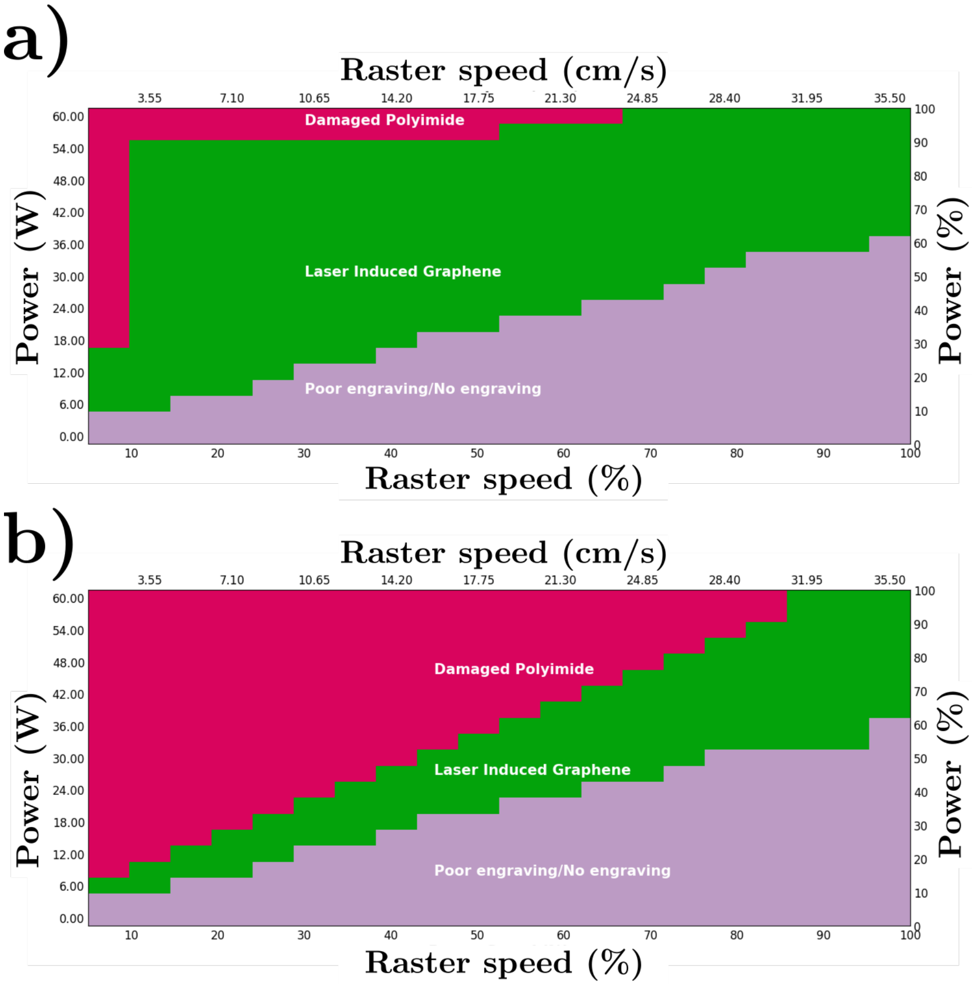

Figure 4.2: a) Graphene quality from thick PI film; b) Graphene quality from thin PI film.

Figure 4.2 demonstrates that the thickness of the PI layer significantly impacts the range of fluences suitable for successful LIG conversion. Thicker PI layers can tolerate higher fluence levels, allowing for a more intense photo-thermal reaction and and, consequently, greater LIG production. This relationship suggests that optimizing PI thickness is essential for maximizing LIG yield, as thicker layers accommodate higher energy input without compromising the quality of the graphene network.

As shown in Figure 4.3, increasing laser power from 10% to 45% decreased the resistance of LIG from 400 **Ω** to 75 **Ω**. However, further increasing the power led to a rise in resistance, likely due to over-carbonization effects. These results indicate a critical power threshold for minimizing resistance, beyond which LIG quality deteriorates.

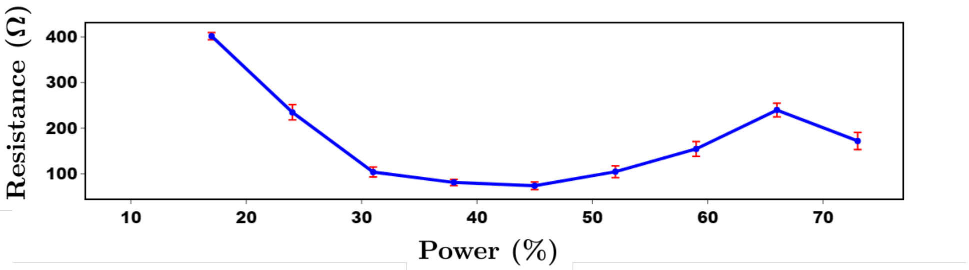

Figure 4.3: Influence of laser power on the electrical resistance of LIG.

4.3.2 Effect of Scanning Speed on LIG Resistance

Scanning speed, or the rate at which the laser moves across the material surface, also significantly impacts LIG properties. It affects energy deposition per unit area. A slower speed allows for higher energy density on each area, facilitating graphene formation. However, excessively low speeds can lead to overheating and increased defect density, which raises resistance.

Conversely, high scanning speeds reduce energy delivery per area, which may result in incomplete carbonization and higher resistance due to insufficient graphene formation.

Experimentally, decreasing the scanning speed from 40% to 5% reduced LIG resistance from 2600 **Ω** to 90 **Ω**, indicating improved graphene formation at slower speeds. However, speeds below this optimum increased resistance and damaged the PI substrate, underscoring the importance of a balanced scanning speed for effective conversion.

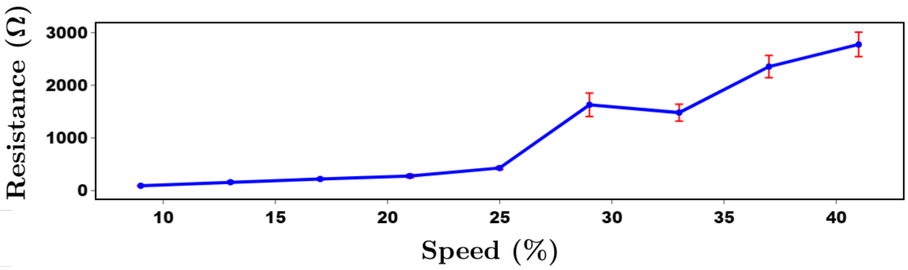

Figure 4.4: Influence of laser speed on the electrical resistance of LIG.

4.3.3 Impact of Focal Distance on LIG Resistance

The focal distance, or the distance between the laser's focal point and the material surface, affects both energy density and laser precision. An optimal focal distance ensures that laser energy is concentrated directly on the surface, achieving efficient graphene conversion. Deviations from this distance reduce surface energy density, leading to incomplete or uneven graphitization and higher resistance. Incorrect focal distance can also broaden the heat-affected zone, causing thermal damage to surrounding areas.

Furthermore, a higher defocus value can lead to an overlap of laser traces during the lasing process. This overlap occurs because a defocused beam has a larger spot size, causing consecutive laser passes to interact with previously lased areas. This can significantly affect LIG formation: the initial pass may create the basic graphene structure, but subsequent overlapping passes can re-heat and potentially re-arrange the graphene network. This re-arrangement can sometimes improve network connectivity by filling in gaps or restructuring disordered regions, but it can also introduce defects if the cumulative energy input becomes excessive.

Experimental results showed that within a defocus range of 0 to 1.5 mm, optimal resistance (85 **Ω**) was achieved at a 1 mm defocus. Higher defocus values reduced fluence, hindering complete graphitization. Although samples at 0 mm defocus showed less variability, their resistance was higher (280 **Ω**), so 0 mm was chosen for further experiments to ensure consistency.

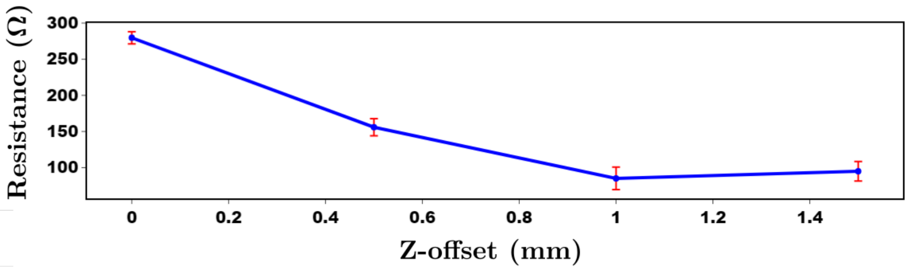

Figure 4.5: Influence of laser focal offset on the electrical resistance of LIG.

4.3.4 Effect of PPI on LIG Resistance

Horizontal resolution, or PPI, determines the density of laser spots on the material's surface. Higher PPI increases spot overlap, while lower PPI leads to more spaced spots with less overlap.

A lower PPI value, with less spot overlap, can improve graphene layer continuity, forming a uniform and conductive network by creating distinct, well-defined traces. However, a lower PPI, when combined with a higher defocus, can also lead to an increased overlap of laser traces. This happens because even though the number of pixels per inch is lower, the broadened laser spot from the defocus can still cause significant interaction between adjacent lines. As with focal distance, this overlap means that areas are exposed to the laser multiple times. The first exposure creates the initial LIG structure, and subsequent overlapping exposures can further process or re-arrange the graphene network. This re-processing can potentially enhance graphitization or connectivity but may also lead to material degradation if the cumulative energy input is too high.

Conversely, high PPI settings increase energy input, similar to low scanning speeds or high power, potentially causing overheating and increased resistance. At very high PPI values, gaps may form in the graphene network, disrupting conductive pathways and raising resistance.

Data showed that increasing the PPI from 500 to 1000 reduced LIG resistance from 220 **Ω** to 147 **Ω**, suggesting that increased overlap improves conductivity by enhancing graphene network uniformity within this range.

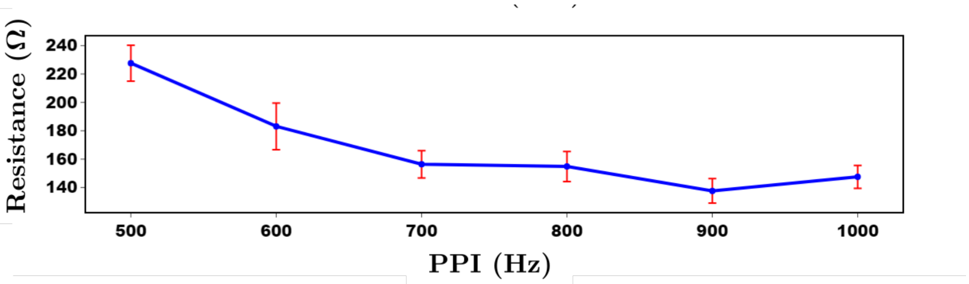

Figure 4.6: Influence of PPI settings on the electrical resistance of LIG.

The resistance of LIG is highly sensitive to the laser processing parameters. Optimal laser power, scanning speed, focal distance, and resolution are crucial for minimizing resistance and maximizing the performance of LIG-based devices. Understanding the interdependencies of these parameters allows for better control over the LIG production process, enabling the fabrication of high-quality graphene suitable for a wide range of applications. The experimental data highlights the importance of precise control over laser settings to achieve the desired electrical properties in LIG.

4.3.5 Structural Characterization

The successful formation of LIG from PI can be confirmed and characterized using various analytical techniques. Among them, Raman spectroscopy is widely employed to assess the structural quality of the graphene produced. The characteristic Raman peaks of LIG appear at the D-band (1350 cm^{-1}), G-band (1580 cm^{-1}), and 2D-band (2700 cm^{-1}), where their intensity and shape provide insights into the degree of graphitization and defect density within the material. Specifically, the G-band corresponds to graphitic sp^2 carbon, the D-band indicates disordered carbon, and the 2D-band represents a second-order overtone of the D-band.

The structural properties of LIG can be quantitatively analysed using key Raman parameters, including the intensity ratio of the D and G bands (I_D/I_G) and the FWHM of the G-band. The I_D/I_G ratio serves as an indicator of disorder, with higher values signifying increased defect density, whereas the FWHM of the G-band provides information on the crystallinity and structural organization of the graphene network.

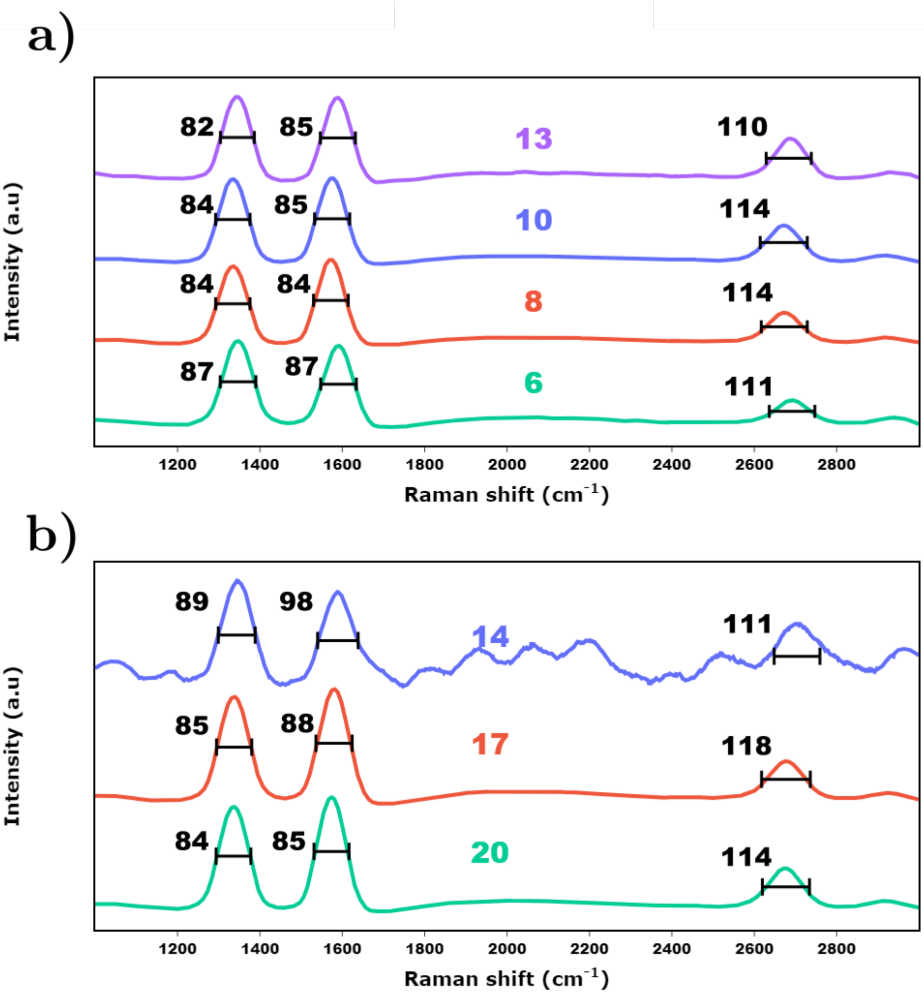

Figure 4.7: a) Raman spectra of LIG samples fabricated at different laser speeds with a fixed power of 20%; b) Raman spectra of LIG samples fabricated at different laser powers with a fixed speed of 8%.

Figure 4.7 presents the Raman spectra of the raw LIG samples, confirming the presence of the characteristic G, D, and 2D bands. The FWHM of the G-band is measured at approximately 85 cm^{-1}, indicative of a disordered graphene lattice. The calculated I_D/I_G ratio and the FWHM of the G-band provide further insights into the structural quality of the LIG.

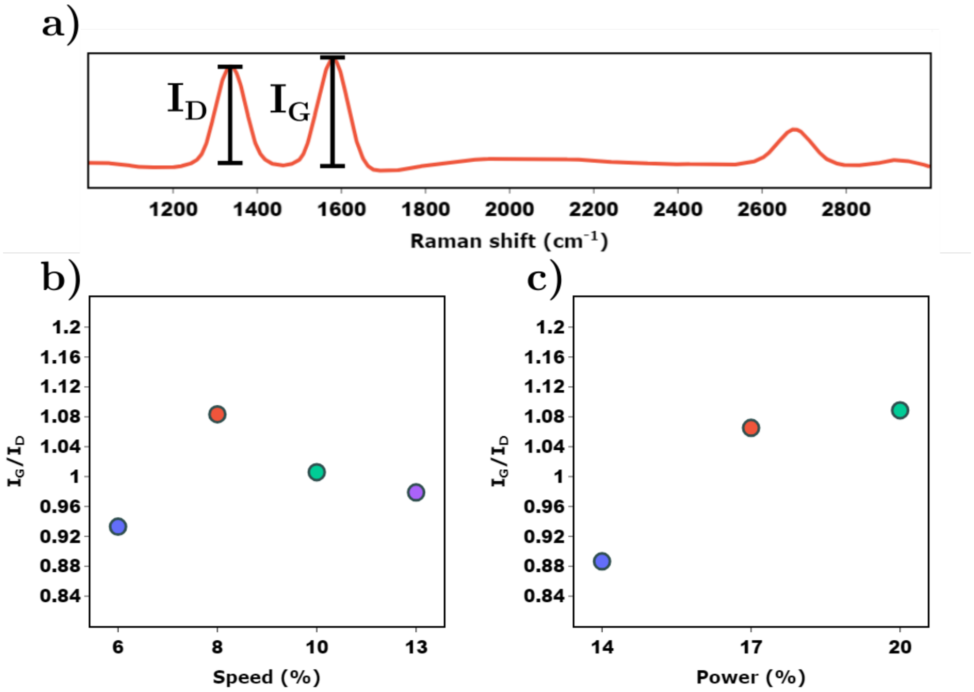

Figure 4.8: a) Distribution of I_D and I_G values; b) I_D/I_G ratio for LIG samples fabricated at different laser speeds with a fixed power of 20%; c) I_D/I_G ratio for LIG samples fabricated at different laser powers with a fixed speed of 8%.

Comparing these results with previous studies [29, 175–177], the observed Raman features and extracted parameters align with the reported characteristics of high-quality graphene-based materials. These findings indicate that the LIG derived from PI exhibits favourable structural characteristics, supporting its potential for diverse applications.

Beyond Raman analysis, SEM imaging was employed to further examine the morphological characteristics of the LIG. As shown in Figure 4.9, the graphene network exhibits a porous architecture, with increasing laser fluence leading to enhanced porosity. At higher fluences, the LIG develops more fibrous and interconnected structures, whereas lower fluence samples display larger voids and less connectivity. Furthermore, low-magnification images reveal that samples processed at lower fluences retain well-defined laser channels, while those fabricated at higher fluences exhibit a more uniform surface morphology, consistent with their higher electrical conductivity. This evolution in structure plays a critical role in facilitating polymer infiltration, which is particularly advantageous for the fabrication of LIG–PDMS composite sensors.

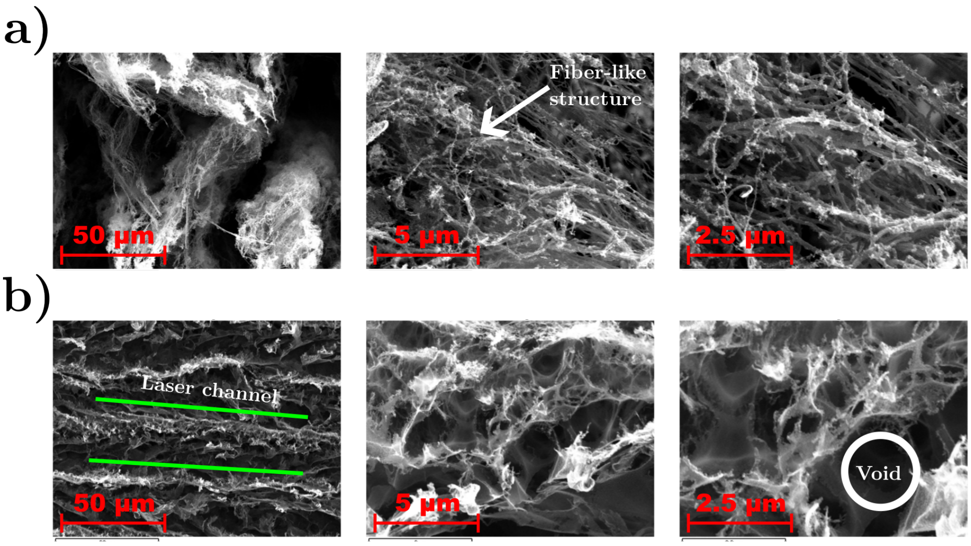

Figure 4.9: a) SEM images of a 20_7 LIG sample at different magnifications; b) SEM images of a 20_13 LIG sample at different magnifications.

These structural insights underscore the importance of optimizing fabrication parameters such as laser settings and precursor materials to enhance the performance of LIG-based sensors. Future work should focus on establishing a more accurate correlation between the Raman characteristics and the electromechanical properties of LIG-PDMS composites, thereby enabling tailored material design for strain sensing and related applications.

Examination through EDX reveals a notable compositional distinction between samples created under different fluence conditions. Specifically, the higher fluence sample exhibits a lower concentration of oxygen compared to its lower fluence counterpart.

	Low fluence	**High fluence**
Oxygen Content (%)	8.97 ± 0.31	1.37 ± 1.16

Table 4.1: Oxygen content for samples manufactured at high fluence (7% speed) and low fluence (13% speed)

This intriguing discovery may find its explanation in the higher laser power applied during the scribing process, potentially leading to increased gas generation. The correlation suggests that the scribing process, influenced by fluence, has a discernible impact on the oxygen content within the graphene structure. This intricate interplay between fluence, scribing conditions, and elemental composition unveils a layer of complexity in understanding the composition of LIG and its dependence on fabrication parameters.

4.4 LIG nanocomposites

One of the key methods to enhance the functionality of LIG is by integrating it with elastomeric substrates like PDMS or Ecoflex. This section delves into the process of producing LIG nanocomposites by curing PDMS or Ecoflex directly on the surface of the produced LIG, enabling effective transfer and integration of LIG into various flexible and stretchable applications.

4.4.1 Fabrication

The production of LIG nanocomposites involves a straightforward yet effective process, particularly when key parameters are carefully controlled. This section details the integration of LIG with elastomeric materials, such as PDMS or Ecoflex, to produce flexible nanocomposites suitable for various applications.

The fabrication process is illustrated in Figure 4.10a. It begins with the formation of LIG on a PI substrate through a CO_2 laser irradiation process. During this step, the PI film undergoes localized photo-thermal conversion, resulting in a porous, conductive graphene network on its surface. The properties of the LIG, such as conductivity and mechanical integrity, are highly dependent on the thickness of the PI film and the specific laser settings used.

Following LIG formation, an elastomer layer is applied onto the LIG surface. This can be achieved through drop casting or spin coating, depending on the desired control over the elastomer's thickness and uniformity. Drop casting is a simpler method, suitable for thicker coatings, whereas spin coating offers precise control, making it ideal for applications requiring uniformity. Figure 4.10b shows an example of the final LIG-composite under torsion, demonstrating its flexibility.

To form the nanocomposite, the elastomer is applied to the LIG network. The low viscosity of the elastomer ensures its penetration into the 3D porous structure of the LIG, and its subsequent curing results in a strong nanocomposite structure. To ensure optimal infiltration of the elastomer into the porous LIG network, the assembly is placed under vacuum after applying the elastomer. This vacuum step removes trapped air, allowing the elastomer to penetrate deeply into the LIG structure, thereby enhancing the mechanical and electrical properties of the final composite. Proper infiltration ensures a strong bond between the elastomer and the LIG network, significantly improving the composite's durability and flexibility.

The curing process solidifies the elastomer and fixes the LIG within its matrix. Curing conditions depend on the elastomer used; for instance, PDMS is typically cured at 100°C for about one hour. This step is critical in determining the mechanical properties of the elastomer and the overall integrity of the composite.

After curing, the composite is carefully peeled away from the PI substrate. Precision is required during this step to avoid damaging the delicate LIG network. Experimental observations indicate that thinner PI substrates often result in poor transfer efficiency due to insufficient polymer infiltration, as the graphene network on thinner films may lack adequate porosity.

Once the LIG-elastomer composite is isolated, electrodes are attached for electrical measurements. Silver epoxy is typically used for its excellent conductivity and strong adhesion properties. As illustrated in Figure 4.10c), electrodes are carefully applied to the ends of the composite to ensure good electrical contact without compromising the LIG structure. The epoxy is then cured, securing the electrodes in place, making the composite ready for various applications, including flexible sensors, wearable electronics, and advanced technologies.

The successful fabrication of high-quality LIG nanocomposites relies on optimizing several critical factors throughout this process:

- **PI Film Thickness:** As mentioned, the thickness of the PI film is critical. Thicker films tend to produce more conductive and porous LIG structures that can be more easily transferred to the elastomer matrix, facilitating better composite integration.
- **Elastomer Application:** The method of elastomer application (e.g., drop casting vs. spin coating) and the subsequent vacuum infiltration significantly affect the quality of the final composite. Uniform and complete infiltration is necessary to maintain the electrical conductivity and mechanical flexibility of the LIG network within the composite.
- **Curing Conditions:** Proper curing of the elastomer is essential to achieve the desired mechanical properties and ensure strong adhesion. The curing temperature and time must be carefully controlled to ensure complete infiltration of the polymer inside the LIG structure and prevent any degradation of the graphene.
- **Electrode Integration:** The attachment of electrodes using silver epoxy requires precision to ensure good electrical contact and avoid introducing undesirable resistance or defects into the electrical path, which can compromise device performance.

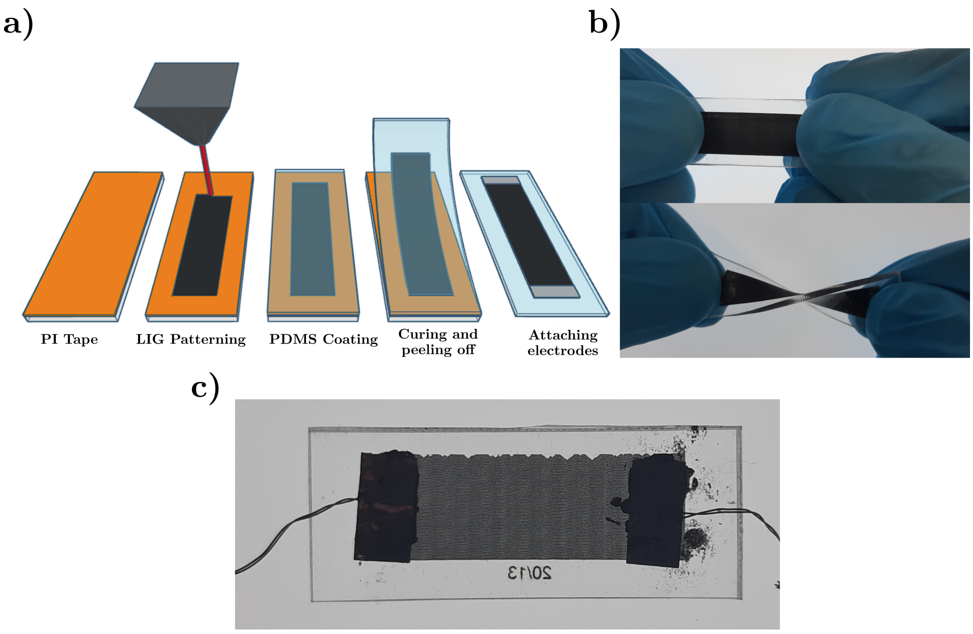

Figure 4.10: a) Schematic of the LIG-composite fabrication process; b) Photograph of the LIG-composite at rest and under torsion, illustrating its flexibility; c) Nanocomposite sensor image illustrating the electrode attachment.

Visual evidence of successful infiltration and the resulting composite structure can be seen in Figure 4.11. The SEM images at different magnifications illustrate the intimate integration between the LIG network and the PDMS elastomer, highlighting the porous yet well-supported graphene structure within the composite.

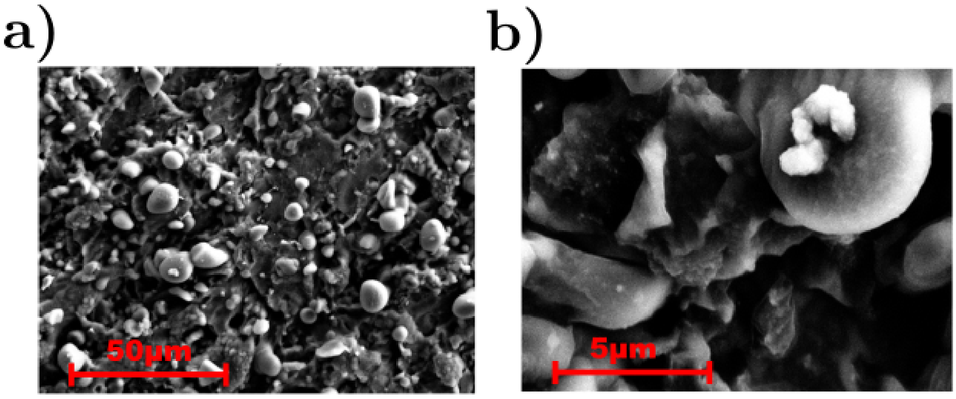

Figure 4.11: SEM image of a LIG-PDMS nanocomposite at different magnifications. a) At 1000x; b) At 10,000x.

In conclusion, the production of LIG nanocomposites by curing PDMS or Ecoflex onto LIG surfaces is a methodical process that, when executed with attention to detail, results in high-performance materials suitable for a wide range of applications.

4.4.2 Electromechanical properties

Electromechanical characterization is a critical aspect of evaluating the performance and functionality of LIG nanocomposites, particularly when these materials are intended for use in advanced applications such as flexible electronics, sensors, and wearable devices. This section provides a comprehensive overview of the techniques and tools employed in the electromechanical characterization of LIG nanocomposites, focusing on understanding their electrical, mechanical, and coupled electromechanical properties.

4.4.3 Influence and Optimization of Laser Parameters

As demonstrated in Section 4.2, laser parameters significantly influence both the formation of graphene and its electrical properties. The structure of the graphene network, which is directly dependent on these parameters, also affects the transfer process to elastomers such as PDMS or Ecoflex. Specifically, a more porous graphene network, resulting from optimized laser settings, allows for deeper penetration of the elastomer into the structure, thereby creating a more interconnected network in the final composite.

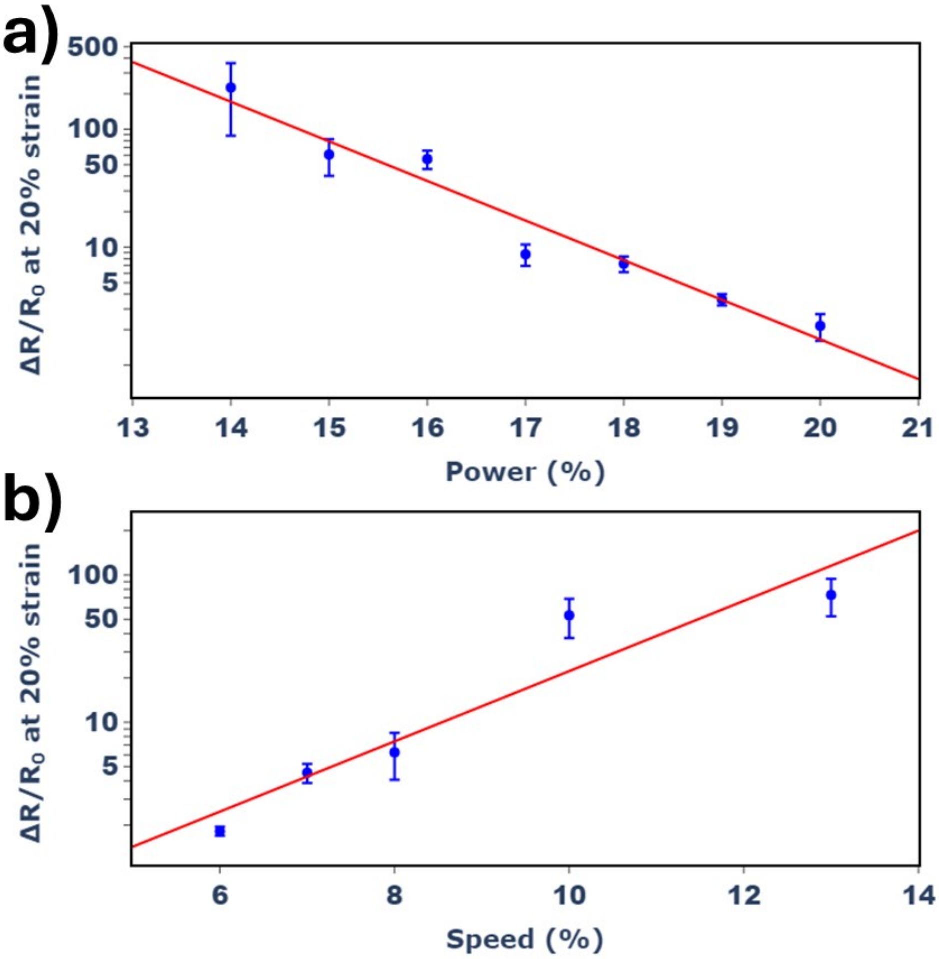

Figure 4.12: Maximum relative change in resistance for different LIG-PDMS composites manufactured with varying laser settings. a) Effect of laser power at 20% strain; b) Effect of laser speed at 20% strain.

Figure 4.12 illustrates the impact of different laser settings on the sensitivity of LIG-PDMS composites. All electromechanical characterizations presented here were performed using the custom-made setup explained in Chapter 3.4.2. The data reveals an exponential trend, indicating that lower laser fluence generally enhances sensor sensitivity to strain. However, reduced fluence also leads to noisier data, compromising the stability of the sensors. This trade-off highlights the need for careful optimization of laser parameters to balance sensitivity and signal reliability.

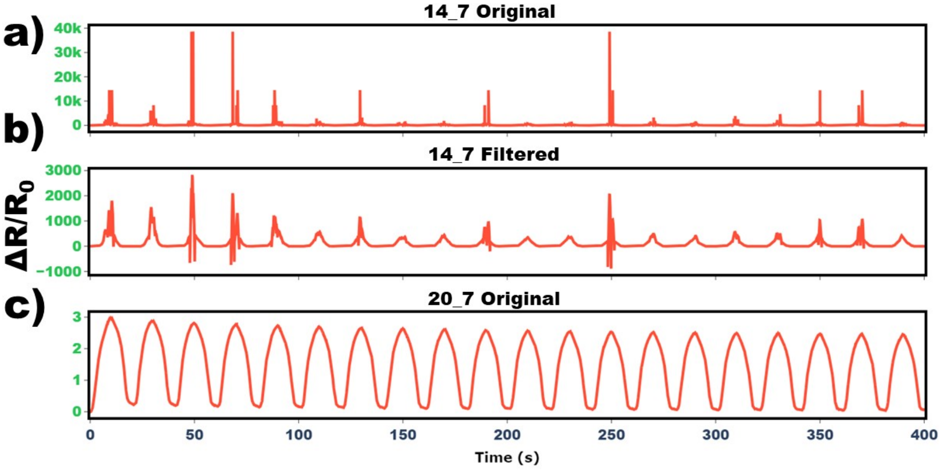

Figure 4.13: a Cyclic testing at 20% strain for a 14_7 sample; b) Filtered data using a Savitzky-Golay filter applied to the 14_7 sample data; c) Cyclic testing at 20% strain for a 20_7 sample.

Figure 4.13 further demonstrates the effect of laser settings on signal quality during cyclic testing at 20% strain. The 14_7 sample exhibits a high level of noise, even after applying a Savitzky-Golay filter, highlighting the limitations of low fluency laser settings for applications requiring clean, stable signals. In contrast, the 20_7 sample shows significantly reduced noise, resulting in a clearer and more reliable response.

These observations underscore the importance of selecting laser parameters based on specific application requirements. For low-strain, high-sensitivity applications, lower fluency settings may be preferred to enhance responsiveness to small deformations. Conversely, for higher-strain applications where signal stability is paramount, higher fluency settings are necessary to minimize noise and ensure consistent performance.

4.4.4 Impact of Multiple Laser Passes and Lasing Orientation

To further refine LIG-based strain sensors, additional studies were conducted on LIG-Ecoflex composites, focusing on optimizing the electromechanical response. Two key factors were investigated: the effect of multiple laser passes and the orientation of lasing relative to the strain direction. Ecoflex was selected as the elastomer due to its lower Young's modulus, skin-safe properties, and suitability for wearable applications.

Sensor Fabrication: The fabrication process followed the methodology outlined in Section 4.4. Ecoflex was spin-coated onto the LIG layer at 1000 rpm for 10 seconds to ensure a thin, uniform layer. The composite was then cured at 90°C for one hour before being carefully peeled off the PI substrate.

Sensor Testing: The fabricated sensors were evaluated under controlled strain conditions using the setup described in Section 3.4.2. Each sensor was subjected to cyclic testing at 5% strain for 20 cycles, with a cycle period of 10 seconds. Key performance metrics, linearity, drift, and hysteresis, were analysed to assess the sensor's reliability and reproducibility.

The following criteria were used to quantify sensor performance:

- **Linearity:** The linearity was evaluated by calculating the R^2 value of the best-fit line during both the loading and unloading phases in the final cycle. This ensures a predictable and proportional response across the strain range. Examples of a highly linear and a non-linear sensor response are shown in Figure 4.14.
- **Drift:** Drift was quantified using the following parameter:

$$D = \frac{R_{\mathrm{peak},1} - R_{\mathrm{peak},\max}}{R_{\mathrm{peak},1}} \tag{4.3}$$

  where $R_{\mathrm{peak},i}$ represents the resistance at the peak of cycle i. This metric captures gradual changes in sensor response over repeated cycling. An example of the drift analysis is shown in Figure 4.15.
- **Hysteresis:** Hysteresis was evaluated by calculating the relative difference between the loading and unloading curves, defined as:

$$H = \frac{\int_0^{\varepsilon_{\max}} |R_{\mathrm{up}}(\varepsilon) - R_{\mathrm{down}}(\varepsilon)|\, d\varepsilon}{R(\varepsilon_{\max})} \tag{4.4}$$

  where $R_{\mathrm{up}}(\varepsilon)$ and $R_{\mathrm{down}}(\varepsilon)$ denote the resistance values during loading and unloading, respectively. This value reflects the energy loss due to deformation and mechanical hysteresis. A visual representation of this method is provided in Figure 4.16.

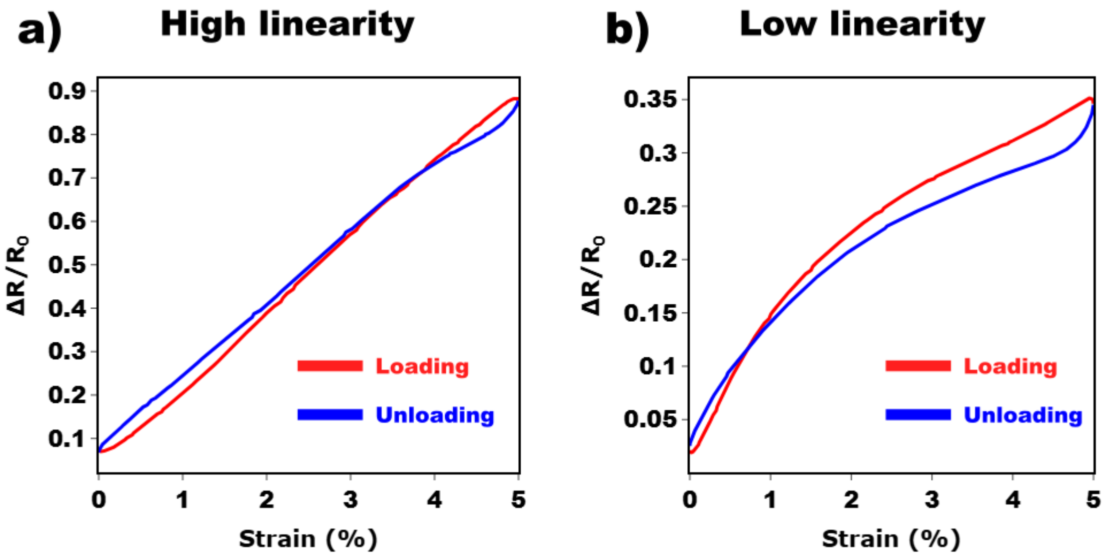

Figure 4.14: Examples of linearity evaluation: a) A highly linear sample with a high R^2 value; b) A non-linear sample with a lower R^2 value.

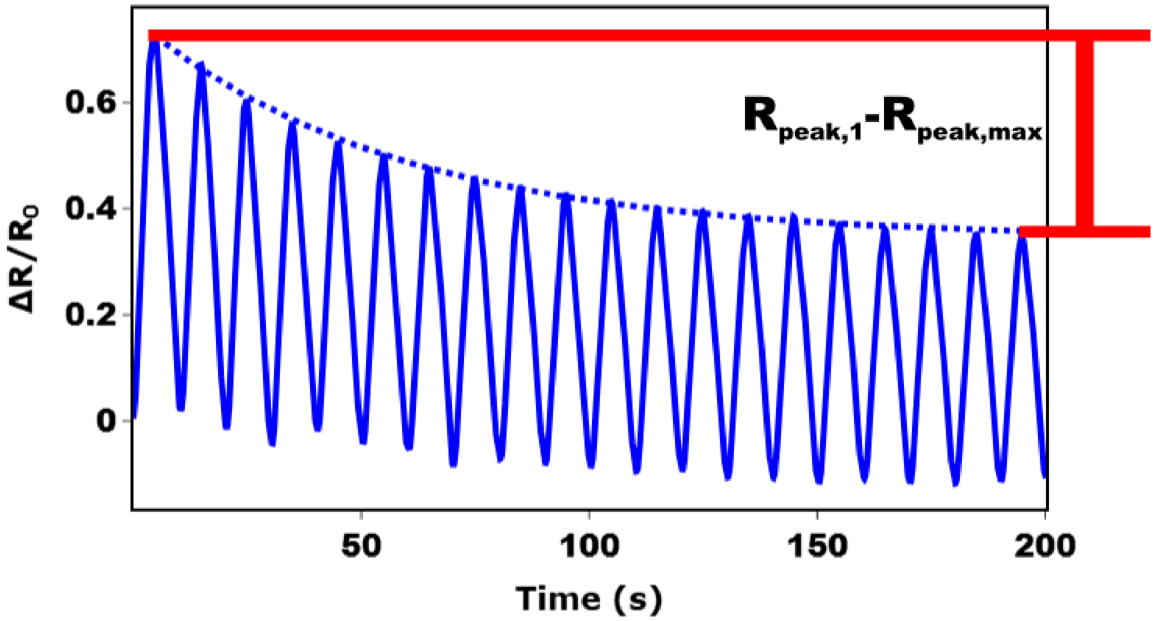

Figure 4.15: Illustration of drift measurement across 20 loading cycles, showing resistance peak evolution.

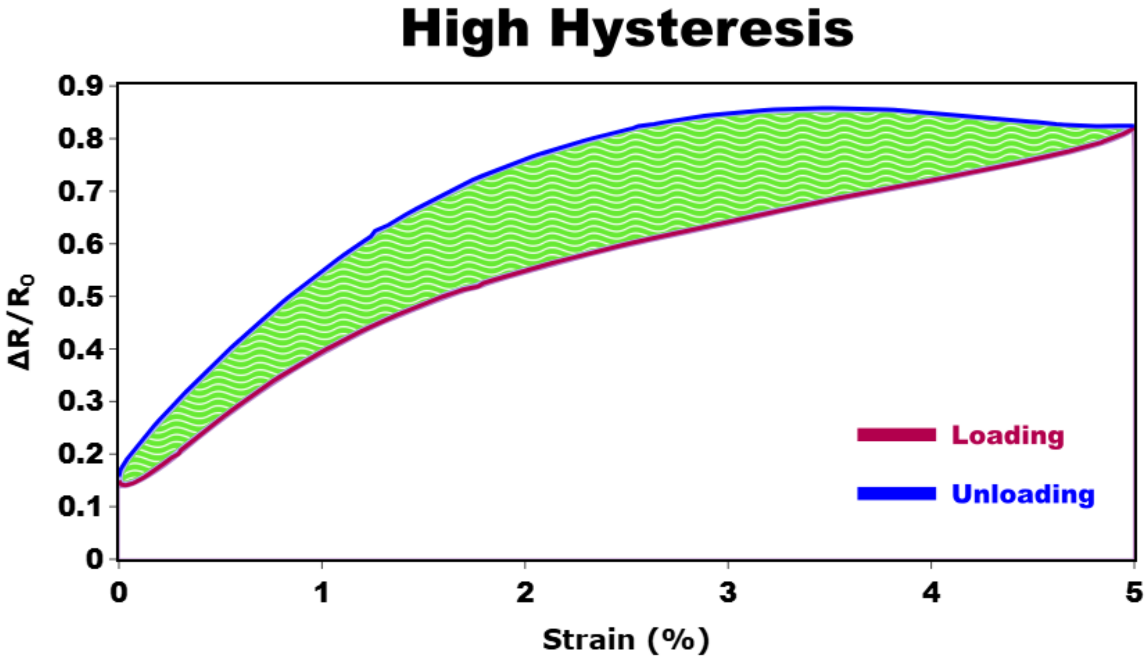

Figure 4.16: Schematic representation of hysteresis evaluation by integrating the absolute difference between loading and unloading curves.

The methodologies described above, illustrated in Figures 4.14, 4.15, and 4.16, were systematically applied to a larger batch of sensors. The compiled results are summarized in Figure 4.17. Specifically, Figure 4.17a shows the R^2 values for loading and unloading phases across different samples, highlighting the linearity of the sensors. Figure 4.17b presents the corresponding hysteresis values, while Figure 4.17c reports the measured drift values.

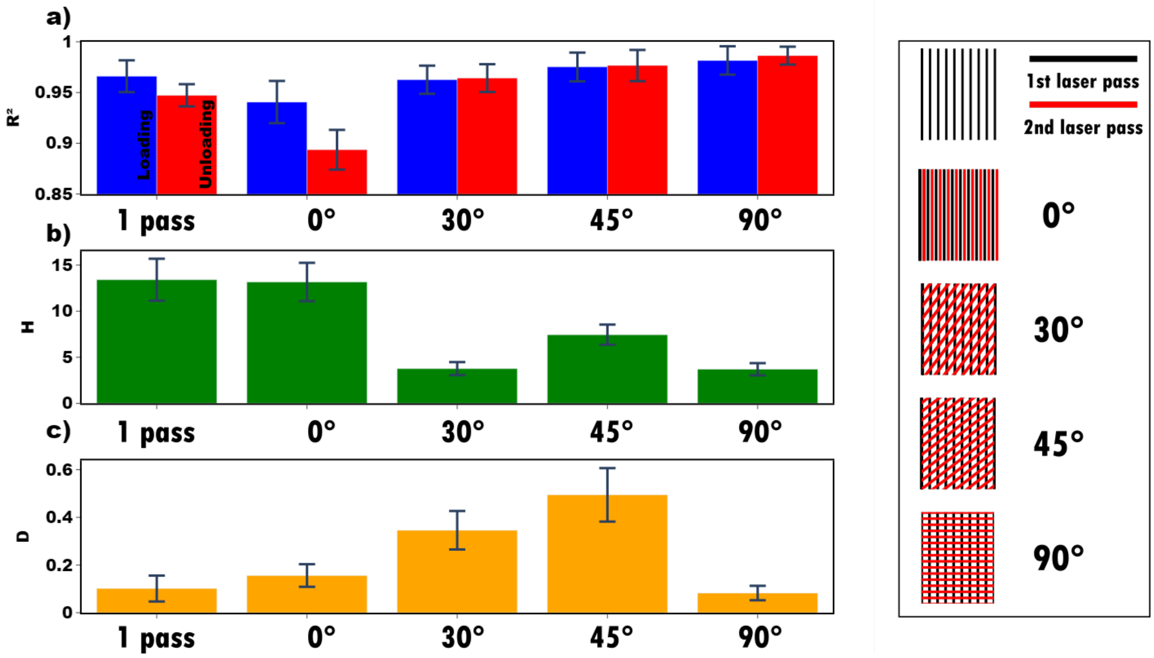

Figure 4.17: Performance assessment of the fabricated sensors: a) R^2 values for loading (blue) and unloading (red) phases across various samples, indicating the linearity of sensor response; b) Hysteresis values as defined in Equation 4.4, reflecting energy loss during strain cycles; c) Drift values calculated using Equation 4.3, demonstrating sensor stability over multiple cycles.

The results presented in Figure 4.17 reveal that the second laser pass and its orientation significantly impact sensor performance. Optimal results were obtained when the first laser pass aligned with the principal strain direction, while the second pass was applied orthogonally. This configuration improved both linearity and hysteresis, leading to more predictable and stable sensor behaviour.

However, drift exhibited notable sensitivity when the second pass was applied at an oblique angle (e.g., 45 degrees). This could be attributed to inconsistencies in maintaining consistent alignment across different samples, despite controlled experimental conditions. The observed trends emphasize the importance of laser patterning strategies in achieving reliable electromechanical performance in LIG-based strain sensors.

4.4.5 Summary of Findings

The collective findings of this study reinforce the critical role of laser parameter optimization in the performance of LIG-based strain sensors. Key insights include:

- Lower laser fluency enhances strain sensitivity but introduces noise, affecting signal stability.
- Higher fluency improves signal clarity but reduces sensor responsiveness to small deformations.

- Multiple laser passes and their orientation influence linearity, hysteresis, and drift, with orthogonal second passes yielding optimal results.

These observations highlight the delicate balance required in laser processing to tailor sensor properties for specific applications.

4.4.6 Selection of Optimal Parameters for Subsequent Work

Based on the comprehensive characterization of laser-induced graphene samples presented in this chapter, the **20_7 configuration** was selected as the optimal parameter set for subsequent composite fabrication and characterization studies. This choice was motivated by the following considerations:

Electrical Properties: The 20_7 sample exhibited a baseline resistance of approximately 800 **Ω** after transfer, which represents an advantageous compromise for practical sensing applications. This resistance is sufficiently low to minimize Joule heating effects during operation and ensure good signal-to-noise ratios in resistance measurements, while remaining high enough to provide measurable resistance changes under applied strain.

Electromechanical Sensitivity: As demonstrated in the strain-resistance characterization, the 20_7 configuration displayed high gauge factors across the tested strain range, indicating superior sensitivity to mechanical deformation. This enhanced responsiveness is critical for detecting small strain variations in composite structures and dynamic loading scenarios.

Signal Stability: While lower fluency samples showed even higher sensitivity, the 20_7 parameters provided acceptable signal stability with reduced noise levels compared to more sensitive but noisier alternatives. This balance between sensitivity and stability is essential for reliable long-term sensing performance and reproducible measurements.

Manufacturing Considerations: The single-pass 20_7 configuration offers practical advantages in terms of fabrication simplicity and throughput compared to multi-pass alternatives. Although orthogonal second passes improved certain performance metrics, the added complexity and potential for interlayer variability made single-pass samples preferable for systematic composite studies where sample-to-sample consistency is paramount.

In parallel, the **20_13 configuration** was retained for comparative studies due to its contrasting resistance-strain profile. The complementary behavior of these two configurations enables investigation of how fundamental electromechanical characteristics influence composite-level performance under combined thermal and mechanical loading.

The next section builds upon these results by exploring additional strategies for optimizing LIG-based nanocomposites using the selected 20_7 parameters as the foundation for composite design and characterization.

4.4.7 Influence of Strain Frequency

To evaluate the influence of strain frequency on the electromechanical response of the sensor, we subjected a group of samples to cyclic loading with identical strain amplitudes while varying the period of the applied cycles. This experimental design isolates the effect of frequency from that of strain magnitude, enabling a focused analysis of the dynamic response characteristics. The absolute resistance changes recorded for different periods are presented in Figure 4.18.

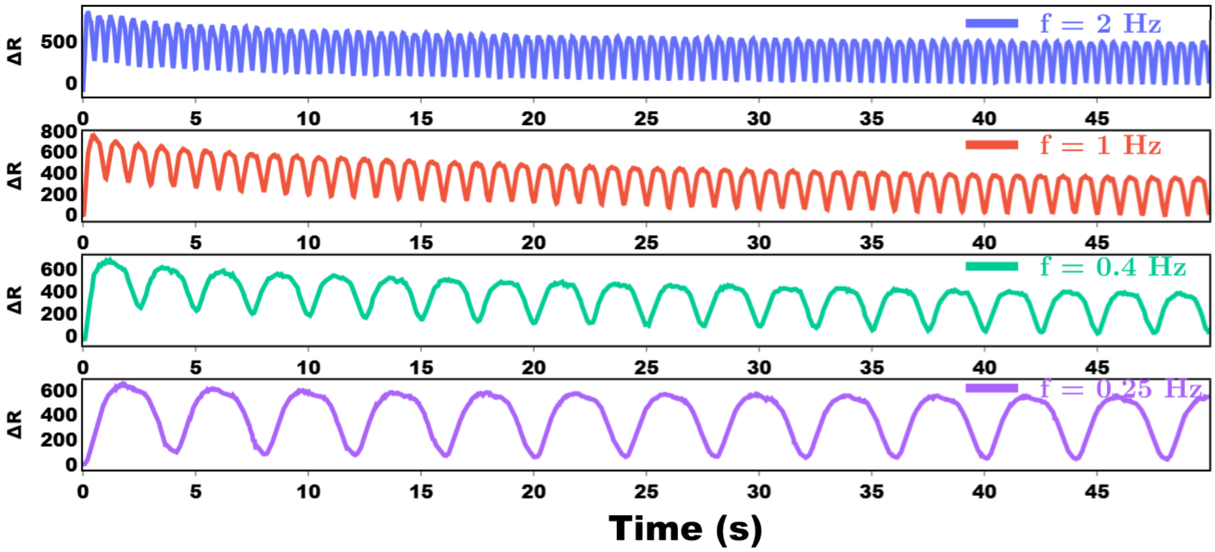

Figure 4.18: Absolute resistance change for a single LIG-based strain sensor subjected to cyclic strain at four different periods, maintaining constant strain amplitude.

To better visualize the temporal evolution of the resistance across cycles, the data were rescaled and plotted against the number of cycles, as shown in Figure 4.19.

As illustrated in Figure 4.19, the initial response of the sensor is markedly influenced by the strain period. At shorter periods (corresponding to higher frequencies), the initial peak in absolute resistance change is significantly higher, and the subsequent decay toward stabilization extends over more cycles. Conversely, for longer periods (lower frequencies), the initial resistance change is less pronounced, and the system stabilizes more rapidly.

Despite these differences in the early stages of cyclic loading, all conditions eventually converge to similar resistance values after a sufficient number of cycles. This behaviour suggests that while the dynamic response of the sensor is sensitive to the strain frequency initially, its long-term stability is largely independent of the input frequency.

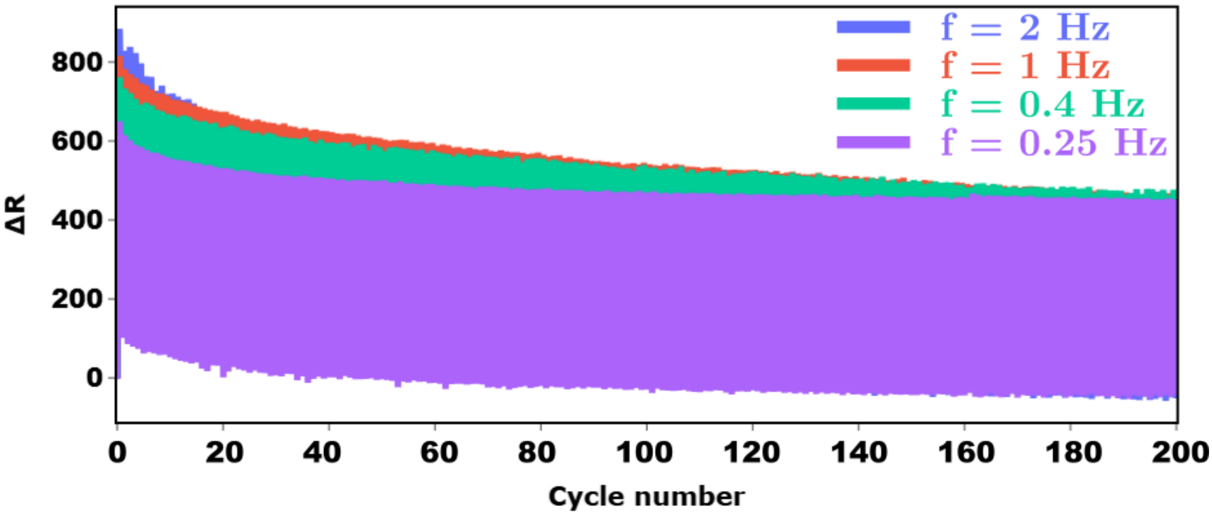

Figure 4.19: Absolute resistance change for a single LIG-based strain sensor subjected to cyclic strain at four different periods, plotted against the number of cycles.

To quantitatively compare this effect, we computed the ratio between the maximum resistance change during the first cycle and that observed after 200 cycles, as shown in Figure 4.20.

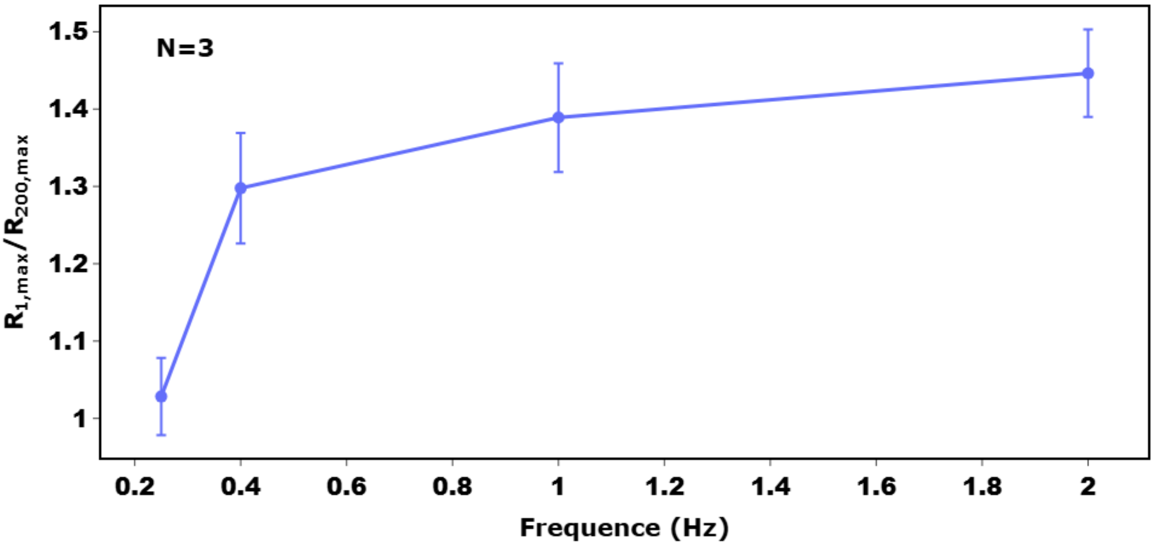

Figure 4.20: Ratio of the initial maximum relative resistance change to the relative resistance change after 200 cycles for sensors tested at different periods.

To further analyse this phenomenon, an exponential decay function was fitted to the peak resistance values recorded at each cycle for every strain period. The decay behaviour was modelled using the standard exponential form:

$$R_{\max}(n) = R_\infty + (R_0 - R_\infty)e^{-n/\tau} \tag{4.5}$$

where $R_{\max}(n)$ is the peak resistance at cycle n, R_0 is the initial peak resistance, R_∞ is the steady-state resistance after many cycles, and τ is the decay constant characterizing the rate at which the sensor response stabilizes. A smaller value of τ corresponds to faster stabilization.

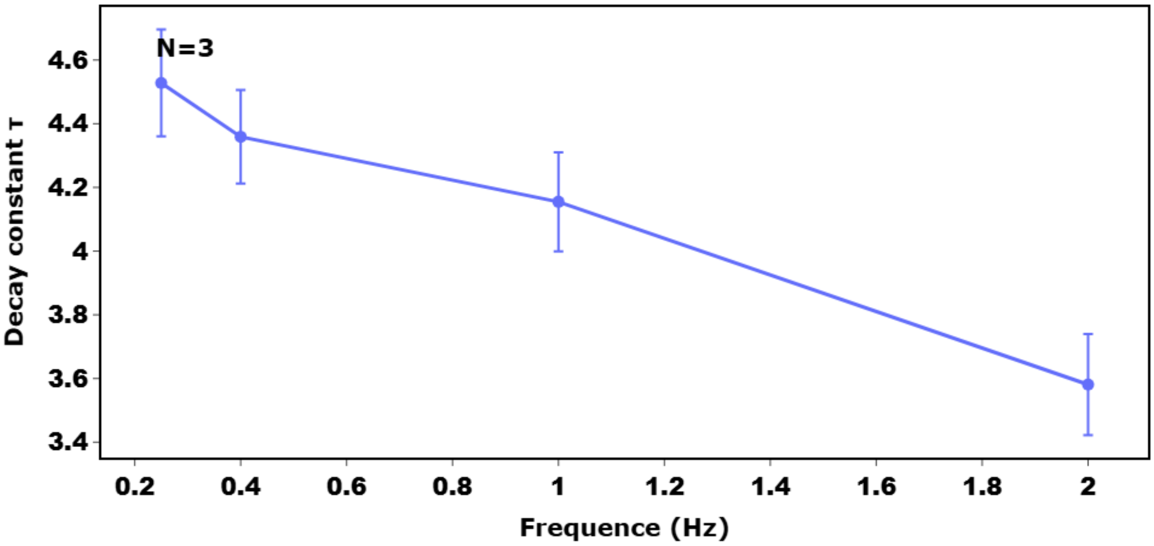

Figure 4.21: Decay constants (τ) obtained from exponential fits for sensors tested at various strain periods. Lower τ values indicate faster stabilization.

Figure 4.21 presents the decay constants for the different strain periods. The results indicate a clear dependence of the decay dynamics on strain frequency. Specifically, higher frequencies are associated with longer decay constants, suggesting a slower relaxation of the sensor response. This could be attributed to viscoelastic effects within the polymer matrix or microstructural rearrangements within the LIG network that require more cycles to stabilize under rapid mechanical loading.

These findings are crucial for applications involving dynamic or high-frequency strain sensing, as they highlight the need to consider response stabilization time during signal processing or calibration.

4.4.8 Fatigue Testing

Fatigue testing is essential to evaluate the long-term stability and reliability of soft sensors under repeated mechanical strain. To investigate the effects of prolonged cyclic loading, we subjected a set of LIG-based strain sensors to 1000 cycles of strain. The relative change in resistance between consecutive cycles was recorded, and to account for noise in the data, a rolling average over 10 cycles was applied. This approach smooths short-term fluctuations and allows for a clearer view of the sensor's overall behaviour over time.

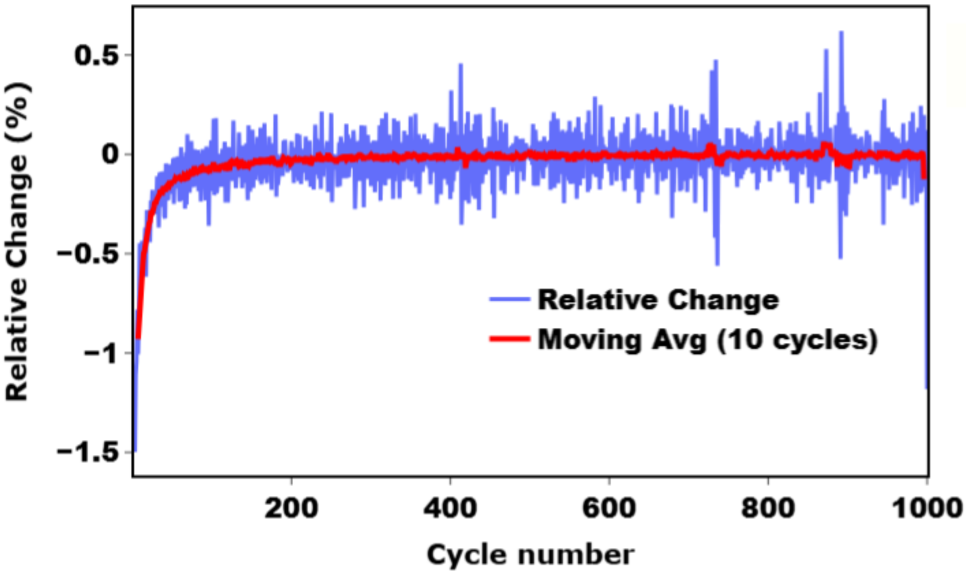

Figure 4.22: Relative change in resistance between consecutive cycles for 1000 cycles of mechanical loading, with a 10-cycle rolling average applied to reduce noise.

To quantify the difference in resistance between consecutive cycles, the relative change in resistance was calculated using the following equation:

$$\Delta R_{\mathrm{rel}}(n) = \frac{R(n) - R(n-1)}{R(n-1)} \times 100$$

Where: - $\Delta R_{\mathrm{rel}}(n)$ is the relative change in resistance between cycle n and the previous cycle $(n-1)$, - $R(n)$ is the resistance at cycle n, - $R(n-1)$ is the resistance at the previous cycle $(n-1)$.

Figure 4.22 presents the relative change in resistance between consecutive cycles for the 1000-cycle fatigue test. The results indicate that the sensor's response stabilizes after a certain number of cycles, and the magnitude of resistance change diminishes as the sensor undergoes repeated strain. This trend is expected in fatigue testing, where initial cycles often exhibit larger resistance variations, which gradually reduce as the sensor undergoes plastic deformation or adaptation to the applied strain.

Additionally, we measured the number of cycles required for the average relative change between consecutive cycles to drop to 0.1%, using 10 samples. On average, this value was found to be 66 ± 12 cycles, demonstrating relatively consistent fatigue performance across the sample set. It is important to note, however, that for samples fabricated with lower laser fluence, the number of cycles to reach this threshold may vary slightly due to increased noise disturbances. These variations could be attributed to differences in the microstructure of the LIG network, which may influence the material's overall resilience to cyclic strain.

These findings provide valuable insights into the durability of LIG-based strain sensors and their suitability for long-term applications. Future work could focus on optimizing the laser processing parameters to minimize fatigue-induced degradation and enhance the longevity of these sensors under extended use.

4.4.9 Influence of design

This section delves into the ways in which LIG nanocomposites can be further optimized for specific applications by altering their geometry. Once the LIG nanocomposite is fabricated, its mechanical and electrical properties can be finely tuned through post-processing techniques, such as laser cutting, to introduce deliberate geometric modifications. These modifications are crucial for tailoring the stress distribution within the material, which directly influences its mechanical response, including the stress-strain behaviour and GF.

A notable method for geometric modification is the implementation of kirigami patterns. Kirigami, an ancient Japanese art of paper cutting, involves making fine cuts in a material to achieve desired mechanical properties. When applied to LIG nanocomposites, kirigami patterns can significantly alter the material's behaviour under strain. Specifically, these patterns allow for higher strain at lower stress levels by creating regions within the material that can stretch and deform more easily. This is achieved without compromising the overall structural integrity, thereby enabling the nanocomposite to withstand larger deformations. [88, 89, 178]

The introduction of kirigami patterns or other geometric modifications into LIG nanocomposites can have a profound impact on the sensitivity of the material. For example, a sample that has been modified with kirigami cuts may exhibit reduced sensitivity to strain, as the cuts allow the material to distribute stress more evenly, thereby lowering the overall strain experienced by the uncut regions. This reduction in sensitivity can be particularly advantageous in applications where sensors are required to function reliably over a wide range of strain. For instance, in wearable electronics or soft robotics, sensors must often endure significant deformation while maintaining accuracy and durability.

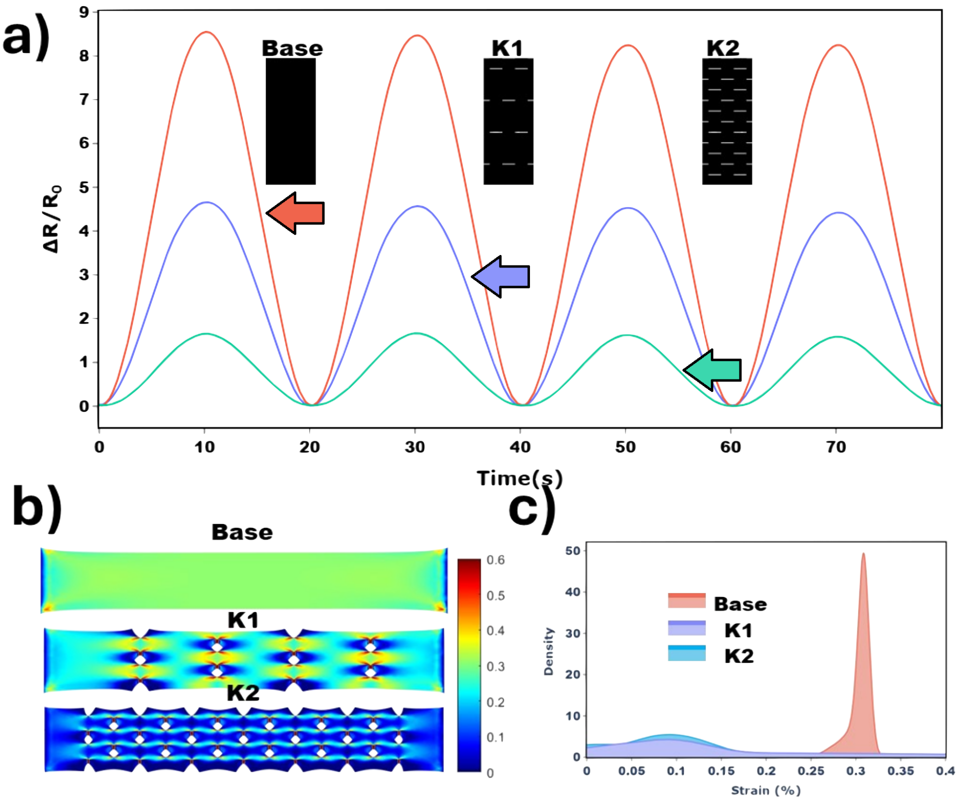

Figure 4.23: a) Strain/Resistance curve for three different samples at 30% strain; b) Simulation result for the same samples shown in A; c) Strain distribution across all three samples according to the simulation.

To investigate this, we studied the electromechanical properties of LIG-Ecoflex nanocomposites subjected to different modification processes. The samples were prepared and tested in three distinct conditions:

- **Base:** No modification was applied.
- **K1:** A first set of laser-induced cuts was made.
- **K2:** A second set of laser-induced cuts was applied.

The electromechanical results for these samples are shown in Figure 4.23A. A notable reduction in sensitivity is observed, with the maximum relative change in resistance decreasing from 8.5 in the Base sample to 1.7 in the K2 sample.

To support our hypothesis that the reduction in sensitivity is linked to an overall decrease in strain across the samples, we conducted COMSOL simulations to analyse the strain distribution under a 30% strain condition. The simulation results, depicted in Figures 4.23B and 4.23C, provide insights into how the strain is distributed across the three different samples.

Figure 4.23B shows the strain distribution across the samples, highlighting that the kirigami pattern helps reduce the mean strain. This is further supported by the strain distribution shown in Figure 4.23C, where a clear drop in mean strain is observed. Specifically, the strain for the Base sample is concentrated around 30%, whereas the K1 and K2 samples are centred around 10%.

Furthermore, by carefully selecting the type and arrangement of geometric modifications, it is possible to customize the performance characteristics of LIG nanocomposites to meet specific application needs. The versatility of this approach lies in its ability to balance the trade-offs between sensitivity, durability, and the operational strain range, making it a powerful tool in the design of advanced strain sensors.

In summary, the post-fabrication geometric tailoring of LIG nanocomposites, particularly through techniques like kirigami, offers a flexible and effective strategy for enhancing the functionality of these materials in diverse applications. By adjusting the geometry, we can fine-tune the mechanical and electrical properties of LIG-based sensors, ensuring they meet the specific demands of their intended use cases. This capability not only broadens the applicability of LIG nanocomposites but also opens new avenues for innovation in the field of flexible electronics and sensor technology.

4.4.10 Theoretical Model

To explain the behaviour of LIG-nanocomposites, we present a theoretical model that links the strain distribution within the material to its electrical response. As shown in Figure 4.23, the strain distribution directly influences the electrical response of the nanocomposites.

We define the effective resistance R_{eff} as a function of the strain distribution across the volume V of the material. The model is represented by the following integral:

$$R_{\text{eff}} = \iiint_V R(\varepsilon)\,\varepsilon(v)\,d\mathbf{v} \tag{4.6}$$

where $R(\varepsilon)$ denotes the resistance as a function of the local strain ε, and $\varepsilon(v)$ represents the strain distribution across the volume element $d\mathbf{v}$.

Model Testing

To validate the proposed model, its predictions were compared with experimental results obtained from the kirigami sensor, as shown in Figure 4.23. The resistance-strain function $R(\varepsilon)$ was approximated using data from the uncut sensor, and the strain distribution $\varepsilon(v)$ was derived from simulation data.

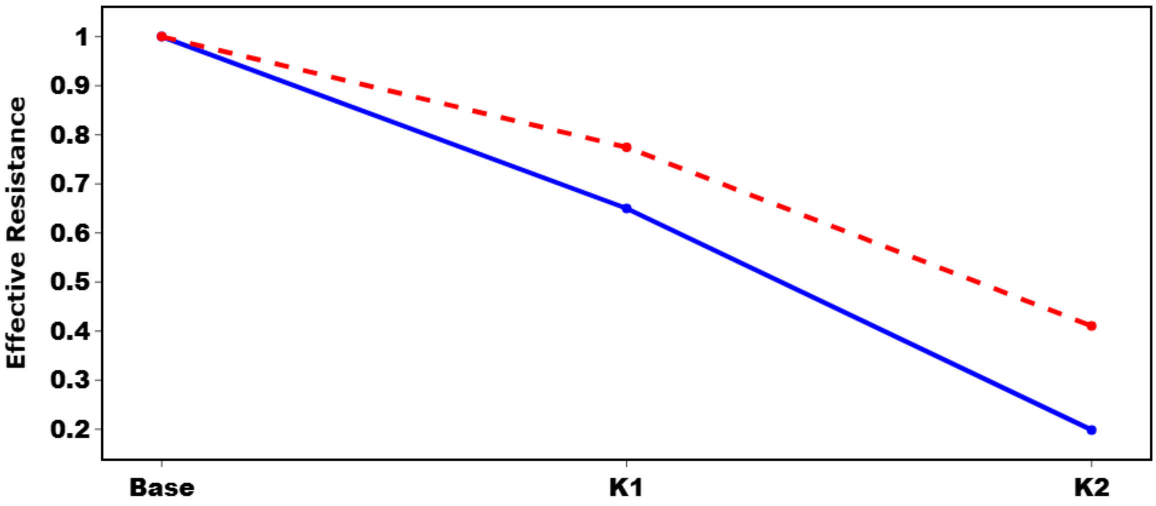

Figure 4.24: Comparison between experimental resistance values and theoretical predictions derived from simulation results at 15% applied strain. The experimental data (solid line) and simulated results (dashed line) are overlaid to illustrate deviations and alignment.

Figure 4.24 illustrates the comparison between the experimental resistance at 15% strain and the theoretical values derived from the model. The results demonstrate a qualitative agreement between the experimental trends and the model's predictions, although noticeable deviations are present. These discrepancies arise from several simplifying assumptions inherent to the model. The function $R(\varepsilon)$ was derived directly from experimental measurements, which introduces potential error propagation into the theoretical predictions. Additionally, the model assumes that the electrical response of each volume element $d\mathbf{v}$ is equivalent to that of the entire sample, implying uniformity in the material structure. However, the actual strain distribution is not uniform due to boundary effects, such as the clamping applied at each end of the sensor. Furthermore, while the model captures the general effects of strain distribution, it does not account for localized variations that could significantly influence the electromechanical response.

Despite these limitations, the model provides valuable insights into how strain distribution impacts the electromechanical behaviour of kirigami sensors. The deviations between experimental and theoretical data highlight the need for further refinement to capture the complex interactions within the structure more accurately. Nevertheless, this work demonstrates the utility of simplified models in exploring the fundamental mechanisms governing strain-sensitive sensor behaviour and lays the groundwork for future improvements.

4.5 Conclusion

This chapter has provided a detailed exploration of the various factors influencing the formation and properties of LIG nanocomposites. We have demonstrated the significant role of laser parameters, such as power, scanning speed, and focal distance, in determining the electrical resistance and structural integrity of LIG. Experimental findings highlight that optimizing these parameters leads to improved conductivity and stability of the resulting nanocomposites. Additionally, the integration of LIG into elastomeric matrices like PDMS and Ecoflex enhances the performance of strain sensors, making them well-suited for applications in flexible electronics and wearables.

Furthermore, we have examined the impact of post-fabrication modifications, including the application of kirigami patterns, which notably affect the mechanical and electrical behaviour of LIG-based composites. This approach offers a promising strategy for tailoring the properties of LIG nanocomposites, enabling their adaptation to a wide range of applications, from strain sensing to flexible electronics.

The following chapter will focus on the development of heat-insensitive LIG strain sensors. Given that temperature sensitivity often limits the performance of strain sensors in practical scenarios, this next chapter aims to address this challenge by designing LIG-based sensors that maintain accuracy under varying thermal conditions. The incorporation of heat-insensitive properties into LIG nanocomposites marks an important step towards the practical deployment of these sensors in a broader range of environments and applications.

Chapter 5

Heat Insensitive LIG Strain Sensors

5.1 Introduction

While strain sensing with LIG sensors has been explored, the effect of temperature on these sensors has often been either overlooked or considered primarily for temperature sensing applications. The heat sensitivity of LIG strain sensors is generally not the focus when studying their strain-sensing capabilities. In this chapter, we explore how different laser settings can influence the heat sensitivity of LIG strain sensors. Furthermore, we propose methods to mitigate the temperature effects on the strain measurement, aiming to enhance the sensors' performance in temperature-variable environments. Additionally, this chapter seeks to develop a theoretical framework for understanding the interplay between laser-induced characteristics and heat sensitivity in LIG-based strain sensors, providing valuable insights for future sensor optimization and applications.

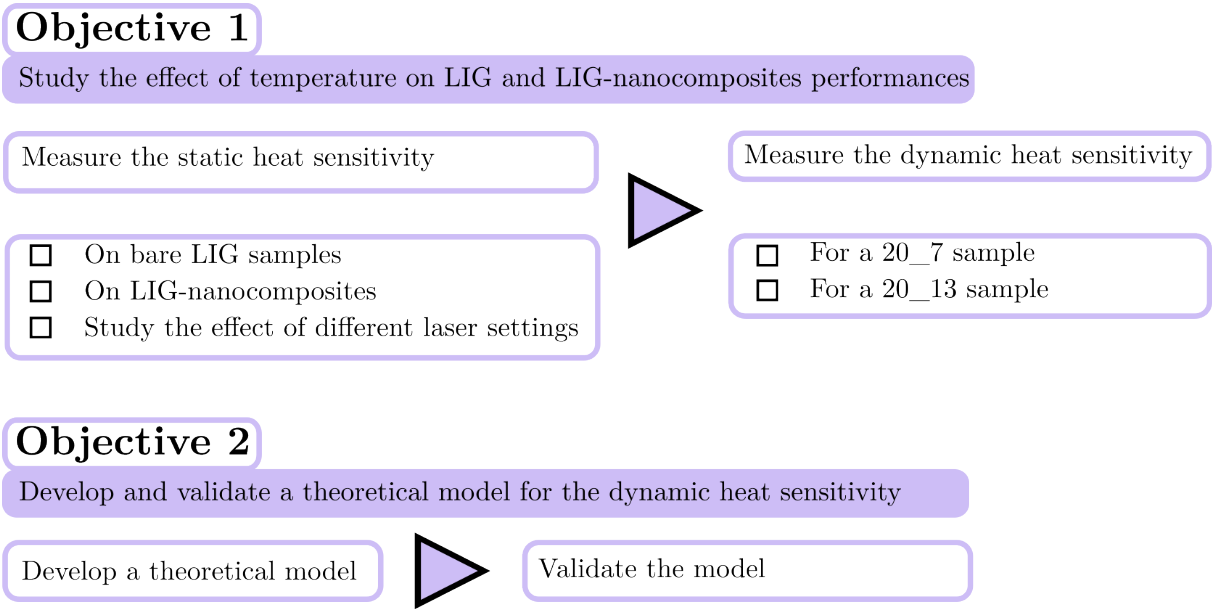

Figure 5.1: Chapter 5 Objectives Flowchart

5.2 Heat Sensitivity of LIG

LIG is classified as a semimetal or semiconductor, exhibiting a negative TCR. This means that the electrical resistance of LIG decreases with increasing temperature, characteristic of materials where electron mobility improves with thermal excitation. This temperature-dependent resistance behaviour is shown in Figure 5.2, which compares LIG samples fabricated under varying laser power and speed settings.

Despite the significant influence of laser parameters, such as power, speed, and resolution, on the structural and electrical properties of LIG, these factors have minimal effect on its TCR. This observation suggests that the primary electron transport mechanisms in LIG remain consistent regardless of variations in structural morphology induced by fabrication settings. The graphene-like network formed during laser processing exhibits high conductivity, and the TCR is dominated by the intrinsic properties of the carbon material itself, rather than changes in porosity or surface area caused by laser-induced variations. Consequently, this robust and stable temperature response makes LIG suitable for applications requiring consistent thermal sensitivity, independent of manufacturing variations.

To evaluate the influence of laser parameters on LIG's TCR, we examined datasets for the power and speed tests separately, as the experiments were conducted on different days, which may have introduced variations in environmental conditions. For the speed parameter, the results showed minimal variance in the normalized resistance values, with a coefficient of 0.00084. The temperature sensitivity also remained independent of the speed setting, with a measured value of $-0.00056 \pm 0.00004\,°C^{-1}$. These measurements were made using the heated 3D printer bed setup described in section 3.6.

Similarly, for the power parameter, the normalized results exhibited minimal variance, with a coefficient of 0.00132. The temperature sensitivity remained consistent across different power settings, with a measured value of $-0.00045 \pm 0.00004\,°C^{-1}$. These findings further reinforce the conclusion that LIG's temperature sensitivity is primarily governed by the intrinsic properties of the material, rather than the specific fabrication parameters.

5.3 Static Heat Sensitivity of LIG-PDMS Composites

To evaluate whether transferring LIG to a polymer, such as PDMS, alters its TCR, static electrical measurements (i.e., without applied strain) were performed on LIG-PDMS composites. Notably, these measurements revealed a shift from the typical negative TCR observed in pure LIG to a positive TCR in the composites. This

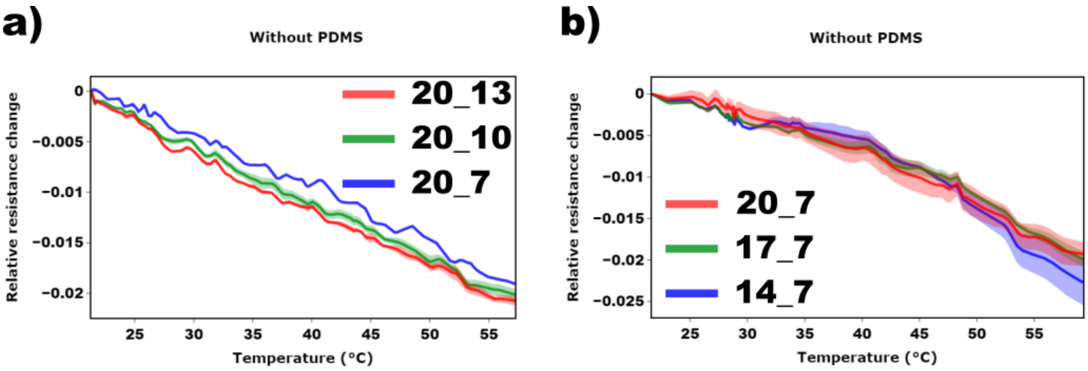

Figure 5.2: Temperature-dependent resistance profiles of raw graphene samples manufactured under varying speed and power conditions. Solid lines represent average responses, and shaded areas depict the range of measurements. a) Resistance change for samples 20__13, 20__10, and 20__7 (constant power, varying speed); b) Resistance change for samples 20__7, 17__7, and 14__7 (constant speed, varying power).

behaviour can be attributed to the thermal expansion properties of PDMS, which induce mechanical strain on the embedded LIG network during heating. As previously discussed, LIG is highly sensitive to strain, and this thermally induced strain results in an increase in resistance, leading to the observed positive TCR.

The strain induced in a material due to thermal expansion can be described mathematically using the relationship:

$$\varepsilon = \alpha \cdot \Delta T, \tag{5.1}$$

where:

- ε is the strain (unitless or expressed as a percentage),
- α is the linear coefficient of thermal expansion (CTE, in ppm/°C or μm/m/°C),
- ΔT is the temperature change (in °C).

For PDMS, which has a linear CTE of $340\,\text{ppm}/^\circ\text{C}$ (as specified by the manufacturer), a temperature increase of $\Delta T = 100\,^\circ\text{C}$ would induce a strain of:

$$\begin{aligned}
&\varepsilon = \alpha \cdot \Delta T, \\
&\varepsilon = \left(340 \times 10^{-6}\right) \cdot 100, \\
&\varepsilon = 0.034\,(\text{unitless}).
\end{aligned}$$

This corresponds to a strain of 3.4%. Such a significant strain level, resulting from the thermal expansion of the PDMS matrix, directly impacts the LIG network embedded within it. The induced strain alters the resistance of the LIG, thereby contributing to the positive TCR observed in the composite.

Additionally, laser parameters used during LIG fabrication play a critical role in influencing the TCR behaviour of the composites. The porosity and connectivity of the LIG network, determined by factors such as laser power, speed, and resolution, directly affect how the composite responds to thermal expansion-induced strain. Different LIG networks embedded within PDMS exhibit distinct strain-resistance responses, as shown in Figure 5.3. These results highlight the importance of optimizing laser fabrication settings to achieve the desired thermal and electrical performance for specific applications.

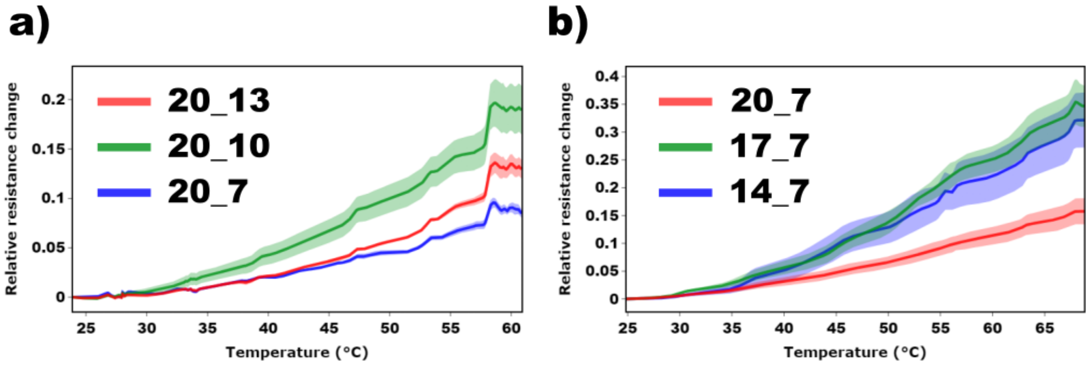

Figure 5.3: Temperature-dependent resistance profiles of LIG-PDMS composites. Solid lines represent average responses, and shaded areas depict the range of measurements. a) Resistance change for composites 20_13, 20_10, and 20_7 (constant power, varying speed); b) Resistance change for composites 20_7, 17_7, and 14_7 (constant speed, varying power).

To confirm that PDMS expansion occurred as previously described, a simple experiment was conducted to measure this effect. A solid dog-bone-shaped PDMS sample was clamped and attached to a force gauge, then subjected to tensile strain. The sample was subsequently heated using a heat gun, leading to a measurable decrease in force, indicating material expansion. We observed a decrease of approximately 4%, which is consistent with the values calculated using the CTE.

Further testing revealed challenges in the manufacturing process, particularly in maintaining low variance in results. Sensors produced under similar conditions often exhibited significant variability, especially at the lower energy limits required for graphene conversion. This variability is illustrated in Figure 5.5, where samples such as 14_7 demonstrate high variance in performance. Additionally, the inclusion of sample 20_6 highlights how factors like the peeling process can induce damage to the LIG network, further contributing to performance inconsistencies.

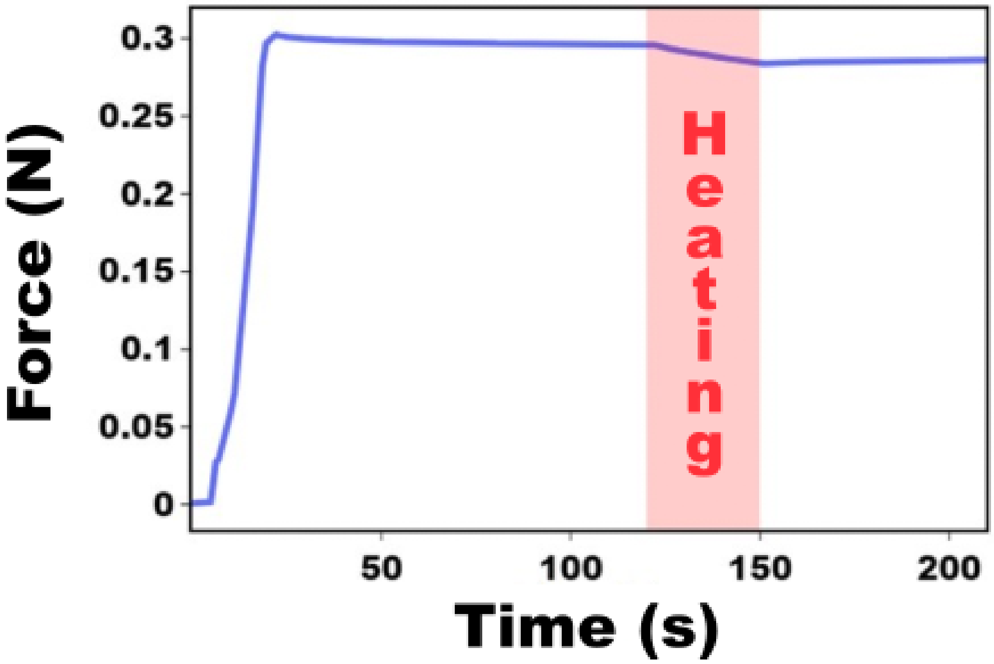

Figure 5.4: Illustration of PDMS expansion under heating.

5.4 Dynamic Heat sensitivity of LIG-PDMS composites

The dynamic heat sensitivity testing of the composites yielded particularly intriguing results. Unlike the straightforward increase in resistance observed during static heat sensitivity experiments, the response of the composites under dynamic conditions proved to be more complex. While all samples exhibited a positive TCR in static tests, their behaviour under strain conditions varied significantly. Some samples displayed an increase in resistance with rising temperature, as expected, whereas others showed a decrease or no significant response. This divergence suggests that the interaction between thermal and mechanical effects is not simply additive but rather influenced by factors such as the composite's microstructure, the distribution of graphene networks, and stress distribution variations across the material.

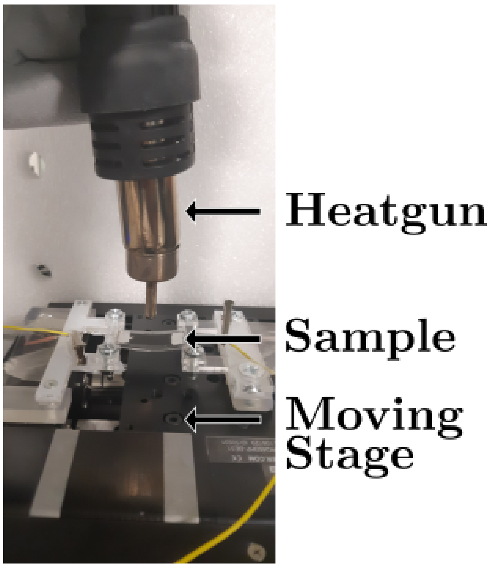

Figure 5.6: Experimental setup for dynamic heating tests, where a heat gun was secured above the samples on the moving stage to record the electrical response during temperature variations.

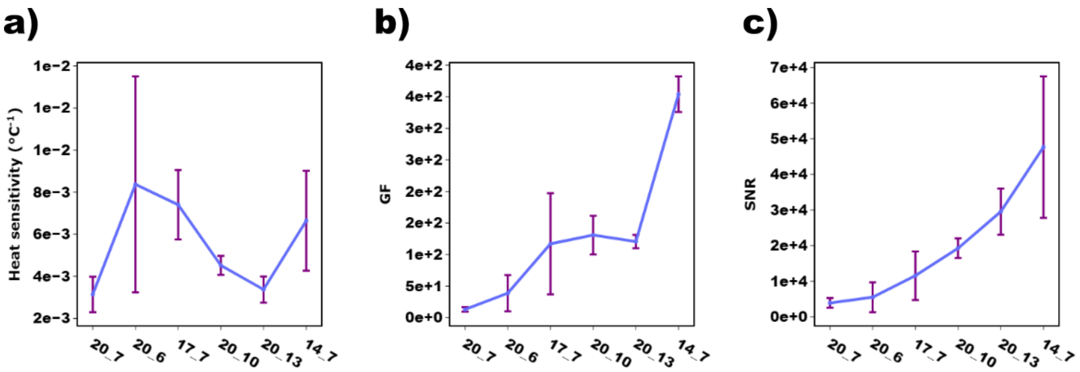

Figure 5.5: Evaluation of heat sensitivity and strain sensitivity for LIG-PDMS composites. a) Heat sensitivity, assessed through the slope of resistance change curves in Figure 5.3; b) Gauge factor of the same sensors, representing strain sensitivity; c) Ratio of heat sensitivity to gauge factor, illustrating the balance between thermal and strain responses.

The experimental setup for dynamic heating tests differed from the one presented in Figure3.8. As shown in Figure5.6, a heat gun was fixed above the samples on the moving stage, enabling real-time monitoring of the electrical response to temperature fluctuations.

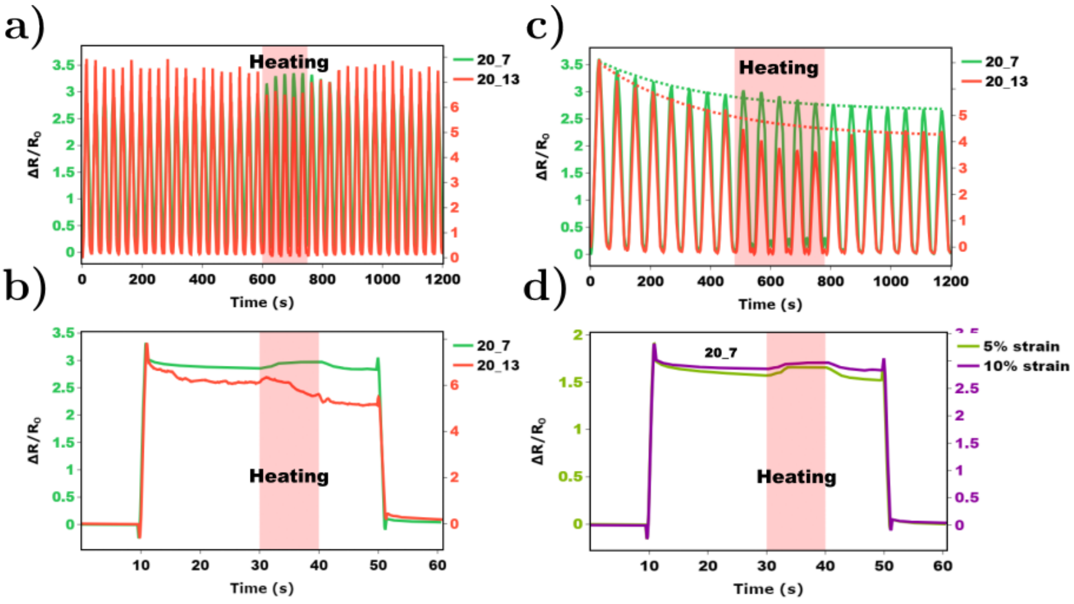

Figure 5.7: a) Effect of heating on samples during cyclic stretching (10% strain applied) at high cycle speed; b) Effect of heating on strain testing at slower cycle speed (10% strain applied); c) Effect of heating on samples during static loading (10% strain applied); d) Effect of strain on thermal sensitivity of the sensors for an optimised sample

As illustrated in Figures 5.7 a) and c), the sensors scrutinised earlier were subjected to an abrupt temperature shift from room temperature to 100°C for 5 cycles during cyclic stretching (10% strain for 45 cycles with a period of 30 s and 10% strain for 20 cycles with a 60 s period respectively). The 20_7 sensors exhibited a notable positive change in resistance, reaching up to 3%, whereas the 20_13 nanocomposite samples demonstrated a significant negative relative change in resistance, exceeding 15%. Given that polymer-based sensors are inherently susceptible to drift during cyclic loading, Figure 5.7c) also presents the fitted exponential decrease to estimate the response in the absence of thermal effects. This approach further emphasizes the positive response of the 20_7 sensors and the negative response of the 20_13 sensors.This experimental investigation reveals a pronounced trend: the TCR within LIG-PDMS nanocomposite sensors under dynamic mechanical loading exhibits variability based on specific laser settings used during fabrication. These dynamic TCR profiles can assume positive, negative, or nearly neutral values, contingent on manufacturing intricacies.

As shown in Figure 5.7b), we further evaluated the sensors using a specific testing protocol: the samples were first subjected to a 10% static strain and held for 20 seconds. Afterward, they were heated for 10 seconds, followed by a cooling period of 10 seconds before being unloaded. The sensors exhibited consistent responses when compared to previous dynamic testing procedures.

Based on these results, it's possible to design sensors that are minimally affected by temperature variations, removing the need for an additional temperature sensor to compensate for thermal effects [179–181]. This significantly simplifies sensor design and integration.

5.4.1 Theoretical model

The variety observed in dynamic TCR results from complex interactions. This variety is primarily driven by the interplay between the relaxation and expansion of PDMS within the nanocomposite structure when it is heated and the interconnectivity and TCR of the LIG network itself. When PDMS is heated, it undergoes faster stress relaxation, altering the strain distribution within the sample. This could explain the drop in the dynamic strain response of 20_13 sample when heated. Additionally, the limited positive response of 20_7 to heating is likely due to the opposing effects of the negative TCR of LIG and the positive thermal expansion coefficient of PDMS.

Our findings reveal that as strain levels increase, the relative change in resistance due to temperature rises diminishes. For instance, at 10% strain, the resistance increase is 4%, compared to 6% at 5% strain (Figure 5.7d). This suggests a complex interplay between strain-induced and temperature-induced resistance changes in the sensors. Operating the sensors at higher strains could, therefore, help minimize the relative impact of temperature-induced resistance variations.

This unexpected result underscores the need for further investigation into the underlying mechanisms governing heat-strain interactions in LIG composites. Understanding the factors that contribute to this variability could lead to the design of more reliable and tunable strain sensors for applications in dynamic environments. To explain these observations, we propose the following theory: when a sample is subjected to mechanical strain, it develops a heterogeneous strain distribution across its structure. Some regions experience higher strain while others experience lower strain, due to inherent non-uniformities in the material. When the sample is heated, the thermal expansion of the PDMS matrix tends to homogenize this strain distribution. Consequently, the overall strain profile becomes more uniform, affecting the sensor's resistance.

Gaussian Strain Distribution

Assuming that the strain distribution in a sample subjected to 10% strain follows a Gaussian profile centered at 10%, with a given standard deviation σ, we hypothesize that this distribution will narrow upon heating. Such a change leads to a more uniform local strain closer to the nominal 10% across the entire sample.

This theoretical framework provides a basis for understanding how thermal and mechanical loads influence LIG-polymer composites, enabling optimization of their performance in practical applications. To analyze this, we model the resistance as a function of strain, $R(\varepsilon)$, which reflects the material's electromechanical behavior. The strain distribution is represented by a normal probability density function (PDF):

$$P_\sigma(\varepsilon) = \frac{1}{\sigma\sqrt{2\pi}} \exp\left(-\frac{(\varepsilon-\mu)^2}{2\sigma^2}\right) \tag{5.2}$$

The effective resistance, R_{eff}, accounting for strain distribution, is computed as:

$$R_{\text{eff}} = \int_{-\infty}^{\infty} R(\varepsilon) P_\sigma(\varepsilon)\, d\varepsilon \tag{5.3}$$

As temperature increases, the strain distribution typically becomes narrower due to the softening of the material, which reduces strain gradients. This narrowing effect is modelled by a decrease in σ. The strain distributions before and after heating are described as:

$$P_{\sigma_1}(\varepsilon) = \frac{1}{\sigma_1\sqrt{2\pi}} \exp\left(-\frac{(\varepsilon-\mu)^2}{2\sigma_1^2}\right) \tag{5.4}$$

$$P_{\sigma_2}(\varepsilon) = \frac{1}{\sigma_2\sqrt{2\pi}} \exp\left(-\frac{(\varepsilon-\mu)^2}{2\sigma_2^2}\right) \tag{5.5}$$

with $\sigma_2 < \sigma_1$. The effective resistances before and after heating are then:

$$R_{\text{eff},1} = \int_{-\infty}^{\infty} R(\varepsilon) P_{\sigma_1}(\varepsilon)\, d\varepsilon \tag{5.6}$$

$$R_{\text{eff},2} = \int_{-\infty}^{\infty} R(\varepsilon) P_{\sigma_2}(\varepsilon)\, d\varepsilon \tag{5.7}$$

The difference in effective resistance, ΔR_{eff}, quantifies the impact of temperature:

$$\Delta R_{\text{eff}} = R_{\text{eff},2} - R_{\text{eff},1} \tag{5.8}$$

If $\Delta R_{\text{eff}} > 0$, the effective resistance increases, suggesting a shift of strain values towards regions of higher resistance. Conversely, $\Delta R_{\text{eff}} < 0$ indicates a concentration of strain around lower-resistance regions.

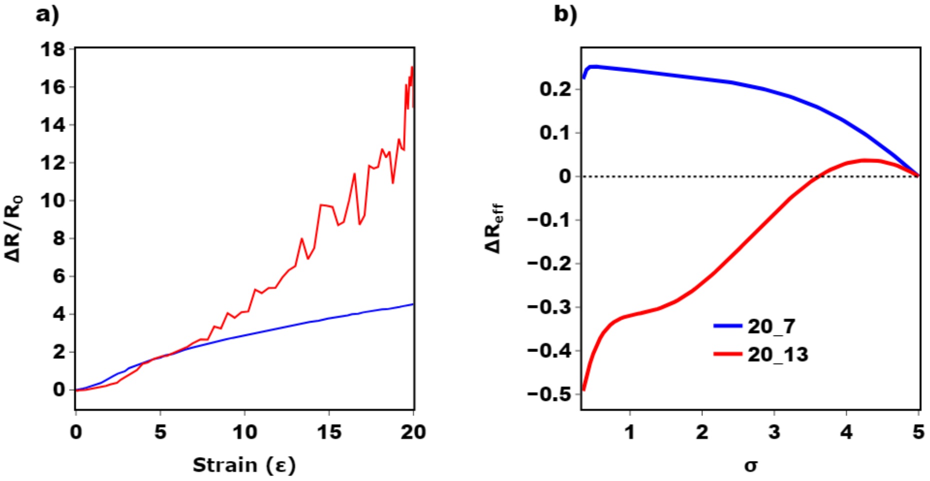

Figure 5.8: a) Resistance versus strain for the 20_7 and 20_13 samples; b) Effective resistance as a function of σ for both samples.

Figure 5.8 illustrates the experimental and modeled results. Panel **a)** shows the resistance-strain relationship for the 20_7 and 20_13 samples, where the former exhibits a convex profile and the latter a concave one. Panel **b)** shows effective resistance as a function of σ. For the 20_7 sample, the effective resistance increases with narrowing strain distribution (smaller σ), whereas for the 20_13 sample, the effective resistance decreases. The slopes of these curves highlight the temperature sensitivity of each sample.

Simulation of Strain Distribution

To further investigate these phenomena, we utilized the model described in Section 4.4.10, applying it to COMSOL simulations of thermal expansion in a PDMS parallelepiped fixed at both ends under strain. Using the simulated strain distribution and the experimental electromechanical data in Figure 5.9a), we evaluated the relationship between temperature and effective resistance.

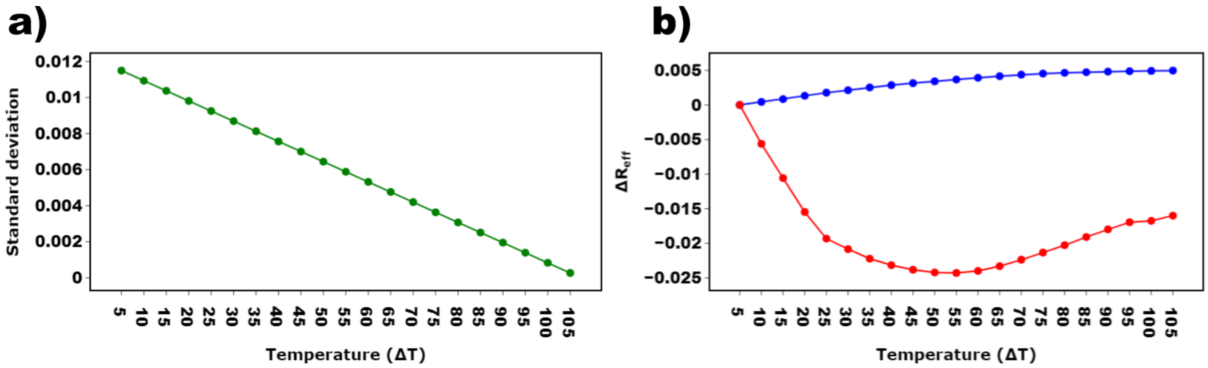

Figure 5.9: a) Standard deviation of the strain distribution at various temperatures; b) Relative change in effective resistance as a function of temperature for the 20_7 and 20_13 samples.

Figure 5.9a) confirms that temperature increases lead to a narrower strain distribution, validating our hypothesis. The relative resistance change, shown in Figure 5.9b), aligns with experimental observations. For the 20_7 sample, the resistance decreases across the temperature range, consistent with Figure 5.7a). Conversely, the 20_13 sample shows an increase in resistance, matching Figure 5.7b). These results underline the contrasting responses to thermal effects in different LIG-polymer composites, emphasizing the importance of tailoring material properties for specific applications.

5.4.2 Model Limitations

While the Gaussian strain distribution model successfully captures the dynamic thermal response observed experimentally, several inherent assumptions and simplifications warrant discussion.

Spatial Independence and Non-Local Effects
The model treats strain as a scalar quantity following a statistical distribution without explicitly accounting for spatial correlations. In reality, strain fields in heterogeneous materials exhibit significant spatial autocorrelation—regions of high strain tend to cluster near defects, interfaces, or geometric stress concentrators. This oversimplification neglects non-local effects where the resistance response at one location may depend on strain states in neighboring regions, particularly relevant for percolating conductive networks in LIG structures.

Time-Independent Steady-State Assumption
Our model assumes instantaneous thermal equilibrium and does not capture transient viscoelastic relaxation dynamics. During heating, PDMS undergoes time-dependent stress relaxation that causes the strain distribution to evolve continuously. The model's static framework cannot describe the temporal evolution from initial heating to steady state, which may be critical for understanding the resistance trajectory observed in Figure 5.7.

Linear Superposition of Thermal and Mechanical Effects

The model implicitly assumes that thermal expansion and mechanical strain effects can be linearly superposed. However, temperature-dependent changes in material properties (Young's modulus, Poisson's ratio, interfacial adhesion) introduce nonlinear coupling between thermal and mechanical fields. At elevated temperatures, the softening of PDMS may alter load transfer mechanisms to the LIG network in ways not captured by simply narrowing the strain distribution.

Homogeneous Material Properties

The integration in Equation (2) assumes a universal resistance-strain relationship $R(\varepsilon)$ applies uniformly across the entire sample. This neglects the inherent heterogeneity of laser-induced graphene, where local variations in graphitization degree, porosity, and sheet structure create spatially varying electromechanical responses. Different regions may exhibit different $R(\varepsilon)$ curves, which would require a more sophisticated treatment involving joint probability distributions.

Boundary Condition Idealization

The COMSOL simulations assume perfect mechanical fixation at the ends and uniform thermal expansion. In experimental fixtures, partial slip, compliance in the grips, and non-uniform heating patterns introduce additional strain heterogeneity not captured by the model. The actual boundary conditions likely fall between the idealized fixed-end and free-expansion limits.

Gaussian Distribution Assumption

While mathematically convenient, the Gaussian form may not accurately represent the true strain distribution, particularly in the tails. Materials with defects or damage often exhibit skewed or multimodal distributions. The choice of a symmetric, unimodal distribution precludes capturing localized strain concentrations or bimodal behavior that might arise from competing mechanisms.

Experimental Validation Strategy

To rigorously test these limitations, we propose the following experimental approach:

1. **Digital Image Correlation (DIC) Mapping**: Apply random speckle patterns to sample surfaces and use DIC to measure full-field strain distributions during heating cycles. This would directly validate the Gaussian assumption and reveal spatial correlations, providing empirical strain histograms for comparison with the model's predicted $P(\varepsilon)$.
2. **Time-Resolved Measurements**: Conduct rapid heating experiments with high-frequency resistance monitoring (>10 Hz) to capture transient dynamics. Comparing the temporal evolution of resistance against model predictions would expose limitations in the steady-state assumption.
3. **Spatially-Resolved Resistance Mapping**: Fabricate samples with segmented electrodes to measure local resistance at different positions along the strain gradient. This would test whether a single $R(\varepsilon)$ function adequately describes the entire sample or if spatial heterogeneity requires a distributed model.

4. **Parametric Temperature Cycling**: Perform experiments with varying heating rates and dwell times to decouple instantaneous thermal effects from time-dependent viscoelastic relaxation. Deviations from model predictions would indicate the importance of transient phenomena.
5. **Boundary Condition Variations**: Systematically vary grip stiffness and sample aspect ratios to probe how boundary conditions influence strain distributions. Comparing samples with different L/W ratios or using compliant versus rigid fixtures would reveal sensitivities not captured by idealized simulations.
6. **Multi-Modal Characterization**: Combine electrical measurements with simultaneous thermal imaging and acoustic emission monitoring to detect phenomena (local delamination, micro-cracking, percolation threshold changes) that manifest in resistance changes but are not explained by strain distribution alone.

These experiments would not only validate the model's predictive capabilities but also identify the dominant physical mechanisms governing the observed thermal-mechanical-electrical coupling in LIG-polymer composites.

5.5 Conclusion

In this chapter, we have explored the impact of laser settings on the heat sensitivity of LIG strain sensors. While temperature effects have often been ignored or considered separately for temperature sensing, we have highlighted the importance of understanding these effects in the context of strain sensing. We have proposed methods to mitigate temperature-induced variations, thus improving the accuracy of strain measurements in temperature-variable environments. Additionally, a theoretical framework was developed to better comprehend the relationship between laser-induced properties and heat sensitivity in LIG sensors. These findings contribute to the broader understanding of LIG strain sensors and provide a foundation for the optimization of their performance in real-world applications where temperature changes are inevitable. Building on the investigation of heat sensitivity in LIG-based strain sensors, the next chapter explores another critical parameter influencing sensor performance: surface wettability. While laser processing conditions play a pivotal role in tuning the electrical and thermal response of LIG, they also significantly impact the morphology and surface energy of the material, both of which directly affect its wettability. The next chapter presents the methodologies used to tailor the wettability of LIG surfaces and discusses how these modifications enable consistent and enhanced integration of nanomaterials into the porous graphene structure.

Chapter 6

Wettability control of LIG

6.1 Introduction

Controlled wettability is a critical parameter in the optimization of LIG-based sensor performance, particularly in the context of doping. Achieving an optimal wettability on the LIG surface is essential for promoting the uniform infiltration of additives and dopants into the graphene network. Hydrophobic surfaces, by by contrast, hinder the penetration of modifying agents, which can ultimately reduce the effectiveness of the doping process and the performance of the final sensor. However, this inherent hydrophobicity can also be advantageous as it prevents the penetration of humidity and water into the sensing film, thereby reducing environmental interference and enhancing sensor stability. Therefore, considering both aspects, hydrophobic surfaces offer a dual benefit in sensor development: while they may pose challenges for liquid-phase doping, they provide crucial protection against environmental effects.

This chapter focuses on strategies to tailor the surface wettability of LIG by modifying its surface morphology. We explore how laser processing parameters and secondary laser treatments can be employed to refine the surface topography, thereby reducing the contact angle and enhancing hydrophilicity. The theoretical framework provided by the Cassie-Baxter equation is used to elucidate the relationship between surface roughness and wettability, offering quantitative insight into how micro-scale modifications influence liquid spreading.

Furthermore, this chapter details the methods used for contact angle measurements, which serve as a key indicator of the success of these surface modifications. Through systematic experimentation, we demonstrate the tunable nature of LIG wettability, from super-hydrophobic to fully wetted states, and discuss the implications of these changes for the doping process and overall sensor performance.

In summary, by establishing controlled wettability, we aim to enhance the diffusion and integration of dopants within the LIG structure, paving the way for improved sensor characteristics and expanded functionality in various applications.

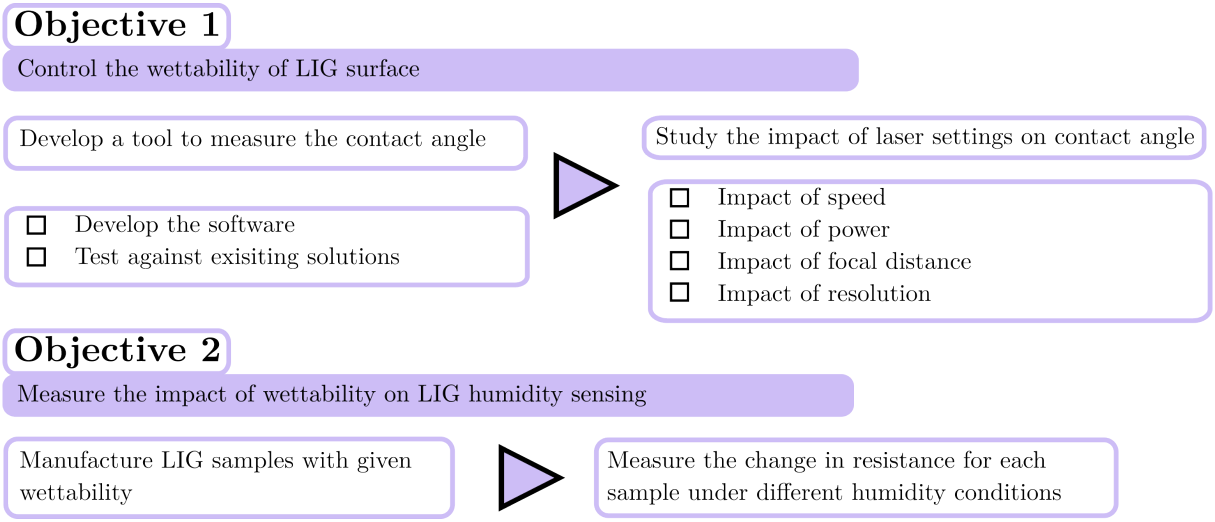

Figure 6.1: Chapter 6 Objectives Flowchart

6.2 Theoretical framework

The wettability of the LIG surface can be effectively controlled by modifying its surface morphology. Surface roughness is a key factor in determining how a liquid interacts with a surface, and it plays a central role in influencing the contact angle. The relationship between surface roughness and wettability is often described by the Cassie-Baxter equation, which accounts for the composite nature of rough surfaces:

$$\cos\theta_C = f_s \cos\theta_Y + f_v \cos\theta_V \tag{6.1}$$

Where:

- θ_C is the apparent contact angle on the composite surface.
- f_s is the fraction of the solid surface area in contact with the liquid.
- θ_Y is the Young contact angle on the flat, homogeneous surface.
- f_v is the fraction of the surface area occupied by air (often $f_v = 1 - f_s$).
- θ_V is the contact angle of the liquid with the air (typically -1 for air).

This equation provides a theoretical framework for understanding the relationship between surface roughness and the wettability of a liquid drop on a textured surface. Specifically, it illustrates how the roughness of a material influences its ability to interact with liquid. By increasing surface roughness, the material can either enhance or reduce its hydrophilicity, depending on the size and distribution of surface features. When the roughness is finely tuned, it can lead to improved liquid spreading and enhanced capillary action, making the surface more hydrophilic.

One effective approach to achieving a hydrophilic LIG surface involves modifying the 3D structure of the LIG without altering the initial laser parameters used for its synthesis. This can be accomplished by applying a secondary laser treatment to the already-formed LIG. During this secondary laser pass, the surface morphology is further refined, creating a more organized structure with smaller air gaps and grooves. This process results in a reduction of surface roughness at the microscopic level, yielding a more uniform and controlled topography.

By minimizing the size and increasing the regularity of the surface features, the secondary laser treatment significantly enhances the wettability of the LIG. The smaller air gaps and more uniformly spaced grooves improve capillary action and facilitate better liquid spreading across the surface. As a result, the LIG becomes more hydrophilic, which is particularly advantageous for applications where the retention of liquid modifying agents or the enhancement of sensor response is critical. Improved wettability ensures that additives can be more efficiently introduced into the graphene network, leading to better doping results and sensor performance.

6.3 Contact angle measurements

Contact angle measurements play a crucial role in characterizing the surface properties of materials, particularly for applications involving wetting, adhesion, and surface energy analysis. Initially, these measurements were performed using a commercial DSA30 Drop Shape Analyzer, a widely used tool for precise contact angle determination. However, to complement the analytical capabilities and provide a more flexible and open-access solution, a custom Python-based image analysis software was developed. This software aims to replicate the functionality of the proprietary DSA30 software while offering additional flexibility in analysing a broader range of samples.

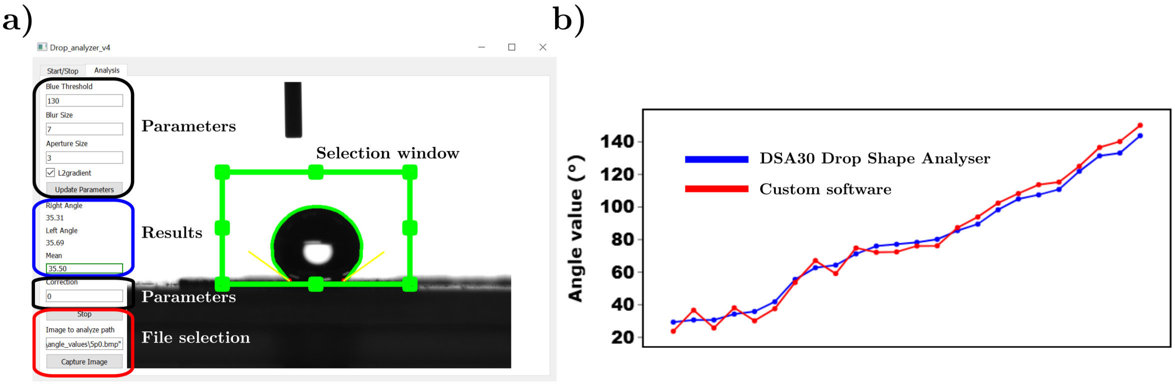

Blue Threshold
130
Blur Size
7
Aperture Size
3
☑ L2gradient
Right Angle
35.31
Left Angle
35.69
Mean
35.50
Correction
0
Image to analyze path
angle_values\5p0.bmp"

Figure 6.2: a) Interface of the custom Python application for contact angle measurement; b) Comparison of contact angle values obtained using the DSA30 software and the custom-built software, highlighting the accuracy and reliability of the custom tool.

The custom software utilizes advanced image processing techniques to isolate the drop shape from the background. A colour filter is applied to enhance the contrast of the drop, followed by contour detection algorithms that define the perimeter of the drop. Once the drop contour is identified, an ellipse fitting algorithm is used to approximate the drop's shape. The contact angle is then calculated by determining the angle between the tangent to the ellipse at the baseline and the horizontal axis.

To evaluate the performance of the custom software, a comparative analysis was conducted with the DSA30 software. The results, presented in Figure 6.2b), show a high degree of agreement between the two methods, with the custom software exhibiting an average absolute error of only 4.4°. However, a slight overestimation of contact angles was observed for super-hydrophobic substrates, as indicated in the comparison graph. This discrepancy can be attributed to the inherent challenges in accurately capturing the contact angle on highly non-wetting surfaces, where the drop's shape may not follow a simple elliptical contour. Despite this, the custom software demonstrated overall performance comparable to the proprietary DSA30 software and offers the advantage of being a cost-effective, open-access tool for contact angle measurements.

6.4 Results

To investigate the impact of laser processing on the wettability of the LIG surface, a series of experiments were conducted using a thin PI film. The samples underwent a first laser pass with varying parameters, including power, speed, distance to the focal plane, and resolution, followed by a secondary laser pass to further modify the surface characteristics.

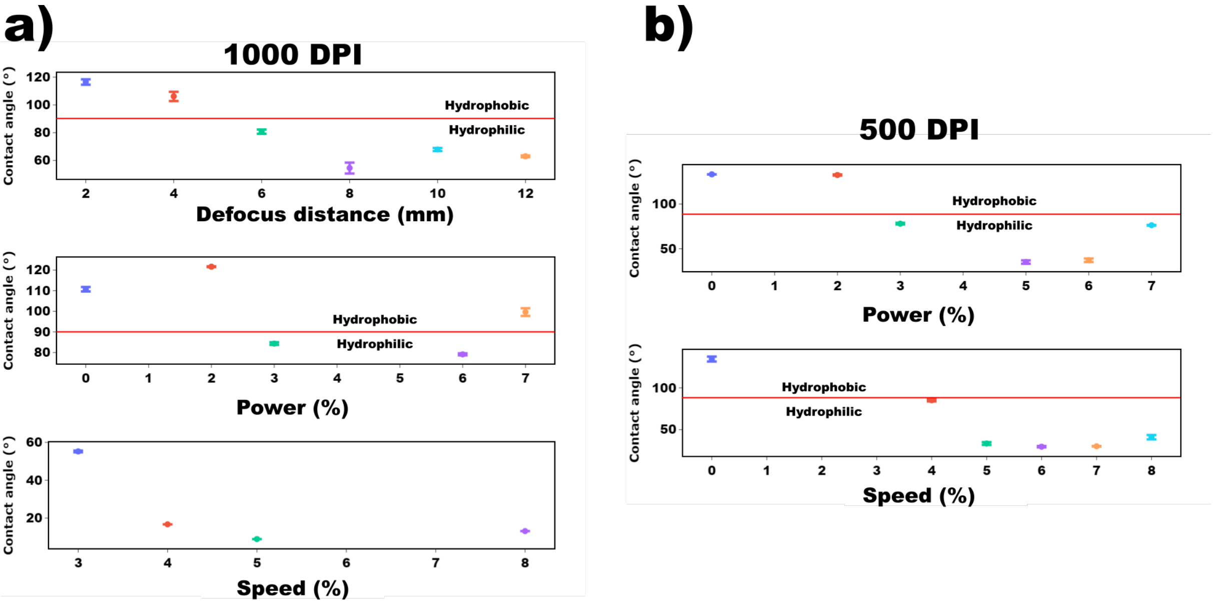

Figure 6.3: Contact angle measurements for LIG samples prepared with different laser parameters, demonstrating tunable wettability ranging from super-hydrophobic to complete wettability.

The data presented in Figure 6.3 indicates that by fine-tuning laser settings, the wettability of the LIG surface can be successfully adjusted from a super-hydrophobic state, where liquid droplets remain largely intact, to a fully wetted state, characterized by rapid liquid infiltration. Such tunability is crucial for tailoring the surface properties to specific applications, such as enhancing sensor sensitivity or ensuring efficient retention of liquid modifying agents.

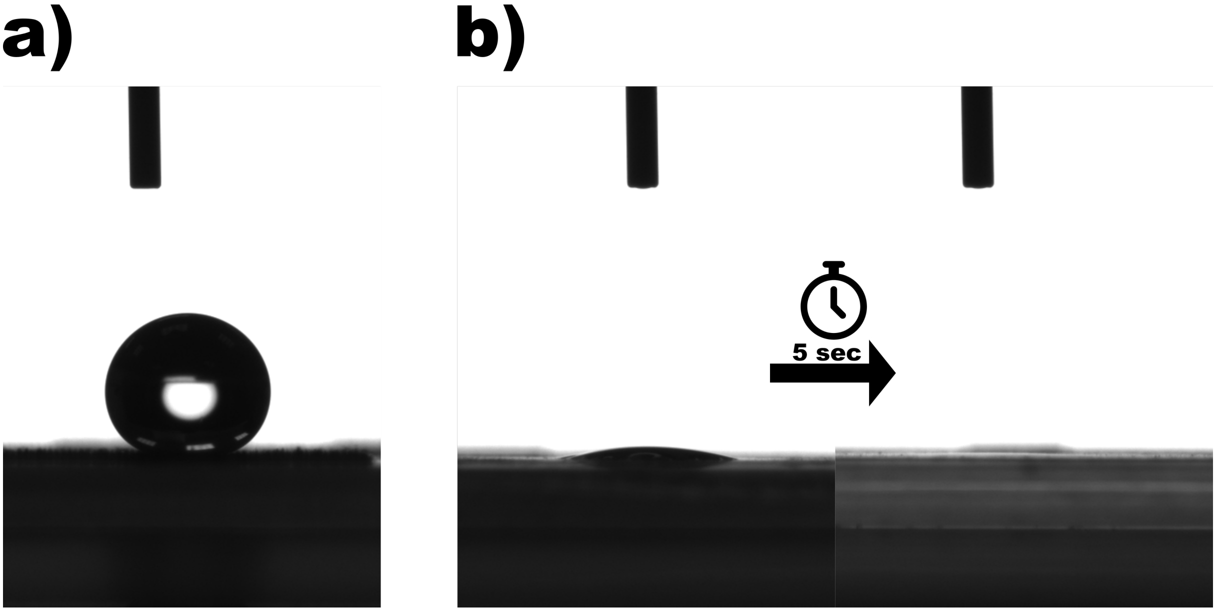

Figure 6.4: a) LIG sample engineered for super-hydrophobicity, demonstrating minimal liquid spreading; b) LIG sample engineered for complete wettability, showing rapid liquid infiltration into the graphene network.

Figure 6.4 further illustrates the distinct outcomes achieved through surface modification: panel (a) shows a super-hydrophobic LIG surface, while panel (b) displays a fully wetted surface as a result of the secondary laser treatment. These results underscore the effective control over surface wettability afforded by adjusting the laser processing parameters.

To further emphasize the versatility of the laser processing system, additional experiments were performed to create patterned surfaces that combine both hydrophilic and hydrophobic regions. Such patterns are designed to control the spatial distribution of water droplets on the substrate. Figure 6.5 shows a chequerboard pattern fabricated on a PI film, along with a demonstration using tonic water under ultraviolet (UV) illumination to reveal the confined liquid regions. These images highlight the precise control over wettability that the laser system offers, opening avenues for advanced applications where selective liquid retention is desired.

Figure 6.5: a) Chequerboard pattern on PI film demonstrating combined hydrophilic and hydrophobic regions; b) Tonic water illuminated under UV light, highlighting the controlled liquid containment within the patterned areas.

Overall, these findings confirm that laser processing can be effectively used to tailor the wettability of LIG surfaces. The ability to control wettability, from super-hydrophobic to hydrophilic states, plays a critical role in both sensor doping and humidity sensing applications. In the next section, we will investigate how these laser-induced modifications influence the electrical properties of LIG, and further explore the integration of polymers to create optimized LIG nanocomposites.

6.5 Hygroscopy

LIG is characterized by its highly porous structure, which significantly increases its surface area and affects both wettability and gas-sensing performance. This elevated surface area offers numerous adsorption sites for gas and water molecules, enhancing sensitivity to environmental changes. However, it also introduces variability in sensor response, particularly under fluctuating humidity conditions, where water uptake can alter the electrical properties of the material.

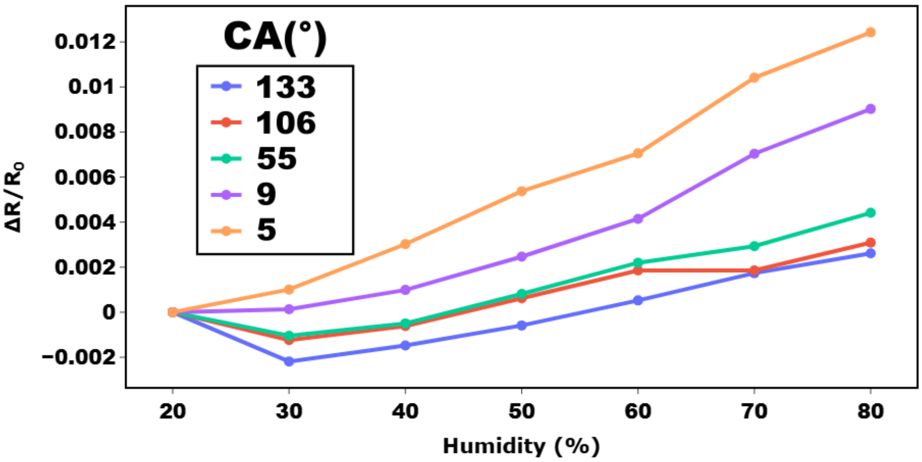

Figure 6.6: Relative change in resistance for LIG samples with different contact angles under varying humidity conditions. Higher contact angles, indicative of more hydrophobic surfaces, exhibit lower sensitivity to humidity due to reduced water penetration into the graphene network.

As shown in Figure 6.6, LIG samples with higher contact angles, corresponding to more hydrophobic surfaces, demonstrate lower sensitivity to humidity. In these cases, electrical resistance increases with rising humidity because water molecules are less able to infiltrate the graphene network and disrupt conductive pathways.

Conversely, experiments conducted on LIG fabricated on thicker PI substrates reveal an opposite trend, illustrated in Figure 6.7. These samples exhibit a decrease in resistance with increasing humidity, likely due to the higher porosity of the LIG structure on thicker PI, which facilitates water uptake. Capillary action within the porous matrix can reorganize the conductive network and increase charge carrier mobility, thereby reducing the overall resistance. [182]

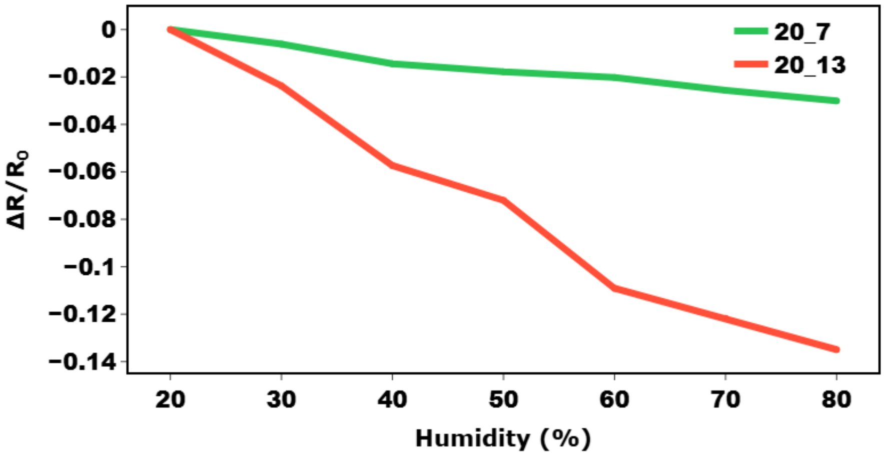

Figure 6.7: Relative change in resistance for two different LIG samples under varying humidity conditions. One set of samples exhibits a decrease in resistance with increasing humidity, likely due to enhanced capillary-driven reorganization in a more porous network.

The contrasting behaviours shown in Figures 6.6 and 6.7 underscore the complex interplay between wettability, porosity, and humidity sensitivity. While a hydrophobic LIG surface resists water infiltration, resulting in increased resistance, a hydrophilic and porous surface facilitates moisture absorption, which can lead to decreased resistance. This environmental dependence represents a significant limitation for LIG-based sensors, particularly in applications where exposure to humidity, such as perspiration in wearable biomedical devices, can compromise measurement fidelity.

To mitigate these limitations and enhance the reliability of strain sensors, LIG can be integrated into polymeric matrices to form nanocomposites. These composites leverage the mechanical and chemical properties of the host polymer to modulate environmental sensitivity. In this study, the hygroscopic response of LIG-PDMS nanocomposites was evaluated under controlled humidity conditions. To investigate the influence of humidity on LIG's electrical properties, twelve samples fabricated with varying laser parameters were tested using the humidity chamber setup described in Section 3.6. Results indicate a consistent resistance decrease of approximately 6% at 60% relative humidity, with remarkably low variance observed across all tested samples.

This reduced humidity sensitivity is attributed to the infiltration of PDMS into the porous LIG network, which restricts water molecule penetration and confines humidity-induced effects to the exposed LIG surface. Moreover, no significant correlation was observed between the laser parameters and the degree of humidity sensitivity, suggesting that the PDMS matrix dominates the moisture response mechanism. These results are presented in Figure 6.8.

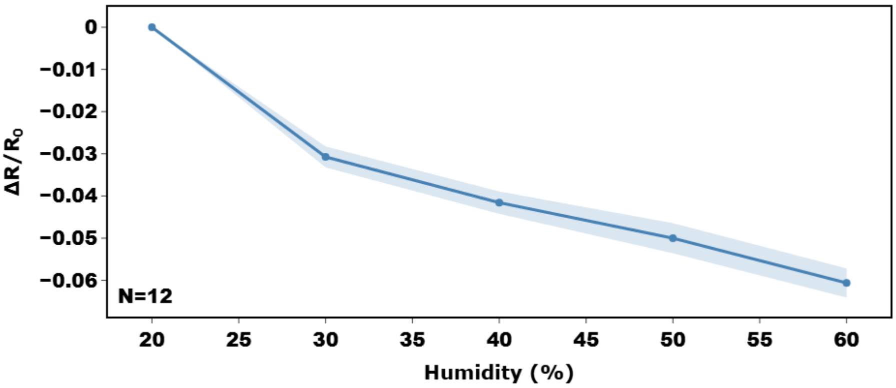

Figure 6.8: Relative change in resistance for different LIG-PDMS nanocomposites exposed to varying humidity levels. A consistent 6% decrease is observed at 60% humidity, with low variance across laser conditions.

6.6 Conclusion

In this chapter, we systematically investigated the influence of laser processing parameters on the wettability of LIG surfaces, using contact angle measurements as a key metric. By varying laser power, scanning speed, focal distance, and resolution, we demonstrated the ability to finely tune the surface wettability of LIG from super-hydrophobic to fully wetting states. To support these findings, we developed a custom Python-based contact angle analysis tool, which showed strong agreement with commercial systems.

Humidity sensing experiments revealed that wettability significantly affects sensor behaviour in humid environments. Hydrophilic surfaces exhibited increased sensitivity due to enhanced water uptake into the porous LIG network, while hydrophobic surfaces showed more stable resistance profiles under varying humidity. Notably, we extended this investigation to LIG-PDMS nanocomposites, which displayed a consistent and reduced response to humidity. The PDMS matrix infiltrated the LIG network, limiting water penetration and localising humidity effects to the exposed surface, regardless of laser parameters. This result highlights the efficacy of polymer integration in mitigating environmental interference, thus improving sensor stability and reliability.

These insights establish a robust foundation for further material optimization. Specifically, the ability to control surface wettability and porosity provides a pathway for improving doping efficiency, as hydrophilic surfaces promote better absorption and uniform distribution of doping solutions. Building on this foundation, the next chapter explores the incorporation of foreign materials into the LIG structure. It focuses on doping strategies to modulate electrical, thermal, and mechanical properties of the resulting nanocomposites, aiming to enhance their performance across diverse sensing applications.

Chapter 7

LIG nanocomposites doping

7.1 Introduction

LIG has emerged as a promising material for soft strain sensors due to its excellent mechanical flexibility, high electrical conductivity, and ease of fabrication. However, as highlighted in previous chapters, LIG-based sensors remain susceptible to environmental factors, particularly temperature variations, which can significantly impact their electrical resistance. To further enhance their performance and reliability, various strategies have been explored, among which doping has gained considerable attention.

Doping involves the incorporation of heteroatoms, metal oxides, or nanoparticles into the LIG network, modifying its physicochemical properties to better suit specific applications. This approach can enhance key sensor characteristics such as sensitivity, selectivity, and stability while also mitigating undesired effects such as temperature-induced resistance fluctuations. By strategically integrating dopants into the LIG structure, it is possible to improve charge transport mechanisms, introduce new functional sites, and tailor the material's response to external stimuli.

The following sections explore the state of the art in LIG doping, focusing on both heteroatom doping and nanoparticle-based modifications. A discussion on the different doping strategies, including pre- and post-synthesis modifications, will also be provided.

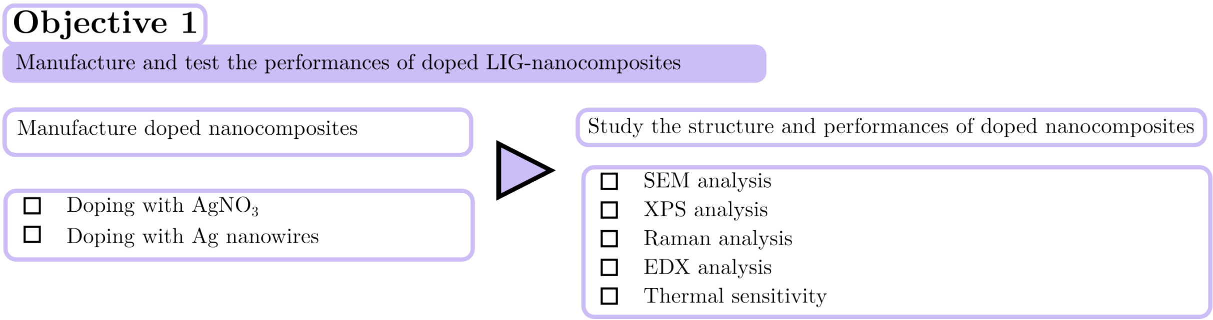

Figure 7.1: Chapter 7 Objectives Flowchart

7.2 Overview of LIG Doping Strategies

The functional properties of LIG can be tailored through various doping strategies, each offering distinct advantages in modifying its electrical, mechanical, and chemical characteristics. A comprehensive review by [183] underscores the potential of doping LIG with heteroatoms and nanoparticles, categorizing the primary approaches into one-step laser irradiation and two-step laser modification. The latter involves post-processing techniques such as deposition, drop-casting, and repeated laser pyrolysis to introduce dopants into the LIG structure.

7.2.1 One-Step In Situ Modification

One-step in situ modification allows for the direct incorporation of heteroatoms or nanoparticles into the graphene lattice during the laser irradiation process itself.

Heteroatom doping of LIG can be directly achieved during laser irradiation, enabling the incorporation of elements such as boron, nitrogen, phosphorus, fluorine, and sulphur into the graphene lattice. This process alters the electronic structure of LIG, thereby enhancing its conductivity, catalytic activity, and stability [184, 185].

Beyond heteroatom doping, this technique can be adapted to introduce metallic and metal oxide nanoparticles into the LIG matrix. By integrating metal-based precursors into the PI substrate prior to laser processing, these precursors undergo decomposition and transformation under the high localized temperatures generated by laser irradiation. This results in LIG composites embedded with nanostructured materials such as gold, copper, cobalt oxide, iron oxide, titanium oxide, or manganese dioxide. Such integration can significantly enhance electrochemical performance, charge transfer capabilities, and sensing properties [186–189]. An illustration of this approach, specifically adding a precursor layer on top of the substrate before lasing, is shown in Figure 7.2b and Figure 7.2c.

7.2.2 Multi-Step Approaches: Duplicated Laser Pyrolysis Method

This two-step approach leverages the intrinsic porosity of LIG to facilitate the efficient penetration and retention of dopants. Initially, LIG is generated via laser irradiation, creating a highly porous structure. In the second step, a dopant, such as a metal salt or nanoparticle precursor, is introduced through solution-based techniques, followed by an additional laser treatment. This second irradiation step serves to integrate the dopants within the LIG framework, promoting the formation of nanoparticles in situ and enhancing their interaction with the graphene network [190–192]. The repeated laser exposure can also induce localized restructuring of the LIG surface, further improving its functional properties. An example of this method is depicted in Figure 7.2a.

These doping methodologies provide a versatile platform for engineering LIG-based materials with tailored electrical, mechanical, and chemical functionalities, expanding their potential applications in sensing, energy storage, and catalysis.

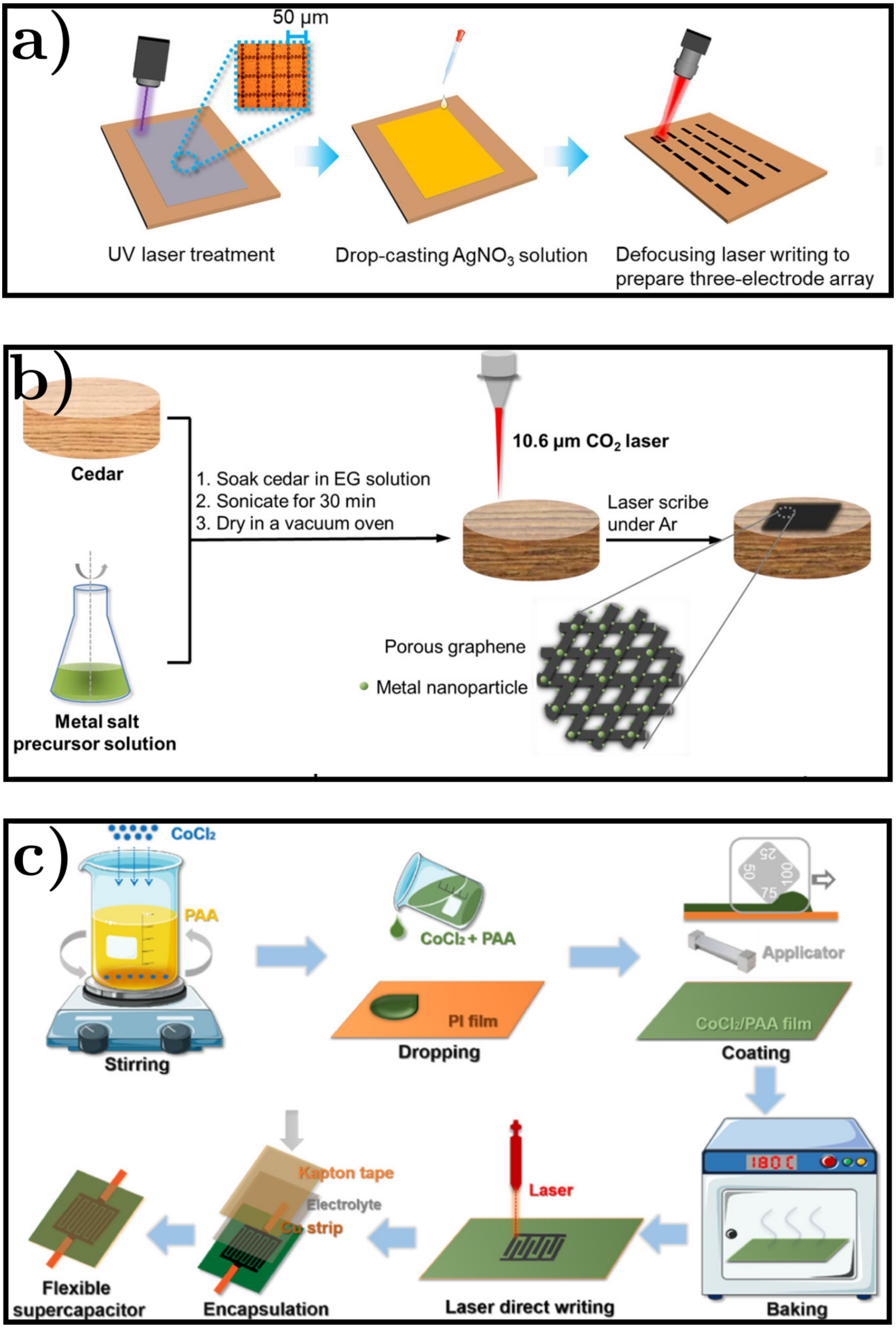

Figure 7.2: Different strategies for LIG modification: a) Illustration of the duplicated laser pyrolysis method (adapted from [188]); b) Illustration of incorporating dopants by mixing them directly into the substrate (adapted from [186]); c) Illustration of adding a dopant layer on top of the substrate before laser processing (adapted from [189]).

7.2.3 Advancements in LIG Performance through Doping

Doping strategies offer a transformative approach to enhancing the functional properties of LIG-based materials, enabling superior performance across a wide range of applications. By carefully selecting dopants and optimizing their integration into the LIG structure, it is possible to develop next-generation sensors and energy storage devices with significantly improved sensitivity, stability, and efficiency.

One of the key advantages of doping is the ability to enhance the electromechanical properties of LIG for strain sensing applications. For instance, [193] demonstrated that incorporating nickel nanoparticles into LIG structures led to a 430% increase in sensitivity compared to undoped LIG sensors. This improvement underscores the potential of nanoparticle doping in fine-tuning LIG's piezoresistive response for high-performance sensing applications.

Similarly, heteroatom doping has proven effective in augmenting the electrochemical properties of LIG. [194] employed nitrogen-doped porous graphene electrodes, where the introduction of electrochemically active species enhanced charge storage capabilities. By laser scribing a PI film pre-coated with a phthalocyanine-based nitrogen dopant, they achieved a 254% increase in capacitance, demonstrating the profound impact of heteroatom doping on energy storage performance.

Beyond strain sensing and energy applications, doping also enables significant advancements in catalytic performance. [44] explored platinum-doped LIG for hydrogen evolution reactions, revealing that $Pt_{1.6}Ni$ nanostructures integrated into LIG exhibited heightened catalytic activity.

Overall, LIG doping serves as a powerful tool for tailoring material properties to meet specific application requirements. Whether through the incorporation of nanoparticles for enhanced strain sensitivity, heteroatom doping for improved electrochemical performance, or metal integration for superior catalytic activity, these strategies significantly expand the capabilities of LIG-based technologies. By refining doping techniques and exploring novel dopant materials, researchers can further push the boundaries of LIG functionality, unlocking new possibilities in sensing, energy storage, and catalysis.

7.3 Silver doping of LIG

In this section, the successful doping of LIG with silver nanoparticles via the drop-casting of silver nitrate is presented. The objective of this work is to modulate the TCR of the LIG samples by introducing metallic particles-specifically silver, which exhibits a positive TCR—into the LIG network, which inherently possesses a negative TCR. This approach aims to achieve a near-zero or minimized overall TCR through compensation between the two opposing thermal responses.

7.3.1 Photoreduction of Silver Nitrate to Elemental Silver

The conversion of silver nitrate ($AgNO_3$) into elemental silver (Ag) is a well-known process that can be induced through various methods, including thermal, chemical, or photo-catalytic reduction. In our process, this conversion is facilitated by the energy input from laser irradiation, which serves as the driving force for the photo-catalytic reaction. [186, 195]

When silver nitrate is exposed to laser energy, the high-intensity light catalyses the reduction of silver ions (Ag^+) to elemental silver (Ag). The overall reaction can be represented as:

$$2AgNO_3 \rightarrow 2Ag + 2NO_2 + \frac{1}{2}O_2 \tag{7.1}$$

In this reaction, silver nitrate decomposes under the influence of laser energy. The silver ions (Ag^+) gain electrons (reduction), forming neutral silver atoms (Ag), which then aggregate into nanoparticles. The by-products of this reaction are nitrogen dioxide (NO_2) and oxygen (O_2), which are released as gases during the process.[196, 197]

The efficiency of this conversion depends on several factors, including the concentration of silver nitrate, the uniformity of its distribution on the LIG surface, and the specific parameters of the laser treatment (e.g., power, speed, and focal distance). Proper tuning of these parameters ensures complete reduction of silver ions and the formation of a homogenous layer of silver nanoparticles, which enhance the electrical and mechanical properties of the LIG composite.[42]

7.3.2 Preparation of the Samples

To achieve a uniform and effective coating of silver nitrate on the LIG surface, the samples were first prepared using the wettability enhancement protocol described in Chapter6. This step ensured consistent absorption and retention of the silver nitrate solution across the porous LIG structure.

A 1M aqueous solution of silver nitrate (Honeywell Fluka™) was then carefully drop-cast onto the treated LIG surface to achieve an even distribution. The samples were left to air dry at room temperature, allowing the solvent to evaporate and leaving behind a thin, homogeneous layer of silver nitrate.

Once dried, the samples underwent a secondary laser processing step using the same CO_2 laser cutter employed for the initial graphene formation. This second exposure was designed to induce the photo-thermal reduction of silver nitrate to elemental silver, facilitated by the laser's energy. This step not only enabled the in-situ formation of silver nanoparticles but also promoted their integration into the graphene matrix. The doping procedure is illustrated in Figure7.3, which outlines the key steps involved in the silver nitrate coating and laser-induced reduction process.

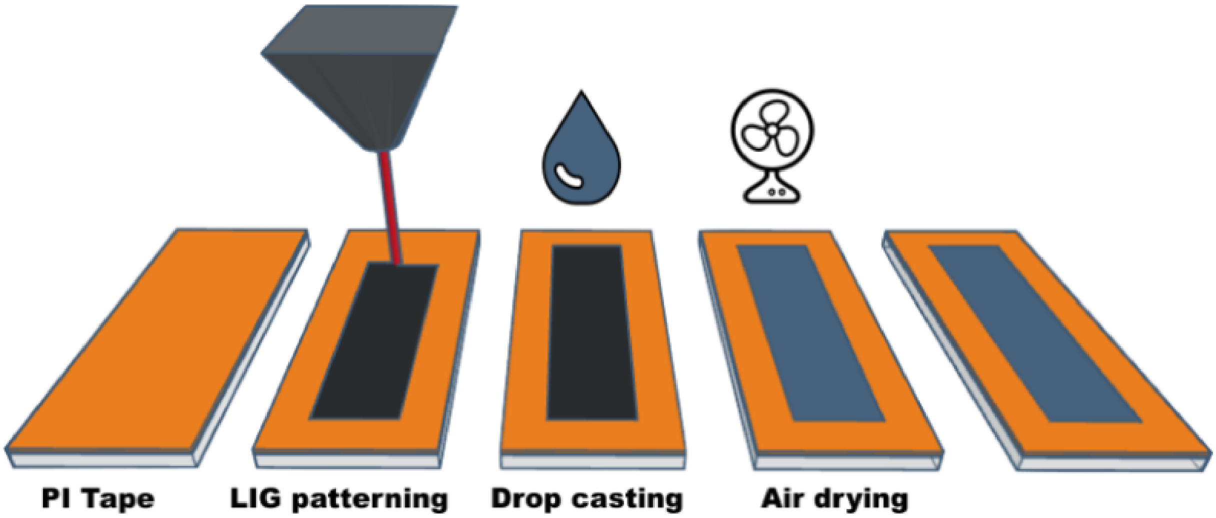

Figure 7.3: Schematic illustration of the silver nitrate doping process onto LIG, followed by laser-assisted reduction.

To further investigate the influence of dopant concentration, additional samples were prepared using varying volumes of silver nitrate solution. Figure7.4 shows photographs of these samples. A visible accumulation of solid residues can be observed along the edges of the LIG region, which becomes more pronounced as the number of deposited drops increases. This edge accumulation likely results from capillary flow and solvent evaporation, which concentrate solutes near the periphery of the wetted area.

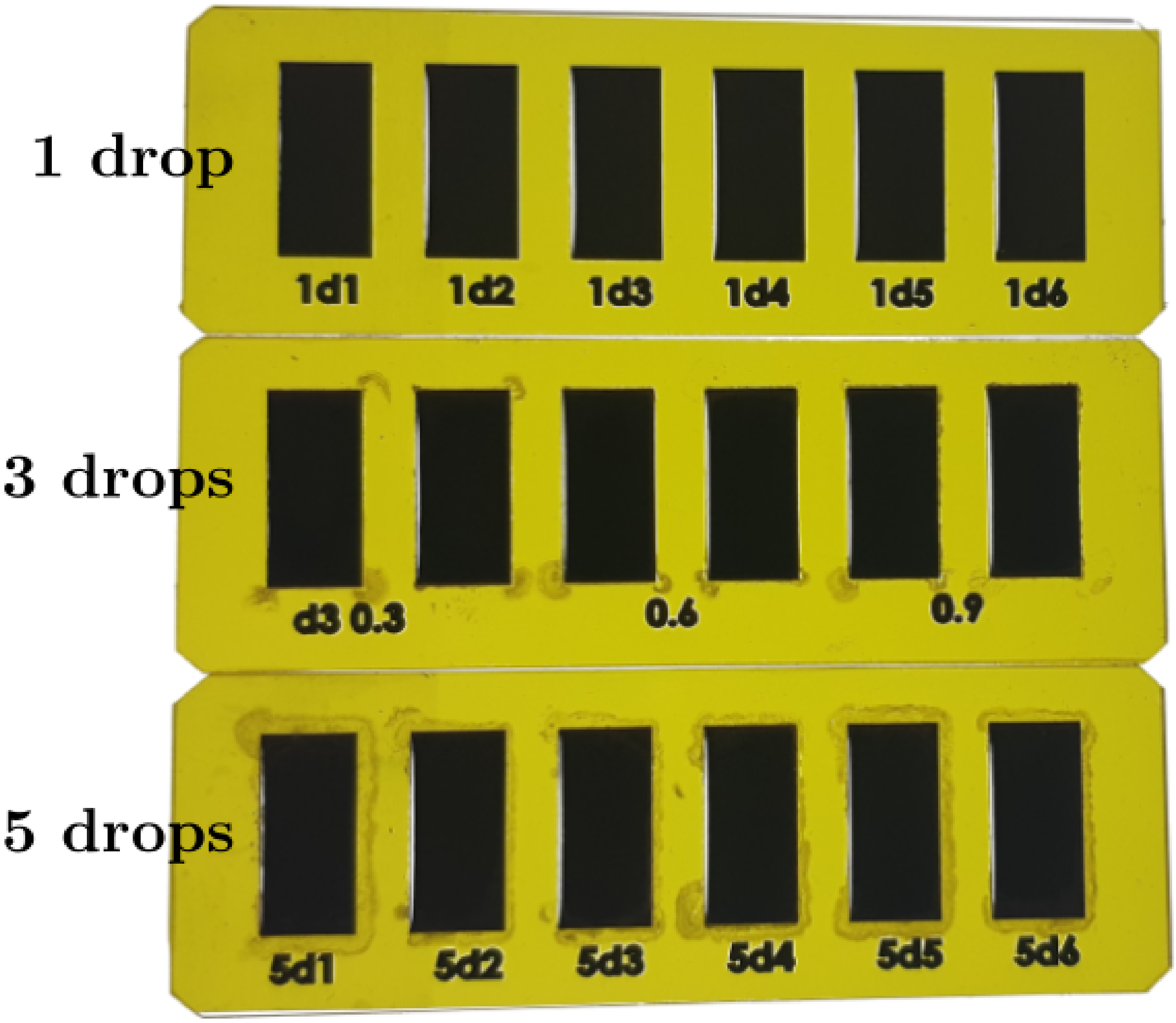

Figure 7.4: Photographs of LIG samples doped with varying volumes of silver nitrate solution. A noticeable build-up of solid deposits is seen at the edges, increasing with the number of deposited drops.

7.3.3 Material characterisation

To evaluate the effectiveness of doping LIG with silver nitrate and the subsequent reduction to elemental silver, a comprehensive characterization was performed. The primary objective was to verify the successful conversion of silver ions to metallic silver and to assess whether the multiple lasering steps impacted the quality of the graphene structure. To ensure the successful reduction of silver nitrate and to analyse the quality of the graphene structure, a series of characterization techniques were employed:

7.3.3.1 Raman Spectroscopy

Raman spectroscopy was employed to analyse the structural integrity of the LIG and to investigate the incorporation and effects of silver nanoparticles. The Raman spectra of doped samples displayed the characteristic peaks associated with the LIG structure, notably the D and G bands. These bands, which represent the disordered and graphitic carbon phases, respectively, were similar to those observed in the non-doped samples, as shown in Figure 7.5. This consistency indicates that the fundamental graphene structure of the LIG remains intact after doping.

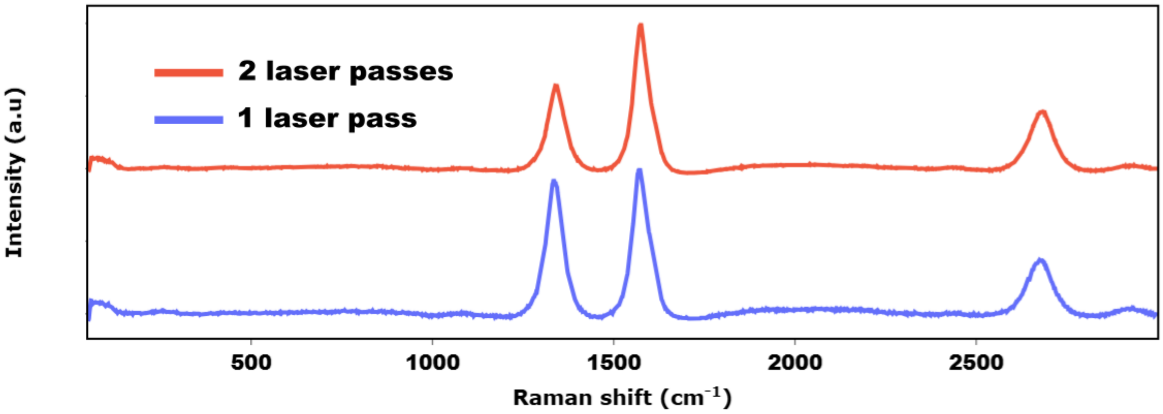

Figure 7.5: Raman spectra of LIG samples produced with one or two laser passes, showing characteristic D and G bands.

Interestingly, as seen in Figures 7.6, 7.7, and 7.8, the intensity of the D band was slightly higher in the doped samples compared to their non-doped counterparts. This increase in D-band intensity suggests that the doping process induces additional structural disorder within the graphene lattice. Such disorder could arise from the incorporation of silver nanoparticles or from localized changes in the graphene network during the reduction process.

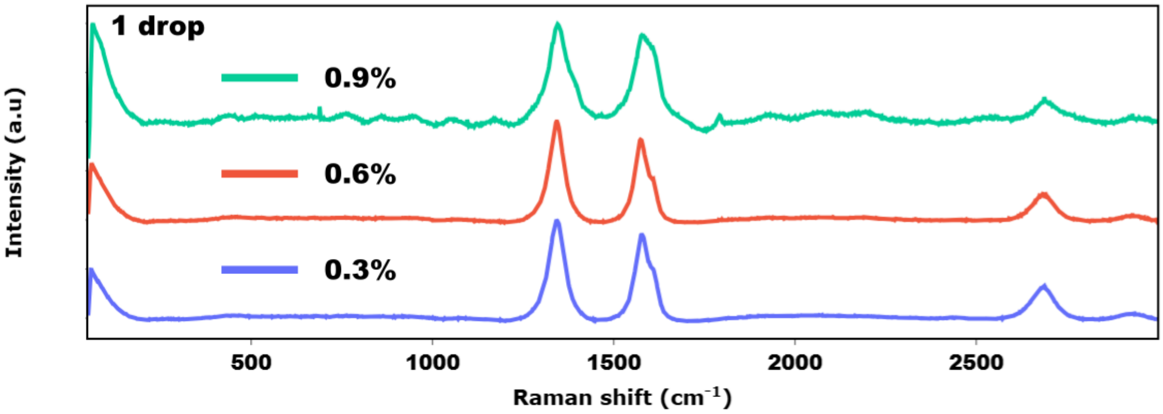

Figure 7.6: Raman spectra of LIG samples doped with one drop of $AgNO_3$ and reduced at various laser powers.

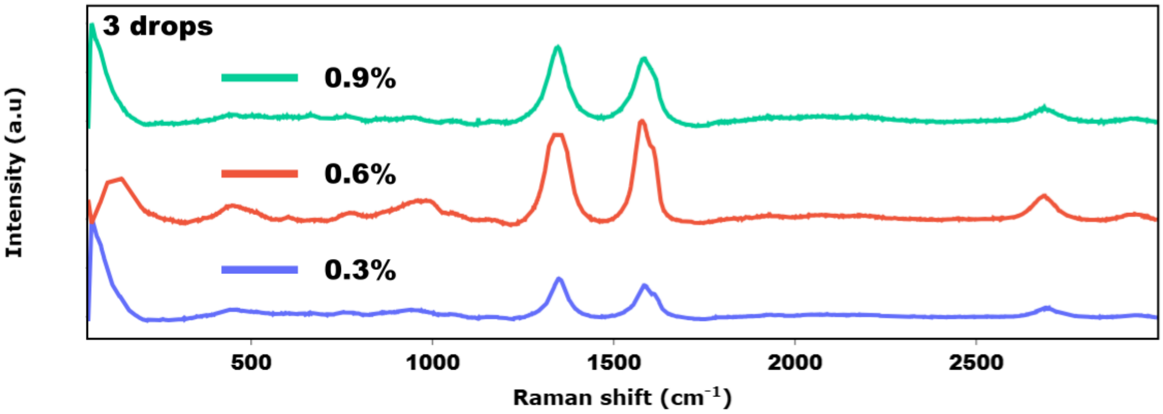

Figure 7.7: Raman spectra of LIG samples doped with three drops of $AgNO_3$ and reduced at various laser powers.

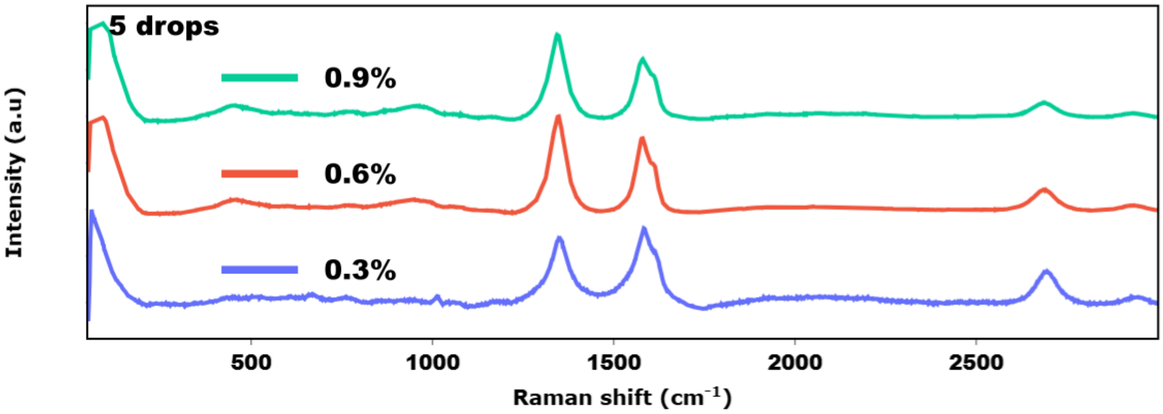

Figure 7.8: Raman spectra of LIG samples doped with five drops of $AgNO_3$ and reduced at various laser powers.

Notably, the laser power used to reduce $AgNO_3$ did not significantly alter the Raman spectra, as evident from the consistent peak positions and relative intensities across different laser settings. This observation implies that the reduction process does not affect the overall graphitic structure of the LIG or the degree of disorder introduced during doping.

An additional peak at lower wavenumbers was detected in the Raman spectra of the doped samples, as highlighted in Figures 7.6, 7.7, and 7.8. This peak is attributed to the presence of silver nanoparticles, suggesting their successful incorporation into the LIG matrix. However, further investigation is necessary to conclusively determine whether this peak arises from reduced silver or residual $AgNO_3$.

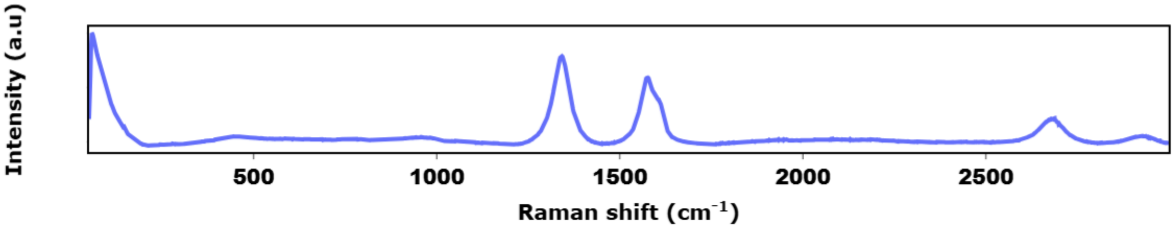

Figure 7.9: Raman spectra of LIG samples doped with one drop of $AgNO_3$ but not reduced using the laser. The additional peak at lower wavenumbers is still observed.

To validate this hypothesis, additional experiments were conducted on LIG samples doped with $AgNO_3$ but without laser reduction. These samples also exhibited the additional peak at lower wavenumbers, as shown in Figure 7.9. This suggests that the observed peak is not solely indicative of reduced silver nanoparticles but may also arise from residual $AgNO_3$. Comprehensive analysis, including complementary techniques is recommended to confirm the chemical state of silver in the doped samples.

Overall, the Raman spectroscopy results highlight the stability of the LIG structure during doping and the need for further studies to fully understand the role of laser reduction in the incorporation of silver nanoparticles.

7.3.3.2 Scanning Electron Microscopy

SEM was employed to investigate the surface morphology of the doped LIG samples and assess the dispersion of silver nanoparticles. The SEM images, shown in Figure 7.10, revealed that the surface morphology of the doped LIG closely resembles that of the bare LIG. No substantial clusters or aggregates of silver nanoparticles were observed across the samples.

This observation suggests that the silver nanoparticles are well-dispersed within the LIG network, maintaining the integrity of the surface morphology. Maintaining a consistent surface morphology is critical, as large aggregates of silver could disrupt the uniformity of the LIG network and compromise its electromechanical properties.

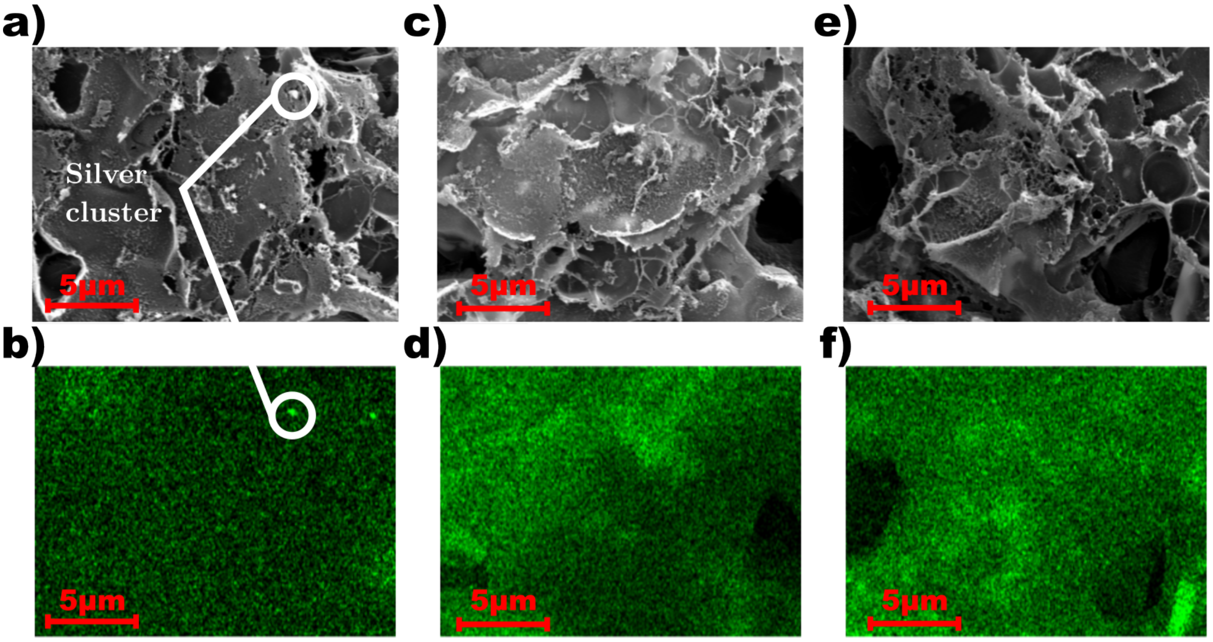

Figure 7.10: SEM images of doped LIG samples. a-b) Doped with one drop of $AgNO_3$; c-d) Doped with five drops of $AgNO_3$; e-f) Doped with one drop of $AgNO_3$ but not reduced using a laser.

Furthermore, SEM imaging of the sample doped with $AgNO_3$ but not reduced by laser (Figure 7.10 e-f) also revealed no visible aggregation of silver particles. This suggests that the distribution of silver remains homogeneous regardless of the laser reduction process. However, a more detailed analysis is required to understand the nanoscale distribution and interaction of silver within the LIG matrix.

7.3.3.3 Energy-Dispersive X-ray Spectroscopy (EDX)

To complement the SEM imaging and provide quantitative insights into the elemental composition of the doped LIG, EDX was conducted. The EDX data, presented in Figure 7.11, confirmed the presence of silver in the doped samples. Silver was found to be uniformly distributed across the surface, indicating successful doping and effective dispersion of silver nanoparticles throughout the LIG network.

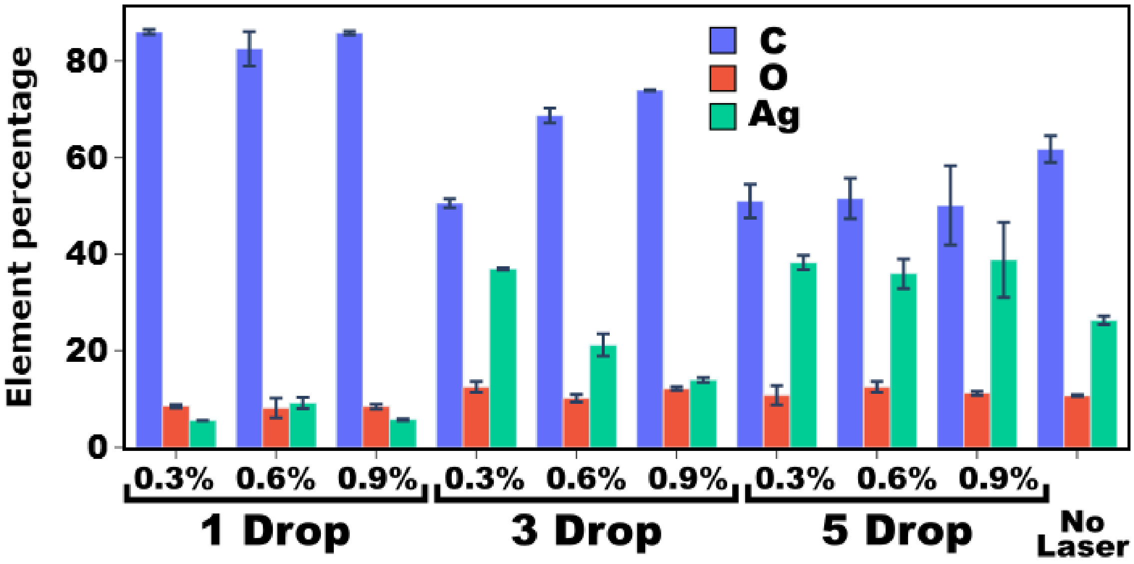

Figure 7.11: EDX analysis showing the elemental composition of Carbon, Oxygen, and Silver in the doped LIG samples.

Quantitative analysis of the EDX data revealed an increase in silver content with the number of $AgNO_3$ drops deposited on the LIG surface. Samples doped with five drops of $AgNO_3$ exhibited a significantly higher silver content compared to those doped with a single drop. This finding confirms that the amount of $AgNO_3$ deposited directly correlates with the silver content of the LIG.

Interestingly, the EDX data showed that the silver content in the samples subjected to laser reduction was slightly lower than in the samples where $AgNO_3$ was not reduced (e.g., Figure 7.11). This reduction in silver content could suggest a modification introduced by the laser reduction process, potentially involving partial ablation or evaporation of silver during the laser pass.

Moreover, variations in the laser power used during the reduction process did not appear to significantly affect the overall silver content. This suggests that the reduction process primarily influences the chemical state of silver rather than its bulk concentration. However, it is important to note that EDX cannot distinguish between different elemental states of silver (e.g., metallic silver versus ionic silver).

In summary, the combined SEM and EDX analyses confirm that the doping process effectively incorporates silver into the LIG structure while maintaining a uniform distribution and consistent surface morphology. However, further characterization is needed to fully understand the interaction between silver and the LIG matrix, particularly at the nanoscale and chemical level.

7.3.3.4 X-ray Photoelectron Spectroscopy (XPS)

XPS was utilized to investigate the chemical states of silver in the doped LIG samples and confirm its reduction to elemental silver. XPS provides critical insights into the surface chemistry, enabling the identification of elemental compositions and bonding states.

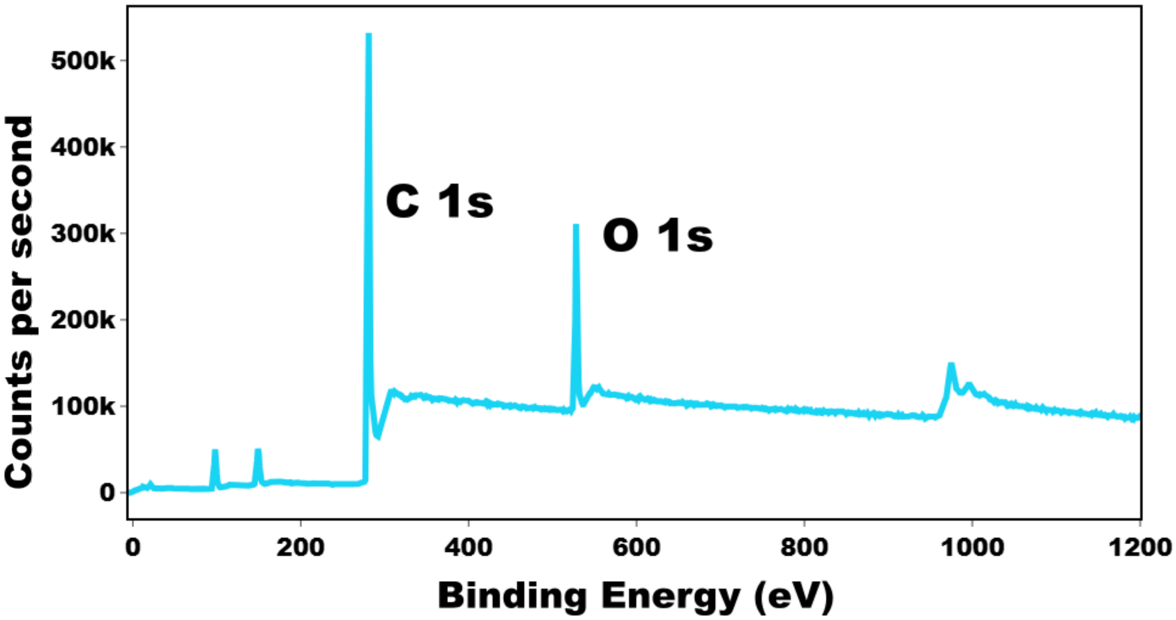

Figure 7.12: XPS spectra of a pristine LIG sample, highlighting the Carbon 1s (~284 eV) and Oxygen 1s (~533 eV) peaks.

Figure 7.12 shows the XPS spectra of a pristine LIG sample, which exhibits two prominent peaks corresponding to Carbon 1s (~284 eV) and Oxygen 1s (~533 eV). These peaks are characteristic of the graphene structure and oxygen-containing functional groups typically present in LIG.

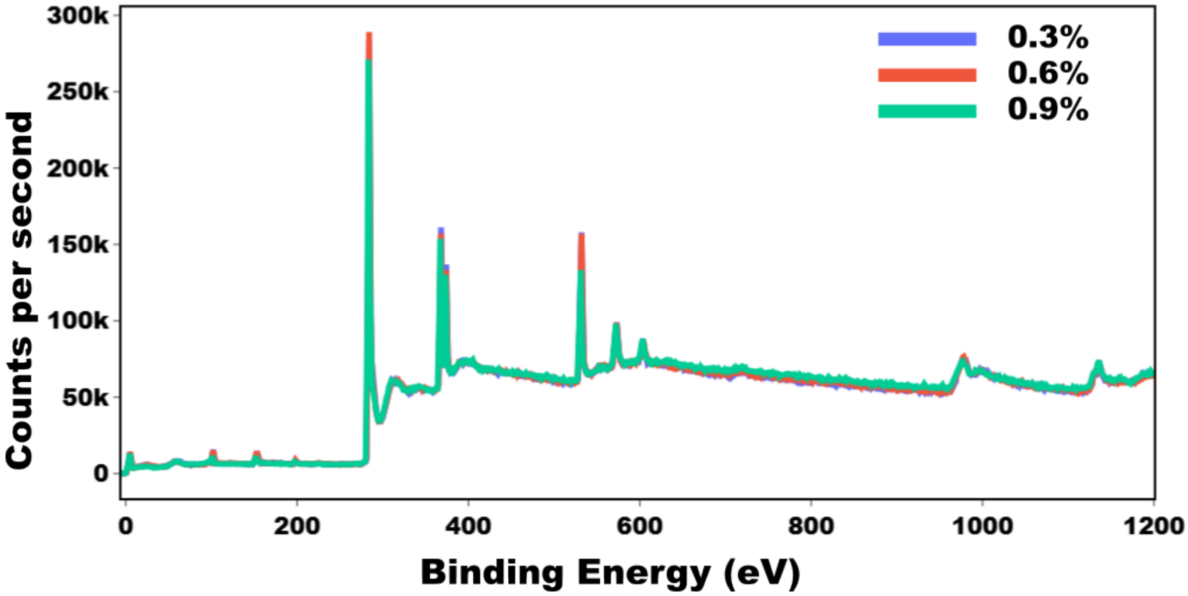

Figure 7.13: XPS spectra of LIG samples doped with one drop of $AgNO_3$ and reduced at different laser powers.

To evaluate the impact of laser reduction power on the chemical structure of the surface, XPS spectra of samples doped with one drop of $AgNO_3$ were analysed. As shown in Figure 7.13, all traces are nearly superimposed, indicating that the laser power does not significantly alter the chemical states of the surface. This suggests that the reduction process is robust across a range of laser powers, and the chemical composition remains consistent.

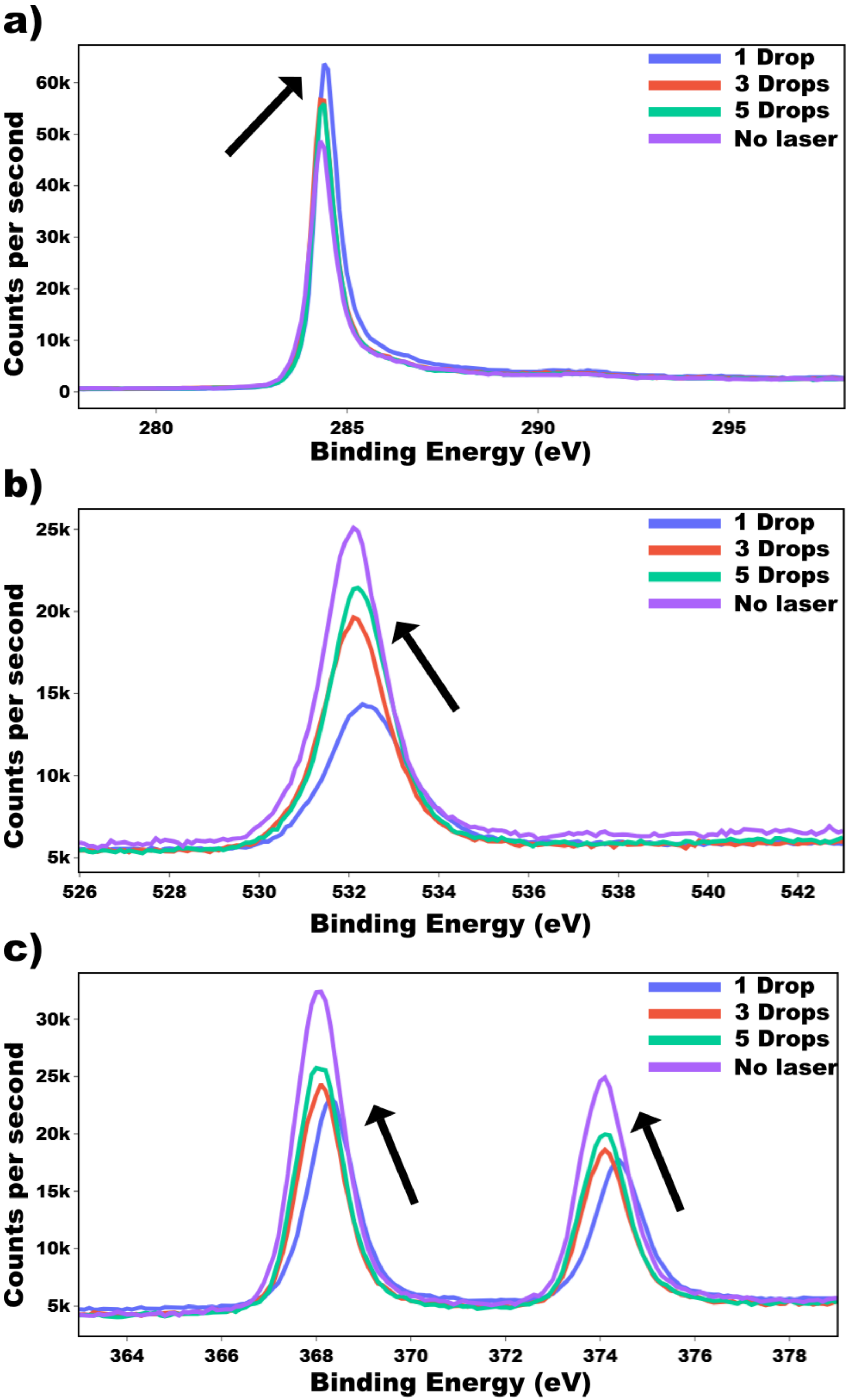
a)
Counts per second
60k
50k
40k
30k
20k
10k
0
280
285
290
295
Binding Energy (eV)
1 Drop
3 Drops
5 Drops
No laser
b)
Counts per second
25k
20k
15k
10k
5k
526
528
530
532
534
536
538
540
542
Binding Energy (eV)
1 Drop
3 Drops
5 Drops
No laser
c)
Counts per second
30k
25k
20k
15k
10k
5k
364
366
368
370
372
374
376
378
Binding Energy (eV)
1 Drop
3 Drops
5 Drops
No laser

Detailed XPS analysis of specific binding energy regions is presented in Figure 7.14. The Carbon 1s and Oxygen 1s peaks (Figure 7.14a and 7.14b, respectively) show a consistent shift toward lower binding energies with an increasing amount of $AgNO_3$ deposited. The shift in the Oxygen 1s peak can be attributed to the formation of Ag-O bonds, as metal oxides typically exhibit binding energies around ~529 eV.

In the Ag 3d region (Figure 7.14c), a similar shift is observed. However, according to Ferraria et al. [198], $AgNO_3$ exhibits a higher binding energy than elemental silver. While the expected shift would indicate a reduction to metallic silver, the observed trend is in the opposite direction, raising questions about the interplay between the deposited silver nitrate and the LIG matrix. This anomaly warrants further investigation to elucidate the precise mechanism of silver reduction.

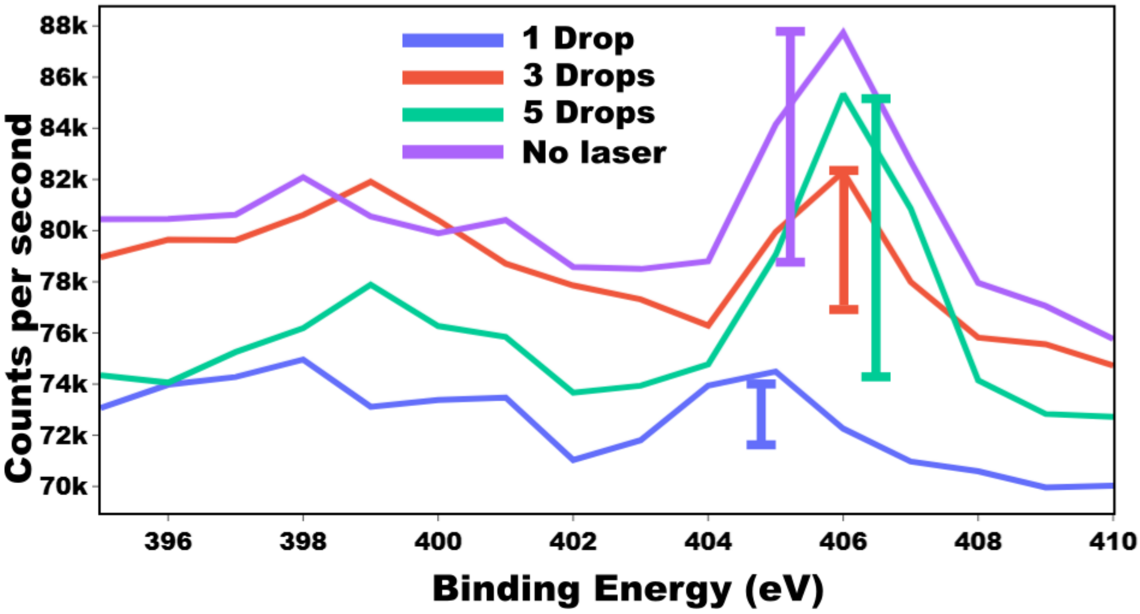

Figure 7.15: XPS spectra highlighting the Nitrogen 1s (~400 eV) peak for samples doped with varying amounts of $AgNO_3$.

The Nitrogen 1s peak (~400 eV) was also examined to assess the fate of $AgNO_3$ during laser reduction. As shown in Figure 7.15, the intensity of the Nitrogen 1s peak increases with additional $AgNO_3$ deposition but is significantly reduced when the sample is subjected to laser reduction. This suggests that with each laser pass, a fraction of $AgNO_3$ is converted to elemental silver, as evidenced by the diminishing Nitrogen 1s signal. However, with increasing amounts of $AgNO_3$, unconverted nitrate persists, resulting in a gradual increase in peak intensity.

The combined findings from XPS analyses provide valuable insights into the chemical states and interactions of silver within the LIG network:

- The reduction of $AgNO_3$ to elemental silver is supported by the decrease in Nitrogen 1s signal intensity post-laser reduction.

- Shifts in the Oxygen 1s and Ag 3d peaks suggest the formation of Ag-O bonds and highlight complexities in the reduction process.
- The laser reduction power does not significantly impact the chemical composition, indicating a robust reduction mechanism.
- Anomalies in peak shifts for the Ag 3d region underline the need for further studies, potentially involving complementary techniques such as Transmission electron microscopy (TEM) or advanced XPS analysis.

7.3.3.5 Temperature Sensitivity

As discussed in a previous study, LIG exhibits a negative TCR, indicating that its electrical resistance decreases as temperature increases. This behaviour is contrasted by the positive TCR of solid silver, which increases its resistance with temperature. This discrepancy between LIG and silver motivates the investigation of the temperature response of LIG-silver composites. Figure 7.16 shows the temperature dependence of the electrical resistance for LIG produced from thin PI films. The observed negative TCR in LIG aligns with the findings presented in Section 4.2, reinforcing the consistency of the material's behaviour across different experimental setups.

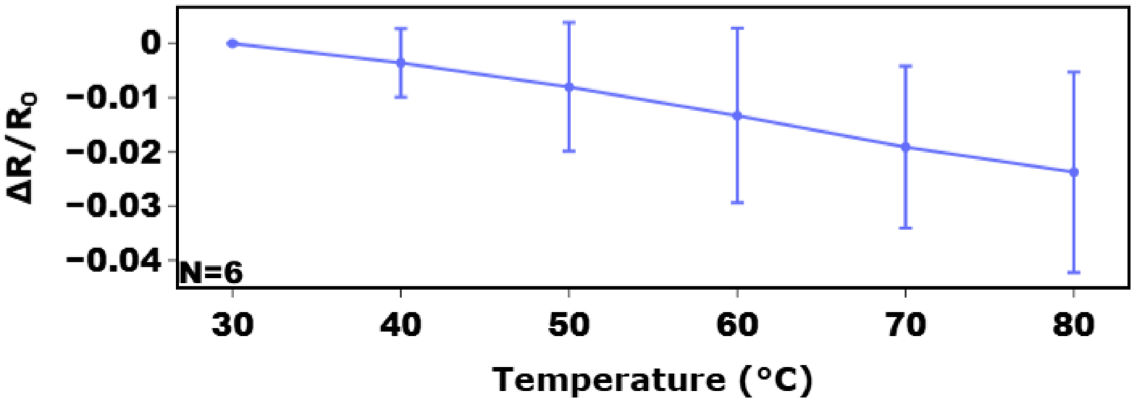

Figure 7.16: Electrical resistance of LIG prepared on thin PI films as a function of temperature, showing a negative TCR.

In Figure 7.17, the electrical resistance of LIG samples doped with $AgNO_3$ is presented. The samples were subjected to a second laser pass with varying power settings. The data indicates a slight increase in TCR after doping, suggesting that the introduction of silver into the LIG network influences its temperature sensitivity. This effect is consistent with the known positive TCR behaviour of silver, which may enhance the overall temperature response of the composite material.

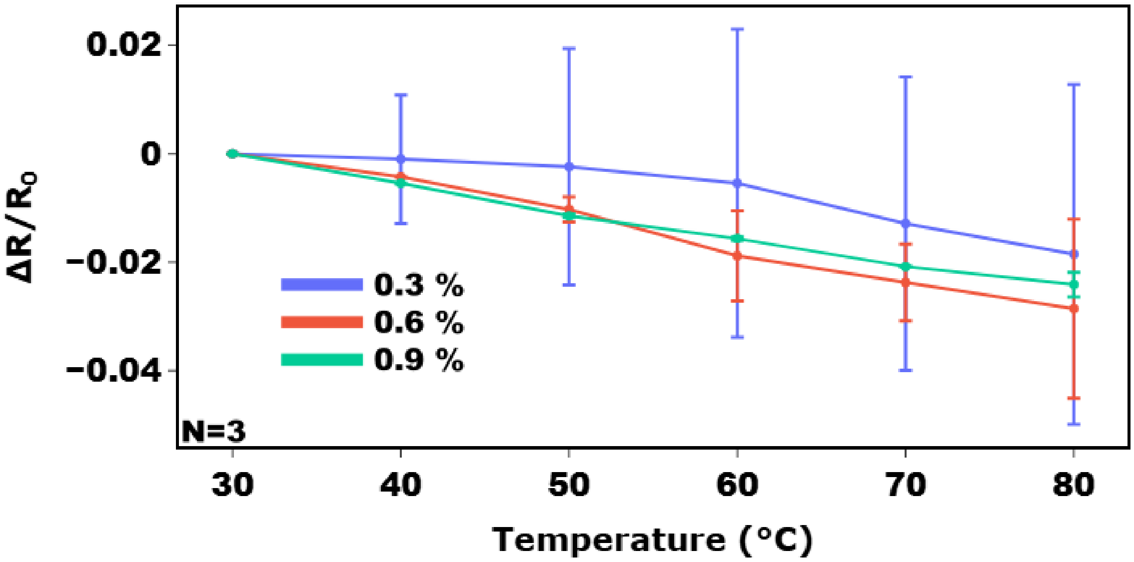

Figure 7.17: Electrical resistance of doped LIG samples as a function of temperature, showing an increase in TCR compared to the bare LIG.

7.4 Silver Nanowire Doping of LIG

In this section, we discuss the thermoelectrical characterization of LIG doped with silver nanowires (Ag-NWs). The addition of Ag-NWs to LIG is expected to significantly influence the electrical and thermal properties of the composite material, given the conductive nature of the silver nanowires.

7.4.1 Fabrication

Following the nanowires synthesis [1], the Ag-NWs were drop-casted onto the surface of the LIG, which had been previously treated to enhance its wettability, as outlined in Chapter 6. This surface modification was essential to promote uniform dispersion and effective penetration of the nanowires within the porous LIG structure, thereby facilitating more efficient doping.

---

[1] The silver nanowires used for doping the LIG nanocomposites were synthesized in collaboration with Dr. Selamneni.

The incorporation of Ag-NWs into the graphene network is expected to improve both electrical conductivity and thermal response by forming additional conductive pathways and enhancing heat dissipation across the composite. Representative Field Emission Scanning Electron Microscopy (FESEM) images of the synthesized silver nanowires deposited on an Indium Tin Oxide (ITO) substrate are presented in Figure 7.18. These images [2] illustrate the morphology and network-like structure of the nanowires at various magnifications.

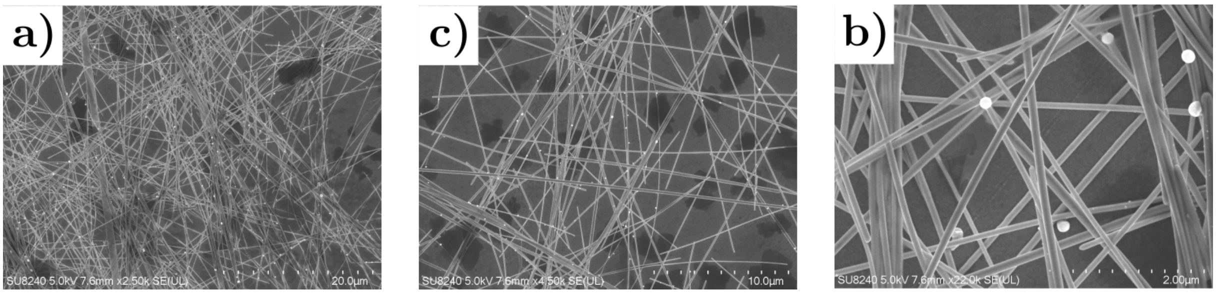

Figure 7.18: FESEM images of silver nanowires on an ITO substrate at different magnifications: a) 2.5k, b) 4.5k, and c) 22k.

7.4.2 Characterization

Electrothermal Characterization

The electrothermal properties of the LIG samples doped with Ag-NWs were characterized to investigate how the doping process affects the material's response to temperature. Figure 7.19 presents the electrothermal behaviour of the doped samples. A positive TCR was observed for the Ag-NWs doped LIG, which is consistent with the metallic electronic structure of silver nanowires. This positive TCR indicates that the resistance of the doped LIG increases with temperature, as expected from the metallic conductivity of silver. The incorporation of Ag-NWs enhances the composite's ability to respond to temperature changes, offering a more pronounced thermal sensitivity compared to pure LIG. This behaviour suggests that silver nanowires can be a valuable dopant for tuning the thermoelectrical properties of LIG for specific applications.

---

[2] provided by Dr. Selamneni

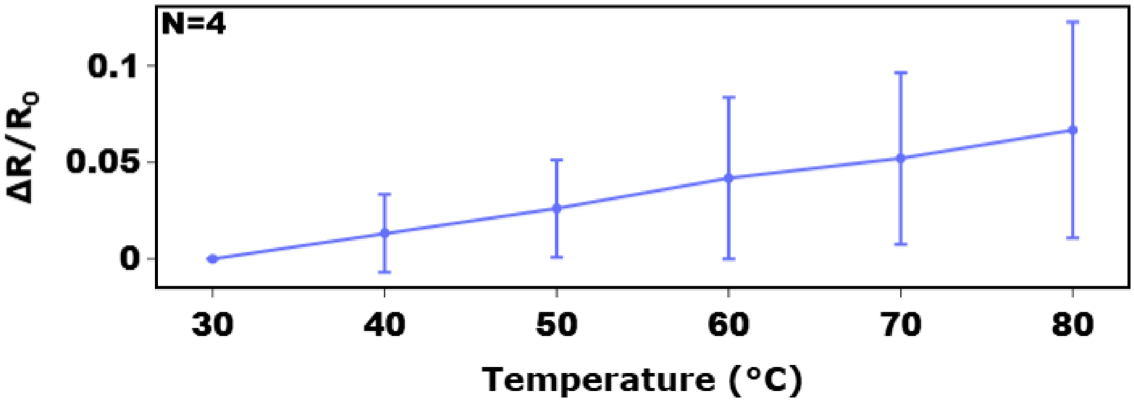

Figure 7.19: Electrothermal characterization of Ag-NWs doped LIG samples, showing a positive TCR, consistent with the metallic nature of silver nanowires.

7.5 Conclusion

This chapter has explored various approaches to doping LIG with metal oxides and nanoparticles, providing a comprehensive overview of how these modifications can significantly enhance the properties and performance of LIG-based sensors. Through both pre- and post-synthesis doping methods, the potential of silver nitrate and silver nanowires to improve the sensitivity, selectivity, and conductivity of LIG has been investigated. These doping strategies not only enhance the charge transfer mechanisms and catalytic properties of LIG but also introduce new functionalities, such as localized surface plasmon resonance (LSPR) effects, making LIG sensors more versatile for a range of applications, from environmental monitoring to dual-mode sensing (although not explored in this study).

The different modification routes, including altering the graphene precursor before laser processing or introducing modifications after graphene synthesis, offer distinct advantages. Pre-synthesis modification allows for the direct incorporation of modifying agents into the precursor material, which can result in enhanced properties such as increased conductivity or mechanical strength. Post-synthesis modification, on the other hand, enables fine-tuning of the LIG's properties through careful control of laser parameters and the introduction of functional agents, facilitating precise adjustments to meet the specific requirements of various applications.

While this initial investigation demonstrates the potential of doping techniques to tailor LIG properties, it also highlights several challenges. Attempts to transfer doped LIG onto soft substrates were unsuccessful, indicating that further optimization is required to ensure reliable adhesion and functional integrity on flexible supports, an essential step for practical wearable and deformable sensor applications. Moreover, the Raman analysis revealed an increase in structural disorder following doping, which is expected to influence the strain response and potentially compromise the electromechanical stability of the material.

Overall, this study underscores both the opportunities and limitations of metal-based doping for LIG modification. Although it provides valuable insight into the tunability of LIG through nanoparticle incorporation, the difficulty in achieving consistent material quality and structural control suggests that this approach may not be the most reliable pathway toward environmentally stable sensors. The following chapter will build upon the work presented here to explore the potential applications of LIG nanocomposites in real-world scenarios.

Chapter 8

Applications

8.1 Introduction

The versatility of LIG nanocomposites has led to their exploration in a variety of cutting-edge applications. The unique combination of mechanical flexibility, electrical conductivity, and responsiveness to deformation makes LIG-based materials particularly well-suited for advanced sensor systems, especially in fields requiring lightweight, durable, and highly sensitive materials.

One of the most promising domains for LIG nanocomposites is body motion monitoring, where their ability to conform to irregular surfaces and respond accurately to subtle mechanical deformations positions them as ideal candidates for wearable sensors. In applications like healthcare, these sensors can be integrated into wearable devices to monitor respiration patterns, joint movements, and other physiological parameters, providing real-time feedback that can improve patient monitoring, rehabilitation, and diagnostics.

In addition to healthcare, LIG nanocomposites are being increasingly integrated into soft robotics, where their flexibility and electromechanical properties enable the creation of soft grippers and actuators. These soft robotic devices can perform delicate tasks with precise control, essential for handling fragile objects or navigating complex environments. The development of such LIG-based systems is paving the way for innovations in automation, prosthetics, and industrial processes where adaptability and gentle handling are crucial.

The following sections will detail the use of LIG nanocomposites across these applications.

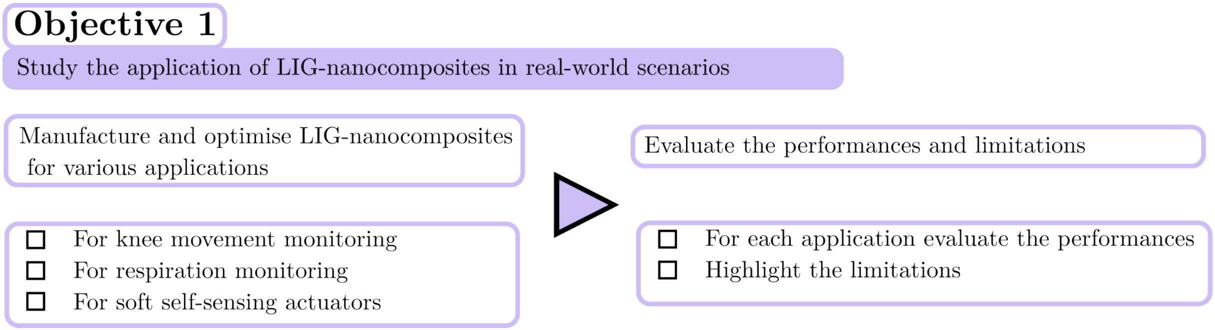

Figure 8.1: Chapter 8 Objectives Flowchart

8.2 Body Movement Monitoring

To assess the effectiveness of LIG nanocomposites for body movement monitoring, a wireless communication system was employed as detailed in Section 3.7. Two LIG sensors were integrated with an ESP32 microcontroller to enable continuous data transmission via Bluetooth to a mobile application developed using MIT App Inventor. This configuration allowed for real-time monitoring and analysis of sensor data, demonstrating the system's potential for practical applications in gait and movement analysis.

The sensors were affixed to a lightweight, flexible fabric using PDMS, ensuring both comfort and durability during use. This assembly was securely wrapped around the legs of test subjects, as shown in Figure 8.2a. The design minimized interference with the subjects' activities, allowing natural movement while maintaining consistent sensor placement. This unobtrusive design was critical in ensuring that the data collected reflected real movement patterns rather than artifacts from the monitoring process.

Test subjects performed a series of controlled tasks, including walking, squatting, jogging, and climbing stairs. The sensors captured dynamic changes in resistance corresponding to these activities, and the data was transmitted in real time to the mobile application for visualization and analysis. Figure 8.2b illustrates representative resistance profiles for these movements, highlighting the sensor's ability to detect and distinguish between different activity types.

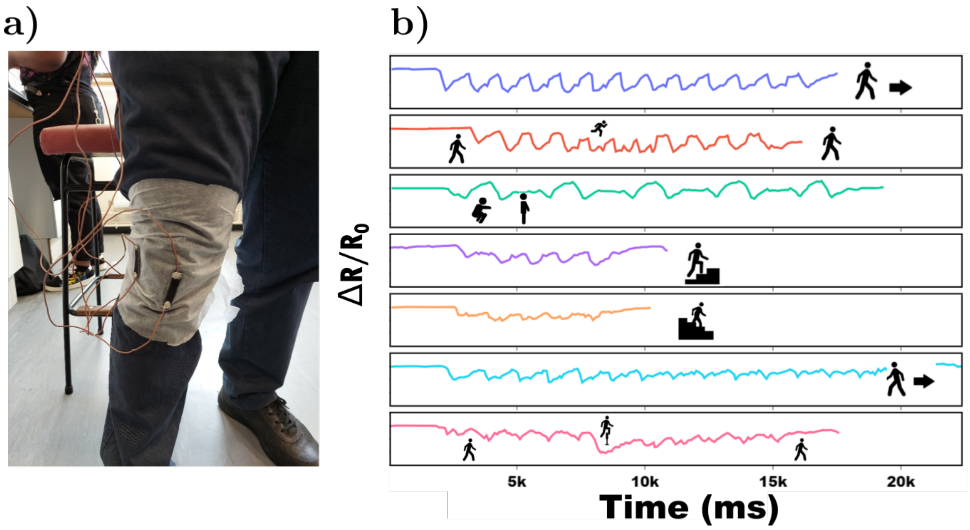

Figure 8.2: a) Sensors attached to a medical bandage and applied to a knee; b) Resistance data transmitted over Bluetooth for various movements.

Although the system effectively tracked simpler movements such as walking and squatting, it struggled with more complex activities such as climbing stairs. These challenges were primarily attributed to increased variability in sensor response due to factors such as body morphology, gait differences, and sensor placement.

8.2.1 Variability Across Individuals

Data collected during normal walking revealed significant differences between individuals, as shown in Figure 8.3. This variability can be attributed to factors such as leg length, stride dynamics, muscle distribution, and body weight. For instance, individuals with shorter strides produced resistance signals with lower amplitude and frequency compared to those with longer strides. Additionally, variations in walking styles altered the strain distribution on the sensor, resulting in diverse resistance profiles.

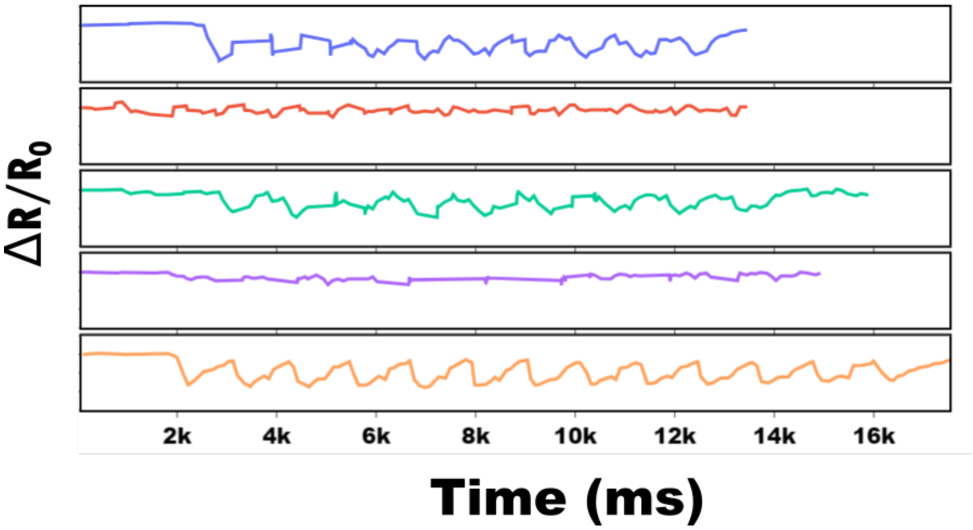

Figure 8.3: Resistance data for different individuals during normal walking.

These discrepancies highlight the limitations of the current system when applied to a diverse population. The lack of a universal calibration mechanism complicates comparative gait analysis, as the sensor outputs are inherently dependent on individual anatomy and movement patterns. This variability underscores the need for further refinement to ensure the device's reliability across different users.

8.2.2 Influence of Sensor Placement

The accuracy of resistance measurements was found to depend heavily on sensor placement. Figure 8.4 illustrates how improper positioning, such as placing the sensor too loosely, at an inconsistent angle, or over areas of high mobility, can lead to distorted readings and noisy data. Conversely, when the sensor was tightly secured and aligned with the primary axis of motion, the resistance signals were cleaner and more consistent.

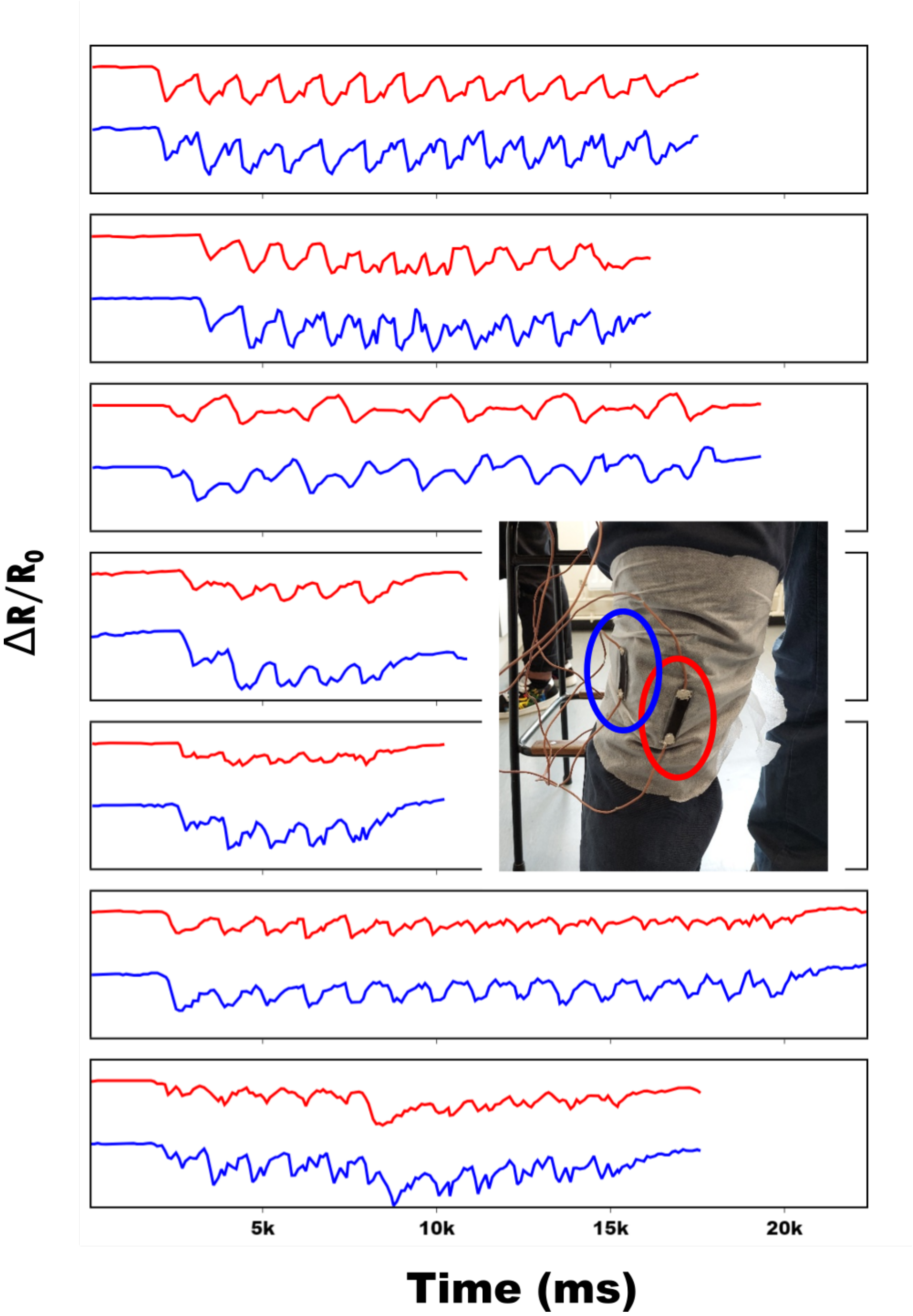

Figure 8.4: Influence of sensor placement on resistance data for gait monitoring.

Misalignment or suboptimal positioning can alter the baseline resistance or introduce excessive noise, as evidenced in Figure 8.4. These issues highlight the need for standardized placement procedures to minimize user-dependent variability and ensure repeatable measurements. This is particularly critical for applications requiring high precision, such as clinical gait analysis or athletic performance monitoring.

8.2.3 Future Directions and Challenges

The findings from Figures 8.2, 8.3, and 8.4 underscore both the potential and the challenges of LIG-based wearable sensors for movement monitoring. The system demonstrates clear utility in capturing basic motion patterns, but several limitations remain:

- **Calibration Across Individuals:** The device's performance varies significantly across users, necessitating the development of adaptive calibration algorithms tailored to individual anatomy and gait patterns.
- **Sensor Placement Sensitivity:** Accurate and consistent placement is crucial for reliable data acquisition, but practical challenges in real-world scenarios often lead to suboptimal positioning. While advanced software algorithms or machine learning models could theoretically compensate for placement variations or individual anatomical differences, such computational approaches impose significant trade-offs. On-board processing would substantially reduce battery life due to increased power consumption, whereas offloading computation to an external device would require continuous data transmission—itself a battery-intensive operation. Therefore, optimizing sensor placement and hardware design remains critical for practical, energy-efficient wearable applications.
- **Complex Activity Detection:** While the sensor performs well for simpler tasks, it struggles to detect and differentiate more complex movements, such as stair climbing or rapid directional changes.

In conclusion, LIG-based sensors offer significant promise for wearable movement monitoring. However, achieving consistent, reliable performance across diverse individuals and activities will require further innovation in both sensor design and system integration, with careful consideration of the balance between algorithmic sophistication and energy efficiency.

8.3 Respiration monitoring LIG strain sensors

This research focuses on the innovative application of soft strain sensors for real-time monitoring of respiration. The soft strain sensors are designed to detect the subtle mechanical deformations of the skin caused by breathing when placed on the chest or abdomen. By measuring changes in electrical resistance corresponding to these deformations, the sensors provide a non-invasive and continuous method for tracking respiratory patterns and rates. This capability is vital for identifying transient respiratory anomalies that may signal the onset of an overdose or an asthma attack, thus enabling timely and potentially life-saving intervention.

To be effective in breathing monitoring, the soft strain sensors must meet several critical performance criteria. High sensitivity is paramount, as it allows the sensors to detect even the smallest mechanical deformations associated with breathing. Additionally, minimizing hysteresis is essential to ensure that the sensors can accurately track rapid changes in respiratory cycles without introducing significant lag or error. Linearity is another key requirement, as a linear response facilitates straightforward calibration and improves the accuracy of subsequent signal processing. Equally important is the reproducibility of sensor performance. Sensors fabricated under identical conditions must exhibit consistent behaviour, especially in clinical environments where multiple sensors may be deployed simultaneously for real-time patient monitoring.

In summary, this section discusses the development and optimization of soft strain sensors utilizing LIG-Ecoflex composites, with a focus on their application in healthcare monitoring, particularly for breathing monitoring. The integration of high sensitivity, linearity, and reproducibility, combined with the precision and scalability of laser manufacturing, underscores the potential of these LIG-based sensors as a reliable solution for real-time respiratory monitoring.

8.3.1 Breathing Detection

Conventional respiratory monitoring systems often rely on bulky wraparound devices that encircle the torso, which can be uncomfortable and intrusive for users. To address these limitations, our goal was to create a more discreet and user-friendly alternative by integrating the developed soft sensors into two innovative configurations.

The first approach involved directly affixing the sensors onto the skin using medical-grade sports tape, offering a secure yet minimally invasive solution. The second approach embedded the sensors into a base-layer T-shirt, ensuring both comfort and seamless integration for continuous, unobtrusive monitoring.

This section evaluates the performance and practicality of both methods, highlighting their potential applications in real-time respiratory monitoring.

8.3.1.1 Sports Tape Approach

To evaluate the feasibility of using our sensors for respiration monitoring, we conducted a preliminary test on a healthy volunteer. This initial trial was instrumental in identifying two primary challenges: the need to minimize parasitic body movements and reduce sensor hysteresis. These issues are critical for ensuring accurate, consistent respiratory measurements, especially in dynamic conditions. Consequently, several design improvements were implemented to optimize sensor performance. These refinements included re-engineering the bandage structure and reducing the overall dimensions of the sensor, as depicted in Figure 8.5.

Figure 8.5 A highlights the design modifications applied to the bandages, such as reducing their length and width, eliminating the base layer of the bandage, and incorporating a layer of dental polymer (orange layer). The dental polymer was chosen for its rigidity relative to the softer Ecoflex material, as it helps prevent motion artifacts from propagating to the sensor, thus enhancing measurement accuracy. A commercially available, medical-grade sports bandage was selected for its strong adhesive properties, negating the need to wrap the bandage around the entire torso while maintaining a neat and unobtrusive design. In Figure 8.5 B, the comparison between the original (50 mm x 8 mm) and the optimized (30 mm x 8 mm) sensor demonstrates the shift toward a smaller, more compact sensor. These adjustments were intended to suppress signal noise and hysteresis without compromising sensor sensitivity or linearity, aspects further explored in subsequent sections of this report.

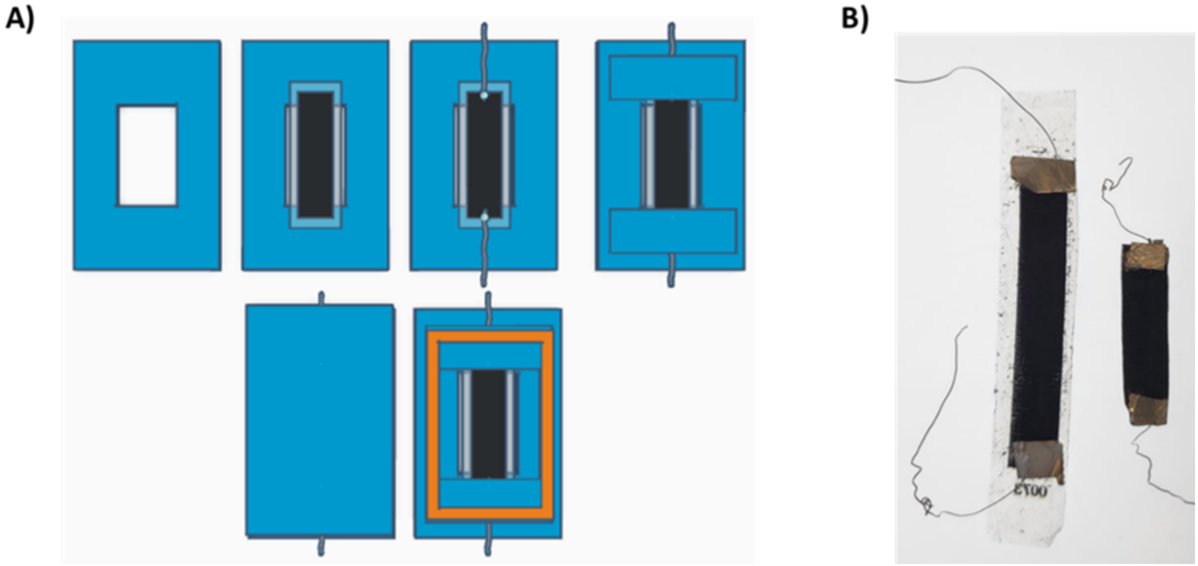

Figure 8.5: a) Design modifications applied to the bandage, including the use of dental polymer; b) Size comparison between the original and reduced sensors.

Following the redesign, additional tests were performed to validate the effectiveness of the new bandages for respiratory monitoring, as shown in Figure 8.6. The primary objectives were to minimize noise caused by body movements and to identify the optimal sensor placement for accurate respiration monitoring. Based on established studies, we selected three promising locations for sensor placement: (1) vertically along the right or left lower rib cage, (2) vertically approximately 4 cm to the right of the navel, and (3) horizontally between the pectoral muscles [199]. Figure 8.6 A shows these locations, while Figure 8.6 B illustrates the comparative analysis of breathing patterns obtained from each position. Our findings indicate that the sensor placement at position 1, along the rib cage, offers the most consistent and reliable results, making it the preferred location for further testing.

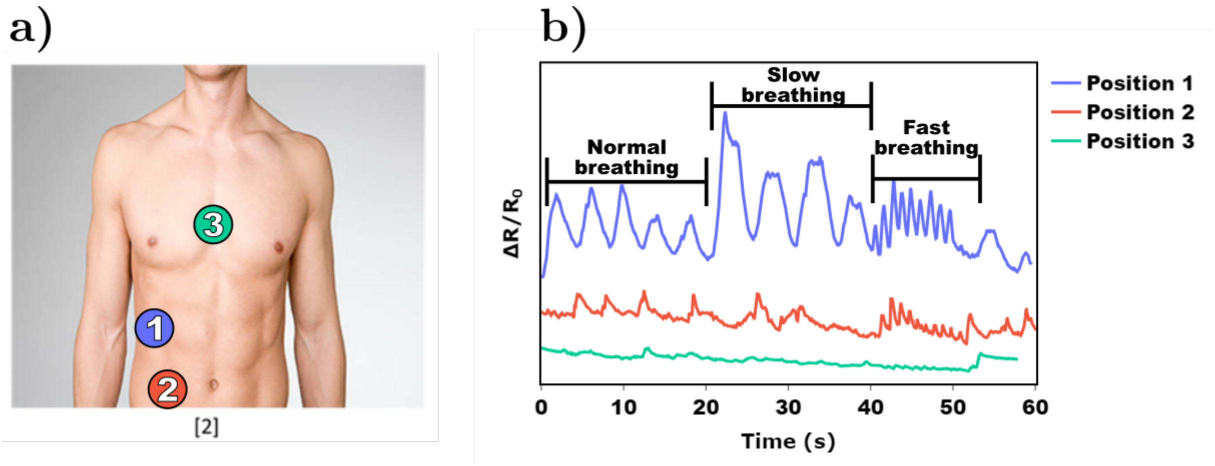

Figure 8.6: a) Sensor placement at three different locations on the torso (image adapted from [200]); b) Comparative breathing patterns recorded at each location.

Once the optimal sensor placement was determined, the focus shifted to evaluating the performance of four distinct bandage designs: (1) full sensor with the base, (2) sensor without the base, (3) sensor sandwiched between bandage layers, and (4) sensor with dental polymer applied to the edges. Normal breathing tests were performed using each design, with sensors positioned at location 1, as shown in Figure 8.7. The results demonstrate that both the sandwiched sensor and the dental polymer-enhanced sensor effectively reduce noise but at the cost of significant signal attenuation. Conversely, the sensors with and without the base exhibited strong, clear signals, making them the most promising options. Although the movement artifacts were not substantial under the conditions tested, further analysis will be required to determine the optimal design for scenarios involving greater motion, such as walking or other daily activities.

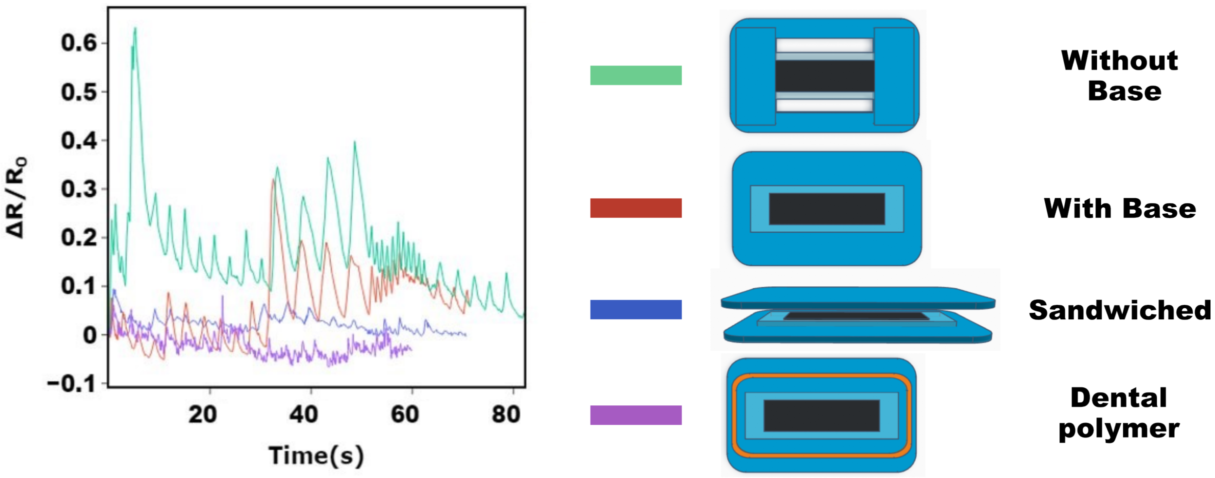

Figure 8.7: Comparison of breathing signal quality across the four different bandage designs.

8.3.1.2 T-shirt Approach

In this approach, the sensors were directly integrated into a base-layer sports T-shirt using Ecoflex elastomer (Figure 8.8A). The sensor placements corresponded to the optimal positions determined from prior experiments, ensuring reliable sensor performance during respiration monitoring. One key advantage of this method was the ability to consistently gather data from the same sensors, reducing variability associated with repeated sensor manufacturing and attachment processes. This allowed for more uniform and reproducible datasets across multiple trials.

During testing, regular breathing exercises were conducted with both sensors affixed to the T-shirt. To assess the robustness of the sensors under motion, arm movements (one arm at a time) were introduced. As seen in the left-hand graphs of Figure 8.8B, the sensors captured respiratory peaks effectively, even amidst arm motion, which induced noticeable spikes in the signal. Despite these spikes, the sensors were able to accurately track respiration from the side opposite to the moving arm, indicating a promising level of motion insensitivity. This suggests that by incorporating advanced data processing techniques, such as machine learning algorithms, it may be possible to filter out these motion-induced artifacts and further improve data quality. The frequency of peaks captured by both sensors, shown in the right-hand graphs (red), demonstrates minimal variation, highlighting the consistency and reliability of the sensors during respiration monitoring.

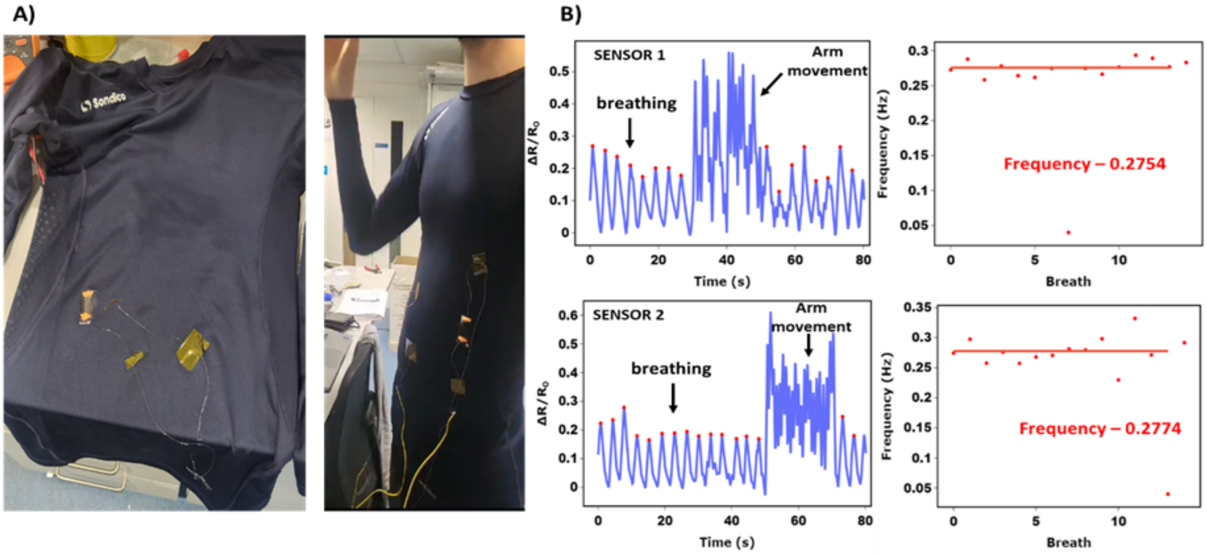

Figure 8.8: a) Two rectangular sensors attached to the base-layer T-shirt; b) Breathing analysis with two sensors, during arm movement (one at a time).

Building on the insights from these tests, circular sensors were selected as the final design due to their improved mechanical and electrical properties. To streamline data collection and enhance the system's portability, an ESP-32 was integrated into the setup. The ESP-32, equipped with both Bluetooth and Wi-Fi, was chosen for its suitability in IoT applications, enabling real-time wireless data transmission (Figure 8.9A). The chip was programmed using C# to interface with the sensors, collect respiration data, and transmit the information to an external device for analysis.

In this refined system, two circular sensors were attached to the T-shirt and connected to the ESP-32 for data acquisition, as illustrated in Figure 8.9B. The ESP-32 managed data transmission while a custom Python-based software was developed to process and visualize the captured signals. The software applied real-time filtering to remove noise and artifacts, providing a cleaner signal output and essential respiratory metrics such as breaths per minute (BPM), as shown in Figure 8.9C. This system significantly improved data clarity and user interaction, making it a promising platform for continuous respiration monitoring in various activities.

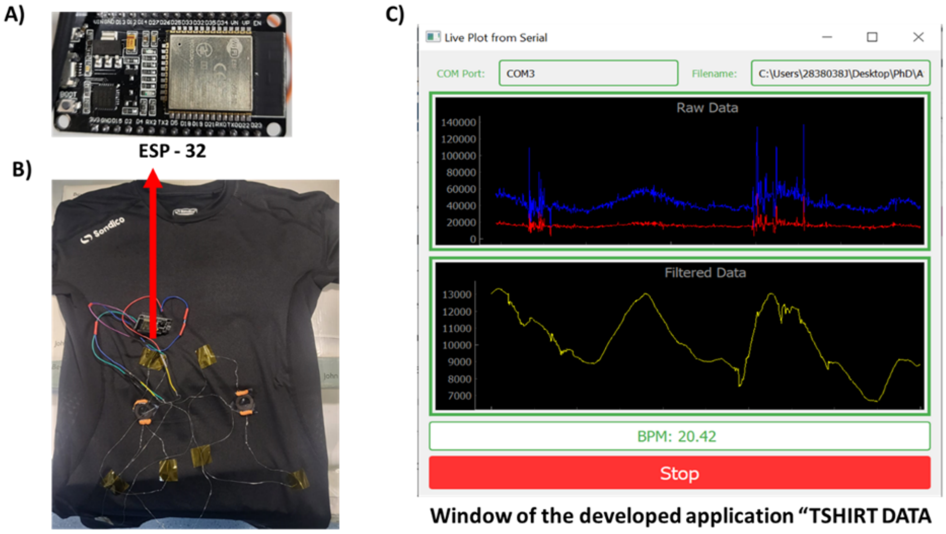

COM Port: COM3

Filename: C:\Users\2838038J\Desktop\PhD\A

BPM: 20.42

ESP - 32

Two circular sensors affixed on the T-shirt with ESP-32

Window of the developed application "TSHIRT DATA COLLECTOR" to capture the data

Figure 8.9: a) ESP-32 for data collection and wireless communication; b) T-shirt affixed with two circular sensors connected to the ESP-32; c) Custom Python program for data visualization and processing.

To validate the functionality of the system, additional trials were conducted where the redesigned T-shirt, fitted with two circular sensors, was worn by volunteers while performing various activities, including standing, sitting, walking, and typing. The data collected during these activities, displayed in Figure 8.10, presents the respiratory patterns of two healthy volunteers, each represented by different color-coded data traces. The system successfully captured respiration data during all activities, although some variation in peak amplitudes was observed between the two subjects. This variability was attributed to differences in body morphology, which influenced how well the T-shirt fit and the initial placement of the sensors on the body. Despite these minor discrepancies, the system proved to be an effective and user-friendly tool for real-time respiration monitoring, with potential applications in wearable health devices.

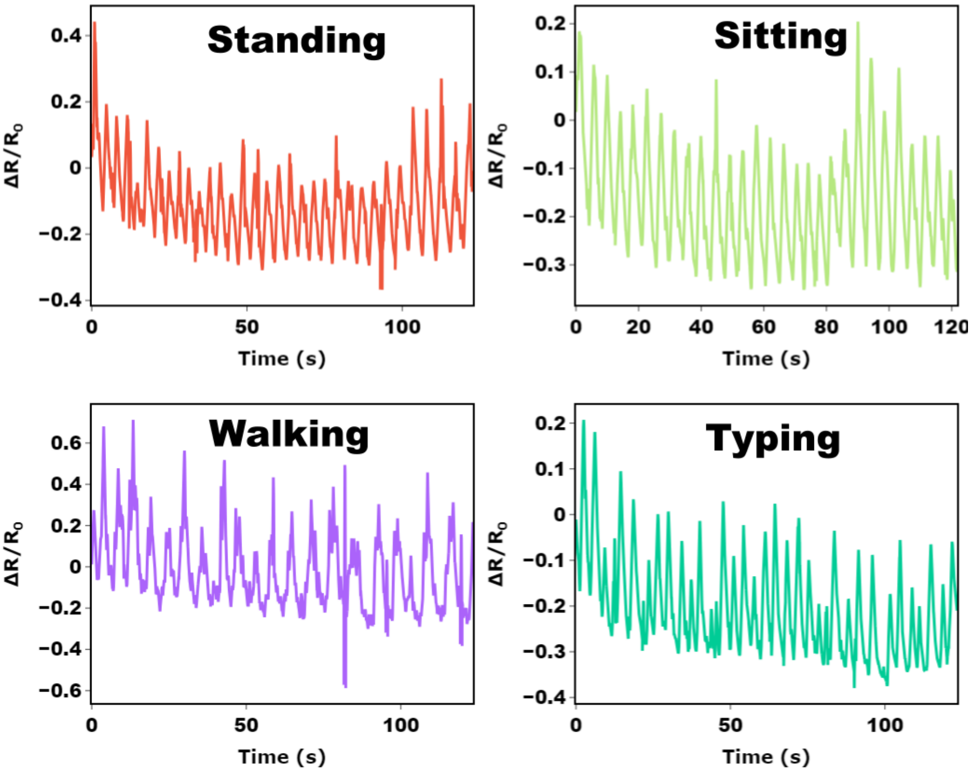

Figure 8.10: Demonstration of the respiratory monitoring system using circular sensors during different activities: sitting, typing, standing, and walking.

8.3.1.3 Data Collection and Analysis

Our sensor system was rigorously tested on a diverse cohort of individuals, which yielded significant information on the complexities of respiratory signal acquisition. The findings reveal a notable variability in signal quality, influenced by individual physiological differences and body morphology. For example, the signals acquired from some individuals exhibited excessive noise, which obscured key respiratory features and complicated the accurate analysis, as shown in Figures 8.11. In other cases, the signals were weak and lacked distinct characteristics, which presented challenges in peak detection and computation of the inter-peak interval. Saturation issues were also observed in individuals with rapid or irregular breathing patterns, where the sensors reached their signal limit, resulting in flattened waveforms.

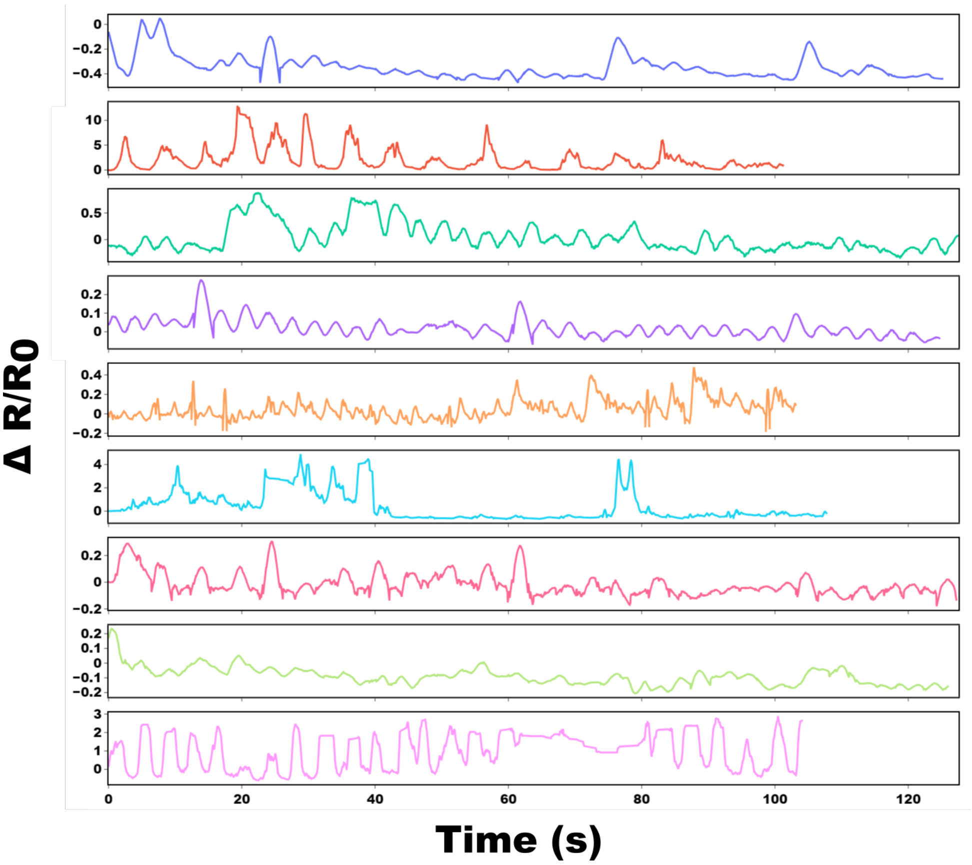

Figure 8.11: Breathing data acquired for different individuals performing the same activity using the same device.

These findings underscore the need to accommodate the wide range of respiratory behaviours encountered across different users. To address this, we have prioritized the development of adaptive algorithms capable of filtering noise, enhancing peak detection, and dynamically adjusting to user-specific variations. These algorithmic improvements aim to maintain the system's sensitivity and accuracy, even in challenging conditions. The results also emphasize the sensor system's ability to capture valuable respiratory data under strenuous scenarios, such as erratic breathing, which is critical for applications like overdose monitoring, where body movements are minimal, and detecting subtle respiration patterns is essential.

Furthermore, the diversity in body morphology among participants significantly influenced sensor performance. The sensor's response is directly affected by the degree of stretching it experiences, which varies between individuals with different body types. For thinner individuals, minimal sensor stretching results in smaller signal amplitudes, whereas larger body types cause greater strain on the sensor, yielding more pronounced signals, as illustrated in Figure 8.12. These differences require careful adjustments in sensor placement and the fit of the T-shirt to ensure optimal contact and signal fidelity. Customization of tightness and positioning is essential for capturing accurate data across a wide range of body types, further reinforcing the need for a universally applicable respiratory monitoring system.

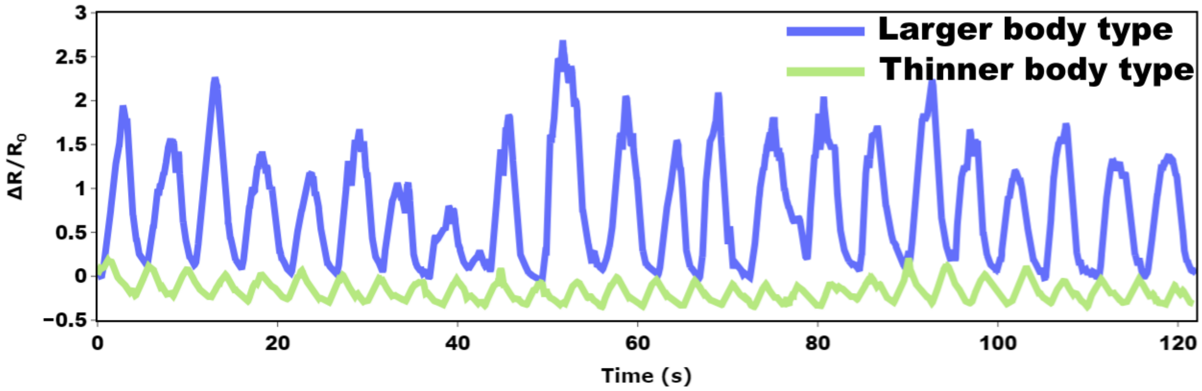

Figure 8.12: Impact of body morphology on data acquisition using the same T-shirt-based sensor system.

To address these challenges, we sought guidance from a clinical advisor whose feedback highlighted the limitations of the T-shirt-based approach due to the wide diversity in user body sizes and shapes. This consultation directed our focus toward exploring alternative methods of sensor attachment, such as medical bandages and plaster-like designs, which provide more conformal skin contact. Comparative analyses of these attachment methods revealed that a plaster-type sensor offers the highest data quality, consistently outperforming other designs in maintaining close skin contact and ensuring stable signal acquisition. Consequently, plaster-based sensor design will be a key focus in our future efforts to improve the precision and reliability of respiratory monitoring in diverse user groups.

8.4 Actuators

Soft robotics has emerged as a transformative field, offering compliant and adaptable solutions for various applications, particularly in delicate interactions and complex environments where rigid counterparts fall short. These systems often rely on soft actuators that mimic biological movements, providing inherent safety and dexterity. However, a significant challenge in the development of soft robotic systems lies in accurately monitoring their complex, often non-linear, deformations and movements. Traditional rigid sensors can compromise the very compliance that defines soft robots, while existing soft sensing solutions often face limitations in terms of durability, integration, and performance under varying environmental conditions, especially elevated temperatures.[201, 202]

Leveraging the heat-insensitive properties of LIG sensors, we developed novel electrothermal actuators, drawing inspiration from the foundational work of Wang et al. [203]. These actuators directly address the aforementioned challenges in soft robotics by exploiting the inherent thermal stability of LIG. This characteristic allows them to maintain consistent electrical resistance, and thus reliable sensing capabilities, even when subjected to elevated temperatures up to 100°C – a crucial advantage for applications where thermal fluctuations are common or even intentionally induced. The design principles behind these actuators were meticulously driven by the goal of utilizing the asymmetric thermal expansion properties of the composite materials involved, specifically PI and PDMS, to generate controlled and repeatable soft actuation. This integrated approach, combining robust actuation with inherent thermal stability and sensing potential, offers a promising pathway for advanced soft robotic systems with enhanced movement monitoring capabilities.

The elasticity moduli of PI and PDMS, denoted as E_1 and E_2, respectively, alongside their thicknesses t_1 and t_2, contribute to the overall mechanical behaviour of the actuator. The CTE of PI and PDMS is represented as α_1 and α_2. The modulus ratio (n) and thickness ratio (m) are defined as $n = \frac{E_1}{E_2}$ and $m = \frac{t_1}{t_2}$. The total thickness of the actuator is $t = t_1 + t_2$. The rolling deformation and the rolling angle induced by thermal expansion can be predicted using the following equations derived from Timoshenko's theory on thermostats [204]:

$$L = L_0(1 + \Delta T \alpha_1) \tag{8.1}$$

$$\frac{1}{\rho} = \frac{6(\alpha_2 - \alpha_1)\Delta T(1+m)^2 L}{t\left(3(1+m)^2 + (1+mn)\left(m^2 + \frac{1}{mn}\right)\right)} \tag{8.2}$$

where L_0 and L represent the initial and final lengths of the actuator, and ΔT is the temperature change.

The fabrication process of LIG-based actuators (Figure 8.13a) began with the laser scribing of LIG patterns onto a commercial PI film using the optimized laser parameters, 20% power and 7% speed. A layer of PDMS was then spin-coated onto the LIG network at 500 rpm for 5 seconds and subsequently cured at 90°C for one hour. After curing, the LIG-PDMS composite was peeled off and electrodes were applied to the ends of the LIG track. The structure was then cut to the desired dimensions, and a layer of commercial PI tape was laminated onto the PDMS.

Actuation was controlled using a DC power supply (TENMA 72-2550), with output voltage determining the actuator's deformation. When voltage was applied, the LIG experienced heating due to the Joule effect, leading to thermal expansion. The differing CTEs of PDMS and PI caused asymmetric expansion, resulting in the desired deformation. As demonstrated in Figure 8.13b, this deformation imparts gripping capabilities to the actuator, highlighting its potential for applications requiring controlled, tailored movement.

Importantly, Figure 8.13c reveals a crucial distinction: changes in resistance during actuation were primarily due to mechanical deformation, not temperature increases. This distinction becomes evident when comparing the substantial difference in resistance response, exceeding 1400%, observed when the sensor operates without constraints, in comparison to the comparatively limited response observed when the sensor is blocked

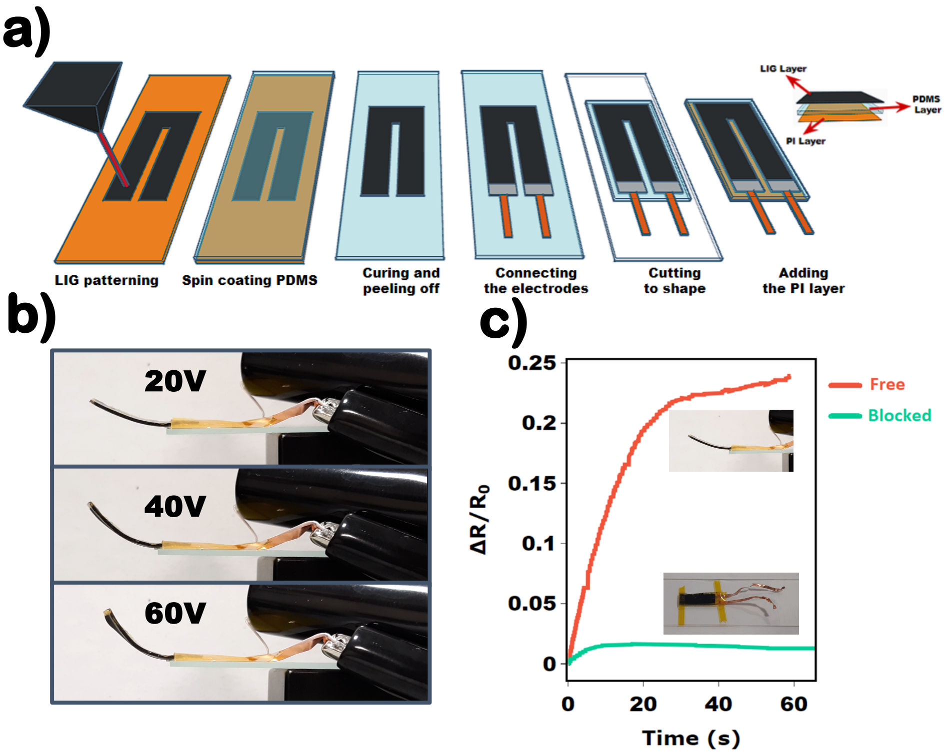

Figure 8.13: a) Actuator manufacturing process; b) Soft actuator deformation at different voltages; c) Relative resistance change of the soft actuator under an activation voltage of 20V.

Applications in Self-Sensing and Soft Robotics

LIG-based actuators have demonstrated promising capabilities for self-sensing applications. By leveraging the inherent piezoresistive properties of LIG, these actuators can detect subtle variations in resistance that correlate with surface topography, enabling non-intrusive height measurements. As shown in Figure 8.14a and 8.14b, the schematics and corresponding results of our topology sensing experiment illustrate how slight resistance variations can be mapped to changes in the object's surface profile. In these experiments, a Keysight™ U1242C digital multimeter was employed to measure the sensor current, with data logged using Keysight™ Handheld Meter Logger Software, ensuring high-precision measurements.

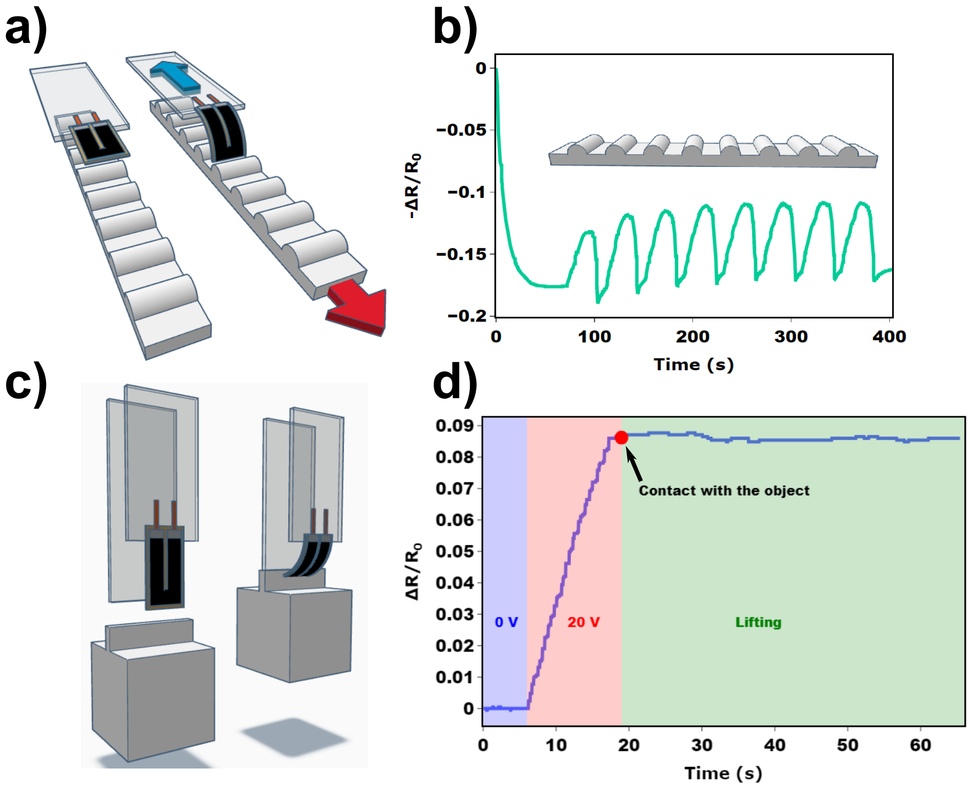

Figure 8.14: a) Schematic of the topology sensing experiment; b) Relative resistance change during topology sensing; c) Schematic of the gripping experiment; d) Relative resistance change during the gripping experiment.

Experimental images further support these findings. Figure 8.15 presents two distinct scenarios: panel a) shows a sensor positioned on a hill with minimal deformation and corresponding low electrical resistance, whereas panel b) depicts a sensor in a valley where maximum deformation results in higher electrical resistance. These images validate the concept that surface morphology can be accurately inferred from resistance measurements.

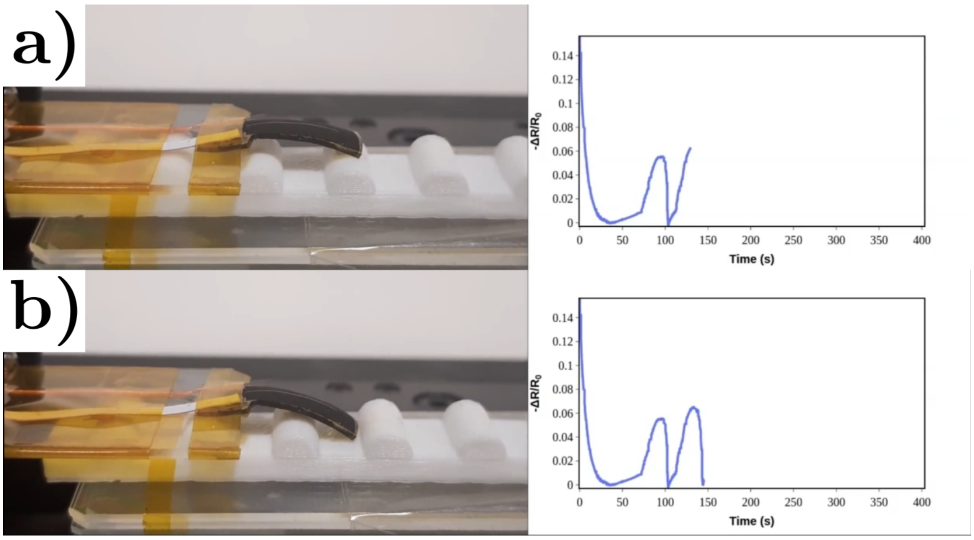

Figure 8.15: a) Sensor on a hill: minimal deformation and low electrical resistance; b) Sensor in a valley: maximum deformation and high electrical resistance.

In addition to self-sensing for topological mapping, LIG-based actuators exhibit significant potential in soft robotics, particularly in the design of soft grippers. As illustrated in Figures 8.14c and 8.14d, our gripping experiments show that the actuators display a gradual increase in resistance as they deform during the approach phase. Once contact is established, the deformation stabilizes, resulting in a near-constant resistance value. This behaviour indicates that the sensors provide reliable and repeatable feedback, with minimal influence from thermal effects due to Joule heating.

Figure 8.16 provides experimental images of the gripping process. Panel a) captures the initial stage with no contact, panel b) shows the stage where the gripper is deforming while approaching the object (reflected by a gradual resistance increase), and panel c) depicts the final stage of complete contact, where the electrical resistance stabilizes due to the absence of further deformation.

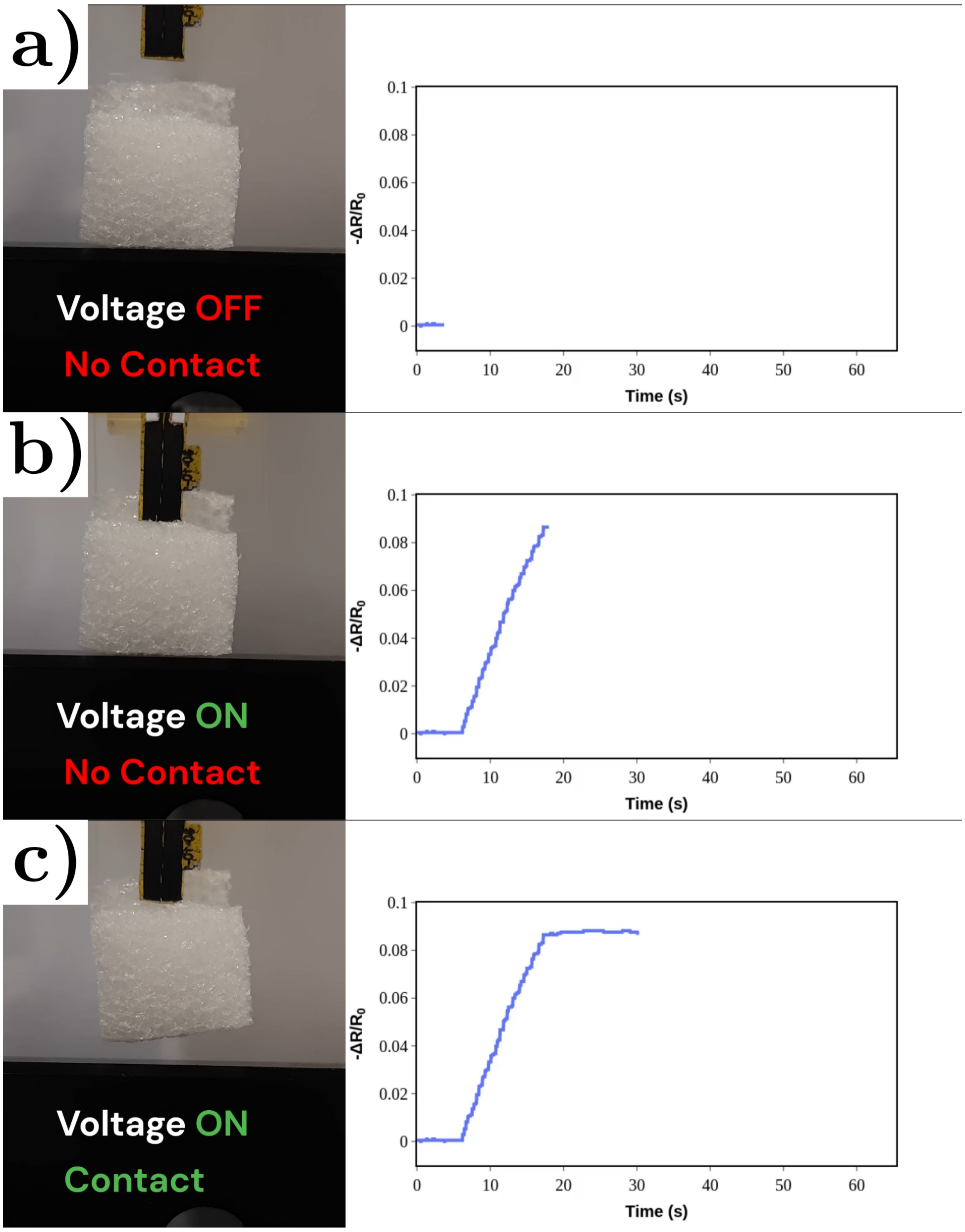

Figure 8.16: Experimental images of the gripping process: a) initial stage with no contact; b) intermediate stage with gradual resistance increase due to deformation; c) final stage with complete contact and stabilized resistance.

Collectively, these results demonstrate the dual functionality of LIG-based sensors in self-sensing and soft robotics applications. The integration of schematics with experimental images provides a comprehensive view of how slight variations in resistance can be correlated with physical deformation, thereby enabling topological mapping and reliable object gripping. This robust sensing capability underpins the potential of LIG-based devices in advanced wearable systems and soft robotic applications.

8.5 Conclusion

The exploration of LIG nanocomposites in various applications has revealed their potential and versatility. In body movement monitoring, LIG-based sensors have shown promise in tracking gait and other physiological parameters, although challenges related to variability across individuals and sensor placement sensitivity need to be addressed. For respiration monitoring, the integration of LIG strain sensors into wearable devices like T-shirts and sports tapes has demonstrated effective real-time monitoring capabilities, with ongoing efforts to improve signal quality and reduce noise. In the realm of actuators, LIG-based electrothermal actuators have exhibited robust performance in self-sensing and soft robotics applications, highlighting their potential for precise and reliable operations. Overall, while LIG nanocomposites offer significant advancements in sensor technology, further refinement and innovation are essential to overcome existing limitations and fully realize their potential in diverse applications.

Chapter 9

Conclusion and Future perspectives

9.1 Conclusion

This thesis has presented a comprehensive investigation into LIG-polymer nanocomposites, advancing the understanding of their fabrication, characterization, and application in soft strain sensing. By combining experimental techniques, theoretical modelling, and practical validation, this work contributes to the field of flexible and wearable electronics.

The research began with the optimisation of LIG fabrication using laser processing techniques, allowing precise control over the microstructure, porosity, and electrical conductivity of the graphene network. The incorporation of conductive nanoparticle doping further enhanced the electromechanical performance of LIG, resulting in improved sensitivity and stability. The successful integration of LIG with polymer matrices, such as PDMS and Ecoflex, demonstrated its compatibility with flexible substrates and its suitability for wearable applications.

A key aspect of this thesis was the development of a custom LabVIEW/Python-based electromechanical testing platform. This platform provided a precise, cost-effective solution for characterizing the strain-resistance behaviour of LIG-polymer nanocomposites. The automated platform was essential for achieving sampling speeds far beyond what manual data collection could provide, enabling the high-resolution, synchronized thermal and mechanical data acquisition required to observe and accurately model the dynamic thermal-mechanical coupling effects described in Chapter 5. This capability played a pivotal role in validating experimental results and guiding the optimization of sensor performance.

A major contribution of this work was the investigation into the heat sensitivity of LIG-based strain sensors. Through a combination of theoretical modelling and experimental validation, the thesis demonstrated how temperature influences strain distribution and electrical resistance in LIG-polymer nanocomposites. A Gaussian strain distribution framework was developed to analyse the combined effects of thermal and mechanical loads. The results revealed that heating reduces the strain distribution's variability, leading to more uniform local strain across the material. This heat-insensitive behaviour was further validated through finite element simulations and experimental studies, offering a comprehensive understanding of the decoupling of thermal and mechanical effects. These findings highlight the robustness of LIG-based sensors for applications in dynamic and thermally variable environments.

The versatility of LIG-based nanocomposite sensors was further demonstrated through their successful application in wearable health monitoring and soft robotic systems. These examples showcase the adaptability of LIG-based sensors for emerging technologies that require flexible and thermally stable sensing solutions.

In conclusion, this thesis has provided new insights into the fabrication, optimization, and application of LIG-polymer nanocomposites. The findings emphasize the importance of material processing, strain modelling, and interdisciplinary approaches in enhancing sensor performance. This work not only advances the current state of LIG-based sensors but also establishes a framework for future exploration of functionalisation strategies, alternative polymer matrices, and novel applications, ultimately paving the way for next-generation flexible electronics.

9.2 Challenges and Future Perspectives

This thesis provides insights and developments in LIG-polymer nanocomposites. While our current understanding has grown, further work is required to overcome existing challenges and pursue new possibilities.

- **Scalability and Manufacturing Consistency:** While laser processing is a cost-effective and scalable alternative to conventional graphene synthesis techniques, achieving consistent LIG quality over large areas remains a significant challenge. Standard CO_2 laser cutters often exhibit spatial power variation across the working bed, due to beam dispersion with distance from the laser source, which leads to non-uniform scribing. Additionally, variability in precursor materials, especially in the case of natural substrates, can result in batch-to-batch discrepancies and surface inhomogeneities [205]. Although promising strategies have been reported to improve LIG uniformity on PI substrates [206, 207], further advancements are necessary to ensure reliable and reproducible manufacturing at scale. Future work could explore the use of multi-laser systems, real-time feedback control, and standardized precursors to mitigate these limitations.
- **Thermal Stability Under Extreme Conditions:** This thesis has demonstrated the feasibility of achieving temperature-insensitive performance in LIG-based sensors within moderate thermal ranges. However, their behaviour under more extreme conditions, such as elevated temperatures, prolonged exposure, or rapid thermal cycling, remains under-explored. Most existing studies limit their temperature range to below 150 °C, which may not capture the full

spectrum of real-world applications [208–210]. Expanding the investigation to include high-temperature environments or harsh thermal transients will be crucial for validating the reliability of LIG nanocomposites in demanding operational scenarios.

- **Toward Multifunctional Sensing:** LIG has demonstrated great potential for multifunctional sensing due to its tunable electrical, mechanical, and chemical properties. It has been successfully employed in detecting a wide range of stimuli, including mechanical deformation (strain and pressure), temperature, humidity, and even biochemical signals. However, most implementations to date rely on integrating multiple, discrete sensors to achieve multimodal functionality, which increases device complexity and overall footprint [160, 211].

  Our work demonstrated that both temperature and strain sensitivities can be independently tuned in LIG-based sensors, temperature sensitivity through material doping and strain sensitivity through structural patterning, such as kirigami designs. By integrating these two approaches, it becomes possible to engineer a novel, multifunctional LIG sensor capable of simultaneously and reliably measuring both strain and temperature using a single sensing element.

  The development of such truly multifunctional LIG-based devices remains a largely unexplored yet promising direction, offering pathways to streamline fabrication, reduce form factor, and enhance system integration. Nevertheless, challenges such as signal cross-sensitivity remain a barrier. As noted by Xu et al. [212], mechanical strain can interfere with chemical signal detection, highlighting the importance of designing architectures and algorithms capable of decoupling overlapping sensor responses. Addressing these issues will be essential to realizing robust, multifunctional LIG sensors for next-generation wearable and environmental monitoring systems.
- **Exploration of Alternative Polymer Matrices and Raw Materials:** While PI remains the most commonly used substrate for LIG formation due to its thermal stability and carbon-rich composition, recent research has begun exploring more sustainable and environmentally friendly alternatives. Natural precursors such as wood, lignin-rich biomass, and cellulose-based materials offer biodegradable and renewable options for LIG fabrication, and have shown promising results in preliminary studies [18, 175, 213]. In parallel, the choice of polymer matrices used for embedding LIG in soft strain sensors also warrants further investigation. Different polymeric substrates can dramatically influence the sensor's mechanical compliance, thermal stability, and signal integrity. For example, although PDMS is widely used for its elasticity and biocompatibility, it has been observed that elevated temperatures can induce signal noise and compromise sensor fidelity [214, 215]. Exploring alternative polymers with tailored thermal and mechanical properties could significantly enhance the performance and application range of LIG-based nanocomposites, particularly in environments requiring greater thermal or chemical stability.
- **Integration with Wireless and Low-Power Systems:** To enable practical deployment of LIG-based sensors in wearable and remote monitoring applications, seamless integration with wireless communication modules and low-power electronics is essential. Current research is increasingly exploring self-powered systems that leverage energy-harvesting technologies to extend sensor autonomy and reduce reliance on external power sources. Among these, TENGS have emerged as a particularly promising solution, offering efficient energy conversion

from mechanical motion, such as human activity or environmental vibrations, into electrical energy [165, 216–218]. These systems provide a viable foundation for powering low-energy devices and enabling more frequent data acquisition, a critical requirement for real-time health and environmental monitoring. Future research could focus on optimizing the energy efficiency, data transmission protocols, and form factor of such integrated systems, ultimately advancing the development of fully autonomous, wireless LIG-based sensor platforms.
- **Broader Application in Emerging Fields:** Beyond wearable health monitoring and soft robotics, LIG-based sensors could find applications in structural health monitoring [219, 220], environmental sensing [38, 221, 222], and automotive or aerospace systems. Collaborative research with other disciplines could unlock new possibilities and broaden the impact of these sensors.

In summary, this thesis lays the foundation for the continued development of LIG-based nanocomposites for soft strain sensing. By addressing the outlined challenges and pursuing the proposed research directions, future work has the potential to unlock the full capabilities of these materials, ultimately contributing to the next generation of flexible and wearable technologies.

Bibliography

1. Castro Neto, A. H., Guinea, F., Peres, N. M., Novoselov, K. S. & Geim, A. K. The electronic properties of graphene. *Reviews of Modern Physics* **81,** 109–162. ISSN: 00346861 (Jan. 2009).
2. Zhu, Y. *et al.* Graphene and graphene oxide: Synthesis, properties, and applications. *Advanced Materials* **22,** 3906–3924. ISSN: 09359648 (Sept. 2010).
3. Novoselov, K. S. *et al. A roadmap for graphene* Oct. 2012.
4. Geim, A. K. Graphene: Status and Prospects. *Science* **324,** 1530–1534. ISSN: 0036-8075. `https://www.science.org/doi/10.1126/science.1158877` (June 2009).
5. Allen, M. J., Tung, V. C. & Kaner, R. B. Honeycomb carbon: A review of graphene. *Chemical Reviews* **110,** 132–145. ISSN: 00092665 (Jan. 2010).
6. Papageorgiou, D. G., Kinloch, I. A. & Young, R. J. *Mechanical properties of graphene and graphene-based nanocomposites* Oct. 2017.
7. Balandin, A. A. *et al.* Superior thermal conductivity of single-layer graphene. *Nano Letters* **8,** 902–907. ISSN: 15306984 (Mar. 2008).
8. Balandin, A. A. Thermal properties of graphene and nanostructured carbon materials. *Nature Materials* **10,** 569–581. ISSN: 14764660 (2011).
9. Kim, K. S. *et al.* Large-scale pattern growth of graphene films for stretchable transparent electrodes. *Nature* **457,** 706–710. ISSN: 00280836 (Feb. 2009).
10. Tan, Y. B. & Lee, J.-M. Graphene for supercapacitor applications. *Journal of Materials Chemistry A* **1,** 14814. ISSN: 2050-7488 (2013).
11. Ke, Q. & Wang, J. *Graphene-based materials for supercapacitor electrodes – A review* Mar. 2016.
12. Wang, Y. *et al.* Supercapacitor devices based on graphene materials. *Journal of Physical Chemistry C* **113,** 13103–13107. ISSN: 19327447 (July 2009).
13. Shao, Y. *et al. Graphene based electrochemical sensors and biosensors: A review* 2010.
14. Pang, S., Hernandez, Y., Feng, X. & Müllen, K. Graphene as transparent electrode material for organic electronics. *Advanced Materials* **23,** 2779–2795. ISSN: 09359648 (July 2011).
15. Soldano, C., Mahmood, A. & Dujardin, E. *Production, properties and potential of graphene* July 2010.
16. Lin, J. *et al.* Laser-induced porous graphene films from commercial polymers. *Nature Communications* **5,** 5714. ISSN: 2041-1723. `https://www.nature.com/articles/ncomms6714` (Dec. 2014).
17. Bai, S. *et al.* Investigation of micro/nano formation mechanism of porous graphene induced by CO2 laser processing on polyimide film. *Journal of Manufacturing Processes* **84,** 555–564. ISSN: 15266125 (Dec. 2022).
18. Chyan, Y. *et al.* Laser-Induced Graphene by Multiple Lasing: Toward Electronics on Cloth, Paper, and Food. *ACS Nano* **12,** 2176–2183. ISSN: 1936086X (Mar. 2018).

19. Bai, S. *et al. Laser-induced graphene: Carbon precursors, fabrication mechanisms, material characteristics, and applications in energy storage* Aug. 2024.
20. Remesh, S. *et al.* Oil palm lignin-derived laser scribed graphene in neutral electrolyte for high-performance microsupercapacitor application. *Journal of Environmental Chemical Engineering* **11.** ISSN: 22133437 (Oct. 2023).
21. Li, X. *et al.* High-Voltage Flexible Microsupercapacitors Based on Laser-Induced Graphene. *ACS Applied Materials and Interfaces* **10,** 26357–26364. ISSN: 19448252 (Aug. 2018).
22. Awasthi, H., Renuka, H., Srivastava, A. K. & Goel, S. Laser-induced graphene-based flexible interdigital electrode realizing micro supercapacitor sustainable in different temperatures. *Energy Storage* **5.** ISSN: 25784862 (Apr. 2023).
23. Xu, Z., Liu, M., Zhang, Y. & Yang, F. Flexible micro-supercapacitors from laser-induced graphene and gel polymer electrolytes. *Journal of Energy Storage* **105.** ISSN: 2352152X (Jan. 2025).
24. Le, T. S. D., Park, S., An, J., Lee, P. S. & Kim, Y. J. Ultrafast Laser Pulses Enable One-Step Graphene Patterning on Woods and Leaves for Green Electronics. *Advanced Functional Materials* **29.** ISSN: 16163028 (Aug. 2019).
25. Kim, Y.-R. *et al.* Green supercapacitor patterned by synthesizing MnO/laser-induced-graphene hetero-nanostructures on wood via femtosecond laser pulses. *Biochar* **6,** 36. ISSN: 2524-7867. `https://link.springer.com/10.1007/s42773-024-00320-7` (Apr. 2024).
26. Kulyk, B. *et al.* Laser-Induced Graphene from Paper for Mechanical Sensing. *ACS Applied Materials and Interfaces* **13,** 10210–10221. ISSN: 19448252 (Mar. 2021).
27. Kim, Y. J. *et al.* Direct-laser-conversion of Kevlar textile to laser-induced-graphene for realizing fast and flexible fabric strain sensors. *CIRP Annals* **71,** 473–476. ISSN: 17260604 (Jan. 2022).
28. Le, T. S. D. *et al. Recent Advances in Laser-Induced Graphene: Mechanism, Fabrication, Properties, and Applications in Flexible Electronics* Nov. 2022.
29. Duy, L. X. *et al.* Laser-induced graphene fibers. *Carbon* **126,** 472–479. ISSN: 00086223. `https://linkinghub.elsevier.com/retrieve/pii/S0008622317310370` (Jan. 2018).
30. Houeix, Y. *et al.* Responsible Humidity Sensor by Direct Laser Writing on Cork Substrate. *Advanced Sustainable Systems.* ISSN: 23667486 (2024).
31. Nam, H. K. *et al.* Smart Wooden Home Enabled by Direct-Written Laser-Induced Graphene. *Advanced Materials Technologies.* ISSN: 2365709X (2023).
32. Li, X. *et al.* Laser fabrication of epidermal paper-based graphene sensors. *Applied Materials Today* **36,** 102051. ISSN: 23529407. `https://linkinghub.elsevier.com/retrieve/pii/S2352940723003207` (Feb. 2024).
33. Zhu, S. *et al.* Sputter-deposited nickel nanoparticles on Kevlar fabrics with laser-induced graphene for efficient solar evaporation. *Chemical Engineering Journal* **452.** ISSN: 13858947 (Jan. 2023).
34. Ye, R. *et al.* Laser-Induced Graphene Formation on Wood. *Advanced Materials* **29.** ISSN: 15214095 (Oct. 2017).
35. Li, Y. *et al.* Laser-Induced Graphene in Controlled Atmospheres: From Superhydrophilic to Superhydrophobic Surfaces. *Advanced Materials* **29.** ISSN: 15214095 (July 2017).

36. Vivaldi, F. M. *et al.* Three-Dimensional (3D) Laser-Induced Graphene: Structure, Properties, and Application to Chemical Sensing. *ACS Applied Materials & Interfaces* **13,** 30245–30260. ISSN: 1944-8244. `https://pubs.acs.org/doi/10.1021/acsami.1c05614` (July 2021).
37. Wang, M. *et al.* A wearable electrochemical biosensor for the monitoring of metabolites and nutrients. *Nature Biomedical Engineering* **6,** 1225–1235. ISSN: 2157846X (Nov. 2022).
38. Wanjari, V. P., Reddy, A. S., Duttagupta, S. P. & Singh, S. P. *Laser-induced graphene-based electrochemical biosensors for environmental applications: a perspective* Mar. 2023.
39. Stanford, M. G., Yang, K., Chyan, Y., Kittrell, C. & Tour, J. M. Laser-Induced Graphene for Flexible and Embeddable Gas Sensors. *ACS Nano* **13,** 3474–3482. ISSN: 1936086X (Mar. 2019).
40. Kumar Adhikari, K. *et al.* Patterned Laser-Induced graphene enabling a High-Performance gas sensing Split-Ring resonator. *Chemical Engineering Journal,* 155984. ISSN: 13858947. `https://linkinghub.elsevier.com/retrieve/pii/S1385894724074758` (Sept. 2024).
41. Zhao, J. *et al.* In situ laser-assisted synthesis and patterning of graphene foam composites as a flexible gas sensing platform. *Chemical Engineering Journal* **456.** ISSN: 13858947 (Jan. 2023).
42. Sharma, C. P. *et al.* Silver nanoparticle doped laser-induced graphene fabrication methodology affects silver nanoparticle size, distribution, biological and electrochemical properties. *Environmental Science: Nano* **11,** 1582–1596. ISSN: 20518161 (Feb. 2024).
43. Li, J. *et al.* CuO nanoparticles embedded in laser-induced graphene for flexible planar micro-supercapacitors. *Surfaces and Interfaces,* 104968. ISSN: 24680230. `https://linkinghub.elsevier.com/retrieve/pii/S2468023024011246` (Aug. 2024).
44. Geun Jo, S., Shin, Y. K., Seo, M. H. & Lee, J. W. Rapid photothermal reduction-derived Pt1.6Ni nanoalloys embedded in laser-induced graphene for hydrogen evolution reaction. *International Journal of Hydrogen Energy* **77,** 101–109. ISSN: 03603199 (Aug. 2024).
45. Pinheiro, T. *et al.* One-Step Laser Synthesis of Copper Nanoparticles and Laser-Induced Graphene in a Paper Substrate for Non-Enzymatic Glucose Sensing. *Advanced Sensor Research.* ISSN: 2751-1219. `https://onlinelibrary.wiley.com/doi/10.1002/adsr.202400052` (Sept. 2024).
46. Zhang, N., Yang, J. & Hu, C. Laser-scribed graphene sensors on nail polish with tunable composition for electrochemical detection of nitrite and glucose. *Sensors and Actuators B: Chemical* **357,** 131394. ISSN: 09254005. `https://doi.org/10.1016/j.snb.2022.131394` (2022).
47. Kwak, D. *et al.* Investigation of Laser Induced Graphene (LIG) on a Flexible Substrate and its Functionalization by Metal Doping for Gas-Sensing Applications. `www.preprints.org` (2024).

48. Kumar, R., Pandey, R., Joanni, E. & Savu, R. Laser-induced and catalyst-free formation of graphene materials for energy storage and sensing applications. *Chemical Engineering Journal* **497,** 154968. ISSN: 13858947. `https://linkinghub.elsevier.com/retrieve/pii/S1385894724064593` (Oct. 2024).
49. Zhu, J. *et al.* Biomimetic Turbinate-like Artificial Nose for Hydrogen Detection Based on 3D Porous Laser-Induced Graphene. *ACS Applied Materials and Interfaces* **11,** 24386–24394. ISSN: 19448252 (July 2019).
50. Yang, L. *et al.* Moisture-resistant, stretchable NOx gas sensors based on laser-induced graphene for environmental monitoring and breath analysis. *Microsystems and Nanoengineering* **8.** ISSN: 20557434 (Dec. 2022).
51. Yang, L. *et al.* Novel gas sensing platform based on a stretchable laser-induced graphene pattern with self-heating capabilities. *Journal of Materials Chemistry A* **8,** 6487–6500. ISSN: 20507496 (Apr. 2020).
52. Song, W. *et al.* Flexible, Stretchable, and Transparent Planar Microsupercapacitors Based on 3D Porous Laser-Induced Graphene. *Small* **14.** ISSN: 16136829 (Jan. 2018).
53. Li, L. *et al.* High-Performance Pseudocapacitive Microsupercapacitors from Laser-Induced Graphene. *Advanced Materials* **28,** 838–845. ISSN: 15214095 (Feb. 2016).
54. Peng, Z. *et al.* Flexible Boron-Doped Laser-Induced Graphene Microsupercapacitors. *ACS Nano* **9,** 5868–5875. ISSN: 1936086X (June 2015).
55. Ma, W., Zhu, J., Wang, Z., Song, W. & Cao, G. *Recent advances in preparation and application of laser-induced graphene in energy storage devices* Dec. 2020.
56. Amjadi, M., Kyung, K. U., Park, I. & Sitti, M. *Stretchable, Skin-Mountable, and Wearable Strain Sensors and Their Potential Applications: A Review* Mar. 2016.
57. Liu, H. *et al.* Electrically conductive polymer composites for smart flexible strain sensors: a critical review. *Journal of Materials Chemistry C* **6,** 12121–12141. ISSN: 2050-7526. `https://xlink.rsc.org/?DOI=C8TC04079F` (2018).
58. Souri, H. *et al.* Wearable and Stretchable Strain Sensors: Materials, Sensing Mechanisms, and Applications. *Advanced Intelligent Systems* **2,** 2000039. ISSN: 2640-4567 (2020).
59. Shen, Z. *et al.* High-Stretchability, Ultralow-Hysteresis ConductingPolymer Hydrogel Strain Sensors for Soft Machines. *Advanced Materials* **34.** ISSN: 15214095 (Aug. 2022).
60. Dickey, M. D. Stretchable and Soft Electronics using Liquid Metals. *Advanced Materials* **29.** ISSN: 0935-9648. `https://onlinelibrary.wiley.com/doi/10.1002/adma.201606425` (July 2017).
61. Dickey, M. D. *et al.* Eutectic gallium-indium (EGaIn): A liquid metal alloy for the formation of stable structures in microchannels at room temperature. *Advanced Functional Materials* **18,** 1097–1104. ISSN: 1616301X (Apr. 2008).
62. Kim, S. *et al.* EGaIn-Silicone-based highly stretchable and flexible strain sensor for real-time two joint robotic motion monitoring. *Sensors and Actuators A: Physical* **342.** ISSN: 09244247 (Aug. 2022).
63. Zhou, Z. *et al.* Liquid Metal Printed Optoelectronics Toward Fast Fabrication of Customized and Erasable Patterned Displays. *Advanced Materials Technologies* **7.** ISSN: 2365709X (May 2022).

64. Wang, H., Chen, S., Yuan, B., Liu, J. & Sun, X. Liquid Metal Transformable Machines. *Accounts of Materials Research* **2,** 1227–1238. ISSN: 26436728 (Dec. 2021).
65. Varga, M., Ladd, C., Ma, S., Holbery, J. & Tröster, G. On-skin liquid metal inertial sensor. *Lab on a Chip* **17,** 3272–3278. ISSN: 14730189 (Oct. 2017).
66. Kim, M. g., Brown, D. K. & Brand, O. Nanofabrication for all-soft and high-density electronic devices based on liquid metal. *Nature Communications* **11.** ISSN: 20411723 (Dec. 2020).
67. Zu, W. *et al.* A Comparative Study of Silver Microflakes in Digitally Printable Liquid Metal Embedded Elastomer Inks for Stretchable Electronics. *Advanced Materials Technologies,* 2200534. ISSN: 2365-709X. `https://onlinelibrary.wiley.com/doi/10.1002/admt.202200534` (July 2022).
68. Gozen, B. A., Tabatabai, A., Ozdoganlar, O. B. & Majidi, C. High-density soft-matter electronics with micron-scale line width. *Advanced Materials* **26,** 5211–5216. ISSN: 15214095 (Aug. 2014).
69. Cheng, W., Luo, Z., Wang, C., Zhao, T. & Xiang, N. Soft crawling robot integrated with liquid metal-based flexible strain sensor and closed-loop feedback control. *Sensors and Actuators A: Physical* **371.** ISSN: 09244247 (June 2024).
70. Park, Y. L., Chen, B. R. & Wood, R. J. Design and fabrication of soft artificial skin using embedded microchannels and liquid conductors. *IEEE Sensors Journal* **12,** 2711–2718. ISSN: 1530437X (2012).
71. Liu, H. *et al.* Electrically conductive thermoplastic elastomer nanocomposites at ultralow graphene loading levels for strain sensor applications. *Journal of Materials Chemistry C* **4,** 157–166. ISSN: 20507526 (2015).
72. Zhang, W., Liu, Q. & Chen, P. Flexible strain sensor based on carbon black/silver nanoparticles composite for humanmotion detection. *Materials* **11.** ISSN: 19961944 (Sept. 2018).
73. Wang, S. *et al.* Network cracks-based wearable strain sensors for subtle and large strain detection of human motions. *Journal of Materials Chemistry C* **6,** 5140–5147. ISSN: 20507526 (2018).
74. Chen, J., Zhu, Y. & Jiang, W. A stretchable and transparent strain sensor based on sandwich-like PDMS/CNTs/PDMS composite containing an ultrathin conductive CNT layer. *Composites Science and Technology* **186.** ISSN: 02663538 (Jan. 2020).
75. Hu, M. *et al.* High-performance strain sensors based on bilayer carbon black/PDMS hybrids. *Advanced Composites and Hybrid Materials* **4,** 514–520. ISSN: 25220136 (Sept. 2021).
76. Naguib, M. *et al.* Two-dimensional nanocrystals produced by exfoliation of Ti 3AlC 2. *Advanced Materials* **23,** 4248–4253. ISSN: 09359648 (Oct. 2011).
77. Ling, Z. *et al.* Flexible and conductive MXene films and nanocomposites with high capacitance. *Proceedings of the National Academy of Sciences of the United States of America* **111,** 16676–16681. ISSN: 10916490 (Nov. 2014).
78. Zhang, Y. Z. *et al. MXene Printing and Patterned Coating for Device Applications* May 2020.
79. Kong, D. *et al.* Highly sensitive strain sensors with wide operation range from strong MXene-composited polyvinyl alcohol/sodium carboxymethylcellulose double network hydrogel. *Advanced Composites and Hybrid Materials.* ISSN: 2522-0128. `https://link.springer.com/10.1007/s42114-022-00531-1` (July 2022).

80. Xu, X. *et al.* Wearable CNT/Ti3C2Tx MXene/PDMS composite strain sensor with enhanced stability for real-time human healthcare monitoring. *Nano Research* **14,** 2875–2883. ISSN: 19980000 (Aug. 2021).
81. Park, S. J., Kim, J., Chu, M. & Khine, M. Highly Flexible Wrinkled Carbon Nanotube Thin Film Strain Sensor to Monitor Human Movement. *Advanced Materials Technologies* **1.** ISSN: 2365709X (Aug. 2016).
82. Zhou, J. *et al.* Multiscale and hierarchical wrinkle enhanced graphene/Ecoflex sensors integrated with human-machine interfaces and cloud-platform. *npj Flexible Electronics* **6,** 55. ISSN: 2397-4621. `https://www.nature.com/articles/s41528-022-00189-1` (Dec. 2022).
83. Chu, Z. *et al.* Superhydrophobic gradient wrinkle strain sensor with ultra-high sensitivity and broad strain range for motion monitoring. *Journal of Materials Chemistry A* **9,** 9634–9643. ISSN: 20507496 (Apr. 2021).
84. Fratzl, P. & Barth, F. G. Biomaterial systems for mechanosensing and actuation. *Nature* **462,** 442–448. ISSN: 00280836 (2009).
85. Sun, H. *et al.* A Highly Sensitive and Stretchable Yarn Strain Sensor for Human Motion Tracking Utilizing a Wrinkle-Assisted Crack Structure. *ACS Applied Materials and Interfaces* **11,** 36052–36062. ISSN: 19448252 (Oct. 2019).
86. Pu, J. H. *et al.* A strain localization directed crack control strategy for designing MXene-based customizable sensitivity and sensing range strain sensors for full-range human motion monitoring. *Nano Energy* **74.** ISSN: 22112855 (Aug. 2020).
87. Zhou, Y. *et al.* Significant stretchability enhancement of a crack-based strain sensor combined with high sensitivity and superior durability for motion monitoring. *ACS Applied Materials and Interfaces* **11,** 7405–7414. ISSN: 19448252 (Feb. 2019).
88. Xu, K. *et al.* Highly stable kirigami-structured stretchable strain sensors for perdurable wearable electronics. *Journal of Materials Chemistry C* **7,** 9609–9617. ISSN: 20507526 (2019).
89. Wang, Z. *et al.* Kirigami-patterned highly stretchable conductors from flexible carbon nanotube-embedded polymer films. *Journal of Materials Chemistry C* **5,** 8714–8722. ISSN: 20507526 (2017).
90. Ma, H. *et al.* Recent Advances in Graphene-Based Humidity Sensors with the Focus of Structural Design: A Review. *IEEE Sensors Journal,* 1–1. ISSN: 1530-437X. `https://ieeexplore.ieee.org/document/10534183/` (2024).
91. Wang, Y., Li, X., Xu, X. & Li, G. Double-layer stretchable composite conductive graphene-hydrogel with wide-range linear sensing and thermal-humidity management for health monitoring. *Chemical Engineering Journal* **498.** ISSN: 13858947 (Oct. 2024).
92. Yoshida, A. *et al.* Printed, All-Carbon-Based Flexible Humidity Sensor Using a Cellulose Nanofiber/Graphene Nanoplatelet Composite. *Carbon Trends* **7,** 100166. ISSN: 26670569. `https://doi.org/10.1016/j.cartre.2022.100166` (2022).
93. Li, Y. *et al.* Temperature Coefficient of Resistance of Transferred Laser-Induced Graphene. *ACS Applied Electronic Materials.* ISSN: 2637-6113. `https://pubs.acs.org/doi/10.1021/acsaelm.4c00639` (May 2024).
94. Nankali, M. *et al.* Highly stretchable and sensitive strain sensors based on carbon nanotube-elastomer nanocomposites: The effect of environmental factors on strain sensing performance. *Journal of Materials Chemistry C* **8,** 6185–6195. ISSN: 20507526 (May 2020).

95. Bang, J., Baek, K., Lim, J., Han, Y. & So, H. Deep Neural Network Regression-Assisted Pressure Sensor for Decoupling Thermal Variations at Different Operating Temperatures. *Advanced Intelligent Systems.* ISSN: 2640-4567. `https://onlinelibrary.wiley.com/doi/10.1002/aisy.202300186` (Aug. 2023).
96. Jung, B. K., Yang, Y. & Oh, S. J. Advances in Non-Interference Sensing for Wearable Sensors: Selectively Detecting Multi-Signals from Pressure, Strain, and Temperature. *JOURNAL OF SENSOR SCIENCE AND TECHNOLOGY* **32,** 340–351. ISSN: 1225-5475. `http://jsstec.org/_common/do.php?a=full&b=42&bidx=3490&aidx=38684` (Nov. 2023).
97. Nag, A. *et al. Graphene-based wearable temperature sensors: A review* Sept. 2022.
98. Zhu, W. B. *et al.* Direct ink writing of a graphene/CNT/silicone composite strain sensor with a near-zero temperature coefficient of resistance. *Journal of Materials Chemistry C* **10,** 8226–8233. ISSN: 20507534 (May 2022).
99. Amjadi, M. & Sitti, M. Self-Sensing Paper Actuators Based on Graphite–Carbon Nanotube Hybrid Films. *Advanced Science* **5.** ISSN: 21983844 (July 2018).
100. Ahuja, P. *et al.* A water-resilient carbon nanotube based strain sensor for monitoring structural integrity. *Journal of Materials Chemistry A* **7,** 19996–20005. ISSN: 20507496 (2019).
101. Gao, Z., Jiang, K., Lou, Z., Han, W. & Shen, G. Water-proof and thermally inert flexible pressure sensors based on zero temperature coefficient of resistance hybrid films. *Journal of Materials Chemistry C* **7,** 9648–9654. ISSN: 20507526 (2019).
102. Su, X., Li, H., Lai, X., Chen, Z. & Zeng, X. Highly Stretchable and Conductive Superhydrophobic Coating for Flexible Electronics. *ACS Applied Materials and Interfaces* **10,** 10587–10597. ISSN: 19448252 (Mar. 2018).
103. Zhang, S., Wen, L., Wang, H., Zhu, K. & Zhang, M. Vertical CNT-Ecoflex nanofins for highly linear broad-range-detection wearable strain sensors. *Journal of Materials Chemistry C* **6,** 5132–5139. ISSN: 20507526 (2018).
104. Wang, X., Deng, Y., Jiang, P., Chen, X. & Yu, H. Low-hysteresis, pressure-insensitive, and transparent capacitive strain sensor for human activity monitoring. *Microsystems & Nanoengineering* **8,** 113. ISSN: 2055-7434. `https://www.nature.com/articles/s41378-022-00450-7` (Oct. 2022).
105. Li, J. *et al.* High-Fidelity, Low-Hysteresis Bionic Flexible Strain Sensors for Soft Machines. *ACS Nano* **18,** 2520–2530. ISSN: 1936086X (Jan. 2024).
106. Thuruthel, T. G., Hughes, J., Georgopoulou, A., Clemens, F. & Iida, F. Using Redundant and Disjoint Time-Variant Soft Robotic Sensors for Accurate Static State Estimation. *IEEE Robotics and Automation Letters* **6,** 2099–2105. ISSN: 23773766 (Apr. 2021).
107. Tang, J., Li, J., Vlassak, J. J. & Suo, Z. Fatigue fracture of hydrogels. *Extreme Mechanics Letters* **10,** 24–31. ISSN: 23524316 (Jan. 2017).
108. Bai, R. *et al.* Fatigue fracture of tough hydrogels. *Extreme Mechanics Letters* **15,** 91–96. ISSN: 23524316 (Sept. 2017).
109. Liu, S. & Li, L. Ultrastretchable and Self-Healing Double-Network Hydrogel for 3D Printing and Strain Sensor. *ACS Applied Materials and Interfaces* **9,** 26429–26437. ISSN: 19448252 (2017).

110. Meng, K. *et al.* Kirigami-Inspired Pressure Sensors for Wearable Dynamic Cardiovascular Monitoring. *Advanced Materials* **34,** 2202478. ISSN: 15214095. `https://onlinelibrary.wiley.com/doi/10.1002/adma.202202478` (Sept. 2022).
111. Khalid, M. A. U. & Chang, S. H. *Flexible strain sensors for wearable applications fabricated using novel functional nanocomposites: A review* Mar. 2022.
112. Amjadi, M., Pichitpajongkit, A., Lee, S., Ryu, S. & Park, I. Highly stretchable and sensitive strain sensor based on silver nanowire-elastomer nanocomposite. *ACS Nano* **8,** 5154–5163. ISSN: 1936086X (May 2014).
113. Yao, S. & Zhu, Y. Wearable multifunctional sensors using printed stretchable conductors made of silver nanowires. *Nanoscale* **6,** 2345–2352. ISSN: 20403364 (Feb. 2014).
114. Cao, Z., Wang, R., He, T., Xu, F. & Sun, J. Interface-Controlled Conductive Fibers for Wearable Strain Sensors and Stretchable Conducting Wires. *ACS Applied Materials and Interfaces* **10,** 14087–14096. ISSN: 19448252 (Apr. 2018).
115. Soe, H. M., Abd Manaf, A., Matsuda, A. & Jaafar, M. Performance of a silver nanoparticles-based polydimethylsiloxane composite strain sensor produced using different fabrication methods. *Sensors and Actuators, A: Physical* **329.** ISSN: 09244247 (Oct. 2021).
116. Lee, S. *et al.* Ag nanowire reinforced highly stretchable conductive fibers for wearable electronics. *Advanced Functional Materials* **25,** 3114–3121. ISSN: 16163028 (June 2015).
117. Luan, J., Wang, Q., Zheng, X., Li, Y. & Wang, N. Flexible metal/polymer composite films embedded with silver nanowires as a stretchable and conductive strain sensor for human motion monitoring. *Micromachines* **10.** ISSN: 2072666X (June 2019).
118. Zhang, L., Li, H., Lai, X., Gao, T. & Zeng, X. Three-dimensional binary-conductive-network silver nanowires@thiolated graphene foam-based room-temperature self-healable strain sensor for human motion detection. *ACS Applied Materials and Interfaces* **12,** 44360–44370. ISSN: 19448252 (Sept. 2020).
119. Yamada, T. *et al.* A stretchable carbon nanotube strain sensor for human-motion detection. *Nature Nanotechnology* **6,** 296–301. ISSN: 17483395 (2011).
120. Shin, U. H. *et al.* Highly stretchable conductors and piezocapacitive strain gauges based on simple contact-transfer patterning of carbon nanotube forests. *Carbon* **80,** 396–404. ISSN: 00086223 (2014).
121. Cohen, D. J., Mitra, D., Peterson, K. & Maharbiz, M. M. A highly elastic, capacitive strain gauge based on percolating nanotube networks. *Nano Letters* **12,** 1821–1825. ISSN: 15306984 (Apr. 2012).
122. Tang, Z. *et al.* Highly Stretchable Core-Sheath Fibers via Wet-Spinning for Wearable Strain Sensors. *ACS Applied Materials and Interfaces* **10,** 6624–6635. ISSN: 19448252 (Feb. 2018).
123. Sun, J. *et al.* Highly stretchable and ultrathin nanopaper composites for epidermal strain sensors. *Nanotechnology* **29.** ISSN: 13616528 (June 2018).
124. Nie, B. *et al.* Flexible and Transparent Strain Sensors with Embedded Multiwalled Carbon Nanotubes Meshes. *ACS Applied Materials and Interfaces* **9,** 40681–40689. ISSN: 19448252 (Nov. 2017).
125. Wang, X. *et al.* A highly stretchable carbon nanotubes/thermoplastic polyurethane fiber-shaped strain sensor with porous structure for human motion monitoring. *Composites Science and Technology* **168,** 126–132. ISSN: 02663538 (Nov. 2018).

126. Jeong, Y. R. *et al.* Highly Stretchable and Sensitive Strain Sensors Using Fragmentized Graphene Foam. *Advanced Functional Materials* **25,** 4228–4236. ISSN: 16163028 (July 2015).
127. Boland, C. S. *et al.* Sensitive, high-strain, high-rate bodily motion sensors based on graphene-rubber composites. *ACS Nano* **8,** 8819–8830. ISSN: 1936086X (Sept. 2014).
128. Wu, S., Peng, S., Han, Z. J., Zhu, H. & Wang, C. H. Ultrasensitive and Stretchable Strain Sensors Based on Mazelike Vertical Graphene Network. *ACS Applied Materials and Interfaces* **10,** 36312–36322. ISSN: 19448252 (Oct. 2018).
129. Huang, S. *et al.* Stretchable Strain Vector Sensor Based on Parallelly Aligned Vertical Graphene. *ACS Applied Materials and Interfaces* **11,** 1294–1302. ISSN: 19448252 (Jan. 2019).
130. Han, F. *et al.* A crack-based nickel@graphene-wrapped polyurethane sponge ternary hybrid obtained by electrodeposition for highly sensitive wearable strain sensors. *Journal of Materials Chemistry C* **5,** 10167–10175. ISSN: 20507526 (2017).
131. Li, G. *et al.* Aligned flexible conductive fibrous networks for highly sensitive, ultrastretchable and wearable strain sensors. *Journal of Materials Chemistry C* **6,** 6575–6583. ISSN: 20507526 (2018).
132. Ma, J. *et al.* Highly Sensitive and Large-Range Strain Sensor with a Self-Compensated Two-Order Structure for Human Motion Detection. *ACS Applied Materials and Interfaces* **11,** 8527–8536. ISSN: 19448252 (Feb. 2019).
133. Lu, N., Lu, C., Yang, S. & Rogers, J. Highly sensitive skin-mountable strain gauges based entirely on elastomers. *Advanced Functional Materials* **22,** 4044–4050. ISSN: 1616301X (Oct. 2012).
134. Mattmann, C., Clemens, F. & Tröster, G. Sensor for measuring strain in textile. *Sensors* **8,** 3719–3732. ISSN: 14248220 (June 2008).
135. Muth, J. T. *et al.* Embedded 3D printing of strain sensors within highly stretchable elastomers. *Advanced Materials* **26,** 6307–6312. ISSN: 15214095 (Sept. 2014).
136. Hwang, B. U. *et al.* Transparent Stretchable Self-Powered Patchable Sensor Platform with Ultrasensitive Recognition of Human Activities. *ACS Nano* **9,** 8801–8810. ISSN: 1936086X (Sept. 2015).
137. Roh, E., Hwang, B. U., Kim, D., Kim, B. Y. & Lee, N. E. Stretchable, Transparent, Ultrasensitive, and Patchable Strain Sensor for Human-Machine Interfaces Comprising a Nanohybrid of Carbon Nanotubes and Conductive Elastomers. *ACS Nano* **9,** 6252–6261. ISSN: 1936086X (June 2015).
138. Guo, X. *et al.* Highly stretchable strain sensor based on SWCNTs/CB synergistic conductive network for wearable human-activity monitoring and recognition. *Smart Materials and Structures* **26.** ISSN: 1361665X (Aug. 2017).
139. Liu, P. *et al.* Fully flexible strain sensor from core-spun elastic threads with integrated electrode and sensing cell based on conductive nanocomposite. *Composites Science and Technology* **159,** 42–49. ISSN: 02663538 (May 2018).
140. Wang, C. *et al.* Carbonized silk fabric for ultrastretchable, highly sensitive, and wearable strain sensors. *Advanced Materials* **28,** 6640–6648. ISSN: 15214095 (Aug. 2016).
141. Yin, B. *et al.* Highly Stretchable, Ultrasensitive, and Wearable Strain Sensors Based on Facilely Prepared Reduced Graphene Oxide Woven Fabrics in an Ethanol Flame. *ACS Applied Materials and Interfaces* **9,** 32054–32064. ISSN: 19448252 (Sept. 2017).

142. Souri, H. & Bhattacharyya, D. Highly sensitive, stretchable and wearable strain sensors using fragmented conductive cotton fabric. *Journal of Materials Chemistry C* **6,** 10524–10531. ISSN: 20507526 (2018).
143. Zhang, M. *et al.* Carbonized Cotton Fabric for High-Performance Wearable Strain Sensors. *Advanced Functional Materials* **27.** ISSN: 16163028 (Jan. 2017).
144. Guo, J. *et al.* Stretchable and Highly Sensitive Optical Strain Sensors for Human-Activity Monitoring and Healthcare. *ACS Applied Materials and Interfaces* **11,** 33589–33598. ISSN: 19448252 (Sept. 2019).
145. Guo, J., Niu, M. & Yang, C. Highly flexible and stretchable optical strain sensing for human motion detection. *Optica* **4,** 1285. ISSN: 23342536 (Oct. 2017).
146. Leber, A., Cholst, B., Sandt, J., Vogel, N. & Kolle, M. Stretchable Thermoplastic Elastomer Optical Fibers for Sensing of Extreme Deformations. *Advanced Functional Materials* **29.** ISSN: 16163028 (Feb. 2019).
147. Wang, D., Sheng, B., Peng, L., Huang, Y. & Ni, Z. Flexible and optical fiber sensors composited by graphene and PDMS for motion detection. *Polymers* **11.** ISSN: 20734360 (2019).
148. Yang, H. *et al.* Stretchable Strain Sensor based on HfSe2/LIG Composite with High Sensitivity and Good Linearity within A Wide Range. *Applied Surface Science,* 157772. ISSN: 01694332. `https://linkinghub.elsevier.com/retrieve/pii/S0169433223014514` (June 2023).
149. Wang, W. *et al.* Fingerprint-Inspired Strain Sensor with Balanced Sensitivity and Strain Range Using Laser-Induced Graphene. *ACS Applied Materials and Interfaces* **14,** 1315–1325. ISSN: 19448252 (Jan. 2022).
150. Guan, M. *et al.* Femtosecond laser-induced graphene for temperature and ultrasensitive flexible strain sensing. *Frontiers of Materials Science* **18.** ISSN: 20950268 (Sept. 2024).
151. Yang, H. *et al.* Three-dimensional surface strain sensor based on LIG/PDMS composite film with adjustable electromechanical performance. *Applied Surface Science,* 159885. ISSN: 01694332. `https://linkinghub.elsevier.com/retrieve/pii/S0169433224005981` (Mar. 2024).
152. Chen, H. *et al.* Advances in Graphene-based Flexible and Wearable Strain Sensors. *Chemical Engineering Journal,* 142576. ISSN: 13858947. `https://linkinghub.elsevier.com/retrieve/pii/S1385894723013074` (Mar. 2023).
153. Parmeggiani, M. *et al.* PDMS/Polyimide Composite as an Elastomeric Substrate for Multifunctional Laser-Induced Graphene Electrodes. *ACS Applied Materials and Interfaces* **11,** 33221–33230. ISSN: 19448252 (Sept. 2019).
154. Ma, Z. & Khoo, B. L. *Recent advances in laser-induced-graphene-based soft skin electronics for intelligent healthcare* 2024.
155. Li, Z., Huang, L., Cheng, L., Guo, W. & Ye, R. *Laser-Induced Graphene-Based Sensors in Health Monitoring: Progress, Sensing Mechanisms, and Applications* 2024.
156. Lamberti, A. *et al.* New insights on laser-induced graphene electrodes for flexible supercapacitors: Tunable morphology and physical properties. *Nanotechnology* **28.** ISSN: 13616528 (Apr. 2017).
157. Wang, Y., Wang, Y., Zhang, P., Liu, F. & Luo, S. Laser-Induced Freestanding Graphene Papers: A New Route of Scalable Fabrication with Tunable Morphologies and Properties for Multifunctional Devices and Structures. *Small* **14.** ISSN: 16136829 (Sept. 2018).

158. Jeong, S. Y. *et al.* Highly skin-conformal laser-induced graphene-based human motion monitoring sensor. *Nanomaterials* **11.** ISSN: 20794991 (Apr. 2021).
159. Kaidarova, A. *et al.* Wearable multifunctional printed graphene sensors. *npj Flexible Electronics* **3.** ISSN: 23974621 (Dec. 2019).
160. Raza, T. *et al.* Wearable and Flexible Multifunctional Sensor Based on Laser-Induced Graphene for the Sports Monitoring System. *ACS Applied Materials and Interfaces* **14,** 54170–54181. ISSN: 19448252 (Dec. 2022).
161. Qin, H. *et al.* Laser-Induced Graphene-Based Smart Textiles for Wireless Cross-Body Metrics. *ACS Applied Nano Materials* **6,** 19158–19167. ISSN: 25740970 (Oct. 2023).
162. Wang, H. *et al.* Laser Writing of Janus Graphene/Kevlar Textile for Intelligent Protective Clothing. *ACS Nano* **14,** 3219–3226. ISSN: 1936086X (Mar. 2020).
163. Yang, D. *et al.* Multimodal E-Textile Enabled by One-Step Maskless Patterning of Femtosecond-Laser-Induced Graphene on Nonwoven, Knit, and Woven Textiles. *ACS Nano.* ISSN: 1936-0851. `https://pubs.acs.org/doi/10.1021/acsnano.3c04120` (Aug. 2023).
164. Cheng, L. *et al.* Laser-Induced Graphene Strain Sensor for Conformable Lip-Reading Recognition and Human-Machine Interaction. *ACS Applied Nano Materials* **6,** 7290–7298. ISSN: 25740970 (May 2023).
165. Guo, W. *et al.* Laser-induced graphene based triboelectric nanogenerator for accurate wireless control and tactile pattern recognition. *Nano Energy* **108.** ISSN: 22112855 (Apr. 2023).
166. Jeong, S.-Y. *et al.* Enhancing Laser-Induced Graphene via Integration of Gold Nanoparticles and Titanium Dioxide for Sensing and Robotics Applications. *ACS Applied Materials & Interfaces.* ISSN: 1944-8244. `https://pubs.acs.org/doi/10.1021/acsami.4c03844` (June 2024).
167. Ling, Y. *et al.* Laser-Induced Graphene for Electrothermally Controlled, Mechanically Guided, 3D Assembly and Human–Soft Actuators Interaction. *Advanced Materials* **32.** ISSN: 15214095 (Apr. 2020).
168. Malard, L. M., Pimenta, M. A., Dresselhaus, G. & Dresselhaus, M. S. *Raman spectroscopy in graphene* Apr. 2009.
169. Cong, C. *et al.* Raman characterization of ABA- and ABC-stacked trilayer graphene. *ACS Nano* **5,** 8760–8768. ISSN: 19360851 (Nov. 2011).
170. Ferrari, A. C. & Basko, D. M. *Raman spectroscopy as a versatile tool for studying the properties of graphene* 2013.
171. Liu, F., Wang, G., Ding, X. & Luo, S. Multifunctional laser-induced graphene enabled polymeric composites. *Composites Communications* **25.** ISSN: 24522139 (June 2021).
172. Svelto, O. in *Principles of Lasers* 1–15 (Springer US, Boston, MA, 2010).
173. Kannatey-Asibu, E. *Principles of Laser Materials Processing* ISBN: 9780470177983 (Wiley, Apr. 2009).
174. Kumar Biswas, R., Vijayaraghavan, R. K., McNally, P., O'Connor, G. M. & Scully, P. Graphene growth kinetics for CO2 laser carbonization of polyimide. *Materials Letters* **307.** ISSN: 18734979 (Jan. 2022).
175. Ye, R., James, D. K. & Tour, J. M. Laser-Induced Graphene. *Accounts of Chemical Research* **51,** 1609–1620. ISSN: 15204898 (July 2018).
176. Herziger, F., Mirzayev, R., Poliani, E. & Maultzsch, J. In-situ Raman study of laser-induced graphene oxidation. *Physica Status Solidi (B) Basic Research* **252,** 2451–2455. ISSN: 15213951 (Nov. 2015).

177. Wahab, H. *et al.* Machine-learning-assisted fabrication: Bayesian optimization of laser-induced graphene patterning using in-situ Raman analysis. *Carbon* **167,** 609–619. ISSN: 00086223 (Oct. 2020).
178. Tao, J., Khosravi, H., Deshpande, V. & Li, S. Engineering by Cuts: How Kirigami Principle Enables Unique Mechanical Properties and Functionalities. *Advanced Science,* 2204733. ISSN: 2198-3844. `https://onlinelibrary.wiley.com/doi/10.1002/advs.202204733` (Oct. 2022).
179. Sun, B. *et al.* A Flexible Bimodal Pressure—Temperature Sensor with 3D Sandwich Structure and Thermal Drift Mitigation. *IEEE Sensors Journal.* ISSN: 15581748 (2025).
180. Wu, Y. *et al.* Temperature-insensitive stretchable conductors based on hierarchical double-layer graphene foams/PEDOT:PSS networks. *Composites Science and Technology* **242,** 110190. ISSN: 02663538. `https://linkinghub.elsevier.com/retrieve/pii/S0266353823002841` (Sept. 2023).
181. Park, T. *et al.* Noninterference Wearable Strain Sensor: Near-Zero Temperature Coefficient of Resistance Nanoparticle Arrays with Thermal Expansion and Transport Engineering. *ACS Nano* **15,** 8120–8129. ISSN: 1936086X. `https://pubs.acs.org/doi/10.1021/acsnano.0c09835` (May 2021).
182. Zhang, J., Wang, M., Yang, Z. & Zhang, X. Highly flexible and stretchable strain sensors based on conductive whisker carbon nanotube films. *Carbon* **176,** 139–147. ISSN: 00086223 (May 2021).
183. Zhang, Q. *et al. Doping of Laser-Induced Graphene and Its Applications* 2023.
184. Nam, K. H., Abdulhafez, M., Najaf Tomaraei, G. & Bedewy, M. Laser-Induced fluorinated graphene for superhydrophobic surfaces with anisotropic wetting and switchable adhesion. *Applied Surface Science* **574.** ISSN: 01694332 (Feb. 2022).
185. Cai, J. *et al.* Laser direct writing of heteroatom-doped porous carbon for high-performance micro-supercapacitors. *Energy Storage Materials* **25,** 404–415. ISSN: 24058297 (Mar. 2020).
186. Han, X. *et al.* Laser-Induced Graphene from Wood Impregnated with Metal Salts and Use in Electrocatalysis. *ACS Applied Nano Materials* **1,** 5053–5061. ISSN: 25740970 (Sept. 2018).
187. Liu, H. *et al.* Laser-oxidized Fe3O4 nanoparticles anchored on 3D macroporous graphene flexible electrodes for ultrahigh-energy in-plane hybrid micro-supercapacitors. *Nano Energy* **77.** ISSN: 22112855 (Nov. 2020).
188. Zhao, G. *et al.* High-performance hydrogen peroxide micro-sensors based on laser-induced fabrication of graphene@Ag electrodes. *Applied Surface Science* **565.** ISSN: 01694332 (Nov. 2021).
189. Xu, R., Liu, P., Ji, G., Gao, L. & Zhao, J. Versatile strategy to design flexible planar-integrated microsupercapacitors based on Co3O4-decorated laser-induced graphene. *ACS Applied Energy Materials* **3,** 10676–10684. ISSN: 25740962 (Nov. 2020).
190. Xu, R., Lu, H., Zheng, Z. & Zhou, T. In Situ Laser Direct Writing of Graphene-Based Layered Hybrid Materials with Superhydrophilicity. *ACS Applied Materials and Interfaces.* ISSN: 19448252 (2024).

191. Ding, X. *et al.* Standalone Stretchable Biophysical Sensing System Based on Laser Direct Write of Patterned Porous Graphene/Co ₃ O ₄ Nanocomposites. *ACS Sensors.* ISSN: 2379-3694. `https://pubs.acs.org/doi/10.1021/acssensors.4c00916` (June 2024).
192. Rathod, S., Snowdon, M., Jones, J., Zhang, K. & Peng, P. In Situ Rapid Fabrication of Graphene–Copper Heterojunctions Using Fiber Laser Direct Writing. *ACS Applied Materials & Interfaces.* ISSN: 1944-8244. `https://pubs.acs.org/doi/10.1021/acsami.3c11552` (Dec. 2023).
193. Nankali, M., Rouhi, M., Jones, J., Rathod, S. & Peng, P. Fiber Laser Writing of Highly Sensitive Nickel Nanoparticle-Incorporated Graphene Strain Sensors. *ACS Applied Materials & Interfaces.* ISSN: 1944-8244. `https://pubs.acs.org/doi/10.1021/acsami.4c07529` (July 2024).
194. Kim, J. *et al.* Rationally engineered interdigitated electrodes with heteroatom doped porous graphene and improved surface wettability for flexible micro-supercapacitors. *Journal of Energy Storage* **86,** 111271. ISSN: 2352152X. `https://linkinghub.elsevier.com/retrieve/pii/S2352152X24008569` (May 2024).
195. Yu, W., Peng, Y., Cao, L., Zhao, W. & Liu, X. Free-standing laser-induced graphene films for high-performance electromagnetic interference shielding. *Carbon* **183,** 600–611. ISSN: 00086223 (Oct. 2021).
196. Mayavan, S., Sim, J. B. & Choi, S. M. Easy synthesis of nitrogen-doped graphene-silver nanoparticle hybrids by thermal treatment of graphite oxide with glycine and silver nitrate. *Carbon* **50,** 5148–5155. ISSN: 00086223 (Nov. 2012).
197. Gan, Y., Bai, S., Hu, S., Zhao, X. & Li, Y. Reaction mechanism of thermally-induced electric conduction of poly(vinyl alcohol)-silver nitrate hybrid films. *RSC Advances* **6,** 56728–56737. ISSN: 20462069 (2016).
198. Ferraria, A. M., Carapeto, A. P. & Botelho Do Rego, A. M. X-ray photoelectron spectroscopy: Silver salts revisited. *Vacuum* **86,** 1988–1991. ISSN: 0042207X (July 2012).
199. Kumar, A. *et al.* Ultrasensitive Strain Sensor Utilizing a AgF-AgNW Hybrid Nanocomposite for Breath Monitoring and Pulmonary Function Analysis. *ACS Applied Materials and Interfaces* **14,** 55402–55413. ISSN: 19448252 (Dec. 2022).
200. `https://www.istockphoto.com/photos/torso`. Accessed: 2024-11-24.
201. Hegde, C. *et al. Sensing in Soft Robotics* Aug. 2023.
202. Yasa, O. *et al.* An Overview of Soft Robotics. *Robotics, and Autonomous Systems Annu. Rev. Control Robot. Auton. Syst. 2023* **36,** 1–29. `https://doi.org/10.1146/annurev-control-062322-` (2025).
203. Wang, H., Zhao, Z., Liu, P., Pan, Y. & Guo, X. Stretchable Sensors and Electro-Thermal Actuators with Self-Sensing Capability Using the Laser-Induced Graphene Technology. *ACS Applied Materials and Interfaces.* ISSN: 19448252 (2022).
204. Timoshenko, S. Analysis of Bi-Metal Thermostats. *Journal of the Optical Society of America* **11,** 233. ISSN: 0030-3941. `https://opg.optica.org/abstract.cfm?URI=josa-11-3-233` (Sept. 1925).
205. Truong, T. T. N., Kim, J. S., Yeun, E. & Kim, J. Wearable capacitive pressure sensor using interdigitated capacitor printed on fabric. *Fashion and Textiles* **9.** ISSN: 21980802 (Dec. 2022).
206. Bobinger, M. R. *et al.* Flexible and robust laser-induced graphene heaters photothermally scribed on bare polyimide substrates. *Carbon* **144,** 116–126. ISSN: 00086223 (Apr. 2019).

207. Shi, X. *et al.* One-Step Scalable Fabrication of Graphene-Integrated Micro-Supercapacitors with Remarkable Flexibility and Exceptional Performance Uniformity. *Advanced Functional Materials* **29.** ISSN: 16163028 (Dec. 2019).
208. Kun, H., Bin, L., Orban, M., Donghai, Q. & Hongbo, Y. Accurate Flexible Temperature Sensor Based on Laser-Induced Graphene Material. *Shock and Vibration* **2021.** ISSN: 10709622 (2021).
209. Kulyk, B. *et al.* Laser-Induced Graphene from Paper by Ultraviolet Irradiation: Humidity and Temperature Sensors. *Advanced Materials Technologies* **7.** ISSN: 2365709X (July 2022).
210. Hou, M. *et al.* Laser induced graphene based high-accurate temperature sensor with thermal meta-shell encirclement. *International Journal of Heat and Mass Transfer* **217.** ISSN: 00179310 (Dec. 2023).
211. Han, T. *et al.* Multifunctional flexible sensor based on laser-induced graphene. *Sensors (Switzerland)* **19.** ISSN: 14248220 (Aug. 2019).
212. Xu, K. *et al.* Toward Integrated Multifunctional Laser-Induced Graphene-Based Skin-Like Flexible Sensor Systems. *ACS Nano.* ISSN: 1936-0851. `https://pubs.acs.org/doi/10.1021/acsnano.4c09062` (Sept. 2024).
213. Coelho, J. *et al.* Paper-based laser-induced graphene for sustainable and flexible microsupercapacitor applications. *Microchimica Acta* **190.** ISSN: 14365073 (Jan. 2023).
214. Lu, Y. *et al.* Stretchable graphene–hydrogel interfaces for wearable and implantable bioelectronics. *Nature Electronics.* ISSN: 2520-1131. `https://www.nature.com/articles/s41928-023-01091-y` (Dec. 2023).
215. Dallinger, A., Kindlhofer, P., Greco, F. & Coclite, A. M. Multiresponsive Soft Actuators Based on a Thermoresponsive Hydrogel and Embedded Laser-Induced Graphene. *ACS Applied Polymer Materials* **3,** 1809–1818. ISSN: 26376105 (2021).
216. Zhang, C. *et al.* Human motion-driven self-powered stretchable sensing platform based on laser-induced graphene foams. *Applied Physics Reviews* **9.** ISSN: 19319401 (Mar. 2022).
217. Yan, Z. *et al.* Flexible High-Resolution Triboelectric Sensor Array Based on Patterned Laser-Induced Graphene for Self-Powered Real-Time Tactile Sensing. *Advanced Functional Materials* **31.** ISSN: 16163028 (June 2021).
218. Xie, B. *et al.* *Laser-induced graphene enabling self-powered wireless direction sensor* in *2022 23rd International Conference on Electronic Packaging Technology, ICEPT 2022* (Institute of Electrical and Electronics Engineers Inc., 2022). ISBN: 9781665499057.
219. He, M., Wang, Y., Wang, S. & Luo, S. Laser-induced graphene enabled 1D fiber electronics. *Carbon* **168,** 308–318. ISSN: 00086223 (Oct. 2020).
220. Groo, L. A. *et al.* Laser induced graphene in fiberglass-reinforced composites for strain and damage sensing. *Composites Science and Technology* **199.** ISSN: 02663538 (Oct. 2020).
221. Francis, C. *et al.* Laser-induced graphene gas sensors for environmental monitoring. *Frontiers in Chemistry* **12.** ISSN: 22962646 (2024).
222. Cheng, L. *et al.* *Laser-induced graphene for environmental applications: Progress and opportunities* July 2021.